ISSN: 1847-9286
Open Access Journal
www.jese-online.org

JESE

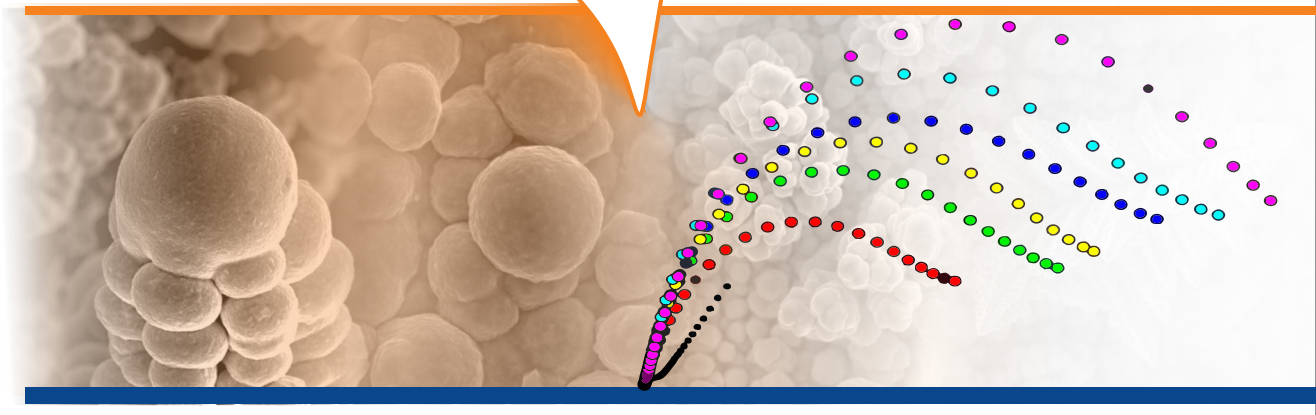

Journal of Electrochemical Science and Engineering

J. Electrochem. Sci. Eng. **12**(**2**) 2022, 237-398

IAPC Publishing

J. Electrochem. Sci. Eng. **12(2)** (2022) 237-252; http://dx.doi.org/10.5599/jese.1135

Open Access : : ISSN 1847-9286

-

Review Paper

A review of the electrochemical corrosion of metals in choline chloride based deep eutectic solvents

Mihael Bučko✉ and Jelena B. Bajat[1]

University of Defence, Military Academy, 33 Pavla Jurišića Šturma St, 11000 Belgrade, Serbia

[1]Faculty of Technology and Metallurgy, University of Belgrade, Karnegijeva 4, 11120 Belgrade, Serbia

Corresponding author: ✉ mbucko@tmf.bg.ac.rs; Tel.: +381-11-3603-464; Fax: +381-11-3603-065

Received: October 19 2021; Accepted: November 3, 2021; Published: November 13, 2021

Abstract

Deep eutectic solvents (DESs) are a class of mixtures with melting points notably lower than those of their raw constituent components. These liquids have found a tremendously wide spectrum of applications in the last two decades of their research, so their contact and interaction with technical metals and alloys are inevitable. Therefore, the corrosivity of DESs towards metals is an extremely important topic. This review summarizes research efforts collected in the last two decades related to the corrosion rate of various metals in different DESs. Since the DESs are mainly composed of organic raw compounds, and by their physicochemical properties they may be regarded as a separate class of ionic liquids, the literature data about DESs corrosivity has been compared to the data related to the corrosivity of various organic solvents and ionic liquids as well. All the results gained until now show significantly low corrosivity of DESs. This observation is discussed in relation to the chemical composition of DESs. The absence of the oxidizing agents, the inhibitory action of organic ions and molecules, high viscosity and low electrical conductivity have been recognized as the main factors contributing to the low metal corrosion rate in DESs.

Keywords

ionic liquids; ethaline; reline; glyceline; hydrogen bond donor

Contents

1. Introduction

Deep eutectic solvents (DESs) refer to mixtures of two or three solid or liquid compounds in a eutectic composition, where an unusually deep melting point depression is observed [1,2]. The preparation of DESs usually consists of simple mixing of the two components for several hours at a slightly elevated temperature until the homogeneous liquid is obtained (Figure 1). The main characteristic of DESs is that they are in a liquid state at room or slightly elevated temperatures [3]. Although they may not be considered ionic liquids, the DESs share many physical characteristics, such as relatively high viscosity and density, low electrolytic conductivity compared to aqueous solutions, low volatility and vapour pressure, and high thermal stability. These attributes make DESs good candidates for the replacement of traditional volatile organic solvents in many industries [4]. In addition, the DESs have some beneficial features compared to conventional ionic liquids: they are usually composed of inexpensive, widely available compounds that are biodegradable and nontoxic [5].

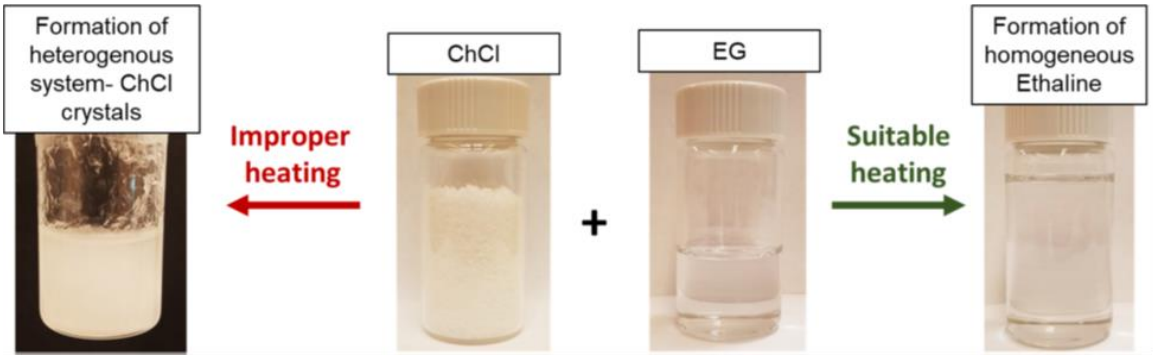

Figure 1. *Preparation of ethaline: dried choline chloride and ethylene glycol are mixed in a controlled atmosphere (Ar-filled glovebox), heated to 80 °C for 2 hours, then cooled to room temperature. Improper heating can lead to the formation of choline chloride crystals (*i.e., *precipitation from solution) [6]. Reprinted with permission from ref. [6], copyright (2019), American Chemical Society*

During the last two decades, DESs have been involved in various applications, the most important being: dissolution of metal oxides and salts in metallurgy [7]; electrolytes in metal and alloy electroplating [8,9]; liquid-liquid extraction [10]; metal extraction [11]; gas solubility and capture [12]; electrolytes in batteries [13] or solar cells [14]; biocatalysis [15]; extraction and preparation of biodiesel [16]; biomass processing [17]; biomolecular structure stabilization [18]; genomics [19]; pharmaceutical and medical applications [20]; nanomaterials synthesis [21].

The DESs have been particularly recognized as a convenient way to extend the range of coating/substrate combinations that may be produced by the electrodeposition process, in comparison to the existing electroplating processes in water-based baths [22-24]. For example, the DESs may be an alternative for the electroplating of metals having electroreduction potential more negative to the potential of water decomposition, such as Ti, Al, and W [22,25,26]. Furthermore, the electroplating in DESs may afford the replacement of the electroplating systems known to be toxic and carcinogenic, such as Cr, Ni and Co [9,23,25,27]. Figure 2 illustrates an example of the surface-sensitive Ni electrodeposition at Pt(111) single crystal surface, from choline chloride + urea DES (reline) [9]. The number of pure metal and alloy coatings that have already been successfully obtained by electrodeposition in DESs is significant, so here only the most important examples are mentioned, including corrosion-resistant coatings like Cu [28-31] and Zn-alloys [32], magnetic alloys like Sm–Co [33,34], semiconducting alloys like $CuGaSe_2$ [35], electrocatalytic surface alloys like Pt–Co [36], *etc*.

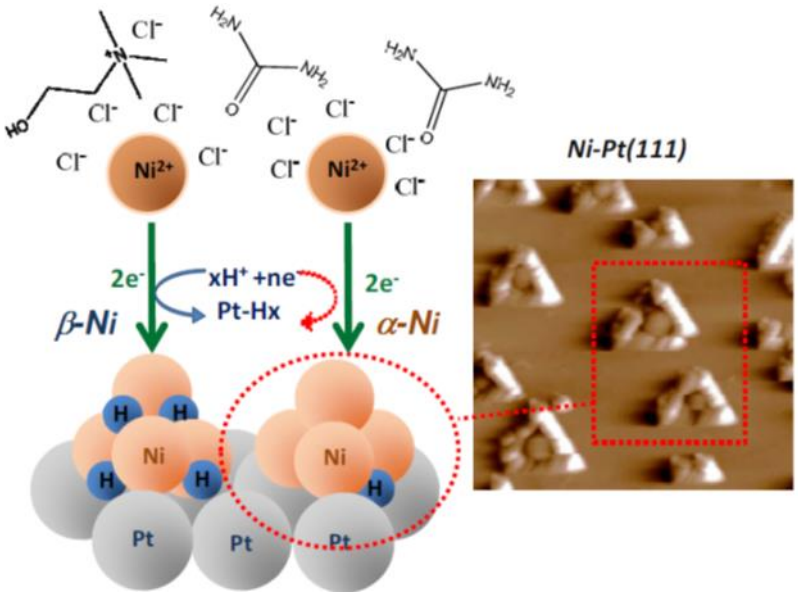

Figure 2. *Representation of Ni(II) electrodeposition in DES on Pt(111) and AFM image (2×2 μm^2) of Ni clusters [9]*
Reprinted with permission from ref. [9] copyright (2018), American Chemical Society

To apply deep eutectic solvents in any large-scale process, it is important to gain knowledge about their corrosivity and interaction with different materials, particularly technical metals and alloys. This article first addresses the important features of the DESs chemical composition: their protic/aprotic character and the presence of strong complexing agents. It further recaps the data related to the metal corrosion rates collected in various DESs and by different measuring methods. Finally, it summarizes the most relevant factors responsible for a generally low corrosion rate in DESs.

2. Chemical composition of deep eutectic solvents

A mixture of any two compounds that exhibits a deep melting temperature decrease at the eutectic ratio of the two components may be regarded as a DES. Up to now, various DESs have been prepared by combining a quaternary ammonium salt, a metal salt or a metal salt hydrate, and a hydrogen bond donor (HBD), usually an organic molecule such as an amide, carboxylic acid, or polyol [2]. Table 1 explains the classification of DESs into five types according to their components [4,22,37]:

Table 1. *Five types of deep eutectic solvents*

	Metal salt	Metal salt hydrate	Organic molecule as HBD
Quaternary ammonium salt	Type 1	Type 2	Type 3
Metal salt hydrate			Type 4
Organic molecule as hydrogen bond acceptor (HBA)			Type 5

It is estimated [38] that there may be 10^6–10^8 potential DES formulations as various binary combinations of ammonium salts, metal salts, and organic molecules. Since the majority of DESs contain an organic compound as one of the constituents, to predict the corrosivity of a particular DES, it is advisable to first analyse the metal corrosion in a particular organic, since the literature about this topic is usually vastly available [39].

Interestingly, up to now, only the metal and alloy corrosion in the Type 3 DESs has been studied, and particularly in DESs containing choline chloride as a quaternary ammonium salt, and as a result, this review focuses primarily on the metal corrosion in Type 3 DESs.

3. Protic character of DESs

Metals with the corrosion potential more negative than the equilibrium potential of hydrogen electrode corrode with the electroreduction of hydrogen proton. The presence of solvated hydrogen proton in protic organic media thus induces corrosion of electronegative metals [39]. It should be held in mind that the most frequently used HBDs in Type 3 DESs (alcohols, amides and carboxylic acids) are protic organic compounds, and so the presence of free hydrogen ions may be expected in these DESs.

The pH value of a DES depends on the ability of the DES's cation, anion, and HBD to act as proton acceptors and proton donors [40,41]. If HA is a protic hydrogen bond donor, then the protonation reaction in DES is

$$HA + Y \rightleftharpoons HY^+ + A^- \quad (1)$$

where Y represents the DES constituent [40,41].

Metal corrosion may occur due to the partial cathodic reaction of the protonated species

$$2HY^+ + 2e^- \rightarrow 2Y + H_2 \quad (2)$$

but also, as it is often the case in organic solutions, due to the direct hydrogen evolution from the non-dissociated proton donor [42]:

$$2HA + 2e^- \rightarrow 2A^- + H_2 \quad (3)$$

The experimentally determined pH values of a few representative choline chloride based Type 3 DESs are listed in Table 2. The pH value of ChCl based DESs is significantly influenced by the type of HBD. The acidity decreases in the following order: DESs with carboxylic acids (citric, glycolic, lactic, malic, malonic, oxalic acid)>polyols (ethylene glycol, glycerol) > sugars(fructose, glucose) > amines and amides (urea, ethanolamine, diethanolamine) [41]. For all choline chloride based DESs, a linear decrease of pH value was observed with the increase in temperature, and as concerning the water influence, the increase in water content decreases the pH for the majority of DESs. However, there are DESs where the opposite was observed, for instance in ChCl-citric acid mixture [41].

Table 2. *Experimentally measured pH values of several DESs*

DES	pH value	Reference
1 ChCl : 1 oxalic acid	1.32	[43]
1 ChCl : 1 malonic acid	2.39	[43]
1 ChCl : 1 citric acid : 3 H_2O	0.63−0.67	[44]
1 ChCl : 2 ethylene glycol	4.77 5.93 (pH indicator) 6.89 (pH glass electrode)	[45] [43] [43]
1 ChCl : 2 glycerol	7.54 7.48	[46] [43]
1 ChCl : 2 urea	10.39 10.07	[46] [47]

The fast metal corrosion due to the rapid hydrogen evolution reaction in acidic DESs was demonstrated by Abbott *et al*. [48], where it was shown that the corrosion rate (expressed in µm per year) for mild steel in oxaline was two orders of magnitude higher in comparison to reline and ethaline, whereas it was one order of magnitude higher for Ni. Interestingly, the corrosion rate of Al was low and very similar in both acidic and pH neutral DESs, probably due to the Al passivation by oxalate anion [48]. High acidity of an organic acid containing DESs is beneficial for the dissolution

of various metal oxides in industrial and recycling processes because the hydrogen protons act as oxygen acceptors and break the metal–oxide bonds [49].

4. High concentration of ligands in DESs

Choline chloride based DESs contain ~5 mol dm^{-3} chloride anions, and these species are well known to be detrimental for metal corrosion in two ways. Firstly, the chloride ions cause the metal oxide film rupture and pitting corrosion. According to the kinetic model of pitting corrosion, the pit initiation starts with the adsorption of chloride ions on the metal oxide surface and their penetration through the oxide film and propagates with the localized dissolution of metal at the metal/oxide interface [50,51]. Secondly, chloride is a ligand that forms complex salts with metal ions, increasing the solubility of metal ions and metal compounds, preventing metal passivation, and displacing the redox electrode potential of the metal to the negative side, making its anodic dissolution easier [52]. As a matter of fact, since the 1990s the halide salts have been used as ligands to promote metal solubility in organic solvents [53].

The catalytic role of chloride anion in the anodic partial reaction of a metal corrosion process is well known for aqueous media, for example, in the cases of copper and steel corrosion [54,55]. It is assumed that the first step in the metal anodic dissolution mechanism is one of the following reactions:

$$Cu + Cl^- \rightleftharpoons CuCl + e^- \quad (4)$$

$$CuCl + Cl^- \rightleftharpoons CuCl_2^- \quad (5)$$

$$Cu + 2Cl^- \rightleftharpoons CuCl_2^- + 2e^- \quad (6)$$

$$Fe + Cl^- \rightleftharpoons FeCl + e^- \quad (7)$$

$$FeCl \rightleftharpoons Fe^+ + Cl^- \quad (8)$$

The identical participation of Cl^- is also very likely present in the metal dissolution process in DESs [28,56]. Furthermore, by identifying FeOCl in the corrosion products at steel immersed in ethaline and reline, Kityk *et al.* [56] concluded that the chloride ion present in large concentrations even changes the mechanism and accelerates steel corrosion in DES, in comparison to water solution. Particularly, Cl^- ions enable the formation of FeOCl, an intermediate compound that facilitates the formation of γ-FeOOH [56].

Due to the high Cl^- concentration in DESs, the majority of metal ions are solvated in DESs in the form of various chloro-complexes. The metal speciation was studied in DES mixtures of choline chloride with several HBDs (urea, ethylene glycol, propylene glycol, and 1,3-propanediol), by dissolving various metal salts, namely sulphates, nitrates, oxides, thiocyanates, and perchlorates [57]. It was found that M^+ ions form $[MCl_2]^-$and $[MCl_3]^{2-}$species and/or their mixtures, depending on the HBD present, for instance $[CuCl_2]^-$ and $[CuCl_3]^{2-}$, $[AgCl_2]^-$and $[AgCl_3]^{2-}$, $[AuCl_3]^{2-}$, *etc*. This speciation is consistent with the chemistry in aqueous solutions with high chloride concentrations [58].

As concerning M(II) salts, in diol-based DESs all M^{2+} ions, except Ni^{2+}, form tetrachloro complexes $[MCl_4]^{2-}$, like for example, $[FeCl_4]^{2-}$, $[ZnCl_4]^{2-}$, $[PtCl_4]^{2-}$, *etc.* Interestingly, chloride was not found in the Ni^{2+}coordination shell, but rather only the $[Ni(HBD)_3]^{2+}$ cationic complexes were detected [57]. Contrary to the diol based DESs, in urea-based DES, the complex ion composition depends on the metal: the late transition metals form tetrachloro complex anions, but early transition metals like Fe, Mn and Cr, form salts with HBD as a ligand, where HBD may be water or urea, *i.e*., $[Mn(HBD)_6]^{2+}$, $[Fe(HBD)_5]^{2+}$ and $[CoCl_3(HBD)]^-$ [57].

Among M(III) salts, the experiments with Cr^{3+} in the same study [57] showed that in ethylene glycol-based DES, chromium forms complex salt with mixed ligands $[Cr(H_2O)_2Cl_4]^{2-}$, and in urea-based DES, the first shell consists only of HBD, *i.e*. $[Cr(HBD)_6]^{3+}$.

Dissimilar metal speciation in DESs compared to water is responsible for the difference in the electrochemical series, *i.e.,* the series of equilibrium electrode potentials for redox reactions of various metal/metal ion couples in different media. Electrode potentials for some redox couples in ethaline were reported [59] and compared to the analogous values in an aqueous, metal chloride containing medium. It was apparent that some equilibrium electrode potentials were positive, while others were more negative compared to the values measured in water. For the redox couples with more negative potential in ethaline, the redox equilibrium in ethaline is shifted to the species with a higher oxidation state compared to the equilibrium in water, and the reverse is true for the couples above the line. It was noticeable that for metals that form strong chloro-complex ions (Au, Pd, Ag), there was a significant negative deviation of the equilibrium redox potential in ethaline. An interesting case was observed for Cu: the equilibrium potential for the redox couple Cu^+/Cu is surprisingly negative in ethaline. However, the potential of the Cu^{2+}/Cu^+ couple is very positive, pointing to the fact that in ethaline, the Cu^+ species is stable along with Cu and Cu^{2+} [59].

Interesting investigations of Cu corrosion in ethaline show that Cu dissolution is accelerated when Cu^{2+} species are present in the medium due to the comproportionation reaction (Eq. 9).

$$CuCl_4^{2-} + Cu \rightarrow 2CuCl_2^- \quad (9)$$

This reaction is well known in chloride-containing aqueous media, and it seems that the analogous mechanism may be applied for the case of ethaline [28,29]. The consequence of this reaction is observed in the electrodeposition process with Cu soluble anode, where the so-called "anomalous dissolution" occurs, *i.e.,* the mass loss of Cu anode is much higher than anticipated based on the amount of charge passed for a single electron transfer. In other words, in case Cu^{2+} is present in ethaline, the anodic dissolution processes occurring at the Cu anode to form $CuCl_2^-$ are coupled with the cathodic process involving the reduction of $CuCl_4^{2-}$ [28,29].

5. Electrochemical tests and measured corrosion rates in DESs

The corrosion rate of various metals in choline chloride-based DESs has been analysed by electrochemical methods in majority of the previous studies, and the reported data are summarized in Table 3. For nearly pH neutral DESs, *i.e.,* with the exception of acidic DESs, generally, it may be concluded that all the sources report significantly low corrosion rates, ranging from around 1 μA cm^{-2} to extremely low values of the order of nA cm^{-2}. For example, the comparison of the surface morphology of Al alloy samples exposed to the air and to reline at 60 °C for 19 days (Figure 3) showed that all the samples were shiny. The brownish deposits at the samples immersed in reline, were not corrosion products or signs of pitting, but rather only reline deposits not removed by the washing process [60].

Except for the results reported in [63], the DESs were reported as of very low corrosivity to various metals, in practically all of the conducted studies available in the literature, in spite of containing strong ligands in high concentration. The Cu dissolution in [63] was promoted by the rotation of the working electrode and the ultrasonic agitation to enhance metal leaching in ethaline. Therefore, it is understandable that the corrosion rate in such working conditions is significantly higher than the values measured in stationary conditions.

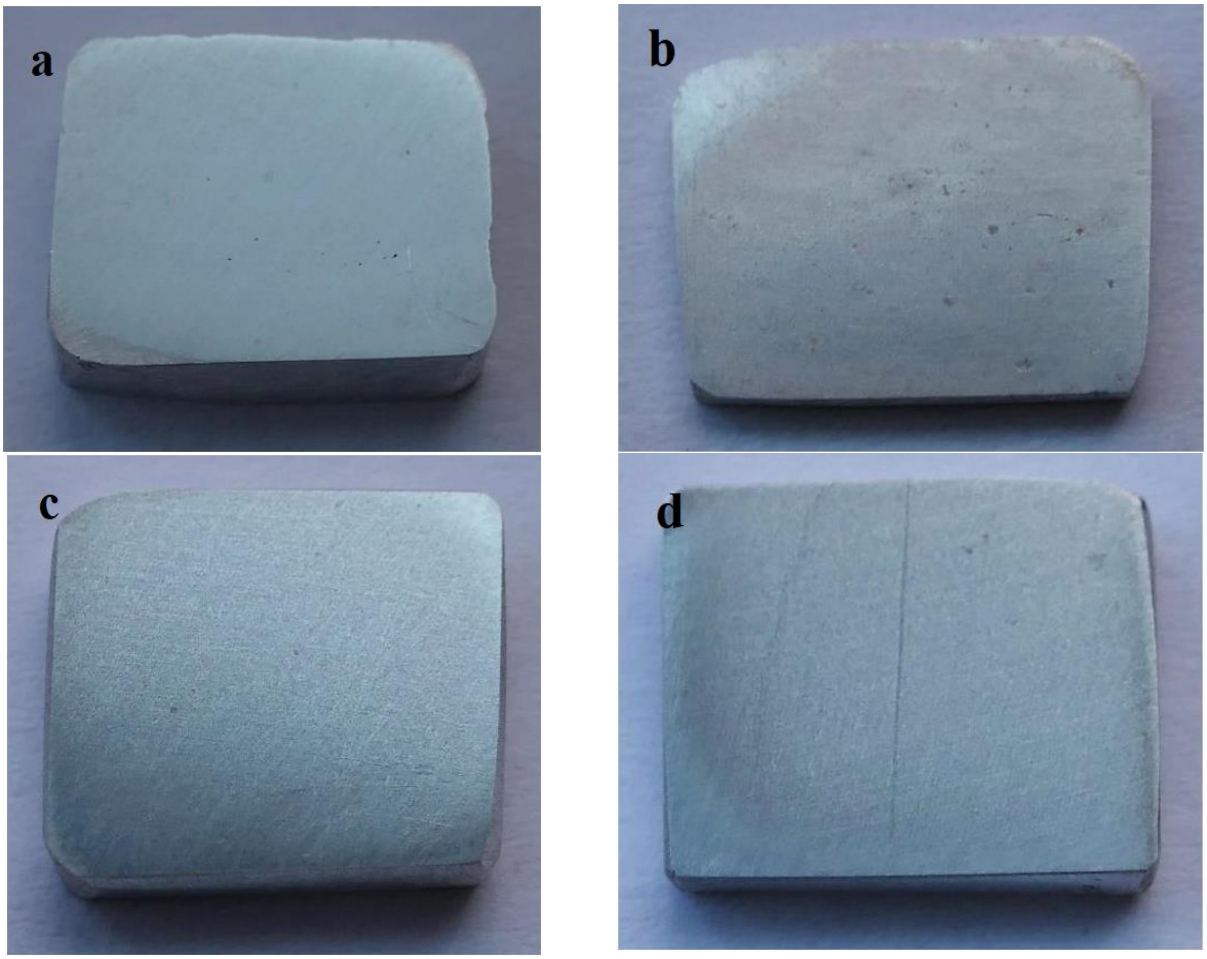

Figure 3. *Visual inspection of the alloy samples after 19 days: (a,c) AA2024-T6, AA6065-T6 in the air; (b,d) AA2024-T6, AA6065-T6 in reline, respectively [60]*
Reprinted with permission from ref. [60] copyright (2020), Elsevier

Very low corrosivity of DESs had been ascribed to the absence of an oxidizing species in DESs, high viscosity and low electrical conductivity of DESs, the formation of a protective layer at the metal surface immersed in DES, or the inhibiting action of the constituting compounds in DESs [48,56,60-62].

The chemical corrosion of a metal in a corrosive medium implies the reaction of metal with species X and the formation of corrosion product:

$$M + X \rightarrow MX \quad (10)$$

In analogy, electrochemical corrosion implies the transfer of electrons from a metal surface to the corrosion agent, *i.e.,* to the species in a corrosive medium capable of metal oxidation:

$$M \rightarrow M^{n+} + ne^- \quad (11)$$

$$ne^- + X \rightarrow X^{n-} \quad (12)$$

The well-known corrosion agents in aqueous media are water molecules, oxygen molecules, and hydrogen ions. Understandably, if these species are present as impurities in non-aqueous media, they also may act as agents inducing metal corrosion.

Yet, in case that the liquid medium does not contain any compound that can act as a corrosion agent for metal, the medium remains chemically inert and the metal corrosion does not occur.

It has been stated [52,56,60] that apart from oxygen and water present as impurities, the pH-neutral choline chloride based DESs do not contain any other species capable of metal oxidation. To support this statement, it is useful to tackle the oxidizing power of the organic compounds representing the most often used constituents in DESs.

Table 3. *Corrosion rate data for several DESs.*

Metal	DES	j_{corr} / μA cm^{-2}	testing method, reference
steel	reline	0.87 at 25 °C 1.72 at 80 °C	Tafel plots, [56]
	reline	10^{-3} at 25 °C 0.02 at 75 °C	Tafel plots, [61]
	ethaline	1.18 at 25 °C 1.78 at 80 °C	Tafel plots, [56]
	ethaline	0.2 at 25 °C 3.9 at 75 °C	Tafel plots, [61]
	glyceline	6 10^{-3} at 25 °C 0.52 at 75 °C	Tafel plots, [61]
	ChCl-malonic acid	5 at 25 °C 187 at 75 °C	Tafel plots, [61]
copper	reline	3.58 at 25 °C 30.45 at 75 °C	Tafel plots, [61]
	reline	340 at 80 °C	Tafel plots, [62]
	ethaline	17.44 at 25 °C 166.53 at 75 °C	Tafel plots, [61]
	ethaline	460 at 50 °C 8700 at 50 °C 27540 at 50 °C	Tafel plots, RDE 5000 rpm [63] Tafel plots, ultrasonic agitation (US) [63] Tafel plots, RDE 5000 rpm + US [63]
	Glyceline	6.03 at 25 °C 31.22 at 75 °C	Tafel plots, [61]
	ChCl-malonic acid	7.43 at 25 °C 333.17 at 75 °C	Tafel plots, [61]
Stainless steel 316	Reline	8×10^{-3} at 25 °C 0.013 at 75 °C	Tafel plots, [61]
	Ethaline	0.014 at 25 °C 0.23 at 75 °C	Tafel plots, [61]
	Glyceline	8×10^{-3} at 25 °C 0.11 at 75 °C	Tafel plots, [61]
	ChCl-malonic acid	0.4 at 25 °C 22.7 at 75 °C	Tafel plots, [61]
Aluminum alloys AA2024 and AA6065	Reline	0.4 at 60 °C	Inductively coupled plasma optical Emission spectroscopy, [60]
Extremely low corrosion rates for mild steel, Ni and Al in reline, ethaline, and glyceline: 1.9 to 5.02 μm year^{-1}			Tafel plots, [48]
Very slow reaction of AZ31B Mg alloy in ethaline, at temperatures up to 85 °C			[64]

Cholinium cation, being the representative of quaternary ammonium cations, is extremely stable toward the electroreduction, even at very negative electrode potentials [65]. Pure ethylene glycol (a constituent of ethaline) is almost inert even to reactive metals like magnesium [66]. As concerning urea (a constituent of reline), although the molten urea is a very versatile solvent that dissolves the majority of inorganic chemicals [67], the data on its corrosivity are very scarce. Yet, it is known from the research in urea production plants that the pure molten urea is not corrosive to stainless steels [68] and in addition, it has been used as a supporting electrolyte with a wide electrochemical window [69]. This brief summary shows that, indeed, the pure organics used for preparing the most common DESs, are not capable of metal oxidation.

The second important reason for the low corrosivity of choline chloride-based DESs is probably the corrosion inhibiting nature of the raw compounds. Like most organics, the choline cation and the common hydrogen bond donors should be easily adsorbed onto a metal surface, which is the main prerequisite for the inhibition of the corrosion process by blocking the anodic and/or cathodic sites. Consequently, the literature on the application of quaternary ammonium ions [70], choline based salts [71], choline based ionic liquids [72], urea [73], ethylene glycol [66, 74], alcohols in general [75], *etc*., as corrosion inhibitors in aqueous media, is extensive.

In [60], very low corrosion of AA2024-T6 and AA6065-T6 alloys in reline was ascribed to the adsorption of choline cation or urea molecules on the metal surface, where one or both of these species constitute the first liquid layer in contact with Al_2O_3 passive film, thus separating and protecting it from the Cl^- anions. It was well documented for various DESs (choline chloride with ethylene glycol, 1,2- ethanediol, 1,2-propanediol, 1,3-propanediol, urea or thiourea) that at negative and open circuit electrode potential, the choline cations and HBD molecules occupy the first layer of adsorbate at the metal surface, whereas at a positive potential, the Cl^- anion is adsorbed [76, 77]. The mechanism of reline adsorption at various 2D nanomaterials was studied using molecular simulation methods [78]. Independently on the material used as a substrate, the number density profiles showed that the first adsorbed layer mainly consisted of urea molecules, while the number of Cl^- ions was significantly low, as presented in Figure 4 [78].

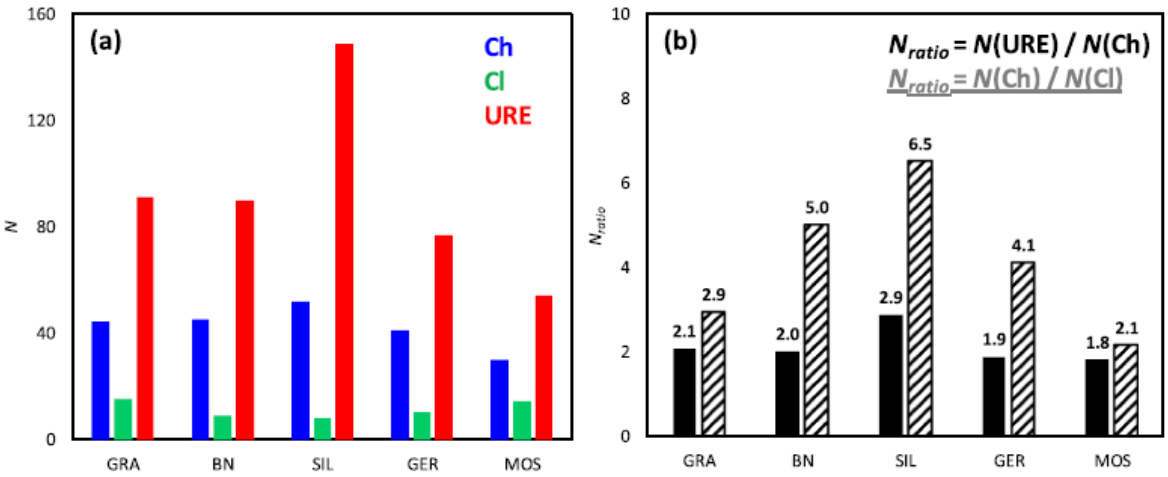

Figure 4. *Number of molecules, N, in the first adsorbed layer for reline adsorbed on graphene, boron nitride, silicene, germanene, and molybdenum disulfide [78]*
Reprinted with permission from ref. [78] copyright (2020), American Chemical Society

Finally, as is the case in other organic media, an important factor of the metal corrosion rate in DES, may be the DES high viscosity or low electrical conductivity. For example, in the case of Zn corrosion in HCl-containing representatives of alcohols, ketones, esters, ethers, aromatics and chlorinated hydrocarbons, the viscosity was singled out as the decisive factor in the corrosion rate since it plays an important part in the transport of the oxidation agent and corrosion products [79]. On the contrary, in the same investigation and same media, for other metals under study (Fe, Al and stainless steel), the electrolytic conductivity of the solvents showed the most notable influence on the corrosion rate. It was concluded that the conductivity of around 10 mS cm^{-1} represents a threshold value below which the corrosion process is considerably retarded, because the corrosion mechanism changes from electrolytic to non-electrolytic. The industrial application of organic media with conductivity lower than the listed threshold value would enable the employment of construction materials that are lower in price without fear of corrosion [79].

It is very important to draw the parallel between the described findings in organic media and the case of DESs, bearing in mind the high viscosity and low electrical conductivity of the majority of DESs, as illustrated in Table 4. For instance, the high reline viscosity and low diffusivity of species in this liquid were assumed to be an important factor in Al-oxide passive film's stability at the Al-alloys in reline. Namely, the passive layer at the AA2024-T6 and AA6065 alloy surfaces remained intact even after 35 days of exposure to reline at 60 °C [60]. It was concluded that the pitting corrosion, even if it occurs at some point, will be terminated due to the significant mass transport limitation in a viscous medium because the diffusion of metal cations within the pit is necessary for a stable pit formation.

Although the conductivity of DESs with common HBDs listed in the table is notably higher than the conductivity of molecular solvents like ethylene glycol and glycerol, it is still well below the critical value of 10 mS cm^{-1}.

Table 4. *Viscosity and electrical conductivity of several DESs, some ionic liquids, and some molecular solvents at 298 K*

Solvent	Viscosity, cP	Conductivity, mS cm^{-1}	Reference
ChCl-malonic acid	721	0.55	[4]
ChCl-urea DES	632	0.75	[4]
ChCl-glycerol	376	1.05	[4]
ChCl-ethylene glycol DES	36	7.61	[4]
C_4mimBF_4 ionic liquid	115	3.5	[4]
Glycerol	967	5 10^{-5}	[80]
Ethylene glycol	16.1	1.4 10^{-4}	[81]

6. Effect of water content

Since choline chloride and typical HBDs in DESs (amides, alcohols, polyols, carboxylic acids, *etc*.) are very hygroscopic substances, a highly hydrophilic behaviour of most choline chloride-based DESs is expected [82]. As an illustration, reline contains 2500 ppm water even after a drying process conducted in a vacuum oven at 353 K over 24 h, and it can absorb atmospheric moisture up to a water concentration of 40 wt.% [83]. Similarly, the as-prepared ethaline contained 2.4 wt.% water even after thorough drying of precursor materials, and after two weeks in the open air, the water content reached 14.3 wt.% [82].

In general, water in DES decreases its kinematic viscosity (Figure 5), increases its electrical conductivity, and notably narrows its electrochemical window [82,84], and all these factors contribute to the increase in the corrosion processes rate. Consequently, it was shown in [85] that the corrosion of mild steel in ethaline and reline is significantly enhanced even with the addition of only 10 wt.% of water.

Very similar observations may be found in numerous researches of the water effect on the corrosivity of ionic liquids. When the corrosion behaviour of carbon steel, austenitic stainless steel, nickel-based alloy, copper, brass and AlMg3 alloy was examined in seven ionic liquids with different chemical structures, the addition of only 10 % of water increased the corrosivity of all ionic liquids significantly [87]. The increased corrosion rate with water addition of up to 8 wt.% was also measured for the case of Mg alloys in 1-butyl-3-methylimidazolium trifluoromethyl sulfonate ionic liquid [88].

The water effect on the metal corrosion rate in ionic liquids and deep eutectic solvents was ascribed to the increased solubility of oxygen as a cathodic species in the corrosion mechanism, higher diffusivity of oxygen, and the easier removal of corrosion products [85,89]. Moreover, it is known that

the presence of water in an ionic liquid can cause anion hydrolysis, increasing electrolyte aggressiveness [89]. This should also be held in mind when a particular DES is selected for technical applications.

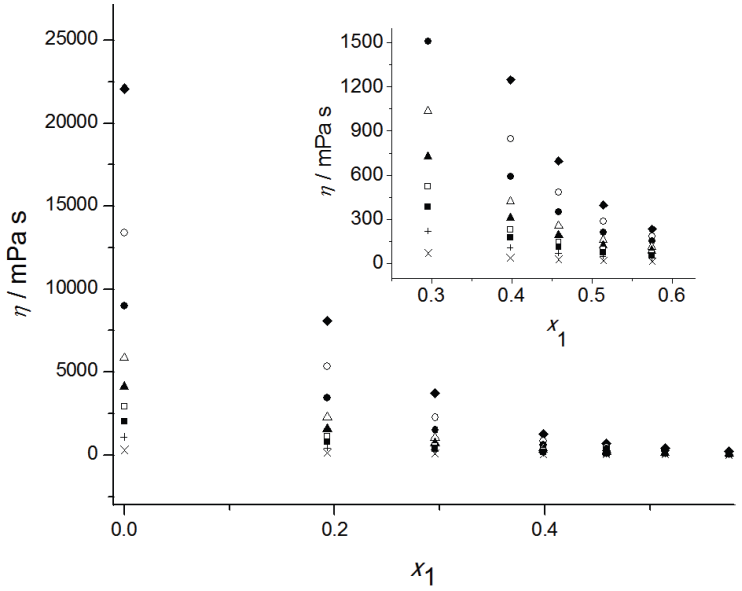

Figure 5. *Experimental values of viscosity vs. water mole fraction for the choline chloride+DL-malic acid DES, where symbols refer to experimental data points at several temperatures: 298.15 K (◆); 303.15 K (○); 308.15 K (●); 313.15 K (Δ); 318.15 K (▲); 323.15K (□); 328.15 K (■); 338.15 K (+); 348.15 K (⌂); 358.15 K (◀) and 363.15 K (×) [86]*
Reprinted with permission from ref. [86] copyright (2017), Serbian Chemical Society

According to the previous knowledge, it may be stated that the appropriate DES handling, storage, and water removal strategies should be developed to minimize the water content in DES in commercial applications.

Finally, when the future application of these types of electrolytes at an industrial scale is taken into account, it should be held in mind that even if the corrosion rates of various metals in DESs are low, future studies should focus on the long exposure to the DESs, which is characteristics of the real-life exploitation. Only a few of the cited studies in this review report the results from the prolonged contact of metals with DESs. In [56], the behaviour of the mild steel was monitored for 30 days of exposure to ethaline and reline, but it was observed that the most significant changes on the sample surface occurred on the first day of immersion. In the other example, the corrosion of Al alloys in reline was monitored for 36 days and it was concluded that the resistance of the passive layer steadily increased over the immersion time [60].

7. Conclusions

In spite of the fact that the term “deep eutectic solvent” may be attributed to as many as 10^6–10^8 various mixtures, the corrosion problem has been raised for a remarkably low number of DESs until now. A comprehensive literature data is nowadays available exclusively for traditional DESs containing choline chloride as their component, so these sources were the focus of the current review. One of the first and still actual applications of DESs has been the dissolution of various metal salts in electroplating, anodic polishing, and metal extraction/recycling by electrolysis due to the very strong solvating power of DESs. However, as this review clearly shows for various metals and DESs, when it comes to the dissolution of metals or alloys in their reduced (M^0) state, the solvating power of DESs shows to be very low, resulting in strikingly low corrosion rates.

This article recognizes the most distinguishing causative factors for the low DES corrosivity, and these are the absence of the oxidizing agents (apart from hydrogen ion, oxygen and water), the inhibiting role of organic DES components, and physical properties that do not allow the rapid corrosion process to occur or enhance the metal passivation process.

Yet, concerning the water impurity influence on their corrosivity, DESs are no different from the majority of other organic solvents or ionic liquids: the increase in water content notably increases the DES aggressiveness. If corrosion problems are to be avoided, strategies to minimize the water content in DES should be applied.

***Acknowledgement**: This research was financed by the Ministry of Education, Science and Technological Development of the Republic of Serbia (Contract No. 451-03-9/2021-14/200135).*

References

[1] A. P. Abbott, G. Capper, D. L. Davies, R. K. Rasheed, V. Tambyrajah, *Chemical Communications* **0** (2003) 70-71. https://doi.org/10.1039/B210714G

[2] B.B. Hansen, S. Spittle, B. A. Ragauskas, M. Dadmun, T.A. Zawodzinski, G.A Chen, D. Poe, Y. Zhang, J. M. Klein, A. Horton, L. Adhikari, T. Zelovich, B. W. Doherty, B. Gurkan, E. J. Maginn, . Baker, M. E. Tuckerman, R. F. Savinell, J. R. Sangoro, *Chemical Reviews* **121** (2021) 1232-1285. https://dx.doi.org/10.1021/acs.chemrev.0c00385

[3] A. P. Abbott, D. Boothby, G. Capper, D. L. Davies, R. K. Rasheed, *Journal of the American Chemical Society* **126** (2004) 9142-9147. https://doi.org/10.1021/ja048266j

[4] E. L. Smith, A. P. Abbott, K. S. Ryder, *Chemical Reviews* **114** (2014) 11060-11082. https://doi.org/10.1021/cr300162p

[5] K. Radošević, M. Cvjetko Bubalo, V. G. Srček, D. Grgas, D. Landeka, T. L. Dragičević, I. Radojčić Redovniković, *Ecotoxicology and Environmental Safety* **112** (2015) 46-53. https://doi.org/10.1016/j.ecoenv.2014.09.034

[6] B. Gurkan, H. Squire, E. Pentzer, *Journal of Physical Chemistry Letters* **10** (2019) 7956-7964. https://doi.org/10.1021/acs.jpclett.9b01980

[7] G. R. Jenkin, A. Z. Al-Bassam, R. C. Harris, A. P. Abbott, D. J. Smith, D. A. Holwell, R. J. Chapman, C .J. Stanley, *Minerals Engineering* **87** (2016) 18-24. https://doi.org/10.1016/j.mineng.2015.09.026

[8] A. P. Abbott, K. J. McKenzie, K. S. Ryder, *ACS Symposium Series* **975** (2007) 186-197. https://doi.org/10.1021/bk-2007-0975.ch013

[9] P. Sebastian, M. I. I. Giannotti, E. Gómez, J. M. Feliu, *ACS Applied Energy Materials* **1** (2018) 1016-1028. https://doi.org/10.1021/acsaem.7b00177

[10] F. S. Oliveira, A. B. Pereiro, L. P. Rebelo, I. M. Marrucho, *Green Chemistry* **15** (2013) 1326-1330. https://doi.org/10.1039/c3gc37030e

[11] N. Schaeffer, M. A. Martins, C. M. Neves, S. P. Pinho, J. A. Coutinho, *Chemical Communications* **54** (2018) 8104-8107. https://doi.org/10.1039/c8cc04152k

[12] S. Sarmad, J. P. Mikkola, X. Ji, *ChemSusChem* **10** (2017) 324-352. https://doi.org/10.1002/-cssc.201600987

[13] M. Chakrabarti, F. Mjalli, I. Alnashef, M. Hashim, M. Hussain, L. Bahadori, C. Low, *Renewable Sustainable Energy Reviews* **30** (2014) 254-270. https://doi.org/10.1016/j.rser.2013.10.004

[14] H. D. Jhong, D. S. H. Wong, C. C. Wan, Y. Y. Wang, T. C. Wei, *Electrochemistry Communications* **11** (2009) 209-211. https://doi.org/10.1016/j.elecom.2008.11.001

[15] M. Pätzold, S. Siebenhaller, S. Kara, A. Liese, C. Syldatk, D. Holtmann, *Trends in Biotechnology* **37** (2019) 943-959. https://doi.org/10.1016/j.tibtech.2019.03.007

[16] H. Zhao, G. A. Baker, *Journal of Chemical Technology and Biotechnology* **88** (2013) 3-12. https://doi.org/10.1002/jctb.3935

[17] K. D. O. Vigier, G. Chatel, F. Jérôme, *ChemCatChem* **7** (2015) 1250-1260. https://doi.org/10.1002/cctc.201500134
[18] R. Esquembre, J. M. Sanz, J. G. Wall, F. del Monte, C. R. Mateo, M. L. Ferrer, *Physical Chemistry Chemical Physics* **15** (2013) 11248-11256. https://doi.org/10.1039/c3cp44299c
[19] I. Mamajanov, A. E. Engelhart, H. D. Bean, N. V. Hud, *Angewandte Chemie International Edition* **49** (2010) 6310-6314. https://doi.org/10.1002/anie.201001561
[20] M. Zakrewsky, A. Banerjee, S. Apte, T. Kern, M. Jones, R. Sesto, A. Koppisch, D. Fox, S. Mitragotri, *Advanced Healthcare Materials* **5** (2016) 1282-1289. https://doi.org/10.1002/adhm.201600086
[21] Y. Huang, F. Shen, J. La, G. Luo, J. Lai, C. Liu, G. Chu, *Particulate Science and Technology* **31** (2013) 81-84. https://doi.org/10.1080/02726351.2011.648823
[22] X. Cunying, W. Qing, Y. Hua, J. Li, *Journal of Solid State Electrochemistry* **18** (2014) 2149-2155. https://doi.org/10.1007/s10008-014-2468-1
[23] R. Bernasconi, G. Panzeri, A. Accogli, F. Liberale, L. Nobili, L. Magagnin, *Electrodeposition from deep eutectic solvents in: Progress and Developments in Ionic Liquids,* IntechOpen (2017) 235-261. https://doi.org/10.5772/64935
[24] A. V. Rudnev, *Russian Chemical Reviews* **89** (2020) 1463-1482. https://doi.org/10.1070/RCR4970
[25] A. P. Abbott, K. J. McKenzie, *Physical Chemistry Chemical Physics* **8** (2006) 4265-4279. https://doi.org/10.1039/B607329H
[26] V. S. Cvetkovic, N. M. Vukicevic, N. Jovicevic, J. S. Stevanovic, J. N. Jovicevic, *Transactions of Nonferrous Metals Society of China* **30** (2020) 823-834. https://doi.org/10.1016/S1003-6326(20)65257-8
[27] Y. H. You, C. Gu, X. Wang, J. Tu, *Surface and Coatings Technology* **206** (2012) 3632-3638. https://doi.org/10.1016/j.surfcoat.2012.03.001
[28] T. A. Green, P. Valverde, S. Roy, *Journal of the Electrochemical Society* **165** (2018) D313-D320. https://doi.org/10.1149/2.0371809jes
[29] T. A. Green, X. Su, S. Roy, *ECS Transactions* **77** (2017) 1247-1253. https://doi.org/10.1149/07711.1247ecs
[30] S. Ghosh, S. Roy, *Surface and Coatings Technology* **238** (2014) 165-173. https://doi.org/10.1016/j.surfcoat.2013.10.069
[31] P. Valverde, T. Green, S. Roy, *ECS Transactions* **77** (2017) 859-864. https://doi.org/10.1149/07711.0859ecst
[32] M. Bučko, D. Culliton, A. J. Betts, J. B. Bajat, *Transactions of the IMF* **95** (2017) 60-64. https://doi.org/10.1080/00202967.2017.1255412
[33] E. Gómez, P. Cojocaru, L. Magagnin, E. Valles, *Journal of Electroanalytical Chemistry* **658** (2011) 18-24. https://doi.org/10.1016/j.jelechem.2011.04.015
[34] P. Cojocaru, L. Magagnin, E. Gomez, E. Vallés, *Materials Letters* **65** (2011) 3597-3600. https://doi.org/10.1016/j.matlet.2011.08.003
[35] M. Steichen, M. Thomassey, S. Siebentritt, P. J. Dale, *Physical Chemistry Chemical Physics* **13** (2011) 4292-4302. https://doi.org/10.1039/C0CP01408G
[36] P. Guillamat, M. Cortés, E. Vallés, E. Gómez, *Surface and Coatings Technology* **206** (2012) 4439-4448. https://doi.org/10.1016/j.surfcoat.2012.04.093
[37] A. P. Abbott, J. C. Barron, K. S. Ryder, D. Wilson, *Chemistry A European Journal* **13** (2007) 6495-6501. https://doi.org/10.1002/chem.200601738
[38] T. Beyersdorff, T. J. S. Schubert, U. Welz-Biermann, W. Pitner, A. P. Abbott, K. J. McKenzie, K. S. Ryder, in D. R. MacFarlane, A. P. Abbott, (eds.), *Electrodeposition from Ionic Liquids*, Wiley-VCH, Weinheim, Germany, 2008, p. 15. https://doi.org/10.1002/9783527682706

[39] E. Heitz, *Corrosion of metals in organic solvents*, in M.G. Fontana *et al.* (eds.), *Advances in Corrosion Science and Technology*, Plenum Press, New York, USA, 1974, p. 149. https://doi.org/10.1007/978-1-4615-9059-0_3
[40] A. P. Abbott, S. S. M. Alabdullah, A. Y. M. Al-Murshedi, K.S. Ryder, *Faraday Discussions* **206** (2018) 365-377. https://doi.org/10.1039/c7fd00153c
[41] T. Lemaoui, F. Abu Hatab, A. S. Darwish, A. Attoui, N. E. H. Hammoudi, G. Almustafa, M. Benaicha, Y. Benguerba, I. M. Alnashef, *ACS Sustainable Chemical Engineering* **9** (2021) 5783-5808. https://doi.org/10.1021/acssuschemeng.0c07367
[42] E. Heitz', C. Kyriazis, *Industrial & Engineering Chemistry Research* **17** (1978) 37-41. https://doi.org/10.1021/i360065a011
[43] S. S. Alabdullah, *pH measurements in ionic liquids*, *Doctoral Thesis*, University of Leicester, 2018.
[44] A. Mitar, M. Panić, J. Prlić Kardum, J. Halambek, A. Sander, K. Zagajski Kučan, I. Radojčić Redovniković, K. Radošević, *Chemical and Biochemical Engineering Quarterly* **33** (2019) 1-18. https://doi.org/10.15255/CABEQ.2018.1454
[45] F. S. Mjalli, O.U. Ahmed, *Asia-Pacific Journal of Chemical Engineering* **12** (2017) 313-320. https://doi.org/10.1002/apj.2074
[46] F. S. Mjalli, O. U. Ahmed, *Korean Journal of Chemical Engineering* **33** (2016) 337-343. https://doi.org/10.1007/s11814-015-0134-7
[47] D. Shah, F. S. Mjalli, *Physical Chemistry Chemical Physics* **16** (2014) 23900-23907. https://doi.org/10.1039/C4CP02600D
[48] A. P. Abbott, E. I. Ahmed, R. C. Harris, K. S. Ryder, *Green Chemistry* **16** (2014) 4156-4161. https://doi.org/10.1039/C4GC00952E
[49] I. M. Pateli, D. Thompson, S. S. M. Alabdullah, A. P. Abbott, G. R. T. Jenkin, J. M. Hartley, *Green Chemistry* **22** (2020) 5476-5486. https://doi.org/10.1039/D0GC02023K
[50] E. McCafferty, *Corrosion Science* **45** (2003) 1421-1438. https://doi.org/10.1016/S0010-938X(02)00231-7
[51] J. Soltis, *Corrosion Science* **90** (2015) 5-22. https://doi.org/10.1016/j.corsci.2014.10.006
[52] X. Li, K. Binnemans, *Chemical Reviews* **121** (2021) 4506-4530. https://doi.org/10.1021/acs.chemrev.0c00917
[53] Y. Nakao, *Journal of the Chemical Society, Chemical Communications* **5** (1992) 426-427. https://doi.org/10.1039/C39920000426
[54] G. Kear, B. D. Barker, F. C. Walsh, *Corrosion Science* **46** (2004) 109-135. https://doi.org/10.1016/S0010-938X(02)00257-3
[55] F. R. Pérez, C. A. Barrero, A. R. H. Walker, K. E. García, K. Nomura, *Materials Chemistry and Physics* **117** (2009) 214-223. https://doi.org/10.1016/j.matchemphys.2009.05.045
[56] A. A. Kityk, Y. D. Rublova, A. Kelm, V. V. Malyshev, N. G. Bannyk, I. Flis-Kabulska, *Journal of Electroanalytical Chemistry* **823** (2018) 234-244. https://doi.org/10.1016/j.jelechem.-2018.06.018
[57] J. M. Hartley, C. M. Ip, G. C. H. Forrest, K. Singh, S. J. Gurman, K. S. Ryder, A. P. Abbott, G. Frisch, *Inorganic Chemistry* **53** (2014) 6280-6288. https://doi.org/10.1021/ic500824r
[58] J. L. Barriada, A. D. Tappin, E. Hywel Evans, E. P. Achterberg, *TrAC Trends in Analytical Chemistry* **26** (2007) 809-817. https://doi.org/10.1016/j.trac.2007.06.004
[59] A. P. Abbott, G. Frisch, S. J. Gurman, A. R. Hillman, J. Hartley, F. Holyoak, K. S. Ryder, *Chemical Communications* **47** (2011) 10031-10033. https://doi.org/10.1039/C1CC13616J
[60] M. Bucko, A. C. Bastos, M. G. S. Ferreira, J. B. Bajat, *Electrochimica Acta* **357** (2020) 136861. https://doi.org/10.1016/j.electacta.2020.136861
[61] T. H. Ibrahim, R. Alhasan, M. Bedrelzaman, M. A. Sabri, N. A. Jabbar, F. S. Mjalli, *International Journal of Electrochemical Science* **14** (2019) 8450-8469. https://doi.org/10.20964/2019.09.27

[62] J. Tang, C. Xu, X. Zhu, H. Liu, X. Wang, M. Huang, Y. Hua, Q. Zhang, Y. Li, *Journal of The Electrochemical Society* **165** (2018) E406-E411. https://doi.org/10.1149/2.0091810jes
[63] M. L. Doche, A. Mandroyan, M. Mourad-Mahmoud, V. Moutarlier, J. Y. Hihn, *Chemical Engineering and Processing: Process Intensification* **121** (2017) 90-96. https://doi.org/10.1016/j.cep.2017.08.006
[64] J. Zhang, C. Gu, W. Yan, J. Tu, X. Ding, *Surface and Coatings Technology* **344** (2018) 702-709. https://doi.org/10.1016/j.surfcoat.2018.04.004
[65] G. H. Lane, *Electrochimica Acta* **83** (2012) 513-528. https://doi.org/10.1016/j.electacta.-2012.08.046
[66] G. Song, D. StJohn, *Corrosion Science* **46** (2004) 1381-1399. https://doi.org/10.1016/j.corsci.-2003.10.008
[67] R. Clark, *Nature* **168** (1951) 876-876. https://doi.org/10.1038/168876a0
[68] D. E. Nichols, D. T. Nguyen, M. M. Norton, B. R. Parker, L. E. Daniels, 202nd *National Meeting of the American Chemical Society*, *The effect of conditioning agents on the corrosive properties of molten urea*, New York, USA, 1991, p. 1
[69] H. Liang, H. Li, Z. Wang, F. Wu, L. Chen, X. Huang, *The Journal of Physical Chemistry B* **105** (2001) 9966-9969. https://doi.org/10.1021/jp0119779
[70] R. J. Meakins, *Journal of Applied Chemistry* **13** (1963) 339-345. https://doi.org/10.1002/jctb.-5010130803
[71] R. Solmaz, *Corrosion Science* **81** (2014) 75-84. https://doi.org/10.1016/j.corsci.2013.12.006
[72] C. Verma, I. B. Obot, I. Bahadur, E.-S. M. Sherif, E. E. Ebenso, *Applied Surface Science* **457** (2018) 134-149. https://doi.org/10.1016/j.apsusc.2018.06.035
[73] S. M. Abd El Haleem, S. Abd El Wanees, E. E. Abd El Aal, A. Farouk, *Corrosion Science* **68** (2013) 1-13. https://doi.org/10.1016/j.corsci.2012.03.021
[74] B. Widyanto, I. Gede Bagus Eka Suputra Wiguna, *Heliyon* **5** (2019) e02006. https://doi.org/10.1016/j.heliyon.2019.e02006
[75] D. Jayaperumal, *Materials Chemistry and Physics* **119** (3) 478-484. https://doi.org/10.1016/j.matchemphys.2009.09.028
[76] J. Wu, R. Zhou, P.M. Radjenovic, S. Liu, D. Wu, J. Li, B. Mao, J. Yan, *Electrochimica Acta* **390** (2021) 138859. https://doi.org/10.1016/j.electacta.2021.138859
[77] R. Costa, M. Figueiredo, C. M. Pereira, F. Silva, *Electrochimica Acta* **55** (2010) 8916-8920. https://doi.org/10.1016/j.electacta.2010.07.070
[78] S. Rozas, M. Atilhan, S. Aparicio, *The Journal of Physical Chemistry B* **124** (2020) 1197-1206. https://doi.org/10.1021/acs.jpclett.9b01980
[79] P. Hronsky, *Corrosion* **37** (1981) 161-170. https://doi.org/10.5006/1.3622160
[80] S. R. Gregory, *Physical properties of glycerine*, in E. Jungermann, N.O.V. Sonntag (eds.) *Glycerine A Key Cosmetic Ingredient*, CRC Press, Boca Raton, USA, 1991, p. 111. https://doi.org/10.1201/9780203753071
[81] V. V. Loskutov, G. N. Kosova, *Russian Journal of Physical Chemistry A* **93** (2019) 260-264. https://doi.org/10.1134/S003602441902016X
[82] J. Raymund Brusas, E. M. B. Dela Pena, *Journal of Electrochemical Science and Technology* (2021) Ahead of print. https://doi.org/10.33961/jecst.2020.01522
[83] D. Cuiling, B. Zhao, C. Xiao-Bo, N. Birbilis, H. Yang, *Scientific Reports* **6** (2016) 29225-29239. https://doi.org/10.1038/srep29225
[84] M. Bucko, S. Roy, P. Valverde-Armas, A. Onjia, A. C. Bastos, J. B. Bajat, *Journal of The Electrochemical Society* **165** (16) (2018) H1059-H1065. https://doi.org/10.1149/2.0921816jes]
[85] Y. D. Rublova, A. A. Kityk, N. G. Bannyk, V. S. Protsenko, F. I. Danilov, *Materials Today: Proceedings* **6** (2019) 232-236. https://doi.org/10.1016/j.matpr.2018.10.099

[86] J. M. Vuksanović, N. M. Todorović, M. Lj. Kijevčanin, S. P. Šerbanović, I. R. Radović, *Journal of the Serbian Chemical Society* **82** (2017) 1287-1302. https://doi.org/10.2298/JSC170316054V
[87] M. Uerdingen, C. Treber, M. Balser, G. Schmitt, C. Werner, *Green Chemistry* **7** (2005) 321-325. https://doi.org/10.1039/B419320M
[88] A. Shkurankov, S. Z. El Abedin, F. Endres, *Australian Journal of Chemistry* **60** (2007) 35-42. https://doi.org/10.1071/CH06305
[89] S. Noori, M. V. Diamanti, M. P. Pedeferri, A. Brenna, M. Ormellese, *Materials and Corrosion* **69** (2018) 1658-1668. https://doi.org/10.1002/maco.201810215

J. Electrochem. Sci. Eng. **12(2)** (2022) 253-264; http://dx.doi.org/10.5599/jese.1077

Open Access : : ISSN 1847-9286

www.jESE-online.org

Original scientific paper

Influence of supporting electrolyte on electrochemical formation of copper nanoparticles and their electrocatalytic properties

Noelia Zurita and Silvana G. García✉

Instituto de Ingeniería Electroquímica y Corrosión (INIEC), Departamento de Ingeniería Química, Universidad Nacional del Sur, Av. Alem 1253, (8000) Bahía Blanca, Argentina

Corresponding authors: ✉ *sgarcia@criba.edu.ar; Tel.: +54-9-291-4595100-3614*

Received: August 11, 2021; Accepted: November 5, 2021; Published: November 22, 2021

Abstract

Comparative analysis of copper nanoparticles (CuNPs) obtained by electrodeposition on highly oriented pyrolytic graphite (HOPG) substrates from different supporting electrolytes containing sulphate anions, was performed. Voltammetric results indicated that Cu electrodeposition follows a diffusion-controlled nucleation and crystal growth model for three solutions studied (Na_2SO_4, H_2SO_4 and Na_2SO_4+H_2SO_4). Na_2SO_4 solution was most effective because the copper reduction occurs at the most positive potential value, reaching the highest current density. Analysis of potentiostatic current transients revealed that the process can be described predominantly by a model involving a 3D-progressive nucleation mechanism, which was corroborated by scanning electron microscopy (SEM) analysis. SEM images showed a high density of hemispherical shaped Cu particles of different sizes (mostly between 80-150 nm), randomly distributed on the HOPG surface for Na_2SO_4 electrolyte solution. In the presence of H_2SO_4, the size dispersion decreased, resulting in particles with greater diameters (up to 339 nm). The electrolyte solution with Na_2SO_4+H_2SO_4 revealed lower particle density with a considerable crystal size dispersion, where very small crystallites are prevailing. Cyclic voltammetry was used to evaluate qualitatively the catalytic activity of CuNPs deposited from three electrolyte solutions towards the nitrate reduction reaction. An enhanced catalytic effect was obtained when copper particles were prepared from either Na_2SO_4 or H_2SO_4 supporting electrolyte.

Keywords

Copper nanocrystals; electrodeposition; plating solution; highly oriented pyrolytic graphite (HOPG); nitrate reduction

Introduction

Recent studies have reported that supported copper nanostructures, in addition to being suitable for a wide range of applications (nanoelectronics [1], biosensing [2,3], optoelectronics [4], *etc.*), show excellent results as electrocatalyst material for different reactions, in particular those of

environmental interest [5-8]. Nitrate ions are one of the chemical species that can be potentially dangerous for human health if their concentration in drinking water and food exceeds the upper limit allowed, as indicated by the World Health Association [9]. Therefore, there is a high necessity for nitrate ions to be detected and quantified. The detrimental effect of nitrate ions comes mainly from nitrogen-based fertilizers contaminating drinking water supplies, and their removal or reduction has gained special attention.

The ability of copper nanostructures as an electrocatalyst material for nitrate reduction has already been studied by several authors [10-12]. In particular, the influence of structural properties of nanoparticles has been analyzed on the reaction performance [13-15]. It has been demonstrated that the final properties of metal nanoparticles are strongly dependent on their surface morphology, which is essentially related to the selected preparation method. The electrodeposition is one of the most used preparation methods because it presents additional advantages. The main assets are simplicity and the possibility of working at room temperature and pressure. In addition, this method allows the kinetic process control and, consequently, the size of particles and the amount of formed deposit.

As stated above, the morphological features of deposits have a significant influence on their electrocatalytic properties. It is well known that variations of the plating solution composition and pH can influence the deposit morphology. Therefore, it is necessary to relate the operating conditions to the shape, size, and distribution of produced nanoparticles.

Previous works addressing the electrodeposition of copper nanoparticles on carbonaceous substrates, have analyzed the influence of some parameters of the electrochemical process on structural features of the deposit [16,17]. In particular, it was found that the pH and concentration of $CuSO_4$ solution have a remarkable effect on the texture and population density of deposited nanostructures the use of Na_2SO_4 supporting electrolyte. For the latter, an intriguing behavior was reported, which deserves a detailed study [18].

On the other hand, the effect of anions present in the electrolytic solution has been analyzed by several authors [19,20]. González *et al*. [19] have investigated Cu^+ intermediate species formed during copper electrodeposition process and demonstrated that in the presence of NO_3^- ions, the value of the reduction peak current increases because this anion is catalytically reduced on Cu nanoparticles freshly electrodeposited on a glassy carbon electrode. Presence of SO_4^{2-} anions in the plating solution does not interfere with the current measurement of the copper reduction, but they are adsorbed considerably, preventing the discharge of Cu^+ ions. For ClO_4^- ions, adsorption is negligible; therefore, a reduction peak current higher than from SO_4^{2-} anions is evidenced. These studies were carried out at pH 3 with a higher Cu^{2+} concentration than in the present study. Bélanger *et al*. [20] analyzed the copper electrodeposition on highly oriented pyrolytic graphite (HOPG) substrates using two different copper salts ($CuSO_4$ and $Cu(NO_3)_2$) in 1.8 M H_2SO_4 aqueous solution and demonstrated that the deposition of copper in the presence of $CuSO_4$ induced the co-deposition of sulfate anions.

In the present work, a comparative analysis of the initial stages of copper electrodeposition on HOPG from different supporting electrolytes containing SO_4^{2-} anions (Na_2SO_4, H_2SO_4 and Na_2SO_4+ H_2SO_4) has been carried out to increase the understanding of the nucleation and growth of copper particles and their electrocatalytic properties. The electrodeposition process is studied using conventional electrochemical techniques (cyclic voltammetry and chronoamperometry), and the copper deposits are characterized by scanning electron microscopy (SEM) with energy-dispersive X-ray spectroscopy (EDX). The catalytic effect for the reduction of nitrate anions in $NaNO_3$ + Na_2SO_4 solution has been qualitatively evaluated by voltammetric measurements for CuNPs deposited from three different sulphate-containing media.

Experimental

The solutions used in this work for metal deposition were prepared with supra pure chemicals (E. Merck, Darmstadt, Germany) and tri-distilled water. The supporting electrolytes added to 1 mM $CuSO_4$ solution were 0.1 M Na_2SO_4, 0.1 M H_2SO_4 and 0.1 M Na_2SO_4 + 0.1 M H_2SO_4, taking into account that the same anion was present in all three cases. The catalytic effect was studied in 0.1 M $NaNO_3$ + + 0.1 M Na_2SO_4 solution. Prior to each experiment, solutions were deaerated by nitrogen bubbling.

Cyclic voltammetric measurements and chronoamperometric studies were carried out in a conventional three-electrode electrochemical cell at a temperature of T = 298 K. HOPG SPI-2 grade substrates (SPI Supplies, USA) were used as working electrodes, which were prepared by cleaving its surface with an adhesive tape immediately prior to each experiment. The electrode was held within a Teflon sheath with an exposed area of 0.216 cm^2. The counter electrode was a Pt sheet (1 cm^2), and the reference electrode was a saturated calomel electrode (SCE), (E_{SCE} = 0.2415 V *vs*. SHE). All electrode potentials mentioned in this work are referred to this electrode. The experiments were performed with an EG&G Princeton Applied Research model 273A potentiostat-galvanostat controlled by a microcomputer.

Cu nanoparticles prepared from different electrolytes by the potentiostatic step technique on HOPG substrates were characterized by SEM using a Zeiss MA 10 microscope integrated with an EDX analyzer.

Results and discussion

Cyclic voltammetry

Electrodeposition of Cu on the HOPG substrate was performed in the following plating solutions: a) 1 mM $CuSO_4$ + 0.1 M Na_2SO_4 (pH 4.66), b) 1 mM $CuSO_4$ + 0.1 M H_2SO_4 (pH 0.95), and c) 1 mM $CuSO_4$ + 0.1 M Na_2SO_4 + 0.1 M H_2SO_4 (pH 1.10). The process was initially examined qualitatively by cyclic voltammetry recorded within the potential range $-0.7 \leq E/V \leq 0.3$, at the scan rate (dE/dt) of 10 mV s^{-1}. As shown in Figure 1, the voltammetric responses of HOPG in three solutions exhibited similar features, including the hysteresis loop (the so-called nucleation loop) formed between cathodic and anodic sweep curves at negative potentials values, which is typical of a nucleation and growth process [21,22]. An extensive analysis of cyclic voltammograms at different scan rates confirming this conclusion was shown elsewhere [23]. During the potential scan towards the negative direction, a cathodic peak is observed, associated with the reduction of Cu^{2+} ions to Cu^0. In the reverse scan, a single anodic peak is evidenced, consistent with the dissolution of Cu clusters deposited previously.

Generally, a single cathodic peak is evidenced as a result of the Cu^{2+} electroreduction process, and it is accepted that it occurs on a global stage *via* 2 electrons. However, it is well known that in an acid medium [24,25] or in the presence of complexing anions such as chloride [26], the electrodeposition of Cu can be considered to occur in two consecutive stages with the formation of Cu^+ ions as intermediate species. These stages can be described by equations (1) and (2)

$$Cu^{2+} + e^- = Cu^+ \quad (1)$$

$$Cu^+ + e^- = Cu^0 \quad (2)$$

with the first reaction being the rate-determining step. In fact, in the case of the electrolyte containing only sulphuric acid, the broad Cu^{2+} reduction peak could be considered to be formed by two waves, which could be associated with two steps of the process.

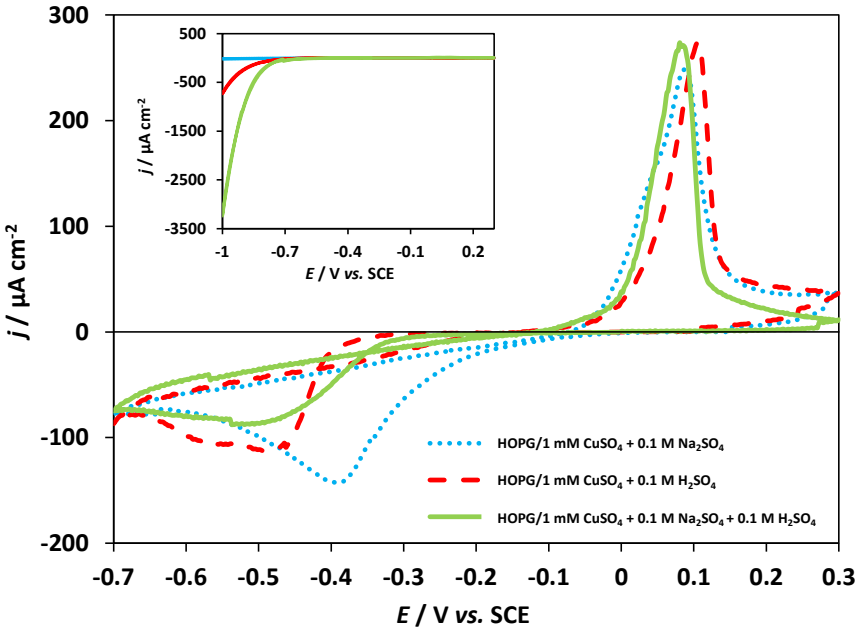

Figure 1. *Cyclic voltammetry of HOPG for 1 mM $CuSO_4$ in 0.1 M Na_2SO_4, 0.1 M H_2SO_4 and 0.1 M Na_2SO_4 + 0.1 M H_2SO_4. |dE/dt|=10 mV s^{-1}. Inset: cyclic voltammograms of HOPG in blank electrolyte solutions*

For comparison, cyclic voltammograms of HOPG electrode immersed in blank solutions (without containing Cu(II) ions) shown in the inset of Figure 1, indicate that the hydrogen evolution reaction occurs at more negative potential values and does not interfere with the Cu electrodeposition process under the conditions considered in this study.

When the supporting electrolyte is Na_2SO_4 (solution a), which is added to the plating bath primarily to increase electrolyte conductivity, the peak corresponding to the reduction of Cu^{2+} ions, is occurring at a more positive potential value (E_{peak}= -0.39 V) than in the other two cases, and reaching the maximum current density value of j_{peak}= -142.68 µA cm^{-2}. The presence of H_2SO_4 in the plating solution (solution b) also favors the conductivity of the electrolyte, showing E_{peak} and j_{peak} at -0.49 V and -112.68 µA cm^{-2}, respectively. According to the observed behavior, it could be inferred that part of SO_4^{2-} ions can be adsorbed on the surface of HOPG substrate, reducing thus the number of active sites for the formation of Cu nuclei, in agreement with the literature reviewed [19,20]. Moreover, Hope and Woods [27] have demonstrated by in-situ surface-enhanced Raman scattering (SERS) that sulphate adsorption occurs during metal electrodeposition. Their spectro-electrochemical investigations revealed that sulphate ions were transient adsorbed species during Cu electrodeposition process, which was not observed for copper surfaces in the absence of metal ions in solution. For the third solution studied (solution c), although the conductivity was higher than of other supporting electrolytes, the most negative E_{peak} for Cu deposition and the lowest j_{peak} values were obtained. The copper nucleation is retarded by this plating solution which provides more sulphate anions at the electrode interface, and consequently, it can be assumed that they could be adsorbed on the surface, blocking more sites for Cu deposition.

The values of E_{peak} and j_{peak} for three studied electrolyte solutions are summarized in Table 1.

Table 1. *Cathodic peak potentials and peak current densities for Cu deposition from three supporting electrolytes containing 1 mM $CuSO_4$*

Supporting electrolyte	0.1 M Na_2SO_4	0.1 M H_2SO_4	0.1 M Na_2SO_4 + 0.1 M H_2SO_4
E_{peak} / V	-0.389	-0.494	-0.519
j_{peak} / µA cm^{-2}	-142.68	-112.68	-87.88

Chronoamperometry

Potentiostatic current transients were carried out to obtain information about the kinetics of copper electrodeposition on the carbonaceous substrate. Representative *j-t* curves were performed applying simple potentiostatic pulses at selected potentials more negative than the cathodic peak potential (see Figure 1) for three cases studied, and they are shown in Figure 2 (inset graphics). These curves exhibit a typical shape of the nucleation process with 3D growth controlled by diffusion of electroactive species [28]. The potentiostatic current transients for three plating solutions showed an increase of current up to maximum, corresponding to the formation of Cu crystallites through the nucleation and growth process, followed by a decreasing region, reflecting the transition to linear diffusion. These results revealed that the presence of sodium sulfate in the plating solution generates the highest current for nucleus formation, which was reached at shorter times.

To analyze the type of nucleation, a commonly used criterion is the application of the theoretical model proposed by Sharifker and Hills [28]. By means of this model, two limiting nucleation mechanisms, instantaneous and progressive, can be distinguished based on the equations (3) and (4):

$$\frac{j^2}{j_m{}^2} = \frac{1.9542}{\frac{t}{t_m}}\left\{1-\exp\left[-1.2564\left(\frac{t}{t_m}\right)\right]\right\}^2 \quad (3)$$

$$\frac{j^2}{j_m{}^2} = \frac{1.2254}{\frac{t}{t_m}}\left\{1-\exp\left[-2.3367\left(\frac{t}{t_m}\right)^2\right]\right\}^2 \quad (4)$$

where the parameters j_m and t_m are the maximum current density of the transient and the time at which the current maximum occurs, respectively.

Eq. (3) corresponds to the instantaneous nucleation where the nuclei are formed and grown on active sites of the carbonaceous substrate, all activated simultaneously. In contrast, Eq. (4) corresponds to the progressive nucleation where the nuclei are formed on preferential sites and activated at different times during the electroreduction process.

As shown in Figure 2, representative potentiostatic current transient data were normalized and compared with both types of the described model. As stated above, the corresponding experimental transients are those included in the inset of the figures from which the type of nucleation is analyzed.

Figure 2a shows a very good correlation for the transient obtained at E= -0.42 V in solution a, with the theoretical curve for progressive nucleation. For solution b, shown in Figure 2b, copper crystallites were generated at *E*= -0.50 V. Cu nucleation begins in a progressive way at short times, passing to an intermediate state until reaching instantaneous nucleation in the last stage. These results are in agreement with those obtained by Huang *et al.* [29]. They demonstrated that for copper deposition on HOPG electrode from 1 mM $CuSO_4$ + 1 M H_2SO_4 solution, the analysis of experimental transients according to the theoretical model proposed by Sharifker and Hills [28] showed a good correlation with the theoretical curve for progressive nucleation for a potential more negative than the reduction peak. At the last stage, nucleation transition from progressive to instantaneous was found at even more negative potential.

When the experiments were performed using the solution c, *i.e.,* cupric sulfate with sodium sulfate and sulfuric acid solution as supporting electrolyte (Figure 2c), the nucleation mode follows predominately progressive nucleation, which is a behavior similar to that of the first electrolytic medium (0.1 M Na_2SO_4). In this case, the deposits were formed at *E*= -0.55 V.

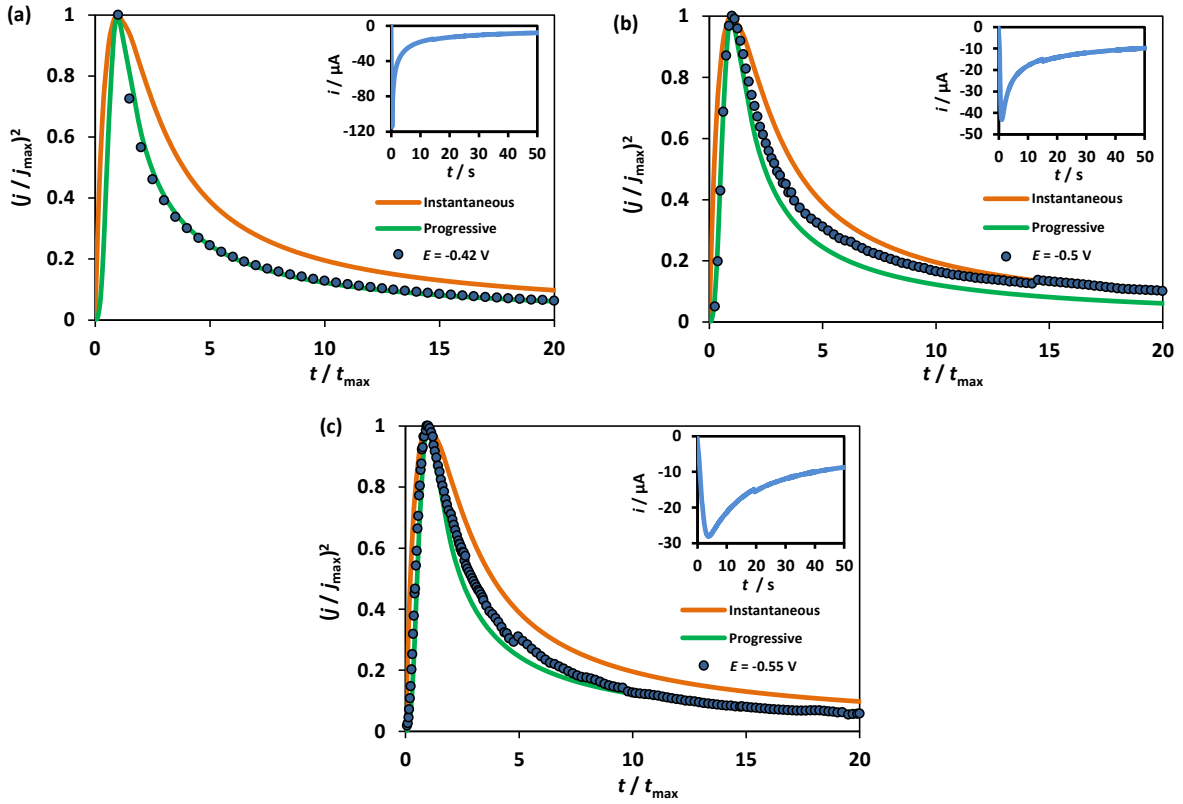

Figure 2. *Non-dimensional* $(j / j_{max})^2$ *vs.* (t / t_{max}) *plots of experimental current transients (shown in insets) for HOPG in solution containing 1 mM* $CuSO_4$ *and: (a) 0.1 M* Na_2SO_4*; (b) 0.1 M* H_2SO_4*; (c) 0.1 M* Na_2SO_4 *+ 0.1 M* H_2SO_4

Surface analysis

Direct information on the shape, size and density of Cu nanoparticles can be acquired by scanning electron microscopy (SEM) analysis. Figure 3 exhibits hemispheric Cu deposits generated by a simple potentiostatic pulse on HOPG substrate in three analyzed solutions.

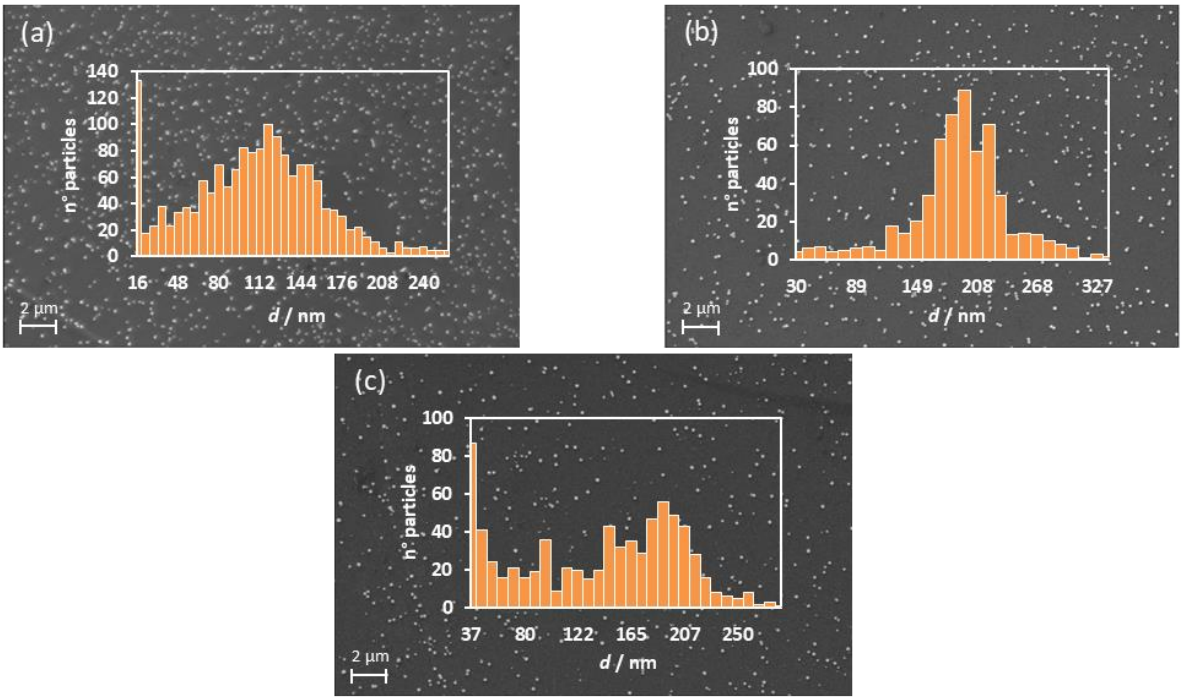

Figure 3. *SEM images of CuNPs electrodeposited on HOPG from 1 mM* $CuSO_4$ *in: (a) 0.1 M* Na_2SO_4*, (b) 0.1 M* H_2SO_4 *and (c) 0.1 M* Na_2SO_4 *+ 0.1 M* H_2SO_4*, and corresponding particle size distribution histograms*

Figure 3a reveals the formation of a considerable density of Cu particles distributed on the HOPG surface when Na_2SO_4 was used as the supporting electrolyte (solution a). These particles were electrodeposited at *E*=-0.42 V during 100 s. Cu structures present different particle sizes (as shown in the corresponding histogram), consistent with progressive nucleation. A large number of small particles can be observed in Figure 3a, with a minimum diameter of 16 nm, and large ones with a maximal diameter of 259.17 nm. Figure 3b shows copper particles obtained by electrodeposition at -0.5 V during 120 s in the copper solution containing H_2SO_4 (solution b). The particle size dispersion is slightly smaller, resulting in the formation of larger copper particles with a maximum diameter value around 339 nm and without the predominance of small particles. Therefore, the particle size distribution tends to conform to the normal distribution, with crystals mostly between 180-210 nm in diameter.

Some of the Cu nuclei formed in solution b are formed on HOPG step edges acting as active sites for metal nucleation, and the presence of crystals forming dimers and trimers are also detected, as shown in Figure 4.

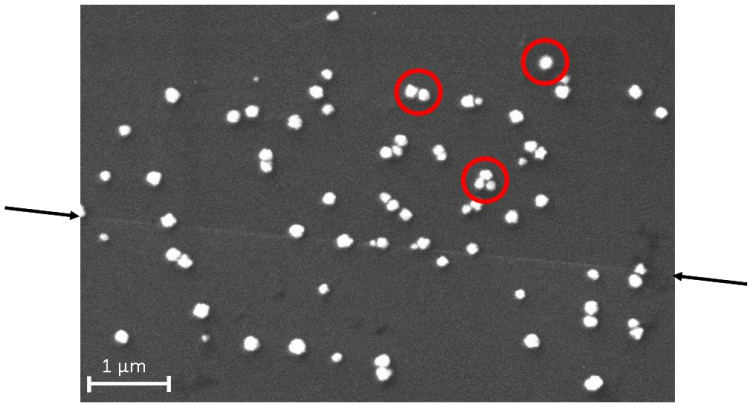

Figure 4. *SEM image of CuNPs electrodeposited from 1 mM $CuSO_4$ + 0.1 M H_2SO_4 showing deposits on HOPG step edges and presence of single particles, dimers and trimers*

As seen in Figure 3c, the number of metallic clusters generated at *E*= -0.55 V during 120 s in the combined electrolyte (solution c) decreases, and a wide range of particle sizes is observed with small particles of 37 nm and larger with a maximum diameter of 300 nm. These crystals grow on random active sites and also on some HOPG step edges.

Generally, SEM images confirmed the progressive nature of copper nucleation derived by the Sharifker and Hills dimensionless analysis for three solutions used.

Figure 5 exhibits SEM images of Cu crystallites formed on the HOPG electrode with marked points where the EDX analysis was performed. Cu structures were generated on the surface substrate after applying a potential pulse at *E*= -0.5 V for 120 s in the solution containing H_2SO_4.

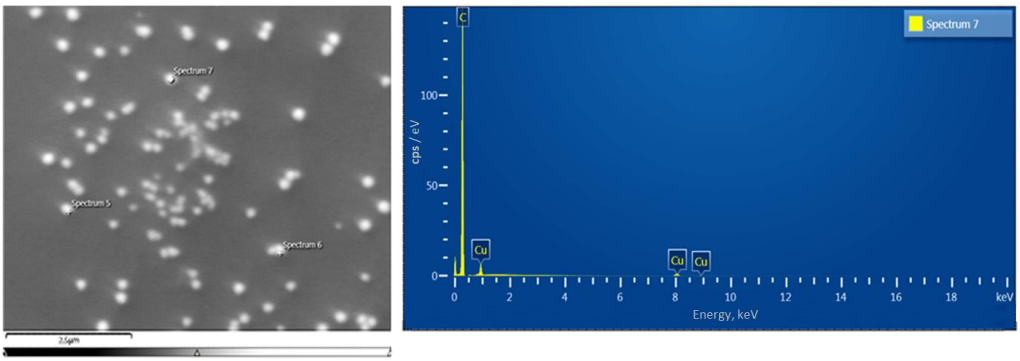

Figure 5. *SEM micrograph of HOPG substrate after Cu deposition from 1 mM $CuSO_4$ + 0.1 M H_2SO_4 solution at -0.5 V for 120 s and representative EDX analysis applied on top of crystallite*

Only the elemental distribution for the most representative point is shown, confirming the presence of Cu besides the signal corresponding to the C substrate (HOPG).

Electrocatalysis

The catalytic activity of CuNPs modified HOPG substrates was evaluated qualitatively by cyclic voltammetry in 0.1 M $NaNO_3$ + 0.1 M Na_2SO_4 solution. Initially, Cu nanoparticles were obtained on the HOPG electrode after applying a single potentiostatic pulse to the electrode immersed in three electrolytes studied at *E*= -0.65 V for 400 s. Potentiostatic pulse parameters, different from those applied for nucleation analysis, were chosen, *i.e.,* a more negative pulse potential and a longer deposition time, to increase the copper-covered area on the HOPG electrode surface, and therefore, to induce more noticeable nitrate anion reduction signal in the voltammetric analysis.

The type of nucleation, in this case, was analyzed anew, as well as the surface characterization by SEM of CuNPs modified HOPG electrode.

Figure 6a show a representative SEM image and the corresponding size distribution of Cu deposits generated when Na_2SO_4 (solution a) was used as the supporting electrolyte.

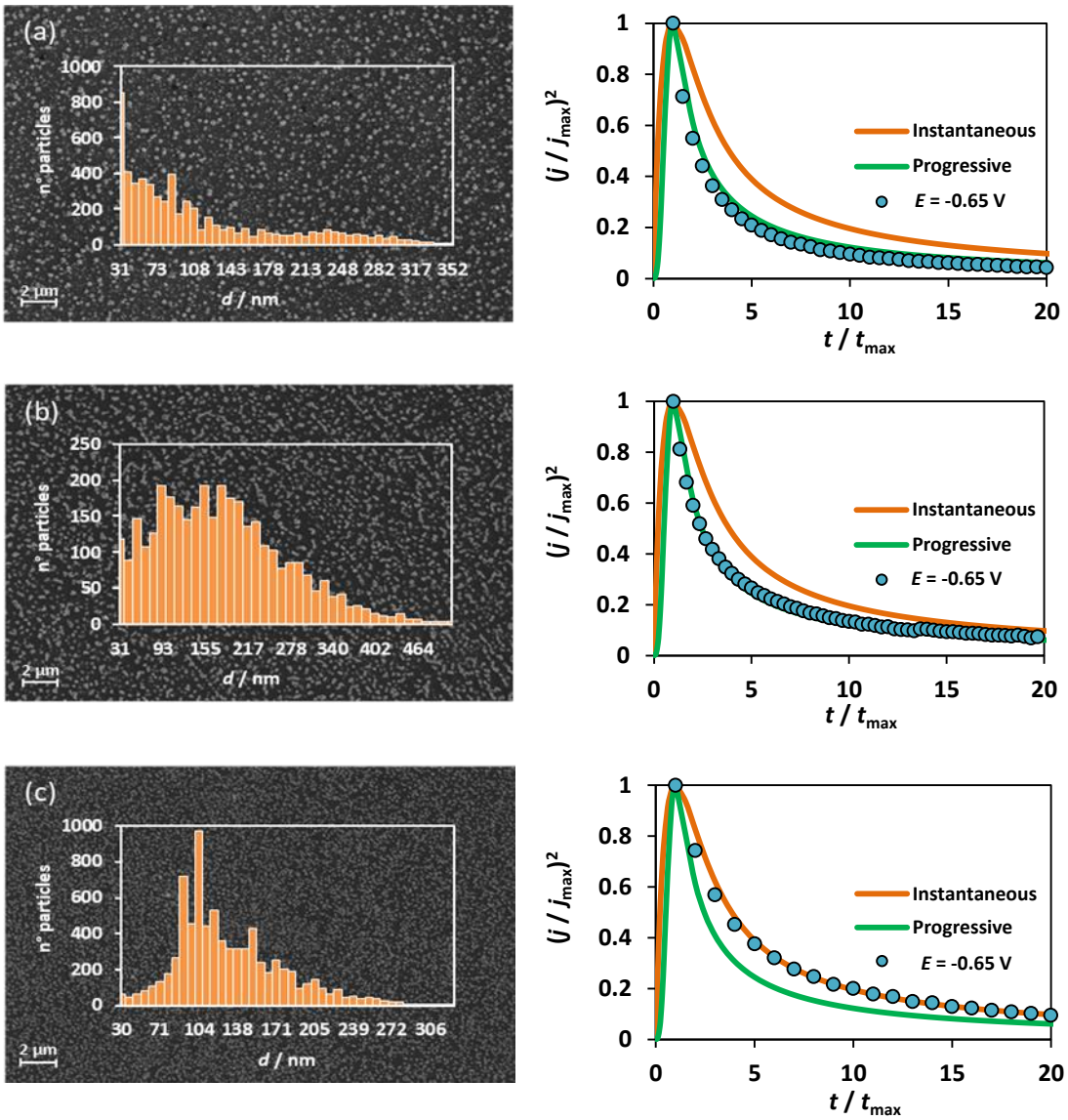

Figure 6. *SEM images of CuNPs electrodeposited from 1 mM $CuSO_4$ in (a) 0.1 M Na_2SO_4, (b) 0.1 M H_2SO_4 and (c) 0.1 M Na_2SO_4 + 0.1 M H_2SO_4, with the corresponding particle size distribution histograms (left), and non-dimensional $(j / j_{max})^2$ vs. (t / t_{max}) plots of experimental current transients (right)*

Crystals of different sizes with a predominance of very small particles of the order of 31-50 nm with maximum diameters of 352 nm, are observed. The covered area was 17 % of the electrode geometric area, calculated from the average of several low magnification SEM images. The type of nucleation analyzed from Sharifker and Hills model leads to a progressive nucleation mode, the same as for *E* = -0.42 V. For the second solution containing H_2SO_4 (solution b), Figure 6b shows a representative SEM image of Cu-decorated HOPG electrode revealing a great disparity in copper particle sizes as a result of the formation of many agglomerates that reached values up to 514 nm, but also a large number of crystallites between 30-50 nm. The covered area of 22 % was estimated. Size diversity of metal deposits is consistent with a progressive nucleation and growth mechanism, which was corroborated throughout the analyzed time range by the theoretical model used. The same nucleation model was obtained previously for *E*=-0.50 V at short times. When the deposits were formed using the third solution (solution c), a large number of deposits with a diameter of approximately 104 nm is observed, some of them reaching a maximum size of 326 nm, with no predominance of particles with diameters less than 50 nm (Figure 6c). In this case, the calculated covered area was 24 % and, unlike for the pulse at *E*= -0.55 V, the nucleation is predominantly instantaneous.

Electrocatalytic properties of CuNPs

After this analysis, the electrocatalytic behavior of CuNPs modified HOPG electrode was evaluated for the nitrate reduction reaction. Figure 7 shows the voltammetric results for different Cu structures generated from three plating electrolytes and recorded in the solution of 0.1 M $NaNO_3$ + 0.1 M Na_2SO_4. Cathodic current peaks observed in the range -0.40 ≤ *E*/V ≤ -0.55, were attributed to the reduction reaction of nitrate ions, while the current increase evidenced at more negative potential values is related to the hydrogen evolution reaction. The voltammetric response for a solid copper electrode in the same solution containing nitrate ions is also shown in Figure 7 for comparison purposes.

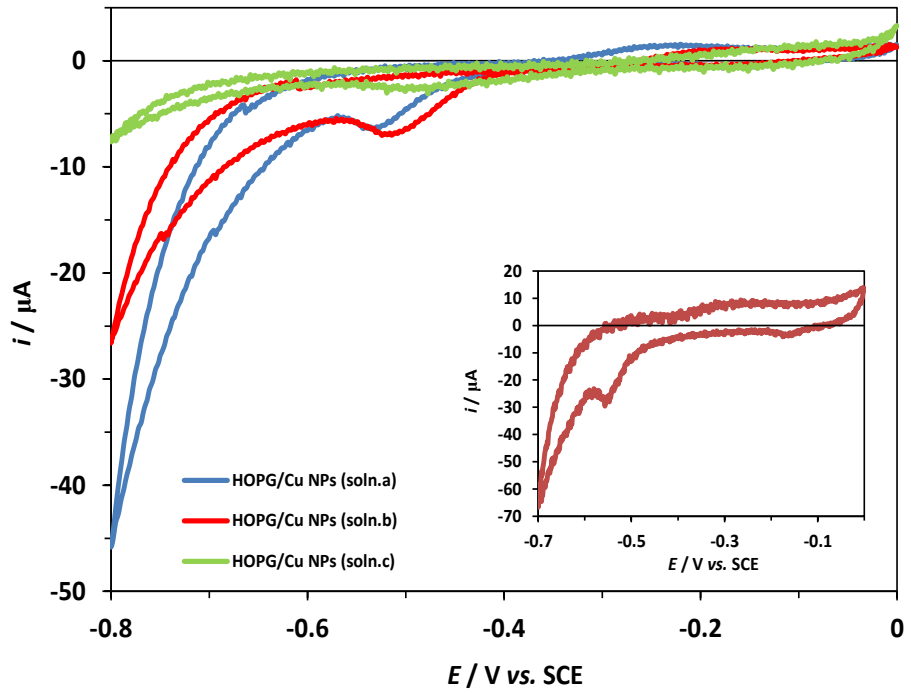

Figure 7. *Cyclic voltammograms of CuNPs electrodeposited on HOPG electrode from three plating solutions and recorded in 0.1 M $NaNO_3$ + 0.1 M Na_2SO_4. Inset: CV of polycrystalline Cu recorded in the same solution. |dE/dt|=10 mV s^{-1}*

The HOPG-modified electrodes showed voltammetric features similar to those of polycrystalline copper, *i.e*., a cathodic peak corresponding to nitrate reduction in the same potential region (-0.45 < *E*/V < 0.6), followed by an abrupt current increase due to hydrogen evolution. The HOPG electrodes modified by copper crystals prepared from solutions containing H_2SO_4 and Na_2SO_4 showed a more pronounced catalytic effect than the one observed for the solution containing both components. It can be inferred that this enhancement of the electrocatalytic effect, is due to the presence of a larger number of crystallites smaller than 50 nm, which favor adsorption of nitrate ions, despite the fact that a larger covered area was found for the third solution. This behavior is in accordance with the findings of other authors [30,31]. A. J. Wain [30] reported that the electrocatalytic activity was increased with decreasing particle size in the range 5–50 nm, which was attributed to the exposure of different reactive facets of the crystallites. Also, Masel *et al.* [31] demonstrated that Ag nanoparticles increased their electrocatalytic activity with decreasing particle size until a certain particle size (5 nm). They also indicated that this behavior could be caused by several reasons, such as variations with a particle size of the number of steps or kink sites of the crystallites, the electronic structure or work function of the particles, or the binding energy of the involved species. Accordingly, the aforementioned assumption is not conclusive and related studies in this regard are in progress.

Table 2 summarizes the values of the peak potential and maximum cathodic current values for nitrate reduction reaction using CuNPs deposited on HOPG surfaces from three supporting electrolyte solutions. The values corresponding to a freshly polished polycrystalline copper electrode were also included.

Table 2. *Cathodic peak potential and maximum cathodic current values of nitrate reduction at CuNPs deposited from different supporting electrolytes*

Supporting electrolyte for CuNPs	Nitrate reduction	
	E_{peak}/ V	i_{max} / μA
Na_2SO_4	-0.54	6.39
H_2SO_4	-0.52	7.04
Na_2SO_4 + H_2SO_4	-0.48	3.12
Solid copper	-0.56	29.50

Conclusions

Formation of HOPG supported copper nanoparticles (CuNPs) by electrodeposition from three different supporting electrolytes containing sulphate anions, and their potential application as electrocatalyst materials for the reduction reaction of nitrate ions were analyzed.

Cyclic voltammetric results indicated that for all supporting electrolyte solutions, the kinetics of the nucleation and growth of CuNPs on HOPG electrodes follows predominately a progressive model, presenting a good correlation with SEM images.

The voltammetric response of CuNPs modified HOPG electrode regarding nitrate reduction showed a better catalytic effect for Cu nanoparticles generated from solutions containing either Na_2SO_4 or H_2SO_4 species.

Acknowledgements*: The authors wish to thank the Universidad Nacional del Sur (Argentina) for the financial support of this work. N. Zurita acknowledges a fellowship granted by CIC (Comisión de Investigaciones Científicas de la Prov. de Buenos Aires).*

References

[1] S. Magdassi, M. Grouchko, A. Kamyshny, *Materials (Basel)* **3(9)** (2010) 4626-4638. https://doi.org/10.3390/ma3094626

[2] Z. Qing, A. Bai, S. Xing, Z. Zou, X. He, K. Wang, R. Yang, *Biosensors and Bioelectronics* **137** (2019) 96-109. https://doi.org/10.1016/j.bios.2019.05.014

[3] Y. Zhang, N. Li, Y. Xiang, D. Wang, P. Zhang, Y. Wang, S. Lu, R. Xu, J. Zhao, *Carbon* **156** (2020) 506-513. https://doi.org/10.1016/j.carbon.2019.10.006

[4] D.-D. Wang, C.-W. Ge, G.-A. Wu, Z.-P. Li, J.-Z. Wang, T.-F. Zhang, Y.-Q. Yu, L.-B. Luo, *Journal of Materials Chemistry C* **5** (2017) 1328-1335. https://doi.org/10.1039/c6tc05117k

[5] M. del C. Aguirre, S. E. Urreta, C. G. Gomez, *Sensors and Actuators B* **284** (2019) 675-683. https://doi.org/10.1016/j.snb.2018.12.124

[6] S. B. Khan, F. Ali, K. Akhtar, *Carbohydrate Polymers* **207** (2019) 650-662. https://doi.org/10.1016/j.carbpol.2018.12.032

[7] R. Suresh Babu, P. Prabhu, S. Sriman Narayanan, *Materials Today: Proceedings* **36(4)** (2019) 867-872. https://doi.org/10.1016/j.matpr.2020.07.020

[8] E. M. Bakhsh, F. Ali, S. B. Khan, H. M. Marwani, E. Y. Danish, A. M. Asiri, *International Journal of Biological Macromolecules* **131** (2019) 666-675. https://doi.org/10.1016/j.ijbiomac.2019.03.095

[9] World Health Organization, *Guidelines for Drinking-water Quality, 3rd Edition*, 2004. https://www.who.int/water_sanitation_health/dwq/GDWQ2004web.pdf

[10] C. Sun, F. Li, H. An, Z. Li, A. M. Bond, J. Zhang, *Electrochimica Acta* **269** (2018) 733-741. https://doi.org/10.1016/j.electacta.2018.03.005

[11] A. M. Stortini, L. M. Moretto, A. Mardegan, M. Ongaro, P. Ugo, *Sensors and Actuators B* **207 Part A** (2015) 186-192. https://doi.org/10.1016/j.snb.2014.09.109

[12] M. R. Majidi, K. Asadpour-Zeynali, B. Hafezi, *International Journal of Electrochemical Science* **6** (2011) 162-170. http://www.electrochemsci.org/papers/vol6/6010162.pdf

[13] D. Reyter, M. Odziemkowski, D. Bélanger, L. Roué, *Journal of the Electrochemical Society* **154(8)** (2007) K36. https://doi.org/10.1149/1.2746805

[14] Y. Li, J.Z. Sun, C. Bian, J. H. Tong, H. P. Dong, H. Zhang, S. H. Xia, *AIP Advances* **5(4)** (2015) 041312. https://doi.org/10.1063/1.4905712

[15] Y.-J. Shih, Z.-L. Wu, C.-Y. Lin, Y.-H. Huang, C.-P. Huang, *Applied Catalysis B* **273** (2020) 119053. https://doi.org/10.1016/j.apcatb.2020.119053

[17] D. Grujicic, B. Pesic, *Electrochimica Acta* **50(22)** (2005) 4426-4443. https://doi.org/10.1016/-j.electacta.2005.02.012

[18] D. Grujicic, B. Pesic, *Electrochimica Acta* **47(18)** (2002) 2901-2912. https://doi.org/10.1016/-S0013-4686(02)00161-5

[19] J. Vazquez-Arenas, G. Vázquez, A. M. Meléndez, I. González, *Journal of The Electrochemical Society* **154(9)** (2007) D473. https://doi.org/10.1149/1.2755873

[20] O. Ghodbane, L. Roué, D. Bélanger, *Electrochimica Acta* **52(12)** (2007) 5843-5855. https://doi.org/10.1016/j.electacta.2007.03.009

[21] S. Fletcher, C. S. Halliday, D. Gates, M. Westcott, T. Lwin, G. Nelson, *Journal of Electroanalytical Chemistry* **159(2)** (1983) 267-285. https://doi.org/10.1016/S0022-0728(83)80627-5

[22] V. A. Isaev, O. V. Grishenkova, Y. P. Zaykov, *Journal of Solid State Electrochemistry* **22** (2018) 2775-2778. https://doi.org/10.1007/s10008-018-3989-9

[23] N. Zurita, S. G. García, *Avances en Ciencias e Ingeneria* **11** (2020) Art. 3. https://www.executivebs.org/publishing.cl/avances-en-ciencias-e-ingenieria-vol-11-nro-1-ano-2020-articulo-3/#aci2020vol11nro1

[24] A. Milchev, T. Zapryanova, *Electrochimica Acta* **51(14)** (2006) 2926-2933. https://doi.org/10.1016/j.electacta.2005.08.045
[25] T. Zapryanova, A. Hrussanova, A. Milchev, *Journal of Electroanalytical Chemistry* **600(2)** (2007) 311-317. https://doi.org/10.1016/j.jelechem.2006.10.002
[26] G. Gunawardena, G. Hills, I. Montenegro, *Journal of Electroanalytical Chemistry and Interfacial Electrochemistry* **184(2)** (1985) 357-369. https://doi.org/10.1016/0022-0728(82)85080-8
[27] G. A. Hope, R. Woods, *Journal of the Electrochemical Society* **151(9)** (2004) C550. https://doi.org/10.1149/1.1774186
[28] B. Scharifker, D. Hills, *Electrochimica Acta* **28(7)** (1982) 879-889. https://doi.org/10.1016/-0013-4686(83)85163-9
[29] L. Huang, E.-S. Lee, K.-B. Kim, *Colloids and Surfaces A* **262(1-3)** (2005) 125-131. https://doi.org/10.1016/j.colsurfa.2005.03.023
[30] A. J. Wain, *Electrochimica Acta* **92** (2013) 383-391. https://doi.org/10.1016/j.electacta.2013.01.074
[31] A. Salehi-Khojin, H.-R. M. Jhong, B. A. Rosen, W. Zhu, S. Ma, P. J. A. Kenis, R. I. Masel, *Journal of Physical Chemistry C* **117(4)** (2013) 1627-1632. https://doi.org/10.1021/jp310509z

J. Electrochem. Sci. Eng. **12(2)** (2022) 265-274; http://dx.doi.org/10.5599/jese.1127

Open Access : : ISSN 1847-9286

www.jESE-online.org

Original scientific paper

Electrochemical studies of lateral flow assay test results for procalcitonin detection

Yachana Gupta, Kalpana, Aditya Sharma Ghrera

Applied Science Department, The NorthCap University, Gurugram, India

Corresponding author: adityasghrera@gmail.com

Received: September 30, 2021; Accepted: November 22, 2021; Published: November 28, 2021

Abstract

In this study, the lateral flow assay (LFA) has been developed for the detection of bacterial infection (BI) by specific biomarker procalcitonin (PCT), without a need for complicated instrumentations and technical expertise. For the development of the assay, gold nanoparticles (AuNP) and their conjugates with antibodies specific to the model antigen PCT are assessed. Polyclonal antibody (pAb) labelled with gold nanoparticles (AuNP) to obtain the AuNP-pAb complex and the specific monoclonal antibody (mAb) have been dropped at the test zone. This complex is placed over the conjugate line of the LFA strip. In the absence of PCT or the presence of other biomarkers, the test line remained colourless, which revealed the specificity of assay towards PCT among a pool of various analytes. Herein, observations have been made through two different platforms for quantitative and qualitative analysis for the detection of PCT biomarker. The qualitative analysis has been performed on the basis of appearance red color in the test band, while for quantitative analysis, a novel approach has been adopted. Herein, the nitrocellulose membrane (paper strip) is cut out from the LFA strip and used for electrochemical studies under similar solution conditions. Different paper strips presented different cyclic voltammograms (CV) that could be correlated to varying PCT concentrations captured at the test line of the paper strip. The qualitative detection limit for PCT using this LFA was determined to be 2 ng ml^{-1} and the quantitative detection limit was 1 ng ml^{-1}. The electrochemical response studies of the paper strip by CV technique revealed the sensitivity value of 0.695 μA ml ng^{-1}.

Keywords

Cyclic voltammetry, lateral flow assay; gold nanoparticles, polyclonal antibody, monoclonal antibody; biomarker

Introduction

Globally, bacterial infections (BI) are one of the primary reasons for illness and death, and they are becoming an increasingly serious problem due to the regular growth of bacteria. According to WHO report, antibiotic-resistant bacteria pose a risk to public health. Therefore, for BI's diagnosis and

immediate response, some on-site detection technique is required [1]. For the clinical utility of BI specific biomarkers, numerous immunoassays like time-resolved fluoro-immunoassay (TRFIA) [2,3], chemi-luminescence immunoassays (CLIA) [4], immunochromatographic tests (ICT), and enzyme-linked immunosorbent assays (ELISA) [5] have been presented in a wide variety of research applications for diagnosis purposes. Nevertheless, the lateral flow immunoassay (LFA) remains an ideal technique for the point of care (POC) testing of BI and any other pathological changes inside the human body [6]. LFA technique allows even unskilled users to perform difficult tests at the point of need in a cost-effective manner and without the need for any additional equipment, which makes it popular among users. As a labeling agent, gold nanoparticles (AuNP) [7] remain of interest to date for LFA development, owing to their enriched intensity, optical stability, biocompatibility, and easy surface modification properties [8,9]. In several already reported studies [10,11], the LFA technique was used to detect BI-specific biomarker procalcitonin (PCT) by AuNP as a label. For the diagnosis of BI or sepsis, PCT acts as a forerunner of the hormone calcitonin and can differentiate between bacterial and viral infections [10,12]. In serum, the value of PCT is < 0.1 ng ml^{-1}, which rises with the severity of the infection. During BI in healthy adults, PCT is < 0.05 μg ml^{-1}, if the systemic infection is unlikely. In the case of localized infection, PCT increases from 0.05 to <0.5 μg ml^{-1}, while in the conditions like major trauma, recent surgery, or severe cardiogenic shock, PCT rises further from 0.5 to <2 μg ml^{-1} [13-15].

Some reported works have developed LFA strips using spherical and popcorn-like AuNP to detect varying PCT concentrations on multiple test lines [16-18]. In the present work, procalcitonin (PCT) has been selected for BI diagnosis as a model antigen taken from the literature [19]. Regarding the new approach to PCT detection, the results of the test line of LFA strips were examined by qualitative and quantitative determinations. Test line qualitative results were obtained with the LFA technique followed by the sandwich assay. On the other hand, the portion of the nitrocellulose (NC) membrane, where the antigen-antibody complex is already formed in the test area of the LFA test strips, was subsequently used to confirm the electrochemical quantification. The effectiveness of electrochemical quantification was dependent on the presence of electron transfer agents at the electrode surface [20]. Electro-chemical studies were carried out for the reliability of the test results and signal intensity [21-23]. Signal detection of redox species curving in the LFA-modified strip indicates the possibility of developing a one-step analysis format with electrochemical quantification. In numerous published papers, it has been shown that as the concentration of analyte increases, the redox peak current of an electron transfer agent decreases due to the slowing of electron transmission between the paper strip and electrolytic solution. These results confirmed the accuracy of the currently presented cyclic voltammetry (CV) studies. From observing CV curves, it was found that the pattern of oxidation currents reduces with increasing concentration and proved that the responses are concentration-dependent [24-27]. Here, the LFA strip test results are validated by the quantitative and qualitative determination of PCT. The purpose of this study is to detect PCT on a paper strip using LFA and electrochemical CV technique. This new paper strip is a convenient method for quantifying PCT with high sensitivity and low detection limit. This study showed that electrochemical detection is independent of AuNP-antibody conjugation and works normally when colorimetric detection suggests a false positive test, whereas LFA can respond to AuNP-antibody conjugation and antigen-antibody interaction.

Experimental

Reagents and instruments

Chloroauric acid, tri-sodium citrate dihydrate, bovine albumin serum (BSA), disodium hydrogen phosphate, and monobasic sodium phosphate were purchased from CDH Chemicals. Sodium

borohydride and Tween-20 were purchased from Thomas Baker (Chemicals), sucrose, tris (hydroxymethyl) methylamine, sodium chloride and sodium azide from Fisher Scientific, while mAb and pAb were purchased from mybiosource.com. Glass fiber sample pad (24×260 mm), polyester conjugation pad (70×260 mm), NC membrane (50×260 mm) and absorption pad (21×260 mm) were purchased from Advanced micro devices (mdi) membrane. The electrochemical characterization has been conducted on an Autolab PGSTAT204 potentiostat/galvanostat (Eco Chemie, The Netherlands) using a three-electrode system with the paper strip as working electrode, Ag/AgCl as reference electrode and platinum foil as a counter electrode, in 0.1 M KCl containing 10 mM $[Fe(CN)_6]^{3-/4-}$.

Preparation of AuNP-antibody conjugate

AuNP were synthesized by the citrate method. For the synthesis, 50 ml of the aqueous solution of (2.5 mM) hydrogen tetrachloroaurate(III) trihydrate ($HAuCl_4 \cdot xH_2O$) was prepared and boiled at about 65 °C, and after that 1ml of 5 % aqueous solution of trisodium citrate (TSC; 1 mL) [28-31] was mixed dropwise. The solution was stirred continuously for 30 minutes, resulting in a color variation from pale yellow/colorless to purple and finally to ruby red (Figure 1). For the conjugation of AuNP with pAb, a purified concentration of 0.2 mg ml^{-1} pAb was diluted in PBS buffer (100 mM, pH 7.4). Potassium carbonate is used to maintain pH to 6.7 with a solution of colloidal gold and diluted antibodies. The diluted solution was incubated for 30 minutes at 25 °C followed by the addition of 0.25 % blocking agent BSA and then continued to stir for twenty minutes. Subsequently defining the sanctified concentration of binding pAb, the AuNP-pAb was prepared. For the prediction of conjugation of AuNP-pAb, the absorption peak was monitored at about 523-526 nm by ultraviolet-visible (UV-Vis) spectroscopy. About 15-20 minutes, the entire solution was centrifuged at 8000 rpm. After centrifugation, the unconjugated antibody supernatant was gradually removed. Pallets were resuspended in buffers 10 mmol PBS, 0.5 % BSA, 5 % sucrose, and 0.1 % freshly prepared solution of sodium azide and stored at 4 °C for future use.

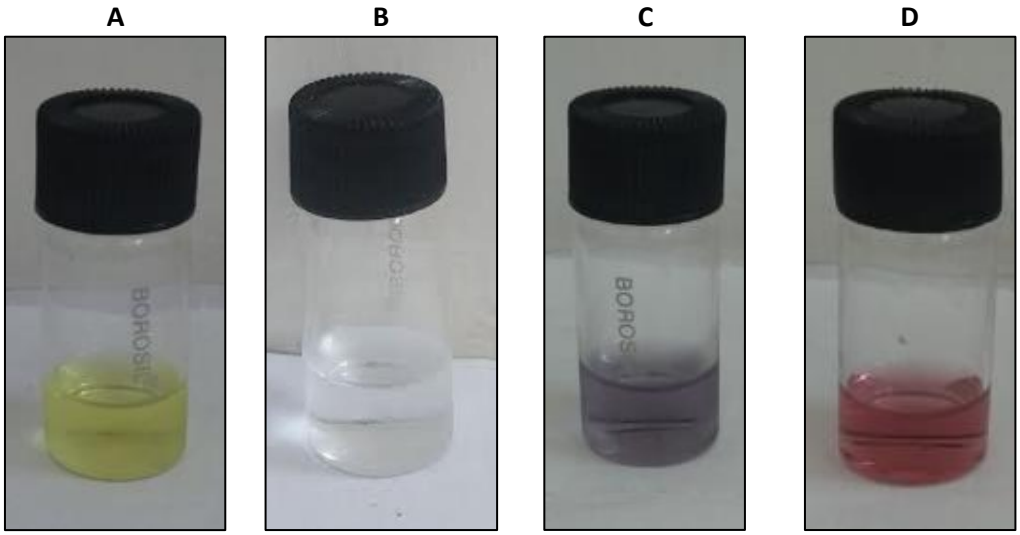

Figure 1. *The appearance of the color of AuNP: (A) 25 mM of $HAuCl_4 \cdot xH_2O$ solution; (B),(C) after adding TSC and continued to stir; (D) ruby red color of prepared AuNP*

Assembling of LFA strip components

The complete assembly parameters of the LFA test are described in Figure 2. The NC membrane has an adhesive plastic backing plate. The conjugate pad (1.4×0.5 cm^2) was pasted in a position overlapping the NC (2.4×0.5 cm^2) membrane by 5 mm. An absorbent pad (2.4×0.5 cm^2) was overlapped on the other side of the membrane by 5 mm. The sample pad (1.3×0.5 cm^2) was further

pasted over the conjugate pad with overlapping of 5 mm length. To confirm the proper placement and operation of the components, the liquid sample was dripped from the sample pad to the absorbent pad. For the preparation of the test line, 0.2 mg ml^{-1} mAb antibody containing PBS was dropped by a micropipette on the NC membrane and dried for 24 h at room temperature. Once fully assembled, LFA strips were stored in a dry place.

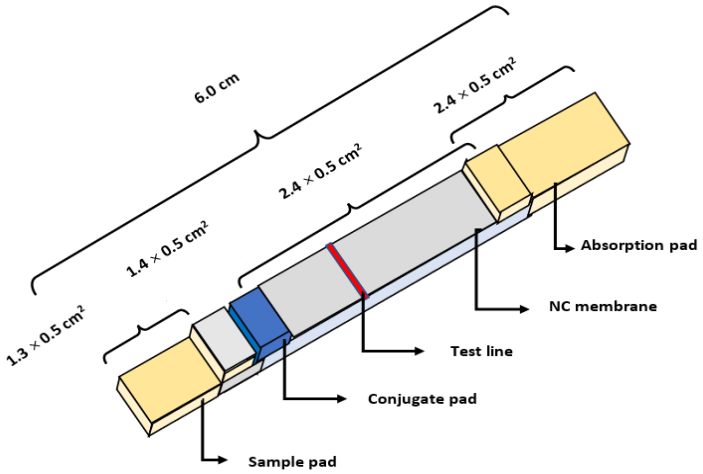

Figure 2. *Schematic illustration of LFA test strip*

Pre-treatment of pads

The glass fiber sample pad strips were pretreated with an aqueous solution containing 1 % sucrose, 1 % BSA, 0.05 % sodium azide, 20 mol l^{-1} sodium borate, and 0.05 % Tween-20 for 60 min. The strips were dried at 45 °C and stored in a dry state for further use. The polyester fiber conjugation pad was immersed in a solution containing 5 % sucrose and 0.05 % sodium azide in water for 90 minutes and then dried for 120 minutes at 50 °C. The conjugation pad was dipped in 5 ml of pre-prepared conjugate (pAb-AuNP) solution for 24 h. The conjugation pad was then dried at 37 °C and stored for further use. The NC membrane was pretreated by 1 % Tween-20 and 1 % BSA for 1 h and dried at 38 °C for 60 minutes and stored in the dry state for further use.

Results and discussion

In this study, we discussed the qualitative and quantitative determination of the BI-specific biomarker PCT because PCT is promising and very sensitive to increased BI levels and is often reported to be more significant than other biomarkers. PCT ranges from 2 to 10 ng ml^{-1} in sepsis, whereas PCT above 10 ng ml^{-1} indicates a state of septic shock. However, PCT concentration of 2 to 0.15 ng/ml indicates uncertainty in the presence of BI. AuNP is used as a labelling agent and PCT-specific mAb was dropped at the test line by a micropipette. When the complex (AuNP-pAb/PCT) moves through the NC membrane and reaches the test line containing mAb, a sandwich complex (AuNP-pAb /mAb/PCT) is formed. The formation of this complex can be visualized by appearing a red-colored band on the test line due to the presence of AuNP in the sandwich complex. The strength of the red color band indicates PCT concentration which has further been quantified using colorimetric and electrochemical techniques.

Characterization of AuNP and pAb-AuNP conjugate

UV-Vis spectroscopy, transmission electron microscopy (TEM), and scanning electron microscopy (SEM) were used for the spectroscopic and morphological characterization of AuNP and its conjugates. UV-Vis spectroscopy can be used to determine the stability of nanoparticle solution over time. When

AuNP are exposed, they appear in a red solution, but when the particles are conjugated, the solution color turns blue/purple and may turn into a clear solution with a black precipitate. Figure 3 shows the UV-visible absorption spectra of AuNP and its conjugate with pAb. In this graph, the red color curve shows bare AuNP, and a black colour curve is indicates for AuNP-pAb conjugation. Bare AuNP peak was recorded at 524 nm, which approves the existence of sphere-shaped AuNP with remarkable colloidal constancy and consistency in size and composition. The peak of AuNP-pAb was recorded at 530 nm, which explains that AuNP-pAb conjugation is taking place. Here, the shift of the peak to the right indicates a longer wavelength with increasing AuNP [32].

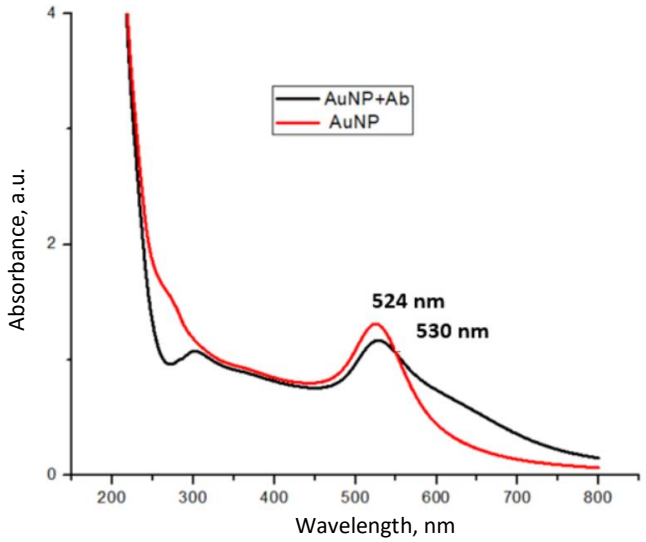

Figure 3. *UV-Vis absorption spectra of AuNP and AuNP-pAb*

For TEM studies, carbon-coated copper grids were used. The prepared AuNP solution (10 µl) was dropped on-grid and dried for 24 h. Experimental data was collected at 200.0 kV and 50000× magnification. The TEM images reveal that synthesized AuNPs are well separated and spherical (Figure 4A), indicating their stable dispersion in the solution condition. Furthermore, the synthesized particles are monodispersed, having a size range from 15.4 -25.6 nm (Figure 4B).

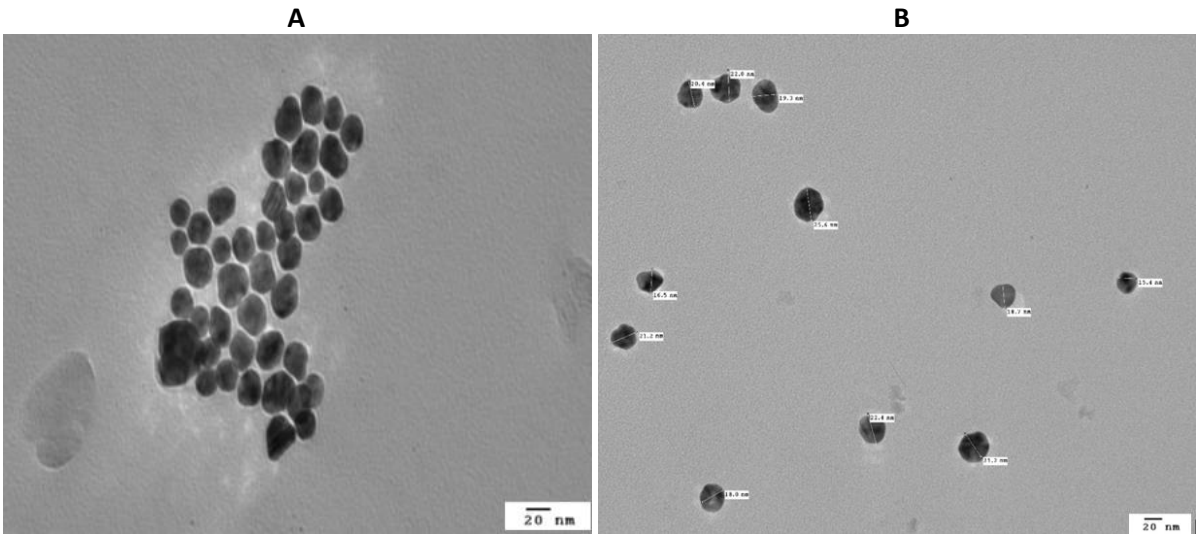

Figure 4. *TEM images of AuNP*

For the preparation of SEM samples, the drop-casting method was applied. By this method, polyvinyl alcohol and AuNP (PVA-AuNP) film were prepared. In this method, the ITO plate surface (1.0×1.0 cm^2)

was ultrasonically cleaned with an aqueous solution of ammonia and ethyl alcohol. The mixed solution (1ml of colloid gold and 5 % PVA) was dropped on the bare surface of ITO. Then the strips were dried at 140 °C for 1.5 h to make PVA-AuNP film [33]. After that, the annealing process of PVA-AuNP film was done and kept about 4-5 h at different temperatures (400-600 °C). Eventually, the strengthened film was cooled at room temperature in the air. The SEM image of the sample has been demonstrated in Figure 5. Experimental data was collected at 20.00 kV and x 1000 magnification.

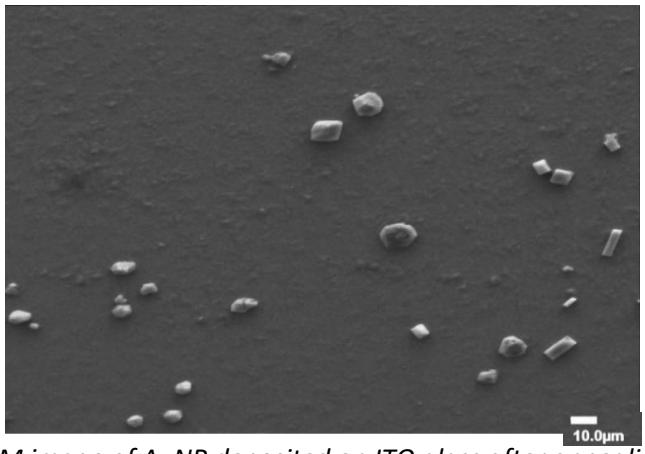

Figure 5. *SEM image of AuNP deposited on ITO glass after annealing at 400 °C*

Optimization of standard sample assay

For the LFA reaction, a sandwich analysis was performed to detect the PCT signal. For this purpose, standard solutions of PCT with concentrations of 1, 2, 10, 20, 30, 40, 50, and 60 ng ml^{-1} were prepared from the stock solution of 0.1 mg ml^{-1} solution in PBS solution (pH 7.4). The sample pad and conjugate pad were pretreated with buffers and used to develop antigen-antibody interaction. The AuNP-pAb complex was applied to the conjugation pad. Samples containing PCT antigen with different standard concentrations were dropped to the sample pad to initiate the reaction. The sample antigen interacts with the pAb-AuNP complex and forms a labeled antigen-antibody complex as it starts flowing through the sample pad. This complex moves across a porous membrane where specific mAb is already present in the test zone, forming a sandwich complex. The test line was drawn on the NC membrane 2.1 cm away from the conjugated pad. When PCT (100 µl) was dropped at sample pad at concentrations of 10 to 60 ng ml^{-1}, a strong red band appeared at the test line (Figure 6d-i).

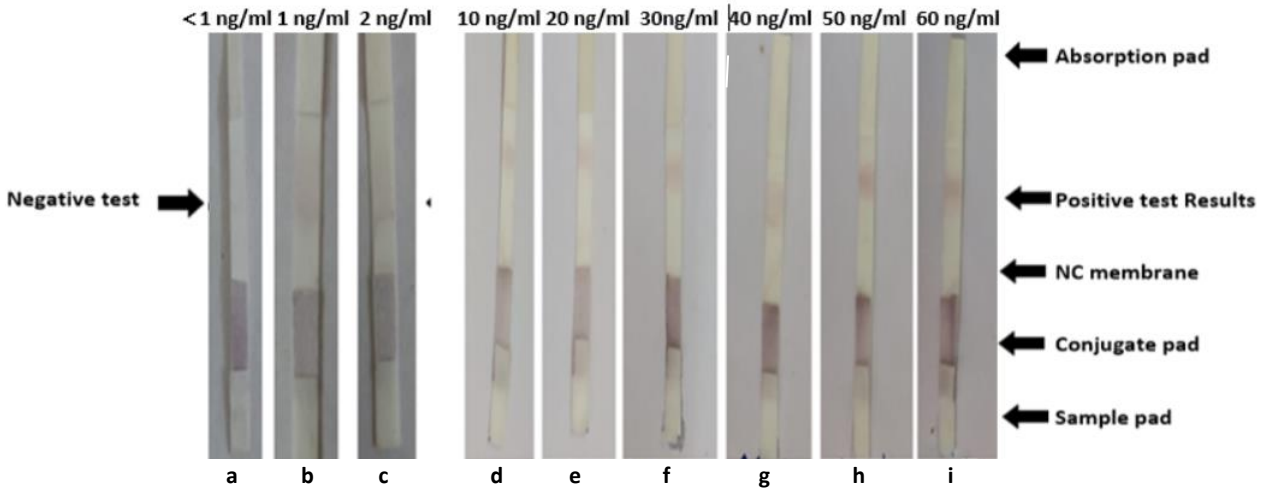

Figure 6. *Illustration of LFA strips test results of different concentrations of PCT: (a) <1 ng ml^{-1} and (b) 1 ng ml^{-1} are showing negative test results; (c) 2 ng ml^{-1} is showing weak positive bands; (d-i) 10 to 60 ng ml^{-1} are showing strong positive test results*

At the concentration of 2 ng ml^{-1}, a weak red band appeared at the test line (Figure 6c), and thus, this concentration has been considered as the qualitative limit of detection of the test assay. However, at 1 ng ml^{-1} (Figure 6b) and lower concentrations (Figure 6a) no bands appeared at the test line, and thus, 1 ng ml^{-1} has been considered as a negative test result.

Electrochemical characterization of LFA strip and response studies

Cyclic voltammetry (CV) studies were conducted for electrochemical detection of a range of PCT concentrations using an Autolab potentiostat/galvanostat instrument with a three-electrode setup. Platinum wire was used as the counter electrode, Ag/AgCl as the reference electrode, and the portion of NC membrane cut from the modified LFA test strip (pAb-AuNP/mAb/PCT) was used as the working electrode (paper strip). For electrochemical analysis, 0.1 M KCl containing 10 mM $[Fe(CN)_6]^{3-/4-}$ solution was used as a redox probe [19,35]. In the present work, CVs were performed with the paper strip as a working electrode which exhibits low conductivity. Thus, to enhance electron transmission between the working electrode and electrolyte and to record oxidation/reduction currents in CV curves, the redox probe $[Fe(CN)_6]^{3-/4-}$ was added as a marker to investigate changes in electrode behaviour after loading different concentrations of PCT on the paper strip [34,36,37].

To obtain voltammetric signals, portions of the NC (2.4×0.5 cm^2) membrane of the strips which have an antigen-antibody complex, were cut (2 cm) and immersed in a redox probe solution (0.1 M KCl containing 10 mM $[Fe(CN)_6]^{3-/4-}$. CVs were performed between -0.4 and 0.8 V at the scan rate of 50 mV s^{-1}. Figure 7A shows decreasing oxidation/reduction currents in recorded CVs for every increase in the concentration of PCT analyte on the paper strip. In an electrochemical investigation through CV, redox currents produced as a result of electron transfer from an electrolyte to a working electrode or *vice versa* were monitored. The intensity of produced redox currents depends upon the electroactive species present in the electrolytic solution. With the help of this mechanism, redox currents are observed to identify the PCT analyte on the paper strip. Oxidation and reduction current peaks are not visible in recorded CVs in our work as the paper strip is a poor conductor and does not facilitate charge transfer. Thus, a characteristic cyclic voltammogram is not obtained even after the application of redox agents. Nevertheless, the recorded CVs of the paper strips in the presence of redox agents in the solution are in conformity with work published by various research groups [38,39]. Thus, to study variation in oxidation current of the strip with respect to varying PCT concentrations, the oxidation CV signal has been recorded at the fixed potential (0.3V). When the concentration of 1 ng ml^{-1} PCT paper strip was investigated by CV, the oxidation current was 60.03 µA, and when the concentration of the analyte was increased to 2 ng ml^{-1}, a decrease of oxidation current to 53.29 µA was observed. On further increasing of the analyte concentration from 10, 20, 30, 40, 50 and 60 ng ml^{-1}, a continuous decrease of oxidation current was observed as 46.96, 37.21, 29.52, 23.49, 21.13 and 17.46 µA, respectively. This can be attributed to higher loading of PCT on the paper strip surface with increasing concentration, which hinders electron transmission between the redox probe and the electrode, and so, the current density is decreased. Using CV current responses, the calibration curve is obtained and presented in Figure 7B as a function of measured oxidation current at 0.3 V and PCT concentration on the paper strip in the range of 1 to 60 ng ml^{-1}. Linear proportionality of this plot indicates that magnitude of current changes linearly with the change in analyte concentration, while the negative slope of this plot indicates that oxidation current decreases with the increase of analyte on the paper strip. The linear proportionality of the current value and PCT concentration in the range from 1 to 60 ng ml^{-1} corresponds to the equation (1), showing the regression coefficient value of 0.97 and sensitivity value of 0.695 µA ml ng^{-1}.

$$I = 0.695\ [C_{PCT}] + 54.646 \quad (1)$$

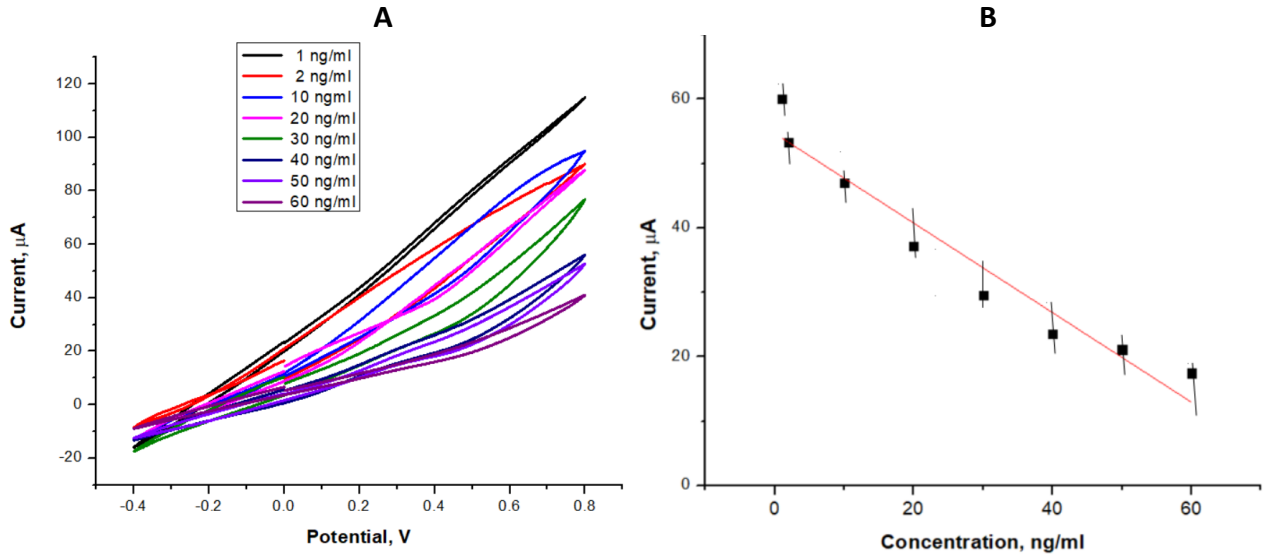

Figure 7. *(A) CV recorded for modified LFA strip as a function of PCT concentrations (1 - 60 ng ml^{-1}) in 0.1 M KCl containing 10 mM $[Fe(CN)_6]^{3-/4-}$; (B) calibration plot of oxidation current at 0.3 V as a function of PCT concentration*

Conclusions

The present paper successfully developed a portable and inexpensive detection test kit for the quantitative and qualitative detection of PCT analyte through LFA and electrochemical CV techniques. Here, AuNP performed excellent specificity and color appearance at the test line. The color intensity on the test zone was directly proportional to the concentration of the PCT analyte. LOD of the LFA technique of 2 ng ml^{-1} was found qualitatively and 1 ng ml^{-1} quantitatively. By electrochemical CV response studies, a linear relation between oxidation current and PCT in the concentration range of 1 to 60 ng ml^{-1} was obtained, with the sensitivity of the modified LFA strip of 0.695 µA ml ng^{-1}. This approach proves that for electrochemical detection of PCT, there is no need to use highly conductive substrates such as gold, silver, ITO, and expensive quantitative equipment. Hence, LFA and electrochemical techniques are convenient and easy POC techniques to detect BI-specific biomarker PCT.

Acknowledgements: *The authors acknowledge the support from The NorthCap University for providing infrastructure and instrumentation facilities. A.S. Ghrera thanks for the financial support received from Science and Engineering Board (DST), India, under the Young Scientist project (YSS/2015/001330). The authors wish to thank and acknowledge AIRF- JNU for the TEM characterisation and acknowledge NorthCap University for SEM characterisation.*

References

[1] Y. Gupta, A.S. Ghrera, *Archives of Microbiology* **203** (2021) 3767-3784. https://doi.org/10.1007/s00203-021-02357-9

[2] L.-M. Lei, J.-S. Wu, N.-Q. Gan, L. R. Song, *Clinica Chimica Acta* **348(1-2)** (2004) 177-180. https://doi.org/10.1016/j.cccn.2004.05.019

[3] T. Yu, S. Gao, A. Yin, Y. Tang, Y. Wu, L. Li, M. Li, *Journal of Immunoassay and Immunochemistry* **34(4)** (2013) 365-375. https://doi.org/10.1080/15321819.2012.744999

[4] L. Cinquanta, D.E. Fontana, N. Bizzaro, *Autoimmunity Highlights* **8(1)** (2017) 9. https://doi.org/10.1007/s13317-017-0097-2

[5] R. Gautam, K. Parajuli, T. Tshokey, J. Stenos, J. B. Sherchand, *BMC Infectious Diseases* **20** (2020) 138. https://doi.org/10.1186/s12879-020-4861-y

[6] S. Sharma, J. Zapatero-Rodríguez, P. Estrela, R. O'Kennedy, *Biosensors (Basel)* **5(3)** (2015) 577-601. https://doi.org/10.3390/bios5030577
[7] B. N. Khlebtsov, R. S. Tumskiy, A. M. Burov, T. E. Pylaev, N. G. Khlebtsov, *ACS Applied Nano Materials* **2(8)** (2019) 5020-5028. https://doi.org/10.1021/acsanm.9b00956
[8] M. Sajid, A.-N. Kawde, M. Daud, *Journal of Saudi Chemical Society* **19(6)** (2015) 689-705. https://doi.org/10.1016/j.jscs.2014.09.001
[9] K. M. Koczula, A. Gallotta, *Essays in Biochemistry* **60(1)** (2016) 111-120. https://doi.org/10.1042/EBC20150012
[10] X.-Y. Shao, C.-R. Wang, C.-M. Xie, X.-G. Wang, R.-L. Liang, W.-W. Xu, *Sensors (Basel)* **17(3)** (2017) 480. https://doi.org/10.3390/s17030480
[11] N. Zhan, Y. Zhou, L. Mei, Y. Han, H. Zhang, *Analytical Sciences* **35(3)** (2019)257-263. https://doi.org/10.2116/analsci.18p357
[12] A. L. Vijayan, Vanimaya, S. Ravindran, R. Saikant, S. Lakshmi, R. Kartik, Manoj. G. *Journal of Intensive Care* **51** (2017) 5. https://doi.org/10.1186/s40560-017-0246-8
[13] P. Schuetz, W. Albrich, B. Mueller, *BMC Medicine* **9** (2011) 107. https://doi.org/10.1186/1741-7015-9-107
[14] A. Hohn, S. Schroeder, A. Gehrt, K. Bernhardt, B. Bein, K. Wegscheider, M. Hochreiter, *BMC Infectious Diseases* **13** (2013) 158. https://doi.org/10.1186/1471-2334-13-158
[15] I. Samsudin, S. D. Vasikaran, *The Clinical Biochemist Reviews* **38(2)** (2017) 59-68. https://pubmed.ncbi.nlm.nih.gov/29332972
[16] K. V. Serebrennikova, J. V. Samsonova, A. P. Osipov, *Microchimica Acta* **186(7)** (2019) 423. https://doi.org/10.1007/s00604-019-3550-2
[17] K. Serebrennikova, J. Samsonova, A. Osipov, *Nano-Micro Letters* **10(2)** (2018) 24. https://doi.org/10.1007/s40820-017-0180-2
[18] K. V. Serebrennikova, J. V. Samsonova, A. P. Osipov, *Moscow University Chemistry Bulletin* **73(3)** (2018) 131-134. https://doi.org/10.3103/S0027131418030070
[19] A. Sharma Ghrera, *Analytica Chimica Acta* **1056** (2019) 26-33. https://doi.org/10.1016/j.aca.2018.12.047
[20] C. M. Pandey, A. Sharma, G. Sumana, I. Tiwari, B. D. Malhotra, *Nanoscale* **5(9)** (2013) 3800-3807. https://doi.org/10.1039/C3NR34355C
[21] A. S. Ghrera, M. K. Pandey, B. D. Malhotra, *Biosensors and Bioelectronics* **80** (2016) 477-482. https://doi.org/10.1016/j.bios.2016.02.013
[22] A. S. Ghrera, C. M. Pandey, Md. A. Ali, B. D. Malhotra, *Applied Physics Letters* **106(19)** (2015) 193703. https://doi.org/10.1063/1.4921203
[23] A. Sharma, C. M. Pandey, G. Sumana, U. Soni, S. Sapra, A. K. Srivastava, T. Chatterjee, B. D. Malhotra, *Biosensors and Bioelectronics* **38(1**) (2012) 107-113. https://doi.org/10.1016/j.bios.2012.05.010
[24] K. Ionue, P. Ferrante, Y. Hirano, T. Yasukawa, H. Shiku, T. Matsue, *Talanta* **73(5)** (2007) 886-892. https://doi.org/10.1016/j.talanta.2007.05.008
[25] Y. Huang, P. Kannan, L. Zhang, T. Chen, D.-H. Kim, *RSC Advances* **5(72)** (2015) 58478-58484. https://doi.org/10.1039/C5RA10990F
[26] W. Iwasaki, C. Kataoka, K. Sawadaishi, K. Suyama, N. Morita, M. Miyazaki, *Sensors* **20(17)** (2020) 4781. https://doi.org/10.3390/s20174781
[27] X. Zhu, P. Shah, S. Stoff, H. Liu, C.-Y. Li, *Analyst* **139(11)** (2014) 2850-2857. https://doi.org/10.1039/C4AN00313F
[28] J. Turkevich, P.C. Stevenson, J. Hillier, *Disscussions of the Faraday Society* **11** (1951) 55-75. https://doi.org/10.1039/DF9511100055
[29] J. Dong, P. L. Carpinone, G. Pyrgiotakis, P. Demokritou, B. M. Moudgil, *Kona Powder and Particle Journal* **37** (2020) 224-232. https://dx.doi.org/10.14356 %2Fkona.2020011

[30] P. Suchomel, L. Kvitek, R. Prucek, A. Panacek, A. Halder, S. Vajda, R. Zboril, *Scientific Reports* **8(1)** (2018) 4589. https://doi.org/10.1038/s41598-018-22976-5
[31] F. F. M. AL-Kazazz, K. A. F. AL-Imarah, I. A. Al-Hasnawi, L. Agelmashotjafar, B. A. Abdul-Majeed, *International Journal* of *Engineering Research and Applications* **3(6)** *(*2013) 21-30.
[32] V. D. Pham, H. Hoang, T. H. Phan, U. Conrad, H. H. Chu, *Advances in Natural Sciences: Nanoscience and Nanotechnology* **3(4)** (2012) 045017. http://dx.doi.org/10.1088/2043-6262/3/4/045017
[33] T. Feng, L. Ding, L. Chen, J. Di, *Journal* of *Experimental Nanoscience* **14(1)** (2019) 13-22. https://doi.org/10.1080/17458080.2018.1520399
[34] W. A. Ameku, W. R. de Araujo, C. J. Rangel, R. A. Ando, Thiago R. L. C. Paixão, *ACS Applied Nano Materials* **2(9)** (2019) 5460-5468. https://doi.org/10.1021/acsanm.9b01057
[35] A. Sharma, Z. Matharu, G. Sumana, P. R. Solanki, C. G. Kim, B. D. Malhotra, *Thin Solid Films* **519(3)** (2010) 1213-1218. https://doi.org/10.1016/j.tsf.2010.08.071
[36] X. Li, C. Zhao, X. Liu, *Microsystems & Nanoengineering* **1** (2015) 15014. https://doi.org/10.1038/micronano.2015.14
[37] S. Kumar, S. Kumar, C.M. Pandey, B.D. Malhotra, *Journal of Physics: Conference Series* **704** (2016) 012010. https://doi.org/10.1088/1742-6596/704/1/012010
[38] L. C. Shriver-Lake, D. Zabetakis, W. J. Dressick, D. A. Stenger, S. A. Trammell, *Sensors* **18(2)** (2018) 328. https://dx.doi.org/10.3390%2Fs18020328
[39] S. A. Trammell, L. C. Shriver-Lake, W. J. Dressick, *Sensors and Actuators B* **239** (2017) 951-961. https://doi.org/10.1016/j.snb.2016.08.087

J. Electrochem. Sci. Eng. **12(2)** (2022) 275-282; http://dx.doi.org/10.5599/jese.1166

Open Access : : ISSN 1847-9286

www.jESE-online.org

Original scientific paper

Electrodeposited palladium as efficient electrocatalyst for hydrazine and methanol electrooxidation and detection

Jelena D. Lović✉

University of Belgrade-Institute of Chemistry, Technology and Metallurgy, Department of Electrochemistry, Njegoševa 12, 11000 Belgrade, Republic of Serbia

Corresponding author: ✉*jelena.lovic@ihtm.bg.ac.rs Tel.: +381-11-337-0389; Fax: +381-11-337-0389*

Received: November 10, 2021; Accepted: December10, 2021; Published: December 17, 2021

Abstract

Electrodeposited palladium was used as an electrocatalyst for electrochemical oxidation of hydrazine and methanol and the development of a sensitive platform for their detection. The electrochemical behavior of the electrode was evaluated by cyclic voltammetry (CV), while electroanalytical properties were determined by differential pulse voltammetry (DPV). The electrodeposited Pd catalyst exhibited good electrocatalytic activity towards oxidation of hydrazine in neutral solution and methanol oxidation in alkaline solution. Under optimized DPV conditions, the electrodeposited Pd electrode shows good sensing capability for hydrazine and methanol detection.

Keywords

Sensitivity; differential pulse voltammetry; electroanalytical properties

Introduction

The interest in fuel cells has been growing over the past few decades, particularly for low-temperature fuel cells, since they can be used in portable electronic devices, electric vehicles, or stationary power supplies. Direct methanol fuel cells (DMFCs) are promising power sources, and as such, they demand highly efficient electrocatalysts for methanol electrooxidation. It was shown that Pd is an appropriate replacement for Pt because of its lower cost, higher tolerance against CO-like species, and better stability [1]. In addition, the choice of potential fuels is varied, and among them, hydrazine is of interest due to its large theoretical energy density, ease of storage and transport, and faster overall oxidation kinetics compared to the carbon-containing compounds [2].

It has been known that organic compounds, such as formaldehyde, isopropanol, methanol, hydrazine, are volatile and harmful to human health. To detect these compounds, many research groups investigate and have already established sensors with rapid response rates, excellent stability, and selectivity. Nanostructures could be promising and effective electrodes for sensing applications and the detection of various chemicals. Electrodeposition is one of the most efficient methods for the

preparation of metals or their alloys as nanostructures with appropriate composition and morphology. This rapid and facile technique provides nucleation and growth of metal nanoparticles with different sizes and shapes depending on applied potential, current, time, or concentration of the solution. In recent years the electrochemical detection of hydrazine or methanol using Pd nanostructures has been reported in the literature. The highly dispersed and ultrafine carbon-supported Pd nanoparticles (Pd NPs) catalyst was synthesized by the $NaBH_4$ reduction method in the presence of ethylenediamine-tetramethylene phosphonic acid (EDTMP) [3]. This Pd/C catalyst exhibited a significant electrocatalytic performance for hydrazine oxidation in 0.05 M H_2SO_4. Rastogi et al. investigated Pd NPs immobilized on organic-inorganic hybrid nanocomposite material coated on a GC electrode as electrocatalyst in the oxidation of hydrazine and its amperometric sensor [4]. Using pulsed electrodeposition technique, Pd species were deposited on the multi-walled carbon nanotubes dispersed in Nafion membrane to catalyze the electrooxidation of hydrazine and investigate their electroanalytical properties [5]. Zhang *et al.* reported the preparation of Pd NPs loaded on cobalt nanoparticles wrapped in nitrogen-doped carbon nanotubes for hydrazine determination [6]. Considering electrochemical methanol sensors, research is directed toward developing electrode materials that can electrochemically oxidize methanol at low potentials with high selectivity, providing high sensitivity. Tao *et al.* proposed an electrochemical methanol sensor based on palladium-nickel nanoparticles dispersed onto the surface of the silicon nanowires [7]. This composite electrode shows good electrooxidation capability for methanol, and because of that, it can be used for its detection. Electrochemical sensor for the determination of methanol-based on Pd NPs supported on Santa Barbara amorphous-15- PrNHEtNH2 (PdNPs@SBA-15-PrEn) is synthetized as well [8].

The aim of this paper is to prepare the electrode applying the electrochemical deposition of Pd without any additives in a simple one-step procedure and to examine its electrocatalytic activity and sensitivity in hydrazine and methanol oxidation. The sensing parameters such as sensitivity and detection limits are determined by means of differential pulse voltammetry (DPV) measurements.

Experimental

All electrochemical measurements were performed using Volta Lab PGZ 402 (Radiometer Analytical, Lyon, France). A conventional three-electrode system was employed, including a gold rotating disk electrode (Au) electrode (geometric surface area 0.196 cm^2) as the working electrode, Pt wire as the counter electrode, and a saturated calomel electrode (SCE) as the reference electrode. A mirror-like polished Au electrode was prepared as previously stated [9]. The electrochemical deposition was performed without any additives in a simple one-step procedure at a potential of -0.16 V within 100 s and 1000 rpm at room temperature from deaerated 0.1 M NaCl solution containing 30 mM $PdCl_2$ as was previously described [10]. In DPV measurements, the accumulation of the hydrazine at the working electrode was carried out for 0.2 s at -400 mV and 0.2 s at -600 mV for methanol. After that, the potential was scanned at a scan rate of 0.125 mV s^{-1}, pulse amplitude of 50 mV, f = 5 Hz and step value 2 mV. All reagents were of analytical grade and purchased from Sigma-Aldrich. All solutions were prepared using nanopure water supplied by a Milli-Q system (Millipore®) with resistivity ≥18.2 MΩ cm. Electrochemical measurements were performed under N_2 atmosphere at ambient temperature.

Results and discussion

Electrochemical oxidation of hydrazine

A complete characterization of prepared Pd catalyst involving structural, morphological, and surface studies, was previously reported [10]. According to SEM measurements, a simple

electrochemical deposition process without surfactants created the morphology of nanorods with a diameter of ~5 nm and an aspect ratio of ~8. A clear rod shape was resolved by TEM image.

It is well known that the electrode surface area and reactant concentration affect the current. In the presented work, one electrodeposited Pd electrocatalyst was examined and it is reasonable to assume that the electrochemically active surface area is the same in all experiments. If the other parameters such as temperature and the viscosity of the solution remain constant, the current is proportional to the reactant concentration. Because of that, the results were given per geometric surface area or just as current intensity.

The electrocatalytic activity of electrodeposited Pd in the oxidation of 0.5 mM hydrazine was investigated in 0.1 M K_2SO_4 (pH 7) at 100 mV s^{-1} as is presented in Fig 1a. Neutral solution was selected as a blank electrolyte since it has been shown that the electrooxidation of hydrazine is more favored under neutral conditions regarding alkaline medium [11,12]. One anodic peak for hydrazine oxidation at 80 mV in the forward scan can be noticed. The absence of a current peak in the backward scan implies that the electrooxidation of hydrazine is an irreversible process that occurs during the positive potential scan.

It has been shown that for the oxidation of hydrazine at platinum electrodes, surface oxides are substantial to electrocatalysis [13]. To establish the necessity of surface oxides, voltammetry was conducted in the absence of hydrazine at the Pd electrode. Figure 1b shows the typical response feature of the Pd surface. The peak in the range of -700 to -400 mV is for the oxidation of the adsorbed and absorbed hydrogen. A reversible redox feature in the potential region -200 – 100 mV is ascribed to the influence of ions in a sulphate electrolyte [14] and possibly also to the effect of the metal loading [15]. As is illustrated in Figure 1b the formation of Pd oxides starts at E > 400 mV, which is a higher overpotential than noticed in hydrazine oxidation. So, the effect of surface palladium oxide on electrocatalytic activity of Pd catalyst should be neglected during the hydrazine electrooxidation.

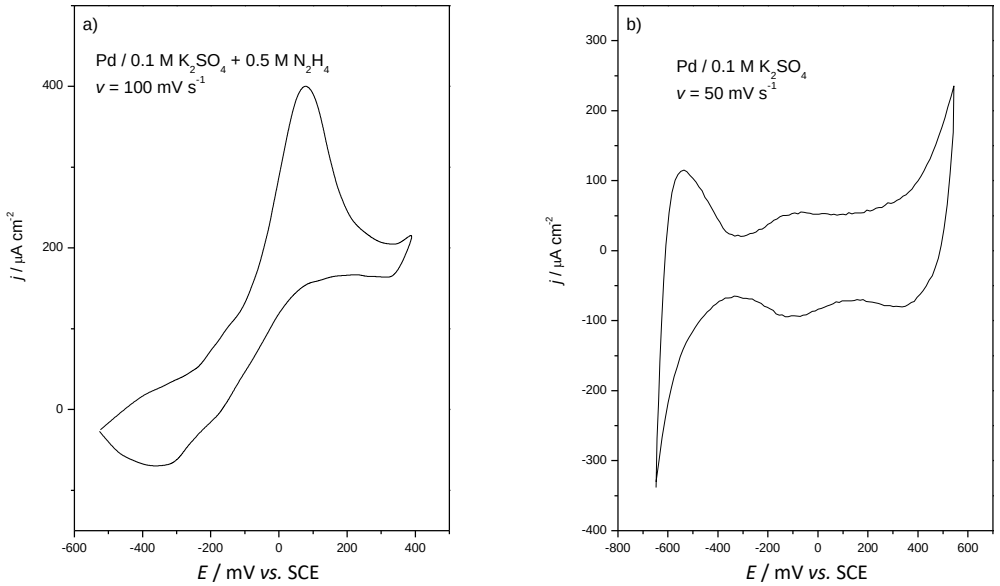

Figure 1. *CV of electrodeposited Pd in 0.1 M K_2SO_4 in the presence (a) and absence (b) of 0.5 M N_2H_4.*

Voltammetric response, forward direction, of Pd electrode towards electrochemical oxidation of hydrazine was investigated as a function of scan rate (Fig. 2). With an increasing scan rate, a positive shift in the oxidation peak potential along with enhancement in catalytic current density was noticed. The plot of current density vs. square root of scan rate (Fig. 3a) showed a linear

dependency, demonstrating that hydrazine electrooxidation on Pd electrode is a diffusion-controlled process which is in accordance with the reported results [3,16].

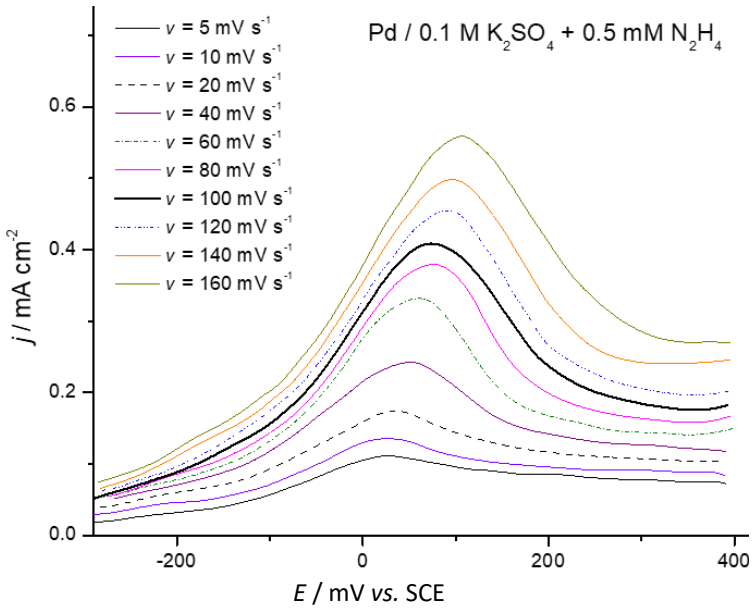

Figure 2. *The forward direction of CVs obtained on Pd electrode towards 0.5 mM N_2H_4 in 0.1 M K_2SO_4 at a scan rate from 5 to 160 mV s^{-1}*

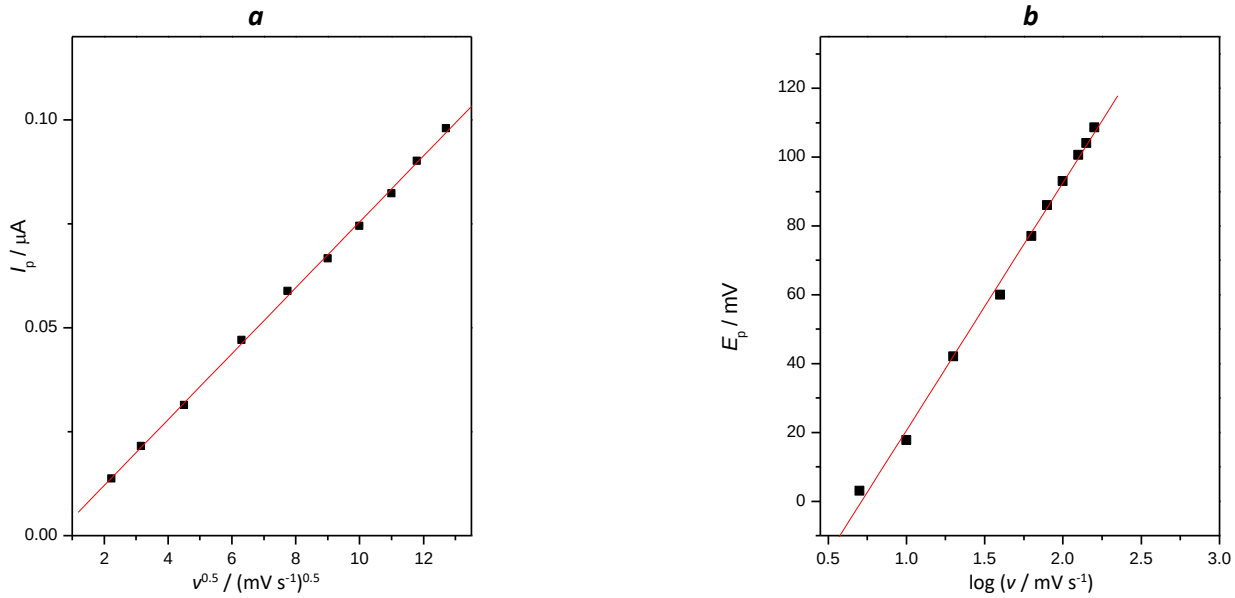

Figure 3. *(a) Plot of peak current vs. square root of scan rate. (b) Plot of peak potential from the log of scan rate. Data collected from Fig. 2*

The oxidation potential simultaneously shifts to positive values with a linear correlation between the peak potential and the logarithm of scan rate, as is presented in Fig. 3b. Bearing in mind that dependency, the Tafel slope was considered using the equation (1) for the irreversible diffusion-controlled process [17]:

$$E_p = b/2 \log v + \text{const.} \quad (1)$$

The slope of the dependency E_p – log v is $b/2$, and it is found to be 62 mV in this work, thus $b = 2 \times 62 = 124$ mV. The Tafel slope is $b = 59/(1-\alpha)n$ (α is the transfer coefficient; n - the number of electrons involved in the rate-determining). It is well known that the first electron transfer of hydrazine oxidation is rate-determining [4,18]. Assuming the number of electrons is 1, the transfer coefficient is estimated as 0.48, illustrating that the rate-limiting step is a one-electron transfer

process. The mechanism of hydrazine oxidation was studied electrochemically at the Pd electrode in solutions of different pHs (pH 2-11), presented in detail [19-21]. It has been shown that the mechanism of hydrazine oxidation depended significantly on the electrolyte solution and the nature of the electrodes [2,19]. Hydrazine is oxidized through the $4e^-$ process with the final product N_2 in an aqueous solution [14,18]. The first intermediate of hydrazine oxidation in aqueous solutions has been identified as the radical ion $N_2H_4^{\bullet+}$ [22] or radical di-cation $N_2H_5^{\bullet 2+}$ [19]. The formation of $N_2H_4^+$ ion was usually regarded as the rate-determining step, while other proposed intermediates are not stable [23].

Electrochemical oxidation of methanol

Figure 4 shows the voltammetric response of investigated Pd catalyst in 1 M NaOH containing 1 mM methanol at 50 mV s^{-1}. Electrodeposited Pd showed two anodic peaks for methanol oxidation at -250 mV in the forward scan and at -430 mV in the backward scan. The peak observed in the forward scan was ascribed to the oxidation of chemisorbed species coming from methanol adsorption on the surface of the catalyst in the presence of adsorbed OH^- species. The peak in the reverse scan might be caused by oxidation of freshly chemisorbed species or carbonaceous species, which are not completely oxidized in the forward scan. OH formation ability of a catalyst is in relation to alcohol oxidation activity. It is well documented in the literature that the kinetics of the alcohol oxidation reaction is enhanced by increasing the concentration of OH^- ions in the solution, thus causing the higher coverage of the electrode surface by OH^- species [24,25]. So, unlike hydrazine, methanol oxidation is determined by the degree of chemisorbed species originating from methanol and OH_{ad} coverage. Kinetic study of methanol electrooxidation reaction on Pd-based catalysts is well described in the literature [25,26].

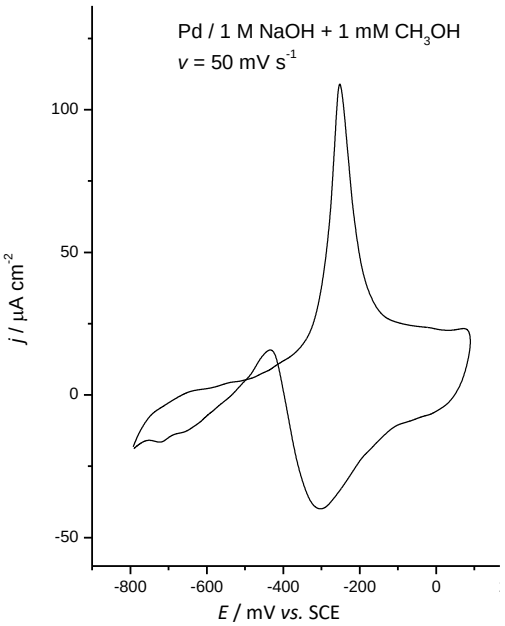

Figure 4. *CV of electrodeposited Pd in 1 M NaOH in the presence of 1 mM CH_3OH at a scan rate 50 mV s^{-1}*

Electroanalytic determination of hydrazine and methanol

To check the analytical performance of the electrodeposited Pd electrode in the electrochemical determination of hydrazine and methanol, DPV and square wave voltammetry (SWV) were tested. Since the DPV showed improved peak current compared to SWV the first-mentioned method was used and optimized to detect these molecules. DPV response of electrodeposited Pd catalyst towards different concentrations of hydrazine was presented in Figure 5a. With increasing hydrazine

concentration, the current of hydrazine oxidation also increases. According to Fig. 5b, the calibration plot of current vs. hydrazine concentration gives a linear dependence in the concentration range of 0.1-2 mM hydrazine. An excellent correlation coefficient (R = 0.999) was obtained as well.

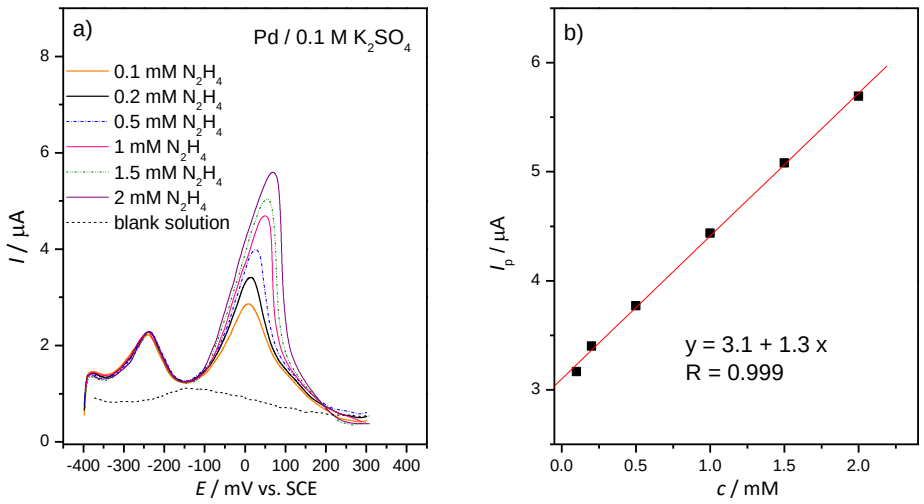

Figure 5. *(a) DPVs obtained on the electrodeposited Pd electrode in the presence of increasing hydrazine concentrations. (b) Dependency of peak current on hydrazine concentration*

Figure 6a shows the results of DPV obtained on the electrodeposited Pd electrode in the presence of an increasing concentration of methanol. Alkaline media were chosen because of their higher activity and poisoning resistance regarding acidic or neutral media. It can be noticed that the addition of methanol leads to a rapid and well-resolved increase of the peak currents at ~300 mV. E_p slightly shifts (~15 mV) towards more positive potentials, indicating that electrodeposited Pd shows satisfactory poison resistance from electrochemically formed intermediates.

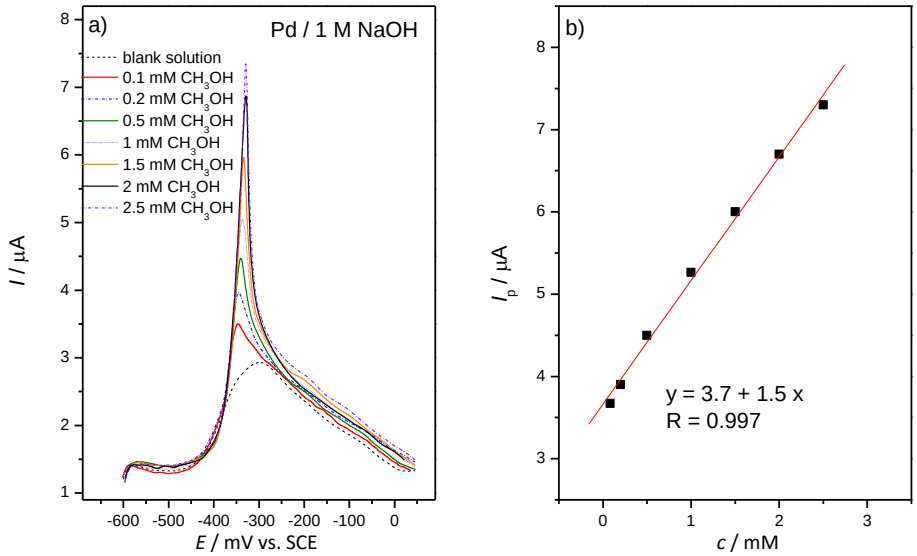

Figure 6. *(a) DPVs obtained on the electrodeposited Pd electrode in the presence of increasing methanol concentration. (b) Dependency of peak current from concentration*

The constructed linear dependency was used to evaluate several electroanalytical parameters. Thus, sensitivity was obtained from the slope of the calibration curve. The other electroanalytical parameters are the limit of detection (LOD) and the limit of quantification (LOQ). LOD demonstrates the lowest compound concentration which can be detected, while LOQ demonstrates the lowest concentration of compound, which can be quantitatively determined. Both LOD and LOQ were

calculated according to the equations *k*' SD / *b*, where *k*' = 3 for LOD and 10 for LOQ, SD is the standard deviation of the intercept and b is the slope of the calibration curve [27]. The obtained electroanalytical parameters are given in Table 1. It should be noted that the comparison of the electrochemical result is not unambiguous, as the electrochemical parameter is dependent on more than one experimental variable.

Table 1. *Determination of investigated compounds by DPV*

Compound	Concentration linear range, mM	Sensitivity, μA mM^{-1}	LOD, mM	LOQ, mM	*R*
Methanol	0.1-2.5	1.5	0.21	0.71	0.997
Hydrazine	0.1-2	1.3	0.09	0.3	0.999

The sensing capability of Pd in hydrazine detection is comparable to that established on Pd species deposited on the multi-walled carbon nanotubes dispersed in the Nafion membrane [5]. Nevertheless, the obtained LOD and LOQ values for both investigated compounds are lower than the reported data obtained on Pd nanostructures [5,8,18,28], indicating the unavoidable improvement of the electrochemical characteristic. Following this strategy, the synthesis of Pd nanostructures of diverse shapes has been extensively used. Additionally, a mixture of metals forming alloys or core-shell structures can be found in literature as an effective way of improving electrocatalytic activity. Enhancing the electrochemical activity and sensitivity towards hydrazine and methanol oxidation will be a matter of future studies.

Conclusions

Electrochemical deposition of Pd was performed without any additives in a simple one-step procedure. Electrodeposited Pd was then used as an electrocatalyst for the electrochemical oxidation of hydrazine and methanol. The electrochemical behavior of the Pd electrode reveals that the effect of surface palladium oxide should be neglected in the course of hydrazine electrooxidation. Conversely, in the case of the oxidation of methanol, surface oxides are necessary to electrocatalysis. The constructed linear dependency of *I*p from hydrazine or methanol concentration was used to evaluate electroanalytical parameters. Some improvements will be a matter of future studies.

Acknowledgement*: This work was financially supported by the Ministry of Education, Science and Technological Development of the Republic of Serbia for the financial support (Contract Nos. 451-03-9/2021-14/200026)*

References

[1] S. S. Munjewar, S. B. Thombre, R. K. Mallick, *Ionics* **23** (2017) 1–18. https://doi.org/10.1007/s11581-016-1864-1

[2] A. Serov, C. Kwak. *Applied Catalysis* B **98** (2010) 1-9. https://doi.org/10.1016/j.apcatb.2010.05.005

[3] Y. Lianga, Y. Zhoua, J. Mab, J. Zhaoa, Y. Chena, Y. Tanga, T. Lua, *Applied Catalysis B* **103** (2011) 388-396. https://doi.org/10.1016/j.apcatb.2011.02.001

[4] P. K. Rastogi, V. Ganesan, S. Krishnamoorthi, *Electrochimica* Acta **125** (2014) 593-600. http://dx.doi.org/10.1016/j.electacta.2014.01.148

[5] D. Gioia, I. G. Casella, *Sensors and Actuators B* **237** (2016) 400-407. http://dx.doi.org/10.1016/j.snb.2016.06.109

[6] Y. Zhang, B. Huang, J. Yeb, J. Ye, *Journal of Electroanalytical Chemistry* **801** (2017) 215-223. http://dx.doi.org/10.1016/j.jelechem.2017.07.036

[7] B. Tao, J. Zhang, S. Hui, X. Chen, L. Wan, *Electrochimica Acta* **55** (2010) 5019-5023. https://doi.org/10.1016/j.electacta.2010.04.013
[8] Z. Karimi, M. Shamsipur, M. A. Tabrizi, S. Rostamnia, *Analytical Biochemistry* **548** (2018) 32-37. https://doi.org/10.1016/j.ab.2018.01.033
[9] J. Mirković, J. Lović, M. Avramov Ivić, D. Mijin. *Electrochimica Acta* **137** (2014) 705-713. http://dx.doi.org/10.1016/j.electacta.2014.06.048
[10] L. Xiao, L. Zhuang, Y. Liu, J. Lu, H. D. Abruna, *Journal of American Chemical Society* **131** (2009) 602-608. http://dx.doi.org/10.1021/ja8063765
[11] E. Habib, *Microchemical Journal* **149** (2019) 104004. https://doi.org/10.1016/j.microc.2019.104004
[12] J. Wang, A. Khaniya, L. Hu, M. J. Beazley, W. E. Kadena, X. Feng, *Journal of Materials Chemistry A* **6** (2018) 18050-18056. http://dx.doi.org/10.1039/c8ta06219f
[13] L. Aldous, R. G. Compton, *Physical Chemistry Chemical Physics* **13** (2011) 5279-5287. http://dx.doi.org/10.1039/c0cp02261f
[14] M. Gerstl, M. Joksch, G. Fafilek, *Journal of Electroanalytical Chemistry* **741** (2015) 1–7. http://dx.doi.org/10.1016/j.jelechem.2015.01.009
[15] E. G. Ciapina, L. B. Viana, R. M. I. S. Santos, M. S. M. Nogueira, O. P. Almeida-Junior, R. S. Nunes, S. F. Santos, R. Z. Nakazato, *International Journal of Hydrogen Energy* **43** (2018) 17748-17752. https://doi.org/10.1016/j.ijhydene.2018.07.137
[16] H. Razmi, A. Azadbakht, M. H. Sadr, *Analytical Science* **21** (2005) 1317-1323. http://dx.doi.org/10.2116/analsci.21.1317
[17] J. A. Harrison, Z. A. Khan, *Journal of Electroanalytical Chemistry* **26** (1970) 1-11. https://doi.org/10.1016/S0022-0728(70)80060-2
[18] J. Li, X. Lin. *Sensors and Actuators B* **126** (2007) 527-535. http://dx.doi.org/10.1016/j.snb.2007.03.044
[19] R. Miao, R. G. Compton, *Electrochimica Acta* **388** (2021) 138655. https://doi.org/10.1016/j.electacta.2021.138655
[20] K. M. Emran, S. M. Ali, H. E. Alanazi, *Journal of Electroanalytical Chemistry* **856** (2020) 113661. https://doi.org/10.1016/j.jelechem.2019.113661
[21] D. A. Finkelstein, R. Imbeault, S. Garbarino, L. Roué, D. Guay, *Journal of Physical Chemistry* **C 120** (2016) 4717-4738. https://doi.org/10.1021/acs.jpcc.5b10156
[22] T. V. Atkinson, A. J. Bard, *Journal of Physical Chemistry* **75** (1971) 2043-2048. https://doi.org/10.1021/j100682a023
[23] X. Q. Cao, B. C. Wang, Q. Su, *Journal of Electroanalytical Chemistry* **361** (1993) 211-214. https://doi.org/10.1016/0022-0728(93)87056-2
[24] J. Liu, J. Ye, C. Xu, S. P. Jiang, Y. Tong, *Electrochemistry Communications* **9** (2007) 2334-2339. https://doi.org/10.1016/j.elecom.2007.06.036
[25] J. Wang, N. Cheng, M. N. Banis, B. Xiao, A. Riese, X. Sun, *Electrochimica Acta* **185** (2015) 267-275. https://doi.org/10.1016/j.electacta.2015.10.151
[26] M. Zar, H. Tabaean, H. Omidvar, A. Saberimehr, G. Hosseinzadeh, *Journal of Nanostructures* **9** (2019) 539-546. https://doi.org/10.22052/JNS.2019.03.015
[27] O. B. da Silva, S. A. S. Machado, *Analytical Methods* **4** (2012) 2348-2354. https://doi.org/10.1039/C2AY25111F
[28] C. Karuppiah, M. Velmurugan, S.-M. Chen, R. Devasenathipathy, R. Karthik, S.-F. Wang, *Electroanalysis* **28** (2016) 808-816. https://doi.org/10.1002/elan.201500453

J. Electrochem. Sci. Eng. **12(2)** (2022) 283-291; http://dx.doi.org/10.5599/jese.1193

Open Access : : ISSN 1847-9286

www.jESE-online.org

Original scientific paper

Electrosynthesis of gold nanocomposites based on a copolymer of 1-vinyl-1,2,4-triazol with crotonic acid

Serzhik H. Sargsyan[1,✉], Artur S. Sargsyan[2], Tatevik S. Sargsyan[2], Karina M. Khizantsyan[1], Ida G. Aghajanyan[1] and Karine S. Margaryan[2]

[1]*National Polytechnic University of Armenia, Teryan 105, 0009 Yerevan Armenia*

[2]*Yerevan State Medical University after Mkhitar Heratsi, Koryun 2, 0025 Yerevan, Armenia*

Corresponding author: ✉artsar86@mail.ru

Received: November 28, 2021; Accepted: January 11, 2022; Published: January 25, 2022

Abstract

In this work, we have synthesized and discussed the results of electrosynthesis of metal-polymer nanocomposites of gold. Nanocoatings were made on pure iron and steel electrodes by combining the process of electropolymerization of 1-vinyl-1.2.4-triazole with crotonic acid and cathodic deposition of gold. Using UV, IR and atomic absorption spectroscopies, X-ray phase analysis, as well as thermogravimetric and elemental analyses, the structure and composition of the synthesized nanocomposites and nanocomposite coatings were studied.

Keywords

Electrolysis; nanocomposite film; electropolymerization; medicine; thermal stability

Introduction

Nanocomposite materials containing gold nanoparticles have unique properties and their development is promising for medicine, nanophotonics and catalysis [1-4].

Electrosynthesis and study of the properties of functional polymers and on this basis obtained nanomaterials, is the most rapidly developing area of modern chemical science. As noted in [2-12], nanomaterials are used in medicine as antibacterial drugs, systems for targeted delivery of contrast agents and drugs, biosensors, and other biomedical purposes.

For wider use in medicine, nanomaterials must have thromboresistance, hydrophilicity, biological activity, biocompatibility, *etc*., and also, due to the presence of functional groups they must have an ability to bind to various substances, including drugs. These properties are characteristic for copolymers of 1-vinyl-1.2.4-triazole (VT) with acrylic acid, which are poorly studied, but promising polymers for medical use [13-16]. Materials based on nanoparticles of various metals are often used in medicine. They are used as coverings for wounds, various medical devices, surgical masks, *etc*. [17-20]. Among metal nanoparticles, gold nanoparticles have the highest antibacterial and antiviral activity [20,21].

The synthesis of new functional thrombo-resistant, non-toxic polymeric materials with gold nanoparticles makes it possible to expand the area of their application, as well as to increase the range of materials used in pharmaceuticals when creating new dosage forms. The properties of these nanocomposites substantially depend on both the nature of the stabilizing polymer matrix and the conditions for the formation of nanoparticles. As a polymer matrix, VT polymers and copolymers can be used since they are non-toxic (LD50 > 3000 mg kg^{-1}) and have high film formation ability, solubility, and biocompatibility [22,23]. In [22,24], a possibility of electrochemical formation of metal-containing nanocomposites and nanocomposite coatings based on vinylazole copolymers has already been reported.

The synthesis and research of nanostructured functional systems, including nanocatalytic ones, are the priority areas of modern science. Due to their unusual physical and chemical properties, which differ from those of bulk metal, metal nanoparticles have a wide variety of potential applications in the field of catalysis, biomedicine, optics, electronics, *etc*. [25-35]. Metal nanoparticles are thermodynamically unstable, and in a relatively pure individual form, they can be obtained only when fixed on a solid as immobile support. To obtain such particles on an electrically conductive carrier, the electrochemical method is widely used in various versions of its implementation [36].

Nanocomposite materials containing gold nanoparticles have unique properties, and their use is promising for medicine [27-29]. Polymer nanocomposites containing zero-valent gold are effective antimicrobial and antiviral agents. The high antibacterial activity of gold nanoparticles is due to its developed surface. In addition, nanoparticles are small enough and capable of penetrating cell membranes and affecting intracellular processes.

In this work, we discuss the results of electrosynthesis of metal-polymer nanocomposites and their coatings on pure iron and steel electrodes when electrochemical (co) polymerization of solid solution with crotonic acid (CA) is combined with the cathodic discharge of metal.

Experimental

The electrochemical initiation of polymerization was carried out in a glass electrolyzer without a diaphragm. Electrosynthesis in galvanostatic and potentiostatic modes was carried out using a ПИ-50.1 potentiogalvanostat with a ПР-8 programmer (Russia). The thickness of films was determined by micrometric and magnetic methods. Elemental analysis was performed on a FLASH EA 1112 series analyzer. The IR spectra of the polymers were recorded on Specord M-80 and Bruker Vertex 70 spectrometers using fine powders pressed into tablets with KBr. Absorption spectra were recorded on a Perkin Elmer Lambda 35 UV/VIS spectrophotometer. The metal content in the composites was determined by elemental and atomic absorption analysis on a Perkin Elmer Analyst 200 spectrometer. The distribution of gold nanoparticles was established on a Leo 906 E TEM (Germany). Thermogravimetric analysis was performed on an MOM derivatograph (Hungary), the temperature rise rate was 5 °C min^{-1}**,** while electrical conductivity was measured using a standard E6-13A teraohmmeter. As electrodes, we used pure ARMCO iron with an iron content of 99.92 % and St-3 with an iron content of 97 %.

1-vinyl-1.2.4-triazole was obtained and purified by the method described in [37], and crotonic acid was purified by sublimation.

General method of electrosynthesis of nanocomposites and coatings

In a glass electrolytic cell with a capacity of 50 ml, electrolysis was carried out [E = -0.1 ... -1.2 V *vs.* Ag/AgCl, j = 1-15 mA cm^{-2}] in aqueous or water-ethanol solutions (bi-distilled water and distilled

ethanol) containing 0.5 - 1 mol l^{-1} of 1-vinyl-1.2.4-triazole, 0.5 - 1 mol l^{-1} of crotonic acid, 1.5 - 4 mmol l^{-1} $HAuCl_4$, 0.02 - 0.05 % 4-tert-butylperoxy-4-oxobutanoic acid (TBOBA), and in some cases 0.05 to 0.07 wt.% chitosan. A pure iron or steel plate with an area of 1 - 2 cm^2 was used as the working electrode (cathode), and a platinum or glassy carbon (SU-12, SU-20) plate with the same area was used as the anode. At high current densities j > 10 mA cm^{-2}, the nanocomposite was deposited onto the electrolyzer floor. After the end of electropolymerization, the electrode package was removed, the cathode with the formed coating was separated, thoroughly washed with distilled water, and dried to the constant weight. The synthesized films were of lilac color, which confirms the presence of incorporated gold particles.

Results and discussion

During the electrolysis of aqueous or water-ethanol solutions of VT and CA or their mixtures at various ratios in the presence of $HAuCl_4$ and chitosan, nanocomposites and nanocomposite coatings with a gold content of 1-10 wt.% are formed only in the presence of a peroxide-type initiator, for example, TBOBA, at the potential of electroreduction of 0.6 - 1.2 V *vs.* Ag/AgCl.

After drying, the formed nanocomposite coatings on the electrodes become insoluble in water and in commonly used organic solvents (DMSO, DMFA, acetonitrile, *etc.*). The copolymer is crosslinked upon heating. In the electronic spectra of gold-containing nanocomposites, in contrast to aqueous solutions of the initial copolymers and $HAuCl_4$, plasmon absorption bands appear with a maximum in the region of nanocomposite coatings containing gold. In Figure 1, absorption bands appear with a maximum in the region of 517-521 nm, which is typical for systems with zero-valent gold.

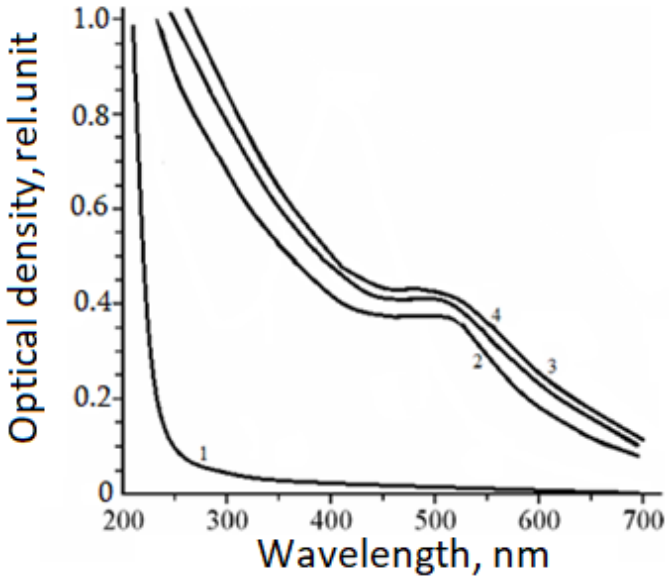

Figure 1. *Electronic absorption spectra of VT-CA copolymer (1), gold 6.8 wt.% (2), gold 7.3 wt.% (3), gold 8.0 wt.% (4)*

The IR spectrum of gold-containing VT-CA copolymer shown in Figure 2 contains bands corresponding to the frequencies of stretching bending vibrations of the triazole ring at 1503, 1434, 1138, 1005, 660 cm^{-1} (C-N, C = N), 1275 cm^{-1} (NN), 3106 cm^{-1} (CH), and a band at 1711 cm^{-1} related to stretching vibrations of the units of the carboxyl group.

Analysis of IR spectra shows that the formation of gold-containing polymer nanocomposites leads to insignificant changes in the chemical structure of the copolymer matrix. Thus, the intensities of the absorption bands of the triazole ring, which can act as coordination centers of gold nano-

particles, show a weak shift (by 3 - 4 cm^{-1}) of one band at 1506 cm^{-1}, which is characteristic of the stretching vibrations of the ring (C-N and C = N).

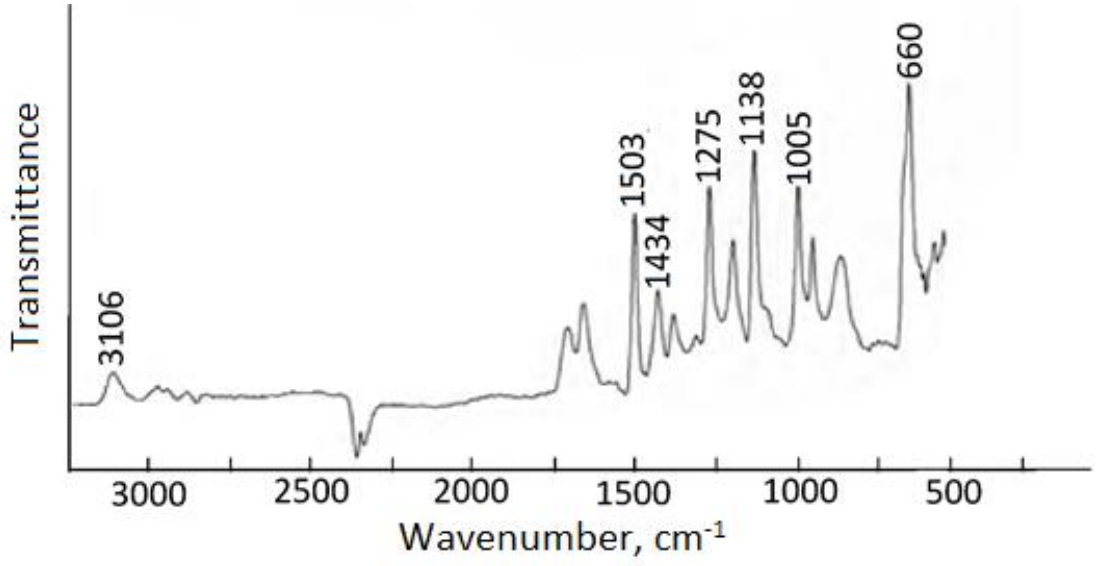

Figure 2. *IR spectrum of gold nanocomposite based on VT-CA copolymer*

This shift may indicate the coordination interaction of the triazole ring with the surface atoms of metal nanoparticles. An intense band in the IR spectra of the copolymers at 1711 cm^{-1} indicates that the carboxyl group of CA in the copolymers is in unionized form. When passing from copolymers to nanocomposites with gold nanoparticles, it can be seen that the number of non-ionized carboxyl groups (–COOH) decreases significantly, and a new absorption band appears at 1577 cm^{-1}, which is characteristic of stretching vibrations of the carboxylate anion ($–COOH^-$).

The gold content in nanocomposite films was 1-8 %, according to the data of elemental analysis and atomic absorption spectroscopy. The intrinsic viscosity of polymer nanocomposites, in contrast to the initial copolymers, increased by an average of 10 - 20 %, which can be explained by the presence of numerous bonds of polymer macromolecules with metal nanoparticles (Table 1).

Table 1. *Nanocomposites based on VT-CA copolymers*

Nanocomposite	*E* / V	Au content, wt. **%**	Yield, %	η / dl·g^{-1}	λ_{max} / nm	Nanoparticle sizes, nm
1	-0.60	6.8	73.4	1.52	521	2 - 10
2	-0.75	7.3	78.5	0.83	517	4 - 6
3	-0.90	8.0	80.1	0.19	517	2 - 4

As can be seen from the results, with an increase in the cathodic potential, the metal content in the nanocomposite increases while the size of the nanoparticles decreases. Coordination occurs due to the nitrogen atoms of the heterocycle. As a result of this work, a nanocomposite of the following structure presented in Scheme 1 is formed.

The solubility of nanocomposites is mainly due to the intramolecular interaction of copolymer macromolecules with gold nanoparticles, due to which relatively loose polymer coils are formed rather unfolded in an aqueous solution since a small amount of nanoparticles participates in the coordination interaction. Polymer coils represent a more compact conformational state of macromolecules of a polymer nanocomposite, in comparison with the initial copolymer, which arises due to partial crosslinking by nanosized particles.

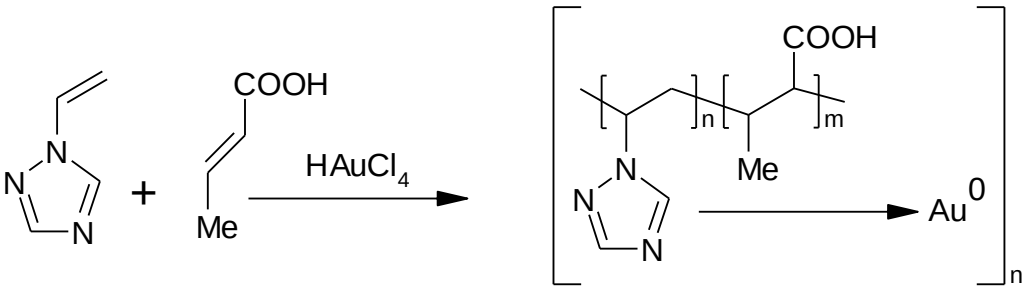

Scheme 1. *Nanocomposite structure*

An increase in gold content over 8 wt.% leads first to a partial and then to a complete loss of solubility. This is due to the enhancement of intermolecular interaction and crosslinking of polymer macromolecules by metal nanoparticles under the influence of multiple cooperative forces. In this case, the intermolecular binding of macromolecules with the surface atoms of gold nanoparticles affects the hydration of the copolymer. The solubility of the copolymer is due to the formation of hydrogen bonds of the triazole ring and carboxyl groups [38,39] (hydrophilic hydration is characteristic of poly-1-vinyl-1.2.4-triazole). Thus, with an increase in the content of gold nanoparticles, the hydration of the polymer nanocomposite decreases down to its complete loss (most of the triazole and carboxyl groups are involved in coordination interaction with gold nanoparticles and do not participate in the formation of hydrogen bonds with water molecules). The formation of organo-inorganic nanocomposites, namely the presence of gold nanoparticles and an amorphous polymer phase, is confirmed by the results of X-ray phase analysis. The approximate sizes of metal nanoparticles are presented by the results of X-ray phase analysis shown in Figure 3.

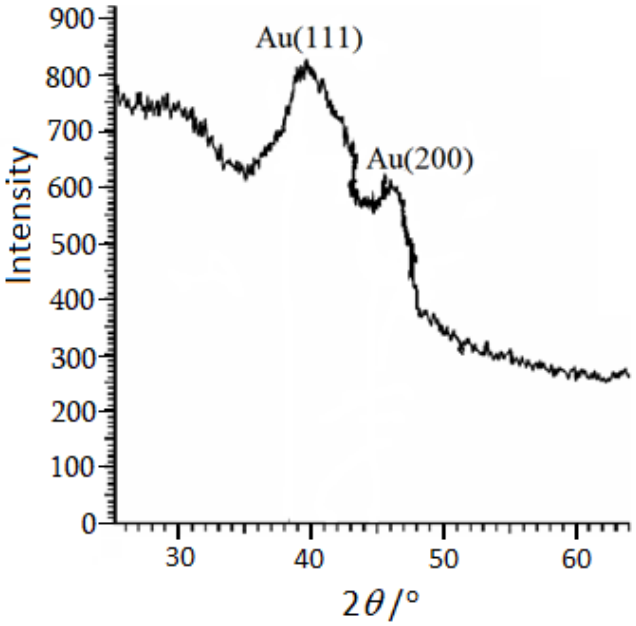

Figure 3. *Fragment of the diffractogram of gold nanocomposite*

In the region where the gold particle Au (111) has d = 0.235 nm, a strongly broadened maximum is observed in the diffractogram of the composite, which confirms the presence of metallic gold in the nanosized state in the studied samples.

The sizes of gold nanoparticles were calculated according to [40]. According to the results of transmission electron microscopy (Figure 4), nanocomposite contains mostly elliptical gold nanoparticles, uniformly distributed in the copolymer matrix, having sizes of 2 - 10 nm.

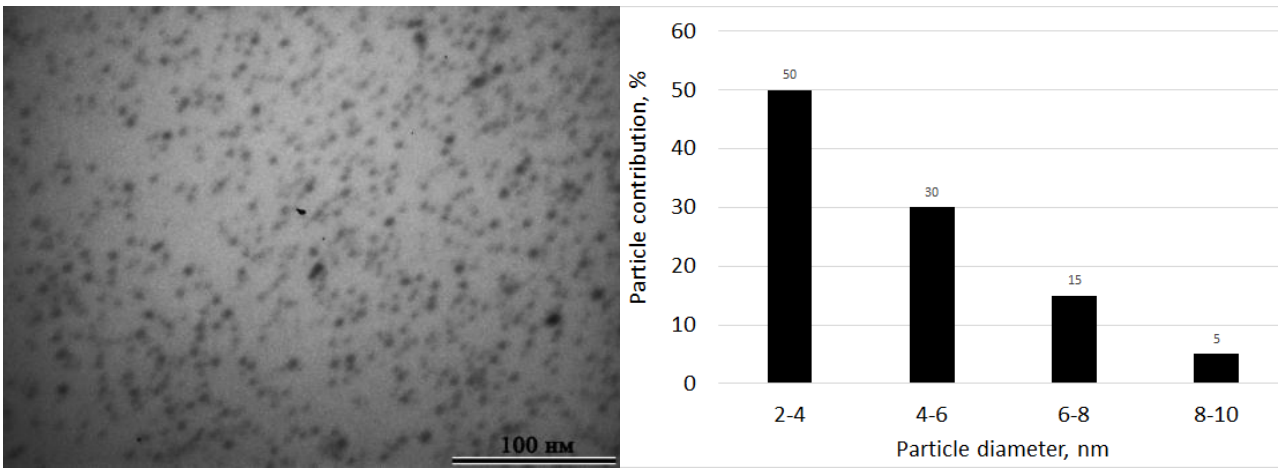

Figure 4. *Electron micrograph (left) and distribution diagram of gold nanoparticles by size (right) in VT-CA copolymer matrix*

The study of the thermal stability of polymer nanocomposites showed that the first stage of polymer matrix destruction is observed in the temperature range from 280 to 400 °C and is accompanied by a gradual weight loss down to 40 %, which refers to the elimination and oxidation of carboxyl and methyl groups (Figure 5).

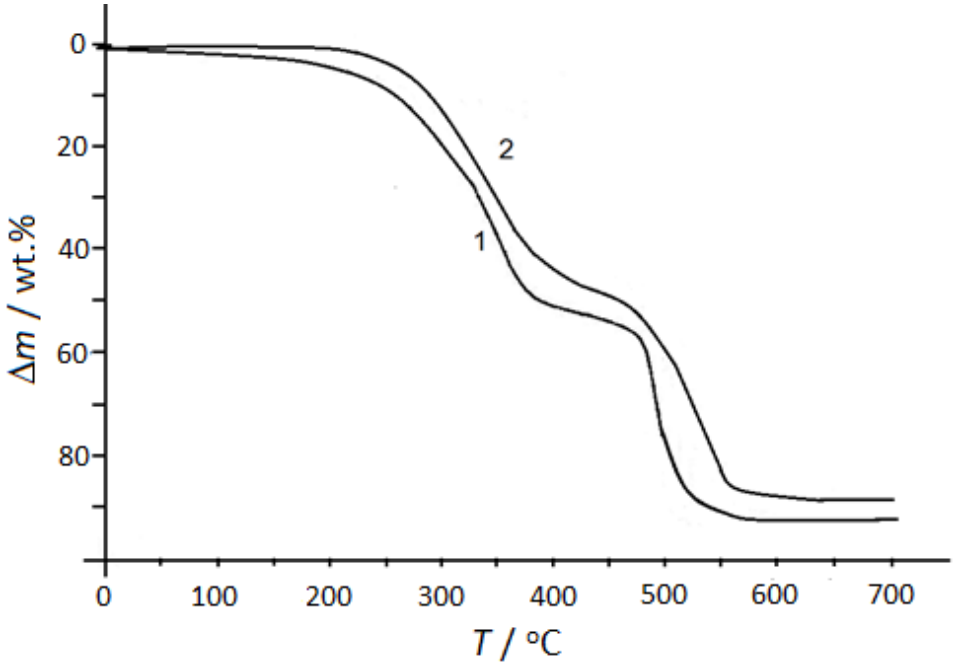

Figure 5*. Thermogravimetric curves: 1- copolymer VT-CA, 2 - gold-bearing nanocomposite*

The next stage of decomposition of the composite occurs in the temperature range 480-570 °C. The gold-containing nanocomposite is thermally more stable than the copolymer, since denser coils of the nanocomposite with the metal are formed.

The electrical conductivity of nanocomposite polymer films based on VT-CA copolymers increases by three orders of magnitude, up to 8.9×10^{-10} - 7.2×10^{-9} S m^{-1}, in comparison with the original copolymers. Pure VT-CA copolymer has no electrical conductivity. The increase in electrical conductivity is apparently due to the contribution to the total electrical conductivity of individual local tunneling currents arising in these samples between electrically conducting metallic gold nanoparticles closely located in the dielectric polymer matrix.

Conclusion

Based on monomeric VT-CA systems, nanocomposites and nanocomposite coatings have been synthesized electrochemically. It was found that, depending on the electrode potential, the nanoparticle size changes from 2 to 10 nm, and the viscosity from 0.19 to 1.52 dl g^{-1}. According to the transmission electron microscopy data, the gold nanoparticles are uniformly distributed over the polymer matrix. The composition and structure of the obtained nanocomposites have been investigated. The synthesized nanocomposites can be used in medicine as thromboresistant, biocompatible polymers.

Acknowledgement: *This study was supported by the Ministry of Education, Science, Culture and Sports RA, Science Committee (project no. 21T-2E068).*

References

[1] A. D. Pomogailo, A. S. Rosenberg, I. E. Uflyand, *Metal Nanoparticles in Polymers*, Khimiya, Moscow, Russia, 2000.

[2] C. N. R. Rao, A. Müller, A. K. Cheetham (Eds.), *The Chemistry of Nanomaterials: Synthesis, Properties and Applications,* Wiley-VCH Verlag GmbH & Co. Weinheim, Germany, 2004. ISBN 3-527-30686-2.

[3] P. Broz (Ed.), *Polymer-Based Nanostructures: Medical Applications*, Roy. Soc. Chem. Pub., Cambridge, UK, 2010.

[4] M. Noroozi, A. Zakaria, M. M. Moksin, Z. A. Wahab, A. Abedin, *International Journal of Molecular Sciences* **13(7)** (2012) 8086-8096. https://doi.org/10.3390/ijms13078086

[5] S. H. Sargsyan, K. S. Margaryan, *Russian Journal of General Chemistry* **84** *(*2014) 550-551. https://doi.org/10.1134/S1070363214030232

[6] A. Tiwari (Ed.), *Recent Developments in Bio-Nanocomposites for Biomedical Applications*, Nova Science Publishers Inc., New York, USA, 2011, p. 511. ISBN 13: 9781617615139

[7] L.-S. Wang, C.-Y. Wang, C.-H. Yang, C.-L. Hsieh, S.-Y. Chen, C.-Y. Shen, J.-J. Wang, K.-S. Huang *International Journal of Nanomedicine* **10(1)** (2015) 2685-2696. https://doi.org/10.2147/IJN.S77410

[8] G.F. Prozorova, A.S. Pozdnyakov, A.I. Emel'Yanov, S.A. Korzhova, T.G. Ermakova, B.A. Trofimov, *Doklady Chemistry* **449(1)** (2013) 87-88. https://doi.org/10.1134/S00125008-13030051

[9] R.A. Hule, D.J. Pochan. *MRS Bulletin* **32(4)** (2007) 354-358. https://doi.org/10.1557/-mrs2007.235

[10] F. Liebig, R. M. Sarhan, M. Bargheer, C. N. Z. Schmitt, A. H. Poghosyan, A. A. Shahinyan, J. Koetz, *RSC Advances* **10(14)** (2020) 8152-8160. https://doi.org/10.1039/D0RA00729C

[11] A. V. Meltonyan, A. H. Poghosyan, S. H. Sargsyan, K. S. Margaryan, A. A. Shahinyan *Colloid and Polymer Science* **297** (2019) 1345-1352. https://doi.org/10.1007/s00396-019-04554-x

[12] A. V. Meltonyan, A. H. Poghosyan, S. H. Sargsyan, K. S. Margaryan, A. A. Shahinyan, *Journal of Polymer Research* **27** (2020) 91. https://doi.org/10.1007/s10965-020-02075-8

[13] A. S. Pozdnyakov, N. P. Kuznetsova, S. A. Korzhova, T. G. Ermakova, T. V. Fadeeva, A. V. Vetohina, G. F. Prozorova, *Russian Chemical Bulletin* **64** (2015) 1440-1444. https://doi.org/10.1007/s11172-015-1029-9

[14] S. H. Sargsyan, K. S. Margaryan, A. S. Sargsyan, *Russian Journal of Applied Chemistry* **91** (2018) 310-313. https://doi.org/10.1134/S1070427218020210

[15] J. S. Kim, E. Kuk, K. N. Yu, J.-H. Kim, S. J. Park, H. J. Lee, S. H. Kim, Y. K. Park, Y. H. Park, C.-Y. Hwang, Y. -K. Kim, Y.-S. Lee, D.H. Jeong, M.-H. Cho. *Nanomedicine: Nanotechnology, Biology and Medicine* **3(1)** (2007) 95-101. https://doi.org/10.1016/j.nano.2006.12.001

[16] M. Rai, A. Yadav, A. Gade. *Biotechnology Advances* **27(1)** (2009) 76-83. https://doi.org/-10.1016/j.biotechadv.2008.09.002
[17] C. A. Mecha, V. L. Pillay, *Journal of Membrane Science* **458** (2014) 149-156. https://doi.org/-10.1016/j.memsci.2014.02.001
[18] E. F. Panarin, *Russian Chemical Bulletin* **66(10)** (2017) 1812-1820. https://doi.org/10.1007/-s11172-017-1952-z
[19] A. S. Pozdnyakov, A. A. Ivanova, A. I. Emelyanov, T. G. Ermakova, G. F. Prozorova, *Russian Chemical Bulletin* **66** (2017) 1099-1103. https://doi.org/10.1007/s11172-017-1860-2
[20] V. V. Kopeikin, E. F. Panarin, *Doklady Chemistry* **380(4-6)** (2001) 277-279. https://doi.org/10.1023/A:1012396522426
[21] M. Davoodbasha, S.-C. Kim, S.-Y. Lee, J.-W. Kim, *Archives of Biochemistry and Biophysics* **605** (2016) 49-58. https://doi.org/10.1016/j.abb.2016.01.013
[22] L. A. Tatarova, T. G. Yermakova, Al. Al. Berlin, Ye. F. Razvodovskii, V. A. Lopyrev, N. F. Kedrina, N. S. Yenikolopyan, *Polymer Science U.S.S.R.* **24(10)** (1982) 2529-2536. https://doi.org/10.1016/0032-3950(82)90127-7
[23] G. F. Prozorova, S. A. Korzhova, T. V. Kon'kova, A. S. Pozdnyakov, T. G. Ermakova, T. V. Fadeeva, S. A. Vereshchagina, B. A. Trofimov, *Russian Chemical Bulletin* **60** (2011) 671. https://doi.org/10.1007/s11172-011-0104-0
[24] K. S. Margaryan, S. H. Sargsyan, A. S. Sargsyan, *Russian Journal of Applied Chemistry* **89** (2016) 1261-1264. https://doi.org/10.1134/S1070427216080073
[25] H. Hirai, N. Toshima, *Polymer-attached catalysis* in *Tailored Metal Catalysts*, Iwasawa, Ed., D. Reidel Pub. Co., Dordrecht, Holand, 1985, pp. 87-140. https://doi.org/10.1007/978-94-009-5261-4_2
[26] A. D. Pomogailo, A. S. Rozenberg, G. I. Dzhardimalieva, *Russian Chemical Reviews* **80(3)** (2011) 257. http://dx.doi.org/10.1070/RC2011v080n03ABEH004079
[27] V.I. Roldugin, *Russian Chemical Reviews* **69(10)** (2000) 821. https://dx.doi.org/10.1070/RC-2000v069n10ABEH000605
[28] M.-C. Daniel, D. Astruc, *Chemical Reviews* **104 (1)** (2004) 293-346. https://doi.org/-10.1021/cr030698+
[29] V. V. Volkov, T. A. Kravchenko, V. I. Roldughin, *Russian Chemical Reviews* **82(5)** (2013) 465. https://doi.org/10.1070/RC2013v082n05ABEH004325
[30] B. I. Kharisov, O. V. Kharissova, U. Ortiz-Méndez, *Handbook of Less Common Nanostructures*, CRC Press, Taylor and Francis Group, Boca Raton, 2012, p. 828.
[31] P.C. Lee, D. Meisel, *The Journal of Physical Chemistry* **86(17)** (1982) 3391-3395. https://doi.org/10.1021/j100214a025
[32] P. Yang, W. Zhang, Y. Du, X.J. Wang, *Journal of Molecular Catalysis A: Chemical* **260(1-2)** (2006) 4-10. https://doi.org/10.1016/j.molcata.2006.06.045
[33] E. J. Kim, J. H. Yeum, H. D. Ghim, S. G. Lee, G. H. Lee, H. J. Lee, S. I. Han, J. H. Choi, *Polymer (Korea)* **35(2)** (2011) 161-165. https://www.cheric.org/PDF/PK/PK35/PK35-2-0161.pdf
[34] S. V. Vasilyeva, M. A. Vorotyntsev, I. Bezverkhyy, E. Lesniewska, O. Heintz, R. Chassagnon, *The Journal of Physical Chemistry C* **112(50)** (2008) 19878-19885. https://doi.org/-10.1021/jp805423t
[35] O. A. Petrii, *Russian Chemical Reviews* **85(2)** (2015) 159. http://dx.doi.org/10.1070/RCR4438
[36] Z.-Y. Zhou, N. Tian, J.-T. Li, I. Broadwell, Sh.-G. Sun *Chemical Society Reviews* **40** (2011) 4167-4185 https://doi.org/10.1039/C0CS00176G
[37] G. F. Prozorova, A. S. Pozdnyakov, S. A. Korzhova, T. G. Ermakova, M. A. Novikov, E. A. Titov, L. M. Sosedova, *Russian Chemical Bulletin* **63** (2014) 2126-2129. https://doi.org/-10.1007/s11172-014-0709-1

[38] N. L. Mazyar, V. Annenkov, V. A. Kruglova, S. M. Anan'ev, E. N. Danilovtseva, A. V. Rokhin, S. V. Zinchenko, *Russian Chemical Bulletin, International Edition* **49(12)** (2000) 2013-2017. https://doi.org/10.1023/A:1009571908805

[39] A. S. Pozdnyakov, A. I. Emel'yanov, T. G. Ermakova, G. F. *Polymer Science B* **56** (2014) 238-246. https://doi.org/10.1134/S1560090414020122

[40] Ch. S. Barrett, T. B. Masalsky, *The structure of metals,* Metallurgy, Moscow, USSR, 1984, p. 681

J. Electrochem. Sci. Eng. **12(2)** (2022) 293-304; http://dx.doi.org/10.5599/jese.1162

Open Access : : ISSN 1847-9286

www.jESE-online.org

Original scientific paper

Synthesis and antioxidant activity of six novel N-ferrocenyl-methyl-N-(nitrophenyl)- and -N-(cyanophenyl)-acetamides: Cyclic voltammetry and molecular docking studies

Abdellatif Kedadra, Touhami Lanez✉, Elhafnaoui Lanez, Hadia Hemmami and Meriem Henni

VTRS Laboratory, Department of Chemistry, Faculty of Sciences, University of El Oued B.P.789, 39000, El Oued, Algeria

Corresponding author: ✉*touhami-lanez@univ-eloued.dz;*

Received: November 8, 2021; Accepted: December 28, 2021; Published: January 25, 2022

Abstract

Cyclic voltammetry (CV) assays were performed to measure superoxide anion radical ($O^{\cdot}_2^-$) scavenging activities of six novel N-ferrocenylmethyl-N-(nitrophenyl)-acetamides and N-ferrocenylmethyl-N-(cyanophenyl)acetamides (FMA1-FMA6), followed by molecular docking simulations and in silico toxicity prediction. The obtained values of IC_{50} from CV assays indicated that all studied compounds showed promising scavenging activity against $O^{\cdot}_2^-$ radicals, with the compounds FMA1, FMA3, and FMA4 possessing the most significant potency. A molecular docking study revealed that all compounds interact with amino acid residues of glutathione reductase via hydrogen bonding and hydrophobic interactions. The compound FMA4 was the most inactive compound against the glutathione reductase enzyme having the highest inhibitory concentration of 2.61 µM and the lowest docking score of -31.85 kJ/mol. Toxicity studies demonstrated that among six studied compounds, FMA4, FMA5, and FMA6 are predicted to be nontoxic.

Keywords

Ferrocene derivatives; superoxide anion radical; binding free energy; toxicity study

Introduction

Recently, ferrocene derivatives have been widely studied because of their versatile potential applications in many research fields such as medicinal chemistry [1–7], material sciences [8], and diagnostic applications fields [9]. N-ferrocenylmethylamines and their derivatives, in particular, N-ferrocenylmethyl-N-(nitrophenyl)- and -N-(cyanophenyl)aniline, have shown important biological activities due to their promising biological potential as anticancer properties [10,11], antimicrobial agents [12], antioxidants [13,14], and anti-proliferative agents against MCF-7 human breast cancer cell lines [15].

Most of ferrocenylmethylaniline derivatives scavenge superoxide free radicals, and this reaction is useful in the inhibition of cancer growth [16]. The superoxide radical scavenging activities of ferrocenylmethylanilines are mainly due to the presence of functionalized aniline in the ferrocene moiety that could donate protons to the superoxide anion radical to form the corresponding radical species. The mechanism might be described by a first proton transfer (Eq. (1)), followed by the electron transfer (Eq. (2)). With a second proton transfer (Eq. (3)) the overall reaction is a two-electron reduction of oxygen (Eq. (4)). In our experimental conditions with ferrocene derivatives, we did not observe the increase of oxygen current reduction, which is expected in the hypothesis of a proton donating mechanism [17].

$$O^{\bullet}{}_2^- + FcH \rightarrow HO^{\bullet}{}_2 + Fc^- \quad (1)$$

$$HO^{\bullet}{}_2 + O^{\bullet}{}_2^- \rightarrow HO_2^- + O_2 \quad (2)$$

$$HO_2^- + FcH \rightarrow H_2O_2 + Fc^- \quad (3)$$

$$O^{\bullet}{}_2^- + 2e + FcH \rightarrow H_2O_2 + 2Fc^- \quad (4)$$

Glutathione, a tripeptide protein naturally produced by the body, is made up of three amino acids: glutamic acid, cysteine, and glycine. It plays an essential antioxidant intracellular role [18], since it is involved in the elimination of reactive oxygen species and acts as a scavenger for various oxygen radicals. The enzyme glutathione reductase (GR), also called glutathione-disulfide reductase, reduces the oxidized form of glutathione disulfide (GSSG) to the reduced glutathione form (GSH). Elevated levels of GSSG/GSH ratio lead to intracellular signal transduction, elimination of free radicals and reactive oxygen species, and the preservation of intracellular redox status [19]. Thus, inhibition of glutathione reductase results in a decrease in GSH, an increase in GSSG, and consequently a high GSSG/GSH ratio. Studying the glutathione reductase inhibition by potentially antioxidant compounds could serve for choosing antioxidants candidates. A good antioxidant candidate should inhibit glutathione reductase enzyme less.

In this work, we describe the synthesis and the scavenging activity against $O^{\bullet}{}_2^-$ of six novel N-ferrocenylmethyl-N-(nitrophenyl)- and N-ferrocenylmethyl-N-(cyanophenyl)acetamides using cyclic voltammetry assays. Further, the compounds were scrutinized through toxicity study and molecular docking to predict the median lethal dose (LD_{50}) and the toxicity class (TC) to afford an insight into the inhibition and binding partialities of the most potent compounds with glutathione reductase.

Experimental

Chemicals

All starting materials and solvents used for the synthesis of N-ferrocenylmethyl-N-(nitrophenyl)- and N-ferrocenylmethyl-N-(cyanophenyl)acetamides were of analytical grade and obtained from different commercial sources and used as received. Tetrabutylammonium tetra-fluoroborate (Bu_4NBF_4) (electrochemical grade 99 %) was from Sigma-Aldrich. Oxygen gas (research-grade 99.99 %) was supplied by Linde Gaz Algérie.

Materials and methods

CV experiments were run on a PGZ301 potentiostat (Radiometer Analytical SAS, France) connected to an electrochemical cell having a volume of 15 mL and equipped with three electrodes: a glassy carbon working electrode of an area equal to 0.013 cm^2, a platinum wire auxiliary electrode, and a Hg/Hg_2Cl_2 reference electrode. The reaction medium was saturated with high-purity commercial oxygen for 15 min before each experiment. ^1H NMR spectra were obtained on a Bruker

Avance DPX 300 MHz spectrometer. All ^{1}H NMR spectra are reported in ppm relative to the central line of the singlet for $CDCl_3$ at 7.28 ppm.

Structure optimization was run using density functional theory implemented in Gaussian 09 package [20]. All calculations were carried out with the unrestricted Becker's three-parameter hybrid exchange functional [20] combined with Lee-Yang-Parr nonlocal correlation function, abbreviated as B3LYP [22–24] with combined basic sets, LanL2DZ [25–27] for optimizing iron atom and 6-311G+(d) for the rest of atoms [28–30].

The in silico toxicity study was performed using the ProTox-II web server [31].

Molecular docking simulations were performed using AutoDock 4.2 docking software [32,33], executed on a Pentium 2.7 GHz and 8 GB Ram microcomputer MB memory with windows 8 operating system.

Synthesis

N-ferrocenylmethyl-N-(nitrophenyl)- and N-ferrocenylmethyl-N-(cyanophenyl)acetamides coded as FMA1-FMA6 were synthesized by coupling the well-known quaternary salt (ferrocenylmethyl)-trimethyl-ammonium iodide [34] with the corresponding substituted anilines, following our previously reported procedure [35,36]. The obtained products were then acetylated using acetic anhydride and their molecular structures are shown in Figure 1. The antioxidant activities of the synthesized compounds against superoxide anion radicals were measured using CV assays.

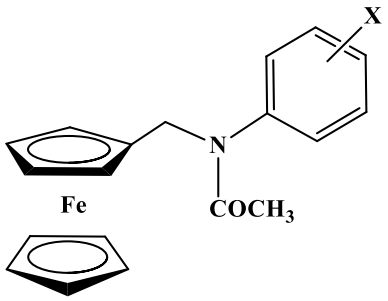

FMA1, X = 2-NO_2; FMA2, X = 3-NO_2; FMA3, X = 4-NO_2;
FMA4, X = 2-CN; FMA5, X = 3-CN; FMA6, X = 4-CN

Figure 1. *Chemical structures of N-ferrocenylmethyl-N-(nitrophenyl)-acetamide and N-ferrocenylmethyl-N-(cyanophenyl)acetamide*

General procedure for the synthesis of compounds (FMA1-FMA6)

The corresponding N-ferrocenylmethyl-N-(nitrophenyl)aniline (500 mg, 1.49 mmol) or N-ferrocenylmethyl-N-(cyanophenyl)aniline (500 mg, 1.58 mmol) was dissolved in acetic anhydride 160 ml (1.7 mmol) and the reaction mixture was heated at 65 °C for 30 minutes under an atmosphere of nitrogen. Then it was allowed to cool to room temperature and poured on 140 ml 0.1 M of an aqueous solution of sodium carbonate and extracted three times with dichloromethane. The combined extracts were evaporated and the obtained residue was recrystallized from a mixture of methanol/water (30/70) to yield a red/orange yellowish solid.

Results and discussion

Antioxidant activity assays against superoxide anion radicals

Superoxide anion radicals ($O^{\cdot}{}_2^-$) scavenging activity assays were used to measure the antioxidant activity of N-ferrocenylmethyl-N-(nitrophenyl)- and N-ferrocenylmethyl-N-(cyanophenyl)-acetamides. The $O^{\cdot}{}_2^-$ was electrochemically generated in situ by one-electron reduction of commercial molecular oxygen dissolved in DMF containing 0.1 M tetrabutylammonium tetra-fluoroborate (Bu_4NBF_4) as a supporting electrolyte. Increased concentrations of each studied compound were then added to the electrochemical cell containing a solution of the generated $O^{\cdot}{}_2^-$, and the cyclic voltammograms were recorded after each addition of the test compounds, in the potential window

from −0.0 to −1.6 V at the scan rate of 0.1 V s^{-1}. Obtained voltammograms of oxygen-saturated DMF containing 0.1 M of Bu_4NBF_4 in the absence and presence of gradually increasing concentrations of the compounds FMA1-FMA6 in the same solvent are shown in Figure 2.

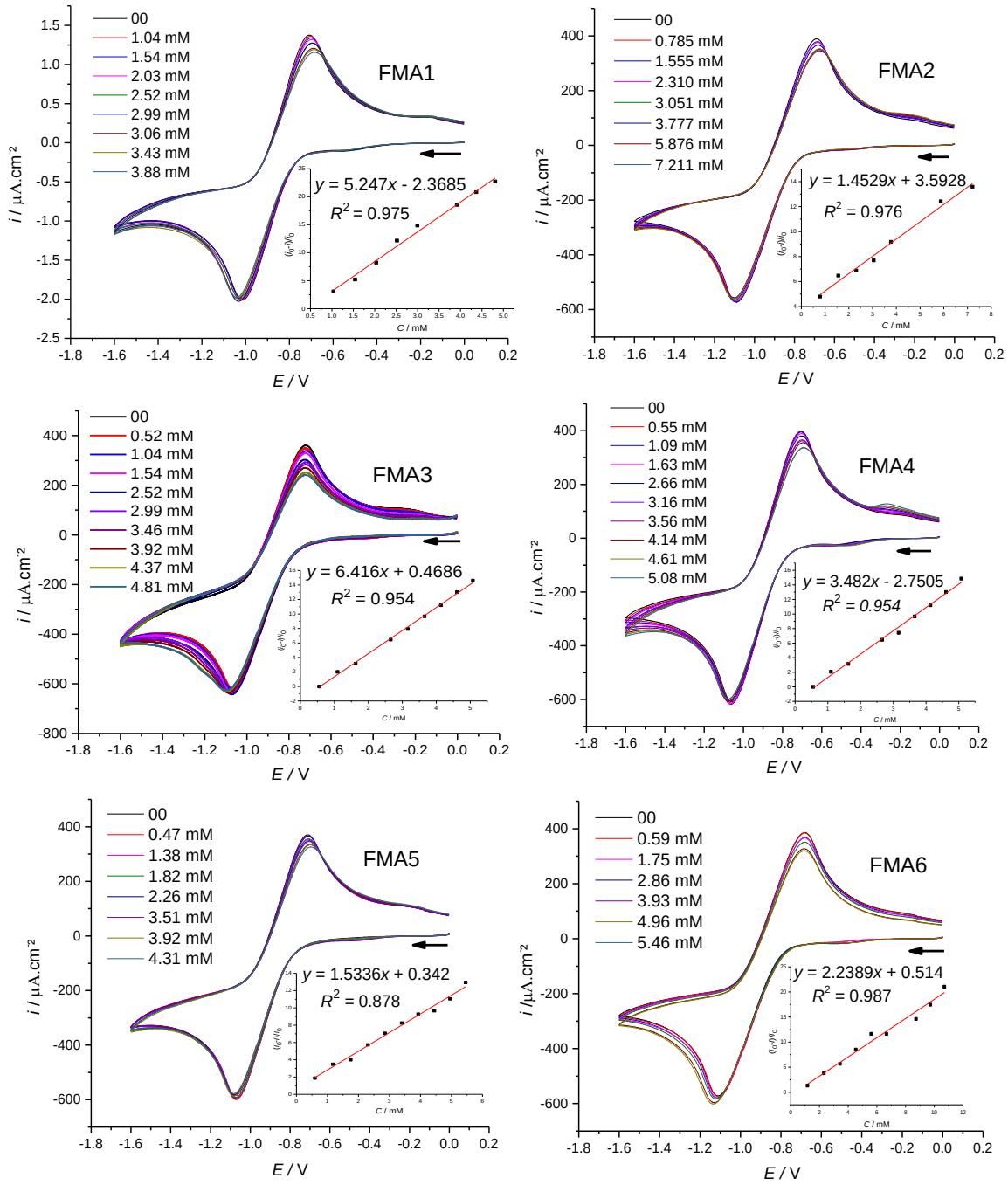

Figure 2. *Cyclic voltammograms of oxygen-saturated DMF in the absence and presence of gradually increased concentrations of FMA1-FMA6. Inset plots of [(i_0 – i) / i_0 vs. c]*

All voltammograms showed a decrease in the anodic peak current density of the $O^{\cdot}{}_2^-/O_2$ redox couple upon addition of gradually increasing concentration of test compounds, and this decrease was used for the calculation of the half-maximal inhibitory concentration (IC_{50}).

The inhibition of $O^{\cdot}{}_2^-$ was calculated using the following equation [17,37,38]

$$O^{\cdot}{}_2 \text{ scavenging activity} = \frac{i_0 - i}{i_0} 100 \quad (5)$$

where i_0 and i are the anodic peak current densities of the superoxide anion radical in the absence and presence of the test sample, respectively.

The half-maximal inhibitory concentration (IC_{50}) values were obtained from the plot of $O^{\bullet}{}_2^-$ scavenging activity against different compound concentrations (inset plots of Figure 2). The antioxidant activity has been expressed as IC_{50}. The IC_{50} value was defined as the concentration of the compound that inhibits the formation of $O^{\bullet}{}_2^-$ by 50 %.

Obtained values of IC_{50} shown in Figure 3 indicate that all N-ferrocenylmethyl-N-(nitrophenyl)- and N-ferrocenylmethyl-N-(cyanophenyl)acetamides showed promising scavenging activity against $O^{\bullet}{}_2^-$ radicals, with the activity of compounds FMA1, FMA3, and FMA4 almost comparable to that of the standard α-tocopherol (7.058 mM) used as a positive control.

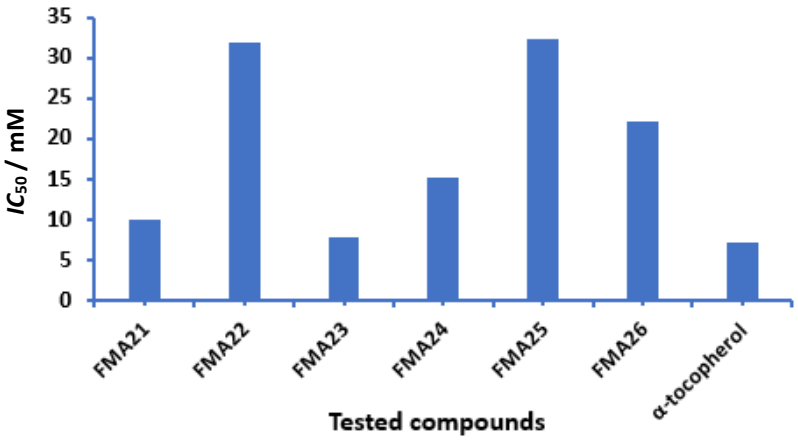

Figure 3. IC$_{50}$ *values of N-ferrocenylmethyl-N-(nitrophenyl)- and N-ferrocenylmethyl-N-(cyanophenyl)acetamides (FMA1-FMA6) and α-tocopherol as a positive control*

Molecular docking study

A molecular docking study was carried out to afford an insight into the inhibition and binding parameters of N-ferrocenylmethyl-N-(nitrophenyl)- and N-ferrocenylmethyl-N-(cyanophenyl)-acetamides with the enzyme glutathione reductase. The enzyme glutathione reductase (GR), also called glutathione-disulfide reductase, reduces glutathione disulfide (GSSG) to glutathione (GSH), which is involved in the elimination of reactive oxygen species and acts as a scavenger for various oxygen radicals. Glutathione exists in reduced (GSH) and oxidized (GSSG) forms, the reaction symbolized by the equation (6):

$$2GHS + NADP^+ \leftrightarrow GSSG + NADPH + H^+ \quad (6)$$

Inhibition of glutathione reductase results in a decrease in reduced glutathione (GSH) and an increase in glutathione disulfide (GSSG) using nicotinamide adenine dinucleotide phosphate (NADPH), particularly from the pentose phosphate pathway in bacteria, plants, and animals to regenerate glutathione, a molecule essential for resistance against oxidative stress and the preservation of intracellular pH. So, studying glutathione reductase inhibition could serve as a good means for the selection of antioxidants candidates. A good antioxidant candidate should reduce the inhibition of the glutathione reductase enzyme.

Rigid receptor and flexible ligand molecular docking models were carried out to study the inhibition of glutathione reductase by N-ferrocenylmethyl-N-(nitrophenyl)- and N-ferrocenylmethyl-N-(cyanophenyl)acetamides, and to understand how strong the interactions are between them. The crystal 3D structure of the glutathione reductase target involved in this study was retrieved from the online data bank, RCSB PDB (https://www.rcsb.org/pdb, ID: 1XAN) [40], Figure 4.

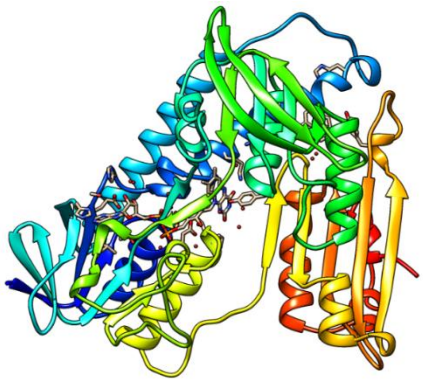

Figure 4. *UCSF chimera ribbons chemical structure view of human glutathione reductase in complex with a xanthene inhibitor (ID: 1xan)*

Receptor preparation

The receptor was first imported into the AutoDockTools interface. Missing atoms were inserted in incomplete residues, alternate conformations were deleted, all water molecules and ligands were removed, and polar hydrogen atoms and charges were added to the receptor structure.

Receptor-ligand docking

In silico molecular docking simulations studies were executed by using the AutoDock 4.2 software [32,33]. Lamarckian genetic algorithms were utilized with the grid box size set at 60×60×60 Å in the *x*, *y*, and *z* directions and the coordinates were fixed at *x* = 69.46, *y* = -17.32, and *z* = 55.62. All docking experiments consisted of 50 docking runs while the other parameters were left to their default values. The best conformation was selected with the lower docking energy for further docking analysis. The visualization of the interaction was generated with the PLIP webserver (protein-ligand interaction profiler) [41,42].

Results from the molecular docking suggest that hydrogen bonding, hydrophobic forces, and π-cation interactions are involved in the binding process. Figure 5 illustrates the interactions of compounds FMA1, FMA2, FMA3, FMA4, FMA5, and FMA6 with the nearby residues in the active site of glutathione reductase.

Interacting residues and their corresponding bond types and length are summarised in Table 1.

Table 1. *Interaction types between ligands FMA1, FMA2, FMA3, FMA4, FMA5, FMA6 and glutathione reductase*

Molecule	Bond type	Amino acid (number of bonds/interactions)	Distance, Å
FMA1	H-bonds	THR339 (2)	2.25, 2.00
	Hydrophobic interactions	ILE198(2), LEU338, PRO340, THR369, PHE372	3.89, 3.95, 3.27, 3.79, 3.41, 3.47
	π-Stacking interactions	TYR197	5.25
FMA2	H-bonds	THR339 (2)	2.62, 1.95
	Hydrophobic interactions	THR369(2), TYR197, ILE198, LEU338, PHE372	3.57, 3.55, 3.34, 3.62, 3.04, 3.45
FMA3	H-bonds	THR339	1.94
	Hydrophobic interactions	TYR197, LEU338, PRO340, THR369, PHE372	3.88, 3.21, 3.81, 3.41, 3.35
	π-stacking interactions	TYR197	5.42
FMA4	H-bonds	TYR197, THR339 (2)	3.10, 2.65, 2.01
	Hydrophobic interactions	THR57, TYR197, ILE198, LEU338, THR369, PHE372	3.82, 3.71, 3.85, 3.25, 3.47, 3.30
	π-stacking interactions	TYR197	5.25
FMA5	H-bonds	SER177, THR339 (2)	3.04, 3.29, 2.96
	Hydrophobic interactions	THR57, TYR197, ILE198, LEU338, THR369, PHE372	3.58, 3.49, 3.86, 3.10, 3.51, 3.37
FMA6	H-bonds	THR339 (2)	2.55, 1.93
	Hydrophobic interactions	THR57, TYR197, LEU338, THR369, PHE372	3.79, 3.56, 3.16, 3.44, 3.37

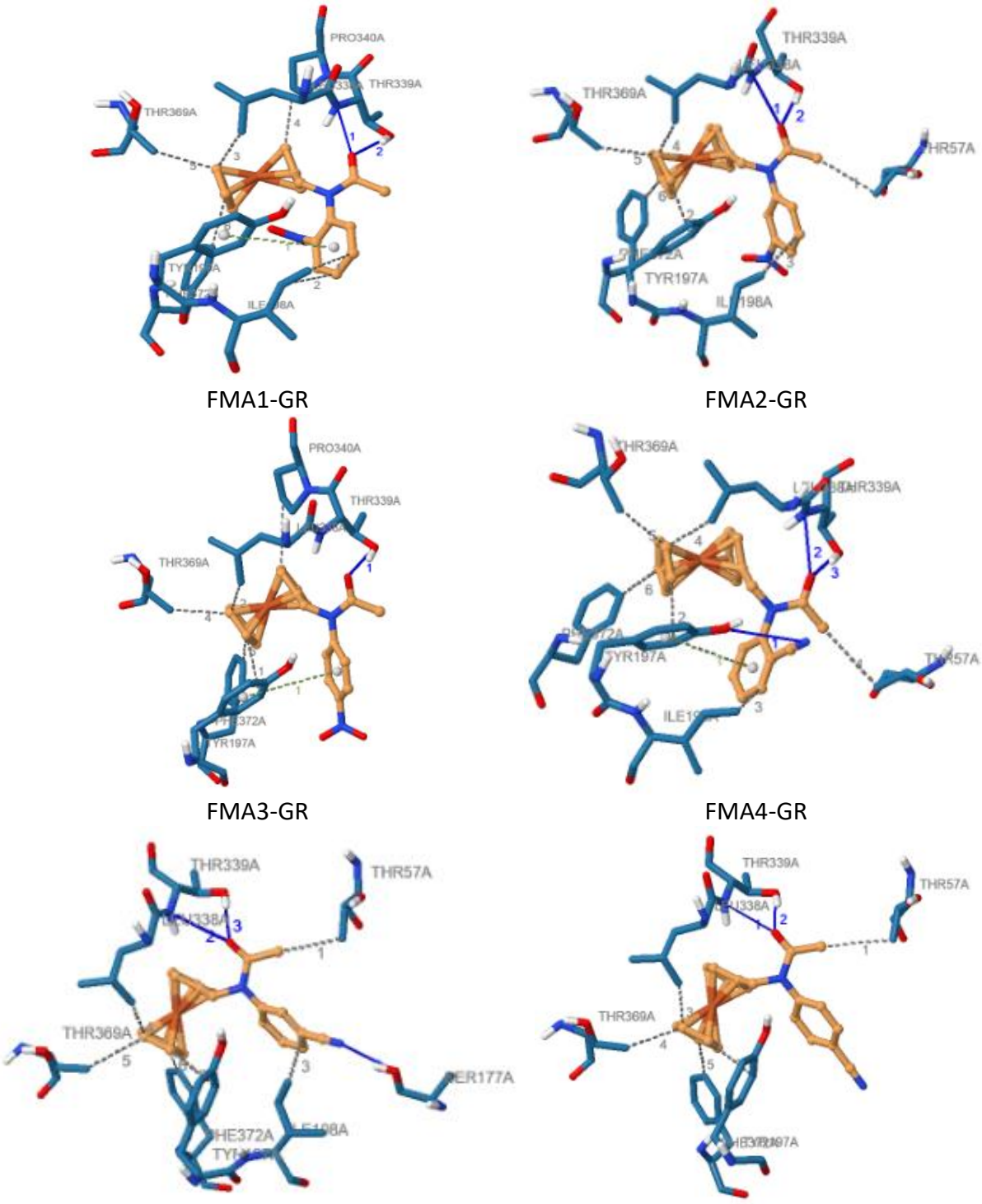

FMA1-GR FMA2-GR

FMA3-GR FMA4-GR

FMA5-GR FMA6-GR

Figure 5. *Best docking poses for glutathione reductase interacting with FMA1, FMA2, FMA3, FMA4, FMA5, and FMA6 illustrating H-bonds, hydrophobic, and π-cation interactions*

It can be seen from this table that besides hydrophobic interactions, compounds FMA4 and FMA5 formed with the GR three hydrogen bonds. Compounds FMA1, FMA2, and FMA6, however, reacted *via* two hydrogen bonds, while the compound FMA3 interacts only *via* one hydrogen bond beside one π-stacking interaction.

Obtained binding free energy and inhibitory concentration from molecular docking study for the compounds FMA1-FMA6 are summarised in Table 2.

Table 2. *Binding free energies and inhibitory concentration obtained from molecular docking study*

Adduct	FMA1-GR	FMA2-GR	FMA3-GR	FMA4-GR	FMA5-GR	FMA6-GR
ΔG / kJ mol^{-1}	-34.90	-34.82	-33.36	-31.85	-33.94	-33.56
IC_{50} / µM	0.76	0.79	1.42	2.61	1.11	1.31

In silico toxicity study

In silico toxicity study aims to help in optimizing compounds regarding their toxicity proprieties. The study could offer an important improvement to the awareness of the full perspective of virtual screening for the identification of target compounds with negligible or no toxicity, which may open a path for the selection of novel nontoxic ferrocenylmethylaniline derivatives with high antioxidant activity.

In silico toxicity study of the compounds FMA1-FMA6 was performed using the ProTox-II web server [31]. It aims to predict hepatotoxicity (Dili), carcinogenicity (Carcino), immunotoxicity (Immuno), mutagenicity (Mutagen), cytotoxicity (Cyto), median lethal dose (LD_{50}), and toxicity class (TC). According to in silico toxicity profiles presented in Table 3, the toxicity class of all compounds was detected to be equal to 3. FMA4, FMA5, and FMA6 were predicted to be nontoxic. FMA1, FMA2, and FMA3 were predicted to be toxic in mutagenicity.

Table 3. *In silico toxicity profiles of the studied compounds*

Molecule	Dili	Carcino	Immuno	Mutagen	Cyto	LD_{50} / mg kg^{-1}	TC
FMA1	inactive	active	inactive	active	inactive	237	3
FMA2	inactive	active	inactive	active	inactive	237	3
FMA3	inactive	active	inactive	active	inactive	237	3
FMA4	inactive	inactive	inactive	inactive	inactive	256	3
FMA5	inactive	inactive	inactive	inactive	inactive	237	3
FMA6	inactive	inactive	inactive	inactive	inactive	256	3

Based on the obtained results from the antioxidant study, molecular docking simulations and toxicity prediction, the compounds FMA2, FMA5, and FMA6 cannot be accepted as antioxidant candidates because they have the lowest antioxidant activity (Figure 1), the highest binding affinities, and the highest inhibitory activities towards the enzyme glutathione reductase (Table 2). Furthermore, the compound FMA1 possesses the highest antioxidant activity (Figure 1), but it cannot be the best antioxidant candidate because it has the highest binding affinity towards the enzyme glutathione reductase and also possesses the lowest inhibitory concentration of 0.76 µM that is necessary to reduce the rate of glutathione reductase enzyme reaction by 50 %. The compounds FMA4 and FMA3 possess the highest antioxidant activities, the lowest binding free energy of -31.85 and -33.36 kJ/mol, and the highest inhibitory concentration of 2.61 and 1.42 µM against glutathione reductase enzyme reaction, respectively, these values indicate weak binding affinity towards the enzyme glutathione reductase compared to the other compounds. Thus, the compounds FMA4 and FMA3 are weaker inhibitors of glutathione reductase. However, although compound FMA3 has higher antioxidant activity than FMA4, it cannot be a good antioxidant candidate because it is predicted as mutagenic (Table 3). Finally, based on what is cited above, the compound FMA4 can be chosen as the best antioxidant candidate.

Detailed procedure for the synthesis of compounds (FMA1-FMA6)

N- ferrocenylmethyl-N-(2-nitrophenyl)acetamide (FMA1)

N- ferrocenylmethyl-N-(2-nitrophenyl)acetamide (275 mg, 49 %) was obtained, as described above, m.p. 148 °C, orange solid.

IR (KBr:) ν = 3381 cm^{-1} (C-H), 1658 cm^{-1} (C=O), 1610 cm^{-1} (C=C), 1506 and 1572 cm^{-1} (C-NO_2)

UV-Vis: λ_{max} (CH_3CN) = 230 and 278 nm (π→π*, Fc, Ar), 431 nm (n→π*, NO_2, CO),

CV (ν = 100 mV s^{-1}, CH_3CN): i_{pa} = 26.02 µA cm^{-2}, i_{pc} = -25.09 µA cm^{-2}, i_{pa}/ i_{pc} = 1.04, E_{pa} = 508 mV *vs.* SCE, E_{pc} = 445 mV *vs.* SCE, ΔE = 63 mV, $E_{1/2}$ = 476.5 mV *vs.* SCE,

NMR ^{1}H (300 MHz, $CDCl_3$): δ = 1.91 ppm (3H, s, H1), 4.16 ppm (2H, m, H2), 4.23 ppm (2H, m, H3), 4.30 ppm (5H, s, H4), 4.64 ppm (2H, s, H5); 6.70 ppm (1H, dd, J = 11.03 Hz, H9), 6.92 ppm (1H, d, J = 11.37 Hz, H8), 7.49 ppm (1H, m, J = 22.18 Hz, H7), 8.24 ppm (1H, dd, J = 13.49 Hz, H6).

N- ferrocenylmethyl-N-(3-nitrophenyl)acetamide (FMA2)

N- ferrocenylmethyl-N-(3-nitrophenyl)acetamide (478 mg, 85 %) was obtained, as described above, m.p. 132 °C, orange leaflet.

IR (KBr:) ν = 3058 cm^{-1} (C-H), 1656 cm^{-1} (C=O), 1612 cm^{-1} (C=C) 1350 and 1531 cm^{-1} (C-NO_2),

UV-Vis: λ_{max} (CH_3CN)) = 232 and 325 nm (π→π*, Fc, Ar), 423 nm (n→π*, NO_2, CO),

CV (100 mV s^{-1}, CH_3CN): i_{pa} =8.06 µA cm^{-2}, i_{pc} = -8.18 µA cm^{-2}, i_{pa}/ i_{pc} = 0.98, E_{pa} = 534 mV *vs.* SCE, E_{pc} = 468 mV *vs.* SCE, ΔE = 66 mV, $E_{1/2}$ = 501 mV *vs.* SCE,

NMR ^{1}H (300 MHz, $CDCl_3$): δ = 1.87 ppm (3H, s, H1), 4.00 ppm (2H, m, H2), 4.07 ppm (2H, m, H3), 4.10 ppm (5H, s, H4), 4.67 ppm (2H, s, H5), 7.29 ppm (1H, t, J = 6.28Hz, H6), 7.53 ppm (1H, t, J = 8.94 Hz, H7), 7.90 ppm (1H, s, H9), 8.18 ppm (1H, d, J = 7.76 Hz H8).

N- ferrocenylmethyl-N-(4-nitrophenyl)acetamide (FMA3)

N- ferrocenylmethyl-N-(4-nitrophenyl)acetamide (461 mg, 82 %) was obtained, as described above, m.p. 158°C, red needles.

IR (KBr:) ν = 3075 cm^{-1} (C-H), 1659 cm^{-1} (C=O), 1602 cm^{-1} (C=C), 1593 cm^{-1} (C-NO_2),

UV-Vis: λ_{max} (CH_3CN)) = 232 nm (π→π*, Fc, Ar), λ = 380 nm (n→π*, NO_2, CO),

CV (100 mV s^{-1}, CH_3CN): i_{pa} = 9.62 µA cm^{-2}, i_{pc} = -9.73 µA cm^{-2}, i_{pa}/ i_{pc} = 0.99, E_{pa} = 494 mV *vs.* SCE, E_{pc} = 431 mV *vs.* SCE, ΔE = 63 mV, $E_{1/2}$ = 462.5 mV *vs.* SCE,

NMR ^{1}H (300 MHz, $CDCl_3$): δ = 1.87 ppm (3H, s, H1), 4.01 ppm (2H, m, H2), 4.07 ppm (2H, m, H3), 4.12 ppm (5H, s, H4), 4.69 ppm (2H, s, H5), 7.17 ppm (2H, d, J = 8.92Hz, H6), 8.22 ppm (2H, d, J = 8.94Hz, H7).

N-ferrocenylmethyl-N-(2-cyanophenyl)acetamide (FMA4)

N-ferrocenylmethyl-N-(2-cyanophenyl)acetamide (FMA4) (311 mg, 55 %) was obtained, as described above, m.p. 146°C, orange reddish solid.

IR (KBr:) ν = 3304 cm^{-1} and 3081 cm^{-1} (C-H), 2210.6 cm^{-1} (CN), 1602.3 cm^{-1} (C=O),

UV-Vis: λ_{max} (CH_3CN)) = 337 nm (π→π*, Fc, Ar), λ = 444 nm (n→π*, CO),

CV (100 mV s^{-1}, CH_3CN): i_{pa} = 100.61 µA cm^{-2}, i_{pc} = -102.13, i_{pa}/ i_{pc} = 1.015, E_{pa} = 525 mV *vs.* SCE, E_{pc} = 421 mV *vs.* SCE, ΔE = 99 mV, $E_{1/2}$ = 475 mV *vs.* SCE,

NMR ^{1}H (300 MHz, $CDCl_3$): δ = 2.13 ppm (3H, s, H1), 4.02 ppm (2H, m, H2), 4.20 ppm (2H, m, H3), 4.22 ppm (5H, s, H4), 4.26 ppm (2H, s, H5), 7.12-7.19 ppm (3H, m, J = 8.92Hz, H7,H8,H9), 7.55 ppm (2H, d, J = 18.95Hz, H6).

N-ferrocenylmethyl-N-(3-cyanophenyl)acetamide (FMA5)

N-ferrocenylmethyl-N-(3-cyanophenyl)acetamide (FMA4) (345 mg, 61 %) was obtained, as described above, m.p. 162°C, orange reddish solid.

IR (KBr:) ν = 3081 cm^{-1} (C-H), 2214.2 cm^{-1} (CN), 1636.1 cm^{-1} (C=O),

UV-Vis: λ_{max} (CH_3CN)) = 433.5 nm (n→π*, CO),

CV (100 mV s^{-1}, CH_3CN): i_{pa} = 10.71, µA cm^{-2}, i_{pc} = -11.09 µA cm^{-2}, i_{pa}/ i_{pc} = 1.03, E_{pa} = 598 mV *vs.* SCE, E_{pc} = 463 mV *vs.* SCE, ΔE = 99 mV, $E_{1/2}$ = 531 mV *vs.* SCE,

NMR ^{1}H (300 MHz, $CDCl_3$): δ = 1.77 ppm (3H, s, H1), 3.99 ppm (2H, m, H2), 4.07 ppm (2H, m, H3), 4.10 ppm (5H, s, H4), 4.63 ppm (2H, s, H5),7.21 ppm (1H, d, J = 7.74Hz, H6), 7.29 ppm (1H, s, H7), 7.48 ppm (1H, t, J = 7.75Hz, H9), 7.61 ppm (1H, d, J = 7.74 Hz, H8).

N-ferrocenylmethyl-N-(4-cyanophenyl)acetamide (FMA6)

N-ferrocenylmethyl-N-(4-cyanophenyl)acetamide (FMA4) (385 mg, 68 %) was obtained, as described above, m.p. 155°C, yellow solid.

IR (KBr:) v = 3081 cm^{-1} (C-H), 2214.2 cm^{-1} (CN), 1636.1 cm^{-1} (C=O),

UV-Vis: λ_{max} (CH_3CN)) = 265.5 nm (π→π*, Fc, Ar),

CV (100 mV s^{-1}, CH_3CN): i_{pa} = 18.61, µA cm^{-2}, i_{pc} = - 18.76 µA cm^{-2}, i_{pa}/ i_{pc} =1, E_{pa} = 488 mV *vs.* SCE, E_{pc} = 426 mV *vs.* SCE, ΔE = 62 mV, $E_{1/2}$ = 457 mV *vs.* SCE,

NMR ^{1}H (300 MHz, $CDCl_3$): δ = 1.82 ppm (3H, s, H1), 4.01 ppm (2H, s, H2), 4.08 ppm (2H, m, H3), 4.12 ppm (5H, s, H4), 4.66 ppm (2H, s, H5), 7.13 ppm (2H, d, J = 8.39 Hz, H6),7.67 ppm (2H, d, J = 8.36 Hz, H7).

The ^{1}H NMR spectra of all the synthesized compounds presented in Figure 6 reveal one downfield singlet at δ= 1.77-2.13 ppm which is ascribed to methyl protons.

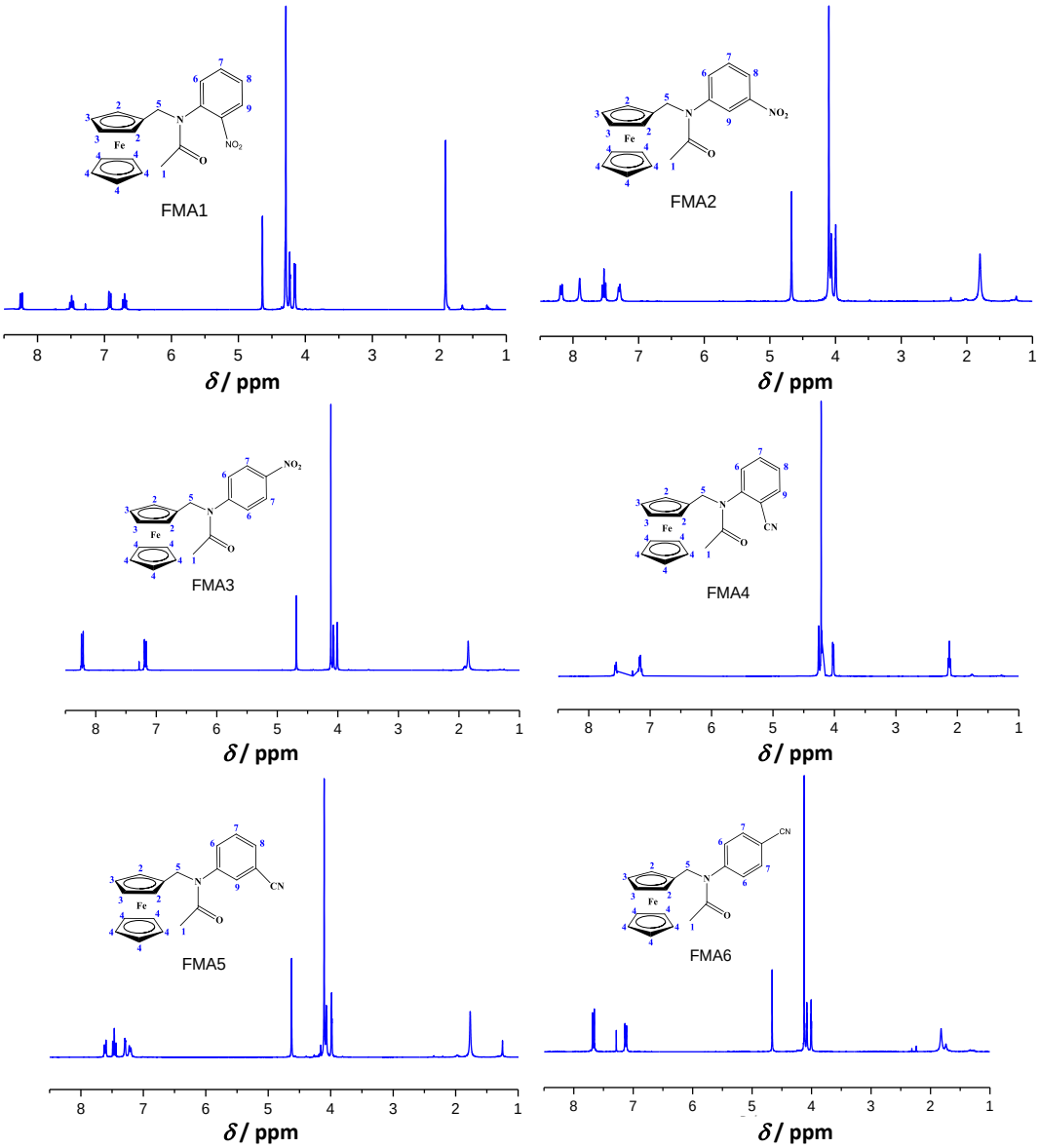

Figure 6. *^{1}H NMR spectra of FMA1, FMA2, FMA3, FMA4, FMA5, and FMA6 compounds*

The α- and β-protons of the substituted ring of ferrocene C_5H_4 appeared as a multiplet at 3.99-4.16 and 4.07-4.23 ppm respectively, the unsubstituted protons of the C_5H_5 ring of ferrocene appeared as a singlet at 4.10 to 4.30 ppm. A singlet appeared at δ = 4.26-4.69 ppm was due to methylene protons, this downfield shift of the methylene protons was observed due to electro-negativity of the nitrogen atom. The aromatic protons appeared in the range of δ= 6.70-8.24 ppm.

Conclusions

In this work, in vitro and in silico studies have been carried out to evaluate the scavenging activity against $O^{\cdot}_{2}{}^{-}$ and the antioxidant activity of six novel N-ferrocenylmethyl-N-(nitrophenyl)acetamides and N-ferrocenylmethyl-N-(cyanophenyl)acetamide using cyclic voltammetry assays. The obtained values of IC_{50} indicated that all derivatives showed promising scavenging activity against $O^{\cdot}_{2}{}^{-}$, with the compounds FMA1, FMA3, and FMA4 possessing the most significant potency. A molecular docking study and an *in silico* toxicity prediction revealed that compound FMA4 is the most inactive compound against glutathione reductase enzyme, having an inhibitory concentration of 2.61 µM and a docking score of -31.85 kJ mol^{-1}, which make the best good antioxidant candidate. The obtained in vitro and in silico results correspond with one another and give room for the design of novel antioxidant ferrocenylmethylaniline derivatives with less activity against glutathione reductase. The *in silico* toxicity study allowed us to predict the toxicity, the median lethal dose (LD_{50}), and the toxicity class (TC) of the studied compounds.

Acknowledgement: *The authors extend thanks and gratitude to the Directorate-general of scientific research and technological development (DGRSDT) of the Algerian Ministry of Higher Education and Research for financial support (project number B00L01UN390120150001).*

References

[1] X. Nie, Y. Xie, Q. Wang, H. Wei, C. Xie, Y. Li, B. Wang, Y. Li, *CyTA-Journal of Food* **19** (2021) 560-570. https://doi.org/10.1080/19476337.2021.1925746

[2] H. Chen, M. Chen, X. Wang, R. Sun, *Polymer Chemistry* **5** (2014) 4251-4258. https://doi.org-/10.1039/C4PY00120F

[3] Q. Zhou, M. Lei, Y. Wu, S. Li, Y. Tong, Z. Li, M. Liu, L. Guo, C. Chen, *Chemosphere* **279** (2021) 130584. https://doi.org/10.1016/j.chemosphere.2021.130584

[4] H. Mahmoudi-Moghaddam, S. Tajik, H. Beitollahi, *Food Chemistry* **286** (2019) 191-196. https://doi.org/10.1016/j.foodchem.2019.01.143

[5] X. Ma, M. Chao, Z. Wang, *Food Chemistry* **138** (2013) 739-744. https://doi.org/10.1016/-j.foodchem.2012.11.004

[6] E. Ertaş, H. Özer, C. Alasalvar, *Food Chemistry* **105** (2007) 756-760. https://doi.org/10.1016/-j.foodchem.2007.01.010

[7] M.I. López, I. Ruisánchez, M.P. Callao, *Spectrochimica Acta Part A: Molecular and Biomolecular Spectroscopy* **111** (2013) 237-241. https://doi.org/10.1016/j.saa.2013.04.031

[8] S. Anmei, Z. Qingmei, C. Yuye, W. Yilin, *Analytica Chimica Acta* **1023** (2018) 115-120. https://doi.org/10.1016/j.aca.2018.03.024

[9] D. Han, M. Yu, D. Knopp, R. Niessner, M. Wu, A. Deng, *Journal of Agricultural and Food Chemistry* **55** (2007) 6424-6430. https://doi.org/10.1021/jf071005j

[10] E. Mejia, Y. Ding, M.F. Mora, C.D. Garcia, *Food Chemistry* **102** (2007) 1027-1033. https://doi.org/10.1016/j.foodchem.2006.06.038

[11] X. Li, X. Sun, M. Li, *ChemistrySelect* **5** (2020) 12777-12784. https://doi.org/10.1002/slct.-202003559

[12] M. Heydari, S.M. Ghoreishi, A. Khoobi, *Measurement* **142** (2019) 105-112. https://doi.org/-10.1016/j.measurement.2019.04.058

[13] R. N. Adams, *Analytical Chemistry* **30** (1958) 1576–1579.

[14] B. J. Sanghavi, A. K. Srivastava, *Electrochimica Acta* **55** (2010) 8638–8648. https://doi.org/-10.1016/j.electacta.2010.07.093

[15] I. G. Svegl, B. Ogorevc, *Journal of Analytical Chemistry* **367** (2000) 701–706. https://doi.org/-10.1007/s002160000465

[16] G. Jeevanandham, K. Vediappan, Z. A. Alothman, T. Altalhi, A. K. Sundramoorthy, *Scientific Reports* **11** (2021) 13266. https://doi.org/10.1038/s41598-021-92620-2
[17] M. R. Ganjali, F. Garkani-Nejad, S. Tajik, H. Beitollahi, E. Pourbasheer, B. Larijanii, *International Journal of Electrochemical Science* **12** (2017) 9972-9982. https://doi.org-/10.20964/2017.11.49
[18] Y. Yao, X. Han, X. Yang, J. Zhao, C. Chai, *Chinese Journal of Chemistry* **39** (2021) 330-336. https://doi.org/10.1002/cjoc.202000398
[19] J. K. Patra, K. H. Baek, *Journal of Photochemistry and Photobiology B: Biology* **173** (2017) 291–300. https://doi.org/10.1016/j.jphotobiol.2017.05.045
[20] Y. Xie, T. Zhang, Y. Chen, Y. Wang, L. Wang, *Talanta* 2020, **213** (2020) 120843. https://doi.org/10.1016/j.talanta.2020.120843
[21] B. Sriram, M. Govindasamy, S. F. Wang, R. J. Ramalingam, H. Al-Lohedan, T. Maiyalagan, *Ultrasonics Sonochemistry* **58** (2019) 104618. https://doi.org/10.1016/j.ultsonch.2019.-104618
[22] H. Li, B. Kou, Y. Yuan, Y. Chai, R. Yuan, *Biosensors and Bioelectronics* **197** (2022) 113758. https://doi.org/10.1016/j.bios.2021.113758
[23] K.S. Park, Z. Ni, A.P. Côté, *Proceedings of the National Academy of Sciences* **103** (2006) 10186-10191. https://doi.org/10.1073/pnas.0602439103
[24] S.R. Venna, M.A. Carreon, *Journal of the American Chemical Society* **132** (2009) 76-78. https://doi.org/10.1021/ja909263x
[25] C. Chizallet, S. Lazare, D. Bazer-Bachi, F. Bonnier, V. Lecocq, E. Soyer, A. A. Quoineaud, N. Bats, *Journal of the American Chemical Society* **132** (2010) 12365-12377. https://doi.org/-10.1021/ja907359t
[26] H. Bux, F. Liang, Y. Li, J. Cravillon, M. Wiebcke, J. Caro, *Journal of the American Chemical Society* 131 (2009) 16000-16001. https://doi.org/10.1021/ja907359t
[27] S. L. Li, Q. Xu, *Energy & Environmental Science* **6** (2013) 1656-1683. https://doi.org/-10.1039/C3EE40507A
[28] M. C. Buzzeo, R. G. Evans, R. G. Compton, *ChemPhysChem* **5** (2004) 1106-1120. https://doi.org/10.1002/cphc.200301017
[29] A. Abo-Hamad, M. A. Alsaadi, M. Hayyan, I. Juneidi, M. A. Hashim, *Electrochimica Acta* **193** (2016) 321-343. https://doi.org/10.1016/j.electacta.2016.02.044
[30] M. Shahsavari, S. Tajik, I. Sheikhshoaie, H. Beitollahi, *Topics in Catalysis* (2021). https://doi.org/10.1007/s11244-021-01471-8
[31] A. J. Bard, L. R. Faulkner, *Electrochemical Methods; Fundamentals and Applications,* 2nd Edition, Wiley, 2001, pp. 580-632. ISBN 978-0-471-04372-0
[32] E. Prabakaran, K. Pandian, *Food Chemistry* **166** (2015) 198-205. https://doi.org/10.1016/j.-foodchem.2014.05.143
[33] Q. Ye, X. Chen, J. Yang, D. Wu, J. Ma, Y. Kong, *Food Chemistry* **287** (2019) 375-381. https://doi.org/10.1016/j.foodchem.2019.02.108
[34] Z. Mo, Y. Zhang, F. Zhao, F. Xiao, G. Guo, B. Zeng, *Food Chemistry* **121** (2010) 233-237. https://doi.org/10.1016/j.foodchem.2009.11.077
[35] V. Vinothkumar, A. Sangili, S. M. Chen, T. W. Chen, M. Abinaya, V. Sethupathi, *International Journal of Electrochemical Science* **15** (2020) 2414-2429. https://doi.org/10.20964/2020.03.08

J. Electrochem. Sci. Eng. **12(2)** (2022) 305-316; http://dx.doi.org/10.5599/jese.1191

Open Access : : ISSN 1847-9286

www.jESE-online.org

Original scientific paper

Modeling and synthesis of carbon-coated $LiMnPO_4$ cathode material: Experimental investigation and optimization using response surface methodology

Redouan El-Khalfaouy[1,2,✉], Khadija Khallouk[2], Alae Elabed[3], Abdellah Addaou[2], Ali Laajeb[2] and Ahmed Lahsini[2]

[1]*Laboratory of Natural Substances, Pharmacology, Environment, Modeling, Health and Quality of Life, Polydisciplinary Faculty of Taza, Sidi Mohamed Ben Abdellah University, B.P. 1223,Taza, Morocco*

[2]*Materials, Processes, Catalysis and Environment Laboratory, High School of Technology, Sidi Mohamed Ben Abdellah University, BP 2427, Fez, Morocco*

[3]*Microbial Biotechnology Laboratory, Faculty of Science and Technology, Sidi Mohammed Ben Abdellah University, BP. 2202, Fez, Morocco*

Corresponding author: ✉redouan.elkhalfaouy@usmba.ac.ma

Received: November 21, 2021; Accepted: January 17, 2022; Published: January 25, 2022

Abstract

Nanostructured $LiMnPO_4$ cathode materials for lithium-ion batteries (LIBs) have been successfully prepared by a modified solvothermal method under controlled conditions. Polyethylene glycol (PEG-10000) was used as a solvent to optimize the particle size/morphology and as a carbon conductive matrix. In order to investigate the effect of synthesis parameters such as concentration of PEG-10000, reaction time and reaction temperature on the $LiMnPO_4$ phase purity, Response surface methodology was carried out to find variations in purity results across the composition. The purity of all materials was checked using HighScore software by comparing the matched lines score to ones of reference data. As a result, it has been found that the pure phospho-olivine material $LiMnPO_4$ can be synthesized using the following optimum conditions: PEG concentration = 0.1 mol l^{-1}, reaction time = 180 min, and reaction temperature = 250 °C. The as-prepared $LiMnPO_4$ under optimum conditions delivered an initial discharge capacity of 128.8 mAh g^{-1} at 0.05 C-rate. The present work provides insights and suggestions for optimizing synthesis conditions of this material, which has been considered the next promising cathode candidate for high-energy lithium-ion batteries.

Keywords

Response surface methodology; olivine structure; solvothermal synthesis; PEG-10000; lithium-ion batteries

Introduction

Rechargeable lithium-ion batteries (LIBs) with high-energy, high power density, durability, and lightweight have become the most requested energy source in order to meet future society's needs in many renewable energy storage systems, starting from laptops, cell phones to electric vehicles. With the increasing demand for higher capacity and improved safety, many efforts have been made to further develop the next generation of LIBs with high volumetric/gravimetric energy density. Most commercial LIBs are currently based on $LiCoO_2$ layered structure as a cathode material. Therefore, one of the main challenges is to replace the commercialized layered structure cathode (which exhibits a theoretical specific capacity of 274 mAh g^{-1}) with other promising and efficient cathode materials.

$LiMPO_4$ (M = Fe, Mn, Co, Ni) olivine-based high-performance cathodes are the recommended alternative cathode materials to replace traditional ones ($LiCoO_2$) due to their low cost, non-toxicity, high thermal and cyclic stability, and environmental impact [1–5]. Compared to the first commercialized cathode, which is $LiFePO_4$, $LiMnPO_4$ is considered as the most promising cathode material in the next generation of lithium-ion batteries due to the high theoretical energy density (701 Wh/kg), which is higher than that of $LiFePO_4$ (586 Wh kg^{-1})[6,7]. Moreover, the low voltage (4.1 V *vs* Li/Li^+) of $LiMnPO_4$, which is positioned within the stable window of the most commercialized electrolytes, makes it the best candidate material compared to $LiCoPO_4$ and $LiNiPO_4$, which have higher potentials, being respectively 4.8 and 5.1 V *vs.* Li/Li^+ [8–10].

However, $LiMnPO_4$ exhibits significantly lower electrochemical performances than $LiFePO_4$ because of two important drawbacks that limit its electrochemical activity, including low electronic conductivity (<10^{-10} S/cm) being even lower than that of LFP (10^{-9} S cm^{-1}), and low lithium-ion diffusion rate ≈10^{-16} cm^2 s^{-1} [11,12]. Furthermore, the anisotropic distortion of the Jahn-Teller lattice in the Mn^{3+} sites and the interface strain during phase transitions between the lithiated and delithiated phases ($LiMnPO_4$-$MnPO_4$) cause a significant volume change (≈8.9 %) compared to $LiFePO_4$-$FePO_4$ (≈7 %) [13,14]. Recently, many attempts have been reported to overcome these limitations [15–17]. The results confirmed that particle size reduction could strongly increase the lithium-ion diffusion during the charge/discharge process [17–19]. The same behavior has been reported by the surface carbon coating [20–22], and the partial substitution of transition elements [23–26].

The synthesis process was also considered a direct approach to achieving desired performances. For this reason, several methods have been applied to prepare $LiMnPO_4$ with high purity, such as spray-pyrolysis [22,27], sol-gel method [28,29], hydrothermal synthesis [30–33], precipitation method [34,35] and solution combustion process [36,37]. Among all these methods, some selected ones offer more advantages such as morphology control, better homogeneity, submicron-sized particles, and larger specific surface area with increased electrochemical performances [38,39]. The solvothermal technique has significant assets compared to other methods such as simplicity to handle, short reaction time, moderate reaction temperature, good crystallinity and high purity [40,41]. The process is widely used for preparing various micro and nanostructured materials such as cathodes/anodes, oxides, semiconductors, ceramics, *etc.*

However, morphology and particle size are difficult to control since they are determined by many factors such as precursor types, additives or surfactants, pH, reaction time/temperature, and physico-chemical properties of the used solvent. Polyethylene glycol (PEG) is an organic solvent that can be easily adsorbed on the crystal's surface by hydrogen bonding, consequently influencing nucleation and crystallite growth.

Based on these advantages of PEG, we report in this work the synthesis of $LiMnPO_4$ cathode material under solvothermal conditions, using the PEG-10000 as a solvent to optimize particle size/morphology and as a carbon-coated source. To the best of our knowledge and after a thorough literature review, no study is presented on optimizing the synthesis parameters of $LiMnPO_4$ using the Response Surface Method (RSM). Figure 1 is a schematic representation of $LiMnPO_4$ synthesis and analysis performed in this work.

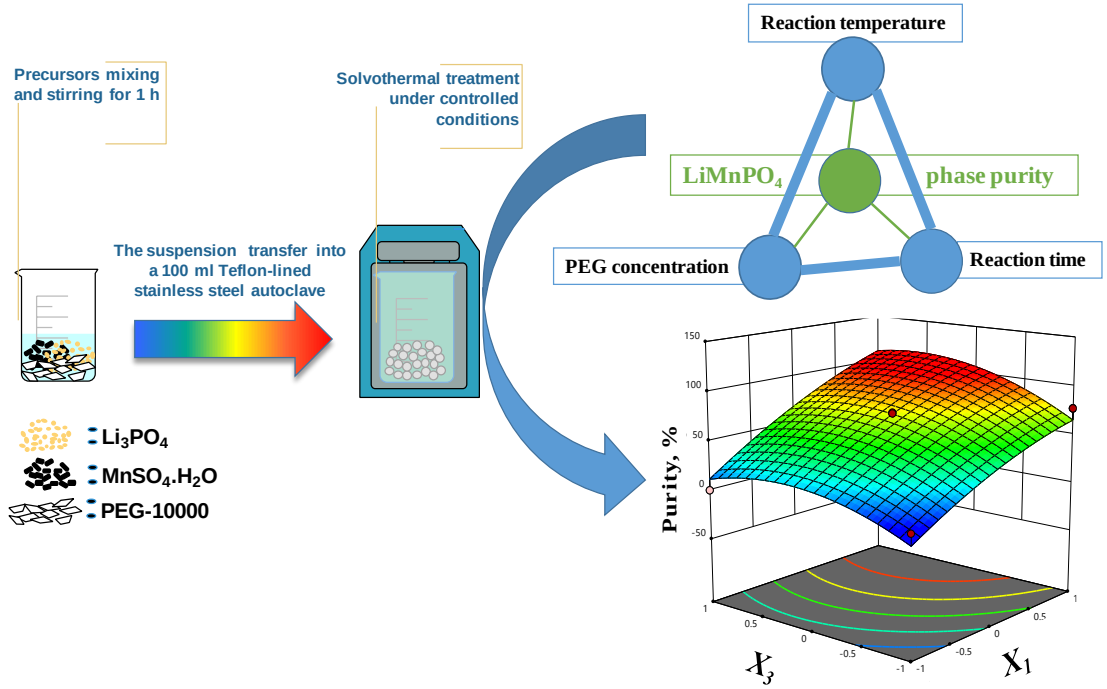

Figure 1. *Schematic figure for $LiMnPO_4$ synthesis and analysis*

Experimental

Materials preparation

All chemical precursors are of analytical grade and used without any further purification. The cathode $LiMnPO_4$ was prepared *via* facile solvothermal reaction using the following raw precursors; Li_3PO_4, $MnSO_4.H_2O$ (99 %, Sigma Aldrich) and PEG-10000 (flakes, Sigma Aldrich). Firstly, Li_3PO_4 intermediate compound was prepared by mixing Li_2CO_3 (99 %, Honeywell Fluka) with $(NH_4)_2HPO_4$ (99 %, Merck) and citric acid (2M) (99.5 %, Merck) in appropriate amounts under magnetic stirring and heat at 90 °C for 60 min. The resulted product was filtered, washed with deionized water (DW) and dried overnight. Then, $MnSO_4{\cdot}H_2O$, Li_3PO_4, and PEG-10000 (with different concentrations: 0.00, 0.05 and 0.1 M) solvent were mixed under vigorous stirring for 60 min. The suspension was transferred into a 100 ml stainless steel autoclave followed by thermal treatment at different temperatures, *i.e.,* 150, 200 and 250 °C for a certain reaction time ranging from 60 to 180 min. The autoclave was then taken out of the furnace and cooled down to room temperature. The obtained products were washed with distilled water several times, collected by filtration, and finally dried at 80 °C overnight. Surface carbon coating of $LiMnPO_4$@C was activated by sintering the as-prepared products at 700 °C for 6 hours under argon atmosphere with a heating rate of 5 °C min^{-1}.

Experimental design and statistical analysis

The Box-Behnken design was used for the response methodology to examine the relationship between one or more dependent response variables and a set of quantitative experimental factors

(independent variables). A mathematical model, followed by the second polynomial equation, was developed to describe the relationship between the predicted response variable (matching lines score (purity) of the synthesized $LiMnPO_4$) and the independent variables of solvothermal synthesis conditions. It was described by eq. (1)

$$Y_{LiMnPO_4} = \beta_0 + \sum_{i=1}^{3} \beta_i X_i + \sum_{i=1}^{3} \beta_{ii} X_i^2 + \sum_{i=1}^{3} \sum_{i \neq j=1}^{3} \beta_{ij} X_i X_j \quad (1)$$

where Y_{LiMnPO_4} is the predicted response variable, X_i, X_j ($1 \leq i, j \leq 3$; $i \neq j$) represent the coded independent variables (solvothermal conditions), β_0 is the intercept coefficient, β_i are linear terms, β_{ii} are squared terms, and β_{ij} are interaction terms.

This study used this design to determine the effect of three factors (PEG concentration, solvothermal reaction time and temperature) on $LiMnPO_4$ phase purity. The ranges and levels of the experimental parameters are depicted in Table 1. The Design-Expert12 software was used to analyze the results of all experiments.

Table 1. *Experimental ranges and levels of independent variables*

Variables	Symbol	Level		
		-1	0	1
PEG concentration, mol l^{-1}	X_1	0	0.05	0.1
Reaction temperature, °C	X_2	150	200	250
Reaction time, min	X_3	60	120	180

Structural, morphological and electrochemical characterization

Crystalline structure and phase purity of all products were analyzed and evaluated by X-ray diffraction using diffractometer PANalytical's X'Pert PRO, with Cu Kα radiation (λ = 1.5418 Å). The surface morphology and the chemical compositions were observed with a scanning electron microscope (FEI QUANTA 200) equipped with EDS for microanalysis of the surface.

The electrochemical tests were performed at room temperature in the potential range between 2.5 and 4.5 V using battery test systems (BaSyTec GmbH, Germany). All experiments were conducted using coin-type cells (CR2032) assembled according to our previous work [25].

Phase and morphology of the intermediate compound Li_3PO_4

All detectable peaks of the as prepared Li_3PO_4 are shown in Figure 2, where the peaks are indexed as Li_3PO_4 according to the standard data PDF # 071-1528.

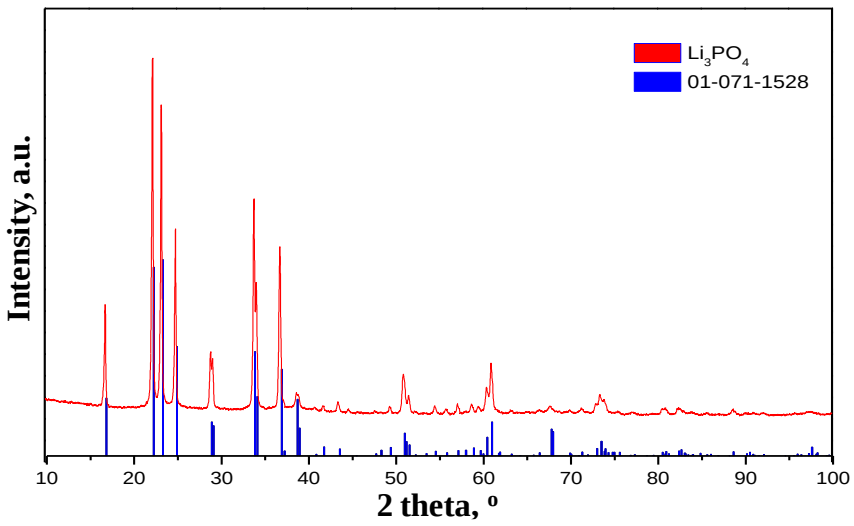

Figure 2*. XRD patterns of as-prepared Li_3PO_4 intermediate compound*

Based on the matching lines score, no impurity-related peaks could be detected, indicating a high level of purity of the as-prepared Li_3PO_4 material. The prepared sample has an orthorhombic crystal structure with a $Pmn2_1$ space group.

Figure 3 shows SEM images of the Li_3PO_4 product at different magnifications, which suggest that the product is of an irregular nanoplate-like structure. The present results are in good agreement with the literature [33,42]. The microstructure of Li_3PO_4 was studied by energy dispersive spectroscopy (EDS) to obtain the elemental composition. The collected EDS results shown in Figure 3, confirm the presence of only P and O atoms with a high amount of carbon (from the sample holder and citric acid), without the appearance of any other element.

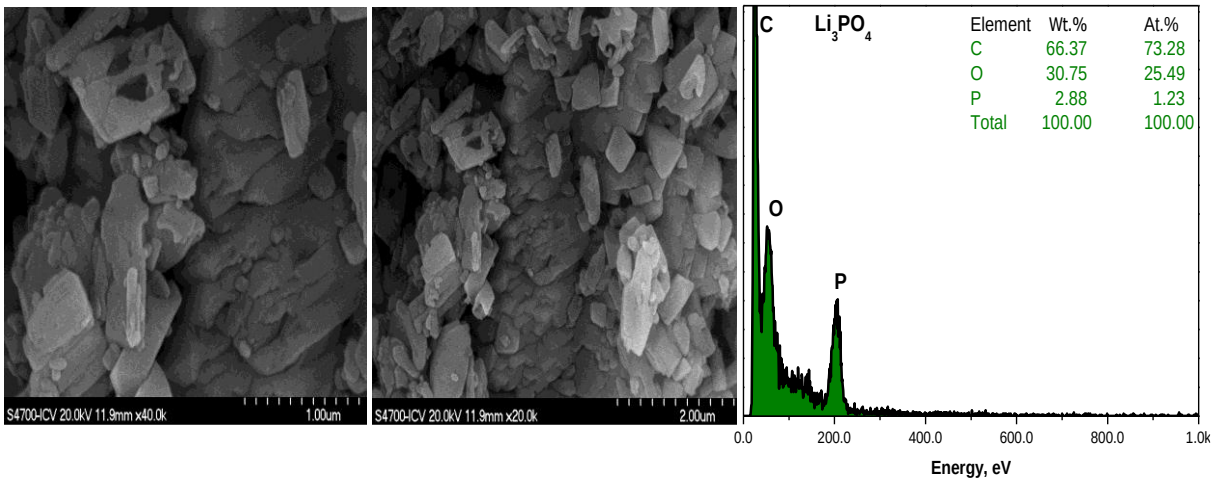

Figure 3. *SEM images and EDS spectrum of the as-prepared Li_3PO_4*

Results and discussion

Effect of operating conditions on $LiMnPO_4$ phase purity

The design matrix composed of 17 experiences, along with their experimental and predicted responses, are shown in Table 2.

Table 2*. Experimental design matrix proposed for $LiMnPO_4$ phase purity*

Run	X_1	X_2	X_3	Matching lines score with reference data #01-074-0375, %	
				Experimental	Predicted
1	0	0	0	75.00	74.60
2	0	0	0	73.00	74.60
3	-1	1	0	12.00	5.75
4	0	0	0	75.00	74.60
5	-1	0	1	10.00	11.75
6	1	1	0	99.00	93.25
7	1	-1	0	91.00	97.25
8	0	0	0	74.00	74.60
9	0	0	0	76.00	74.60
10	0	1	1	50.00	44.50
11	1	0	-1	77.00	65.25
12	0	1	-1	30.00	32.50
13	0	-1	-1	11.00	16.50
14	-1	-1	0	6.00	11.75
15	1	0	1	100.00	99.25
16	-1	0	-1	3.00	8.25
17	0	-1	1	88.00	70.50

The results show good agreement between experimental and predicted responses. The matched lines score with reference data#01-074-0375 (purity) of $LiMnPO_4$ was found to range from 3 to 100 %.

Based on the results presented in Table 2, the coefficients of the developed model in eq. (1) are estimated using multiple regression analysis technique. The polynomial model for the phase purity of $LiMnPO_4$ is represented by eq. (2):

$$Y_{LiMnPO_4} = 74.60 + 43.25X_1 - 2.50\,X_2 + 16.50X_3 + 0.50X_1X_2 + 6.50X_1X_3 - \\ - 10.50X_2X_3 - 9.30X_1^2 - 13.30X_2^2 - 20.30X_3^2 \quad (2)$$

The fit quality of the $LiMnPO_4$ purity model was attested with an analysis of variance (ANOVA) [43]. Generally, the suitability of the model is confirmed by higher Fisher's value (*F*-value) with probability (*p*-value) as low as possible ($p<0.05$)[44]. Table 3 shows the analysis of variance (*F*-test) and the p-value for this experiment. The *p*-value of this model is about 0.0002, which indicates that the model was suitable for use in this experiment.

Table 3. *Analysis of variance (ANOVA) for the fitted quadric polynomial model for optimization of $LiMnPO_4$ phase purity*

Source	Degree of freedom	Sum of squares	Mean square	*F*-value	*p*-value
Model	3	17192.50	5730.83	14.61	0.0002
Residual	4	5.20	1.30	-	-
Corrected total sum of squares	17	72621.00	4271.82	-	-
R^2 = 0.93					
Adjusted R^2= 0.90					

The calculated *F*-value for the regression is higher than 14, much higher than the value from Fisher tables ($F_{3,4}$ = 6.69, for a 95 % confidence level), confirming that the model is well fitted to the experimental data [45,46]**.**

The determination coefficient (R^2) quantitatively evaluates the correlation between the experimental data and the predicted responses [47]. With R^2 = 0.93, we conclude that the predicted values match the experimental values perfectly. The adjusted $R^2 \approx 0.90$ is very close to the corresponding R^2 value, which confirms that the model is highly significant [48].

The regression coefficients of eq. (2) and the corresponding p-values are presented in Table 4. From this result, we can conclude that the linear effect of PEG concentration (X_1) and reaction time (X_3) are the principal determining factors for the response on $LiMnPO_4$ phase purity.

Table 4. *Estimated regression coefficients and corresponding p-values obtained during Box-Behnken design for $LiMnPO_4$ material purity:*

Parameter	Term	Estimate regression coefficient	Standard error	*F*-value	*p*-value
β_0	Intercept	74.60	6.26	12.05	0.0017
β_1	X_1	43.25	4.91	77.50	< 0.0001
β_2	X_2	-2.50	4.91	0.2589	0.6265
β_3	X_3	16.50	4.91	11.28	0.0121
β_{11}	X_1X_1	-9.30	6.77	1.89	0.2120
β_{12}	X_1X_2	0.5000	6.95	0.0052	0.9446
β_{22}	X_2X_2	-13.30	6.77	3.86	0.0903
β_{13}	X_1X_3	-10.50	6.95	2.28	0.1745
β_{23}	X_2X_3	6.50	6.95	0.8752	0.3807
β_{33}	X_3X_3	-20.30	6.77	8.99	0.0200

The response surface plot as a function of PEG concentration (X_1) and reaction time (X_3) is presented in Figure 4(a). X_1X_3 was chosen as the interaction key, which exhibits a low p = 0.1745 compared to others that are not significant (since they exhibit a p-value higher than 0.1) [49,50].

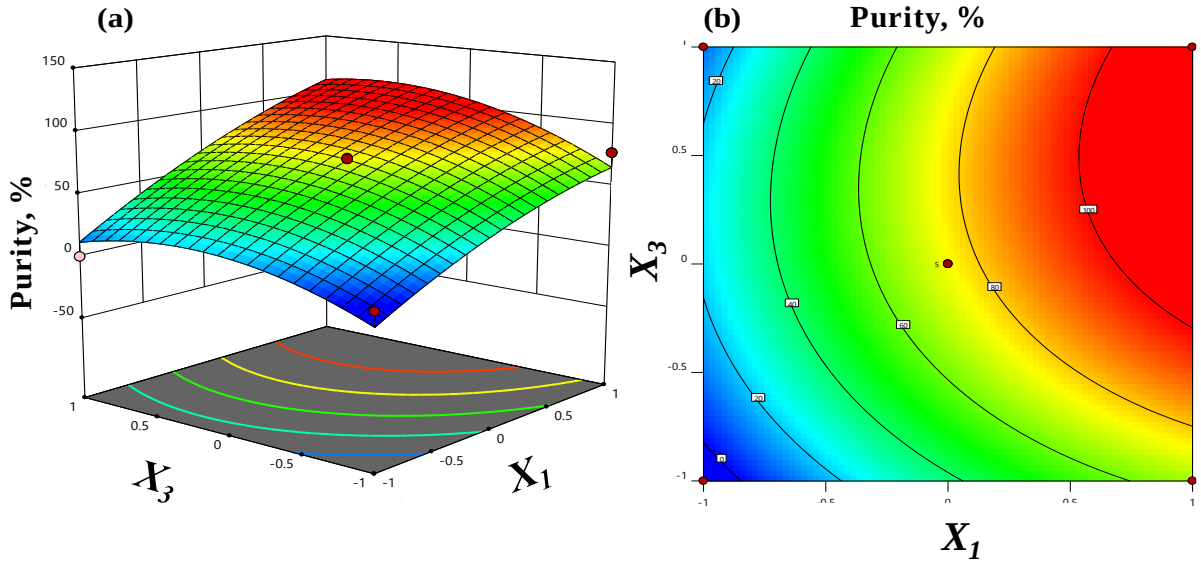

***Figure 4**. 3D response surface (a) and contour plot (b) of $LiMnPO_4$ phase purity for different coded values of X_1 (PEG concentration) and X_3 (reaction time)*

The combined effects of the two factors are positive and statistically significant, as also revealed by the contour lines presented in Figure 4(b). The optimum conditions for maximum $LiMnPO_4$ phase purity are as follows: c_{PEG} = 0.1 mol l^{-1}, T = 250 °C and τ = 180 min.

The synthesized material $LiMnPO_4$ under optimum conditions was characterized by X-Ray diffraction to confirm the phase purity. Figure 5 shows XRD results of the pure sample before and after calcination. It is clearly seen that the two patterns are very similar, with a difference in the peaks intensity which is much higher for the calcined sample. It is also observed that thermal treatment has not a remarkable effect on the formation process of the $LiMnPO_4$ phase and does not change the purity of the material, which indicates that the reaction has been done in the autoclave under solvothermal/optimum conditions. On the other hand, the main objective of calcination is the conversion of PEG layer adhered on the surface of the particles to the carbon layer, which promotes a higher electronic conductivity and consequently an improvement of the electrochemical performances.

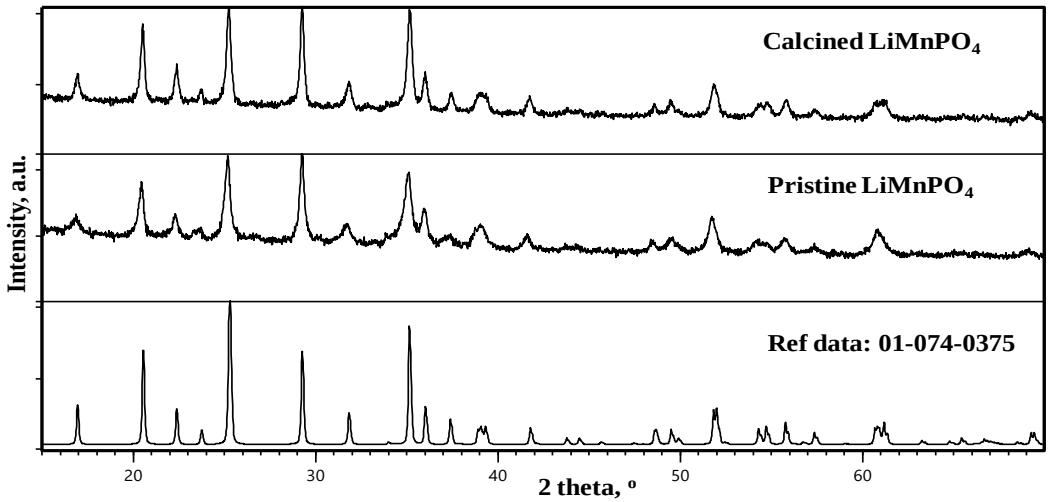

***Figure 5.** XRD patterns of pristine and calcined $LiMnPO_4$ material synthesized under optimum conditions*

The obtained results also confirm that a pure phospho-olivine structure $LiMnPO_4$ can be generated with a PEG-10000 concentration of 0.1 mol l^{-1}, a reaction temperature of 250 °C and a reaction time of 180 min. This pure phase was indexed as $LiMnPO_4$ crystal structure according to the standard data #01-074-0375, crystallizes in the orthorhombic system with the Pmnb space group.

During the thermal treatment process, most materials are generally subjected to some changes in the crystal structure, *i.e.*, crystallite size and microstrain (such as crystal lattice defects, stacking errors, displacement, *etc.* [51]). In order to verify these two parameters, both samples before and after calcination were examined by the Williamson - Hall (W-H) method as explained previously [35,36]. The W-H curves for all samples are displayed in Figure 6.

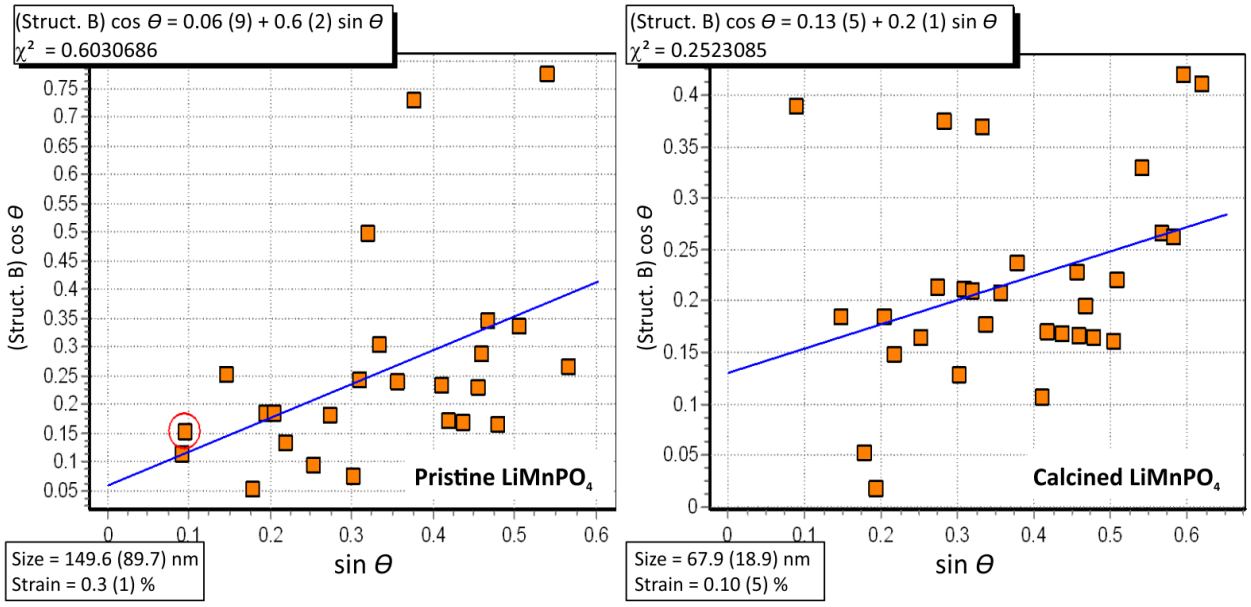

Figure 6. *Williamson-Hall plots of pristine and calcined $LiMnPO_4$ obtained under optimum conditions (Struct.B means structural broadening)*

According to these results, we can state that the crystallites size after calcination is about 68 ± 19 nm, which is strictly lower than that of the pristine material (150 ± 90 nm). This difference could be due to the thermal process that leads to the coalescence of the polyethylene glycol particles remaining adhered to the $LiMnPO_4$ material surface during the synthesis steps, leading to the formation of smaller, well-carbonated nanocrystallites. The lowest microstrain value of about 0.1 ± 5 % was observed for the calcined sample, while the highest strain value of 0.3 ± 1 % was detected for the pristine one. It can be noticed that crystal lattice defects can be reduced using an optimized PEG-10000 concentration, which can act as a protective matrix during the synthesis process due to the viscous property of this solvent.

Figure 7 shows the corresponding SEM images of the obtained products, pristine $LiMnPO_4$ and calcined $LiMnPO_4$@C materials. The surface morphology of the pristine sample seems like particles embedded in a polyethylene glycol matrix. However, the calcined sample image shows irregular secondary particles, with degradation of PEG matrix formed during synthesis steps, which confirms the transformation of PEG particles still adhered on the $LiMnPO_4$ material surface to a thin carbon layer.

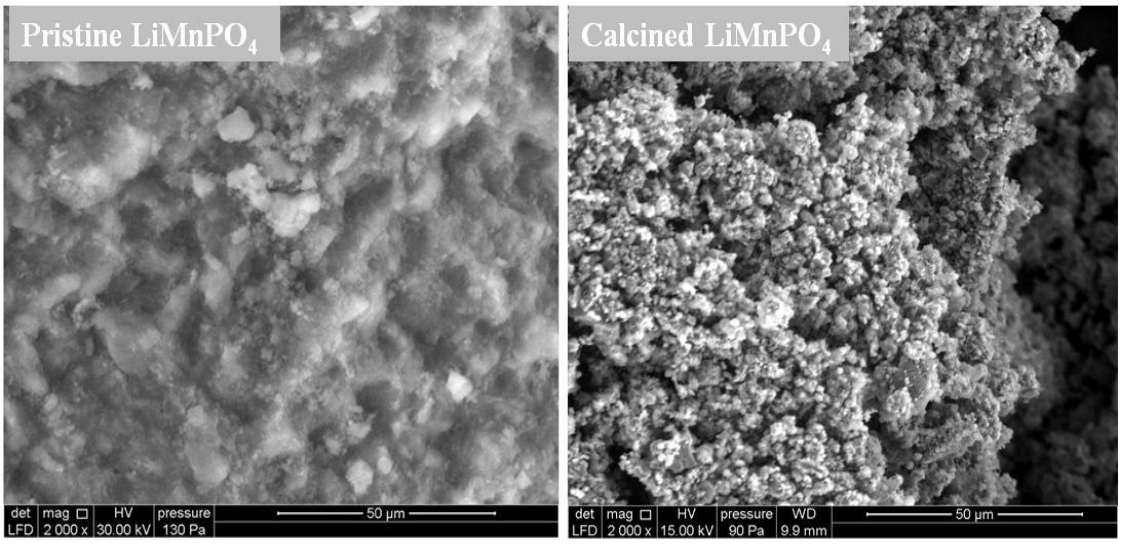

Figure 7. *SEM images of the synthesized pristine and calcined $LiMnPO_4$ material under optimum conditions*

Electrochemical performance of calcined $LiMnPO_4$@Ccathode material

The charge-discharge behavior of the calcined $LiMnPO_4$@C obtained under optimum conditions was studied using the "galvanostatic charging–discharging" method in the potential range of 2.5 to 4.5 V. As seen in Figure 8, the charge-discharge curves of the 1st, 2nd and 3rd cycles exhibit clear charge/discharge plateaus around 4.25 and 4.05 V, which is in agreement with the electrochemical de-lithiation/lithiation process, respectively [52]. The initial charge-discharge specific capacities were 164.8 and 128.8 mAh g^{-1} at 0.05 C-rate, respectively, which can be mainly attributed to the nanostructured crystallite size with the reduced microstrain that promotes good inter-calation/disintercalation of lithium ions within $LiMnPO_4$@C material structure [36,53]. Our findings are in good agreement with some previous works, where it was confirmed that $LiMnPO_4$ olivine structure without impurity could generate improved electrochemical performances [54]. However, the initial coulombic efficiency of about 78.2 % is mainly affected by unavoidable passivation phenomena of the electrolyte and the active electrode materials [55].

The as-prepared material under optimum synthesis conditions will be subjected to a wide range of electrochemical characterization in order to fully explain the different reaction mechanisms during the charge-discharge process.

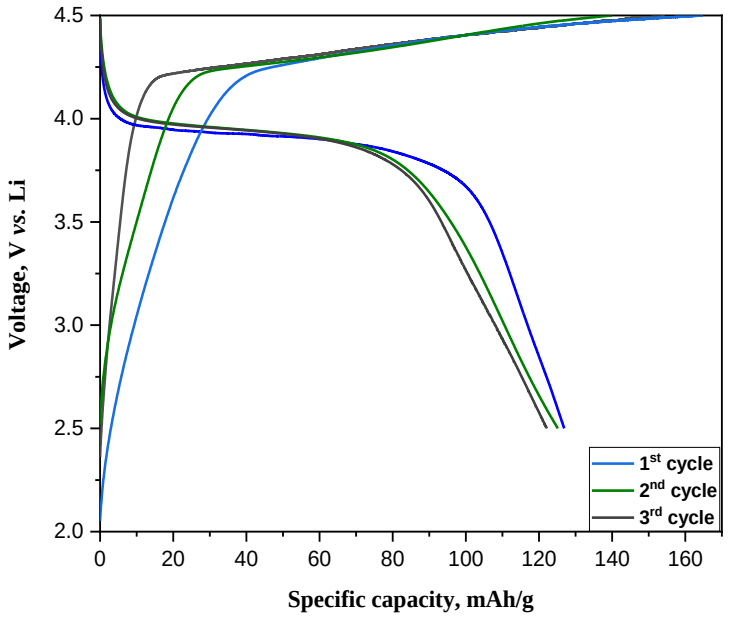

Figure 8. *Charge–discharge profiles of prepared $LiMnPO_4$@C material at 0.05 C-rate*

Conclusions

During this study, the intermediate compound Li_3PO_4 was firstly synthesized by a simple precipitation method. Thereafter, the main material $LiMnPO_4$ was prepared by solvothermal reaction under controlled conditions. The objective of this research was the optimization of solvothermal synthesis parameters using response surface methodology based on Box-Behnken design. Three independent variables were considered in this study, which are the concentration of solvent (PEG), reaction time and reaction temperature. The RSM optimization of operating conditions for the preparation of the pure $LiMnPO_4$ phase was applied. Analysis of variance (ANOVA) confirmed that the proposed regression model is in good agreement with the experimental data, providing a high determination and adjusted determination coefficients.The obtained results confirmed that the optimum conditions for maximum $LiMnPO_4$ phase purity are: c_{PEG} = 0.1 mol l^{-1}, T = 250 °C and τ = 180 min. The material synthesized under optimum conditions was subjected to supplementary characterization techniques to study the crystalline structure and the surface morphology. The results suggested that the used precursors, as well as the synthesis parameters, can directly affect the material purity and the structural properties.

This as-prepared cathode material $LiMnPO_4$@C, can display an initial charge-discharge capacity of 164.8 and 128.8 mAh g^{-1} at 0.05 C-rate, respectively, with moderated initial coulombic efficiency of about 78.2 %. Further investigations on the prepared material (such as particle size reduction, improved carbon coating, *etc.*) will be conducted to improve its electrochemical performance.

References

[1] K. Saravanan, P. Balaya, M. V. Reddy, B. V. R. Chowdari, J. J. Vittal, *Energy and Environmental Science* **3(4)** (2010) 457-464. https://doi.org/10.1039/b923576k

[2] J. Fan, J. Chen, Y. Chen, H. Huang, Z. Wei, M. Zheng, Q. Dong, *Journal of Materials Chemistry A* **2(14)** (2014) 4870-4873. https://doi.org/10.1039/C3TA15210C

[3] B. Kang, G. Ceder, *Nature* **458(7235)** (2009) 190-193. https://doi.org/10.1038/nature07853

[4] S. Ma, M. Jiang, P. Tao, C. Song, J. Wu, J. Wang, T. Deng, W. Shang, *Progress in Natural Science: Materials International* **28(6)** (2018) 653-666. https://doi.org/10.1016/j.pnsc.2018.11.002

[5] J. Zhang, S. Luo, L. Chang, S. Bao, J. Liu, *Electrochimica Acta* **193** (2016) 16-23. https://doi.org/10.1016/j.electacta.2016.02.018

[6] A. K. Padhi, K. S. Nanjundaswamy, J. B. Goodenough, *Journal of the Electrochemical Society* **144(4)** (1997) 1188-1194. https://doi.org/10.1149/1.1837571

[7] M. K. Devaraju, I. Honma, *Advanced Energy Materials* **2(3)** (2012) 284-297. https://doi.org/10.1002/aenm.201100642

[8] J. Wolfenstine, J. Allen, *Journal of Power Sources* **142(1–2)** (2005) 389–90. https://doi.org/10.1016/j.jpowsour.2004.11.024

[9] J. Yang, J. J. Xu, *Journal of the Electrochemical Society* **153(4)** (2006) A716. https://doi.org/10.1149/1.2168410

[10] K. Amine, H. Yasuda, M. Yamachi, *Electrochemical and Solid-State Letters* **3(4)** (2000) 178-179. https://doi.org/10.1149/1.1390994

[11] M. S. Kim, J. P. Jegal, K. C. Roh, K. B. Kim, *Journal of Materials Chemistry A* **2(27)** (2014) 10607-10613. https://doi.org/10.1039/C4TA01197J

[12] C. Delacourt, L. Laffont, R. Bouchet, C. Wurm, J. B. Leriche, M. Morcrette, J. M. Tarascon, C. Masquelier, *Journal of the Electrochemical Society* **152(5)** (2005) 913-921. https://doi.org/10.1149/1.1884787

[13] P. Nie, L. Shen, F. Zhang, L. Chen, H. Deng, X. Zhang, *CrystEngComm.* **14(13)** (2012) 4284-4288. https://doi.org/10.1039/C2CE25094B
[14] Z. X. Nie, C. Y. Ouyang, J. Z. Chen, Z. Y. Zhong, Y. L. Du, D. S. Liu, S. Q. Shi, M.S . Lei, *Solid State Communications* **150(1–2)** (2010) 40-44. https://doi.org/10.1016/j.ssc.2009.10.010
[15] S. Zhong, Y. Xu, Y. Li, H. Zeng, W. Li, J. Wang, *Rare Metals* **31(5)** (2012) 474-478. https://doi.org/10.1007/s12598-012-0542-3
[16] H. C. Dinh, S. Il Mho, Y. Kang, I. H. Yeo, *Journal of Power Sources* **244** (2013) 189-195. https://doi.org/10.1016/j.jpowsour.2013.01.191
[17] M. Pivko, M. Bele, E. Tchernychova, N. Z. Logar, R. Dominko, M. Gaberscek, *Chemistry of Materials* **24(6)** (2012) 1041-1047.https://doi.org/10.1021/cm203095d
[18] J. Yoshida, M. Stark, J. Holzbock, N. Hüsing, S. Nakanishi, H. Iba, H. Abe, M. Naito, *Journal of Power Sources* **226** (2013) 122-126. https://doi.org/10.1016/j.jpowsour.2012.09.081
[19] P. Barpanda, K. Djellab, N. Recham, M. Armand, J. M. Tarascon, *Journal of Materials Chemistry* **21(27)** (2011) 10143-10152. https://doi.org/10.1039/C0JM04423G
[20] Z. Bakenov, I. Taniguchi, *Journal of Power Sources* **195(21)** (2010) 7445-7451. https://doi.org/10.1016/j.jpowsour.2010.05.023
[21] T. N.L. Doan, Z. Bakenov, I. Taniguchi, *Advanced Powder Technology* **21(2)** (2010) 187-196. https://doi.org/10.1016/j.apt.2009.10.016
[22] T. N. L. Doan, I. Taniguchi, *Journal of Power Sources* **196(3)** (2011) 1399-1408. https://doi.org/10.1016/j.jpowsour.2010.08.067
[23] L. Damen, F. De Giorgio, S. Monaco, F. Veronesi, M. Mastragostino, *Journal of Power Sources* **218** (2012) 250-253. https://doi.org/10.1016/j.jpowsour.2012.06.090
[24] R. El Khalfaouy, S. Turan, K. B. Dermenci, U. Savaci, A. Addaou, A. Laajeb, A. Lahsini, *Ceramics International* **45(14)** (2019) 17688-17695. https://doi.org/10.1016/j.ceramint.2019.05.336.
[25] R. El Khalfaouy, A. Addaou, A. Laajeb, A. Lahsini, *Journal of Alloys and Compounds* **775** (2019) 836-844. https://doi.org/10.1016/j.jallcom.2018.10.161
[26] R. El-Khalfaouy, S. Turan, M. A. Rodriguez, K. B. Dermenci, U. Savacı, A. Addaou, A. Laajeb, A. Lahsini, *Journal of Applied Electrochemistry* **51(4)** (2021) 681-689. https://doi.org/10.1007/s10800-020-01528-8
[27] Z. Bakenov, I. Taniguchi, *Electrochemistry Communications* **12(1)** (2010) 75-78. https://doi.org/10.1016/j.elecom.2009.10.039
[28] N.-H. Kwon, T. Drezen, I. Exnar, I. Teerlinck, M. Isono, M. Graetzel, *Electrochemical and Solid-State Letters* **9(6)** (2006) A277. https://doi.org/10.1149/1.2191432
[29] D. Di, T. Hu, J. Hassoun, *Journal of Alloys and Compounds* **693** (2017) 730-737. https://doi.org/10.1016/j.jallcom.2016.09.193
[30] S. Luo, Y. Sun, S. Bao, J. Li, J. Zhang, T. Yi, *Journal of Electroanalytical Chemistry* **832** (2019) 196-203. https://doi.org/10.1016/j.jelechem.2018.10.062
[31] S.F. Yang, P.Y. Zavalij, M.S. Whittingham, *Electrochemistry Communications* **3(9)** (2001) 505-508. https://doi.org/10.1016/S1388-2481(01)00200-4
[32] G. Chen, J. D. Wilcox, T. J. Richardson, *Electrochemical and Solid-State Letters* **11(11)** (2008) A190. https://doi.org/10.1149/1.2971169
[33] K. Zhu, W. Zhang, J. Du, X. Liu, J. Tian, H. Ma, S. Liu, Z. Shan, *Journal of Power Sources* **300** (2015) 139-146. https://doi.org/10.1016/j.jpowsour.2015.08.065
[34] R. El Khalfaouy, A. Elabed, A. Addaou, A. Laajeb, A. Lahsini, *Arabian Journal for Science and Engineering* **44** (2019) 123-129. https://doi.org/10.1007/s13369-018-3248-5
[35] Y. Cao, J. Duan, G. Hu, F. Jiang, Z. Peng, *Electrochimica Acta* **98** (2013) 183-189. https://doi.org/10.1016/j.electacta.2013.03.014

[36] R. El Khalfaouy, A. Addaou, A. Laajeb, A. Lahsini, *International Journal of Hydrogen Energy* **44(33)** (2019) 18272-18282. https://doi.org/10.1016/j.ijhydene.2019.05.129
[37] S. Vedala, M. Sushama, *Materials Today: Proceedings* **5(1)** (2018) 1649-1656. https://doi.org/10.1016/j.matpr.2017.11.259
[38] T. Drezen, N. H. Kwon, P. Bowen, I. Teerlinck, M. Isono, I. Exnar, *Journal of Power Sources* **174(2)** (2007) 949-953. https://doi.org/10.1016/j.jpowsour.2007.06.203
[39] N. N. Bramnik, H. Ehrenberg, *Journal of Alloys and Compounds* **464(1–2)** (2008) 259-264. https://doi.org/10.1016/j.jallcom.2007.09.118
[40] J. Su, B.Q. Wei, J.P. Rong, W. Y. Yin, Z. X. Ye, X. Q. Tian, L. Ren, M. H. Cao, C. W. Hu, *Journal of Solid State Chemistry* **184(11)** (2011) 2909-2919. https://doi.org/10.1016/j.jssc.2011.08.042
[41] S. L. Yang, R. G. Ma, M. J. Hu, L. J. Xi, Z. G. Lu, C. Y. Chung, *Journal of Materials Chemistry* **22(48)** (2012) 25402-25408. https://doi.org/10.1039/C2JM34193J
[42] W. Zhang, Z. Shan, K. Zhu, S. Liu, X. Liu, J. Tian, *Electrochimica Acta* **153** (2015) 385-392. https://doi.org/10.1016/j.electacta.2014.12.012
[43] C. M. Borror, *Journal of Quality Technology* **39(3)** (2007) 297. https://doi.org/10.1080/00224065.2007.11917695
[44] M. Mir, S. M. Ghoreishi, *Chemical Engineering and Technology* **38(5)** (2015) 835-843. https://doi.org/10.1002/ceat.201300328
[45] L. Cesar, S. Garcia-Segura, N. Bocchi, E. Brillas, *Applied Catalysis B* **103(1–2)** (2011) 21-30. https://doi.org/10.1016/j.apcatb.2011.01.003
[46] J. Herney-Ramirez, M. Lampinen, M. A. Vicente, C. A. Costa, L. M. Madeira, *Industrial and Engineering Chemistry Research* **47(2)**(2008) 284-294.https://doi.org/10.1021/ie070990y
[47] A. Long, H. Zhang, Y. Lei, *Separation and Purification Technology* **118** (2013) 612-619. https://doi.org/10.1016/j.seppur.2013.08.001
[48] T. Xu, Y. Liu, F. Ge, L. Liu, Y. Ouyang, *Applied Surface Science* **280** (2013) 926-932. https://doi.org/10.1016/j.apsusc.2013.05.098
[49] H. Xu, S. Qi, Y. Li, Y. Zhao, J. W. Li, *Environmental Science and Pollution Research* **20** (2013) 5764-5772. https://doi.org/10.1007/s11356-013-1578-0
[50] J. Wu, H. Zhang, N. Oturan, Y. Wang, L. Chen, M. A. Oturan, *Chemosphere* **87(6)** (2012) 614-620. https://doi.org/10.1016/j.chemosphere.2012.01.036
[51] R. Muruganantham, M. Sivakumar, R. Subadevi, *Journal of Power Sources* **300** (2015) 496-506. https://doi.org/10.1016/j.jpowsour.2015.09.103
[52] Y. Hong, Z. Tang, S. Wang, W. Quan, Z. Zhang, *Journal of Materials Chemistry A* **3(19)** (2015) 10267-10274. https://doi.org/10.1039/C5TA01218J
[53] S.-Y. Cao,L.-J. Chang,S.-H. Luo ,X.-L. Bi, A.-L. Wei, J.-N. Liu, *Particle and Particle Systems Characterization* **39(2)** (2021) 2100203. https://doi.org/10.1002/ppsc.202100203
[54] D. Fujimoto, Y. Lei, Z.-H. Huang, F. Kang, J. Kawamura, *International Journal of Electrochemistry* **2014** (2014) 768912. https://doi.org/10.1155/2014/768912
[55] D. Choi, D. Wang, I. T. Bae, J. Xiao, Z. Nie, W. Wang, V. V. Viswanathan, Y. J. Lee, J. G. Zhang, G. L. Graff, Z. Yang, J. Liu, *Nano Letters* **10(8)** (2010) 2799-2805. https://doi.org/10.1021/-nl1007085

J. Electrochem. Sci. Eng. **12(2)** (2022) 317-329; http://dx.doi.org/10.5599/jese.1100

Open Access : : ISSN 1847-9286

www.jESE-online.org

Original scientific paper

Construction of new sensors with copper and cobalt complexes anchored on organofunctionalized silica and their use for electrocatalytic oxidation of reagents of biological interest

Marco A. G. Benetti, Denise I. Soares, Giovanna G. Alves, Eduardo D. A. Pinto and Angélica M. Lazarin ✉

Departamento de Química, Universidade Estadual de Maringá, Av. Colombo, 5790, 87020-900 Maringá, PR, Brazil

Corresponding author: ✉*amlazarin2@uem.br; Tel.: +55 4432633241; Fax: +55 44 30311011*

eceived: September 1, 2021; Accepted: February 14, 2022; Published: February 24, 2022

Abstract

This work describes the development and application of chemically modified carbon paste electrode (CMCPE) with metal ion complexes of transition metals Co(II) and Cu(II) anchored on functionalized silica (SF). The prepared CMCPE was used for the determination of dopamine (DA) in the presence of pyridoxine (VB_6) in commercially available pharmaceutical formulation, without any treatment of samples. The CMCPEs were built by incorporating graphite and functionalized silica and complexes of metal ions (Cu and Co) anchored by nitrogen groups on the silica surface. The electrochemical analysis was performed by cyclic voltammetry, while a drug analyzed in the present study was Revivan ampoules (DA determination).

Keywords

Chemically modified carbon electrode; functionalized silica; metal complexes; dopamine, vitamin B_6, cyclic voltammetry

Introduction

In many studies detected in the literature associated with the preparing of chemically modified silica, particular regard has been put to modifying materials containing transition metal ions that create supported complexes on the silica surface. Such materials are used to construct chemically modified electrodes (CME), which are usually linked with electroanalysis and eletrocatalysis [1-3].

Due to the mechanical rigidity, chemical inertia and large surface area, chemically modified silica gel has also been used as a stationary phase for high-performance liquid chromatography [4], for immobilizing enzymes [5], catalysts [6] and as an adsorbent of metal ions in aqueous solution and not aqueous [7,8].

The present investigation describes the development and application of chemically modified carbon paste electrodes (CMCPE) with metal ion complexes of transition metals Co(II) and Cu(II) anchored on the functionalized silica, for the determination of dopamine (DA) in the presence of pyridoxine (VB_6) in commercially available pharmaceutical formulation, without any sample treatment. The cyclic voltammetry technique was used, and the drug analyzed in the present study is Revivan drug ampoules (DA determination).

It must be added that VB_6 plays an important role in neurotransmitters synthesis, such as DA synthesis, and also participates in amino acid degradation reactions [9]. DA is an important neurotransmitter in the central nervous system (CNS) of mammals, having a concentration in extracellular fluid lower than that of ascorbic acid (AA) [10]. The voltammetric response with vitreous carbon electrode for dopamine, therefore, suffers the interference of ascorbic acid, which coexists *in vivo* in extracellular fluid of basic central nervous system, as anions in high concentration, and it has an oxidation potential close to dopamine (lower concentration) [11].

Experimental

Materials

All solutions were prepared using Millipore Milli-Q water. All chemicals were of analytical reagent grade and used without further purification. Silica gel (Merck), 3-(2-aminoethyl)aminopropyl]trimethoxysilane (Synth), ethanol (Synth**),** m-aminobenzoic acid (Sigma), hydrochloric acid (Merck), sodium hydroxide (Synth), ethylenediaminetetraacetic acid (Synth), copper chloride (Merck), and cobalt chloride (Merck) were used for all preparations. Graphite powder (1-2 mm particle size, Aldrich) and mineral oil (Aldrich) of high purity were used for the preparation of carbon paste. The supporting electrolyte used for all experiments was 0.10 mol dm^{-3} phosphate buffer solution (PBS). Pyridoxine (Merck) and dopamine (Sigma) were used as analytes.

AETS modified agent coated on the silica gel surface

Silica gel was degassed at 423 K under vacuum (10^{-3} atm) for 8 hours. About 40 g of this material was mixed with 32.0 cm^3 of [3-(2-aminoethyl)aminopropyl] trimethoxysilane dissolved in 350 cm^3 of dry toluene. The mixture was kept under reflux, mechanical stirring and inert nitrogen atmosphere for 12 hours. The resulting silica was firstly washed and filtered with ethanol and ethyl ether, and then in a Sohxlet extractor for 24 hours with ethanol, and finally dried at 353 K under vacuum (333 K). The prepared solid was named SF-AETS.

Modification of SF-AETS silica with MABA

In 10 g of SF-AETS silica suspended in 50.0 cm^3 of bidistilled ethanol, the reagent m-aminobenzoic acid (MABA) was added. The mixture was refluxed under mechanical stirring for one hour, then filtered and washed with ethanol and anhydrous ethyl ether. The silica obtained was named SF-AETS/MABA.

Characterization

The nitrogen amount in SF-AETS and SF-AETS/MABA samples was determined by nitrogen elemental analysis on Perkin-Elmer Analyzer 2400 series H CHNS/O device. Infrared spectra of samples were performed on Perkin-Elmer FTIR spectrophotometer, model 1600, by using pressed KBr pellets in the 4000-400 cm^{-1} range with 4 cm^{-1} of resolution. Thermogravimetric curves were recorded using a DuPont model 1090 B apparatus, coupled to a model 951 thermobalance, by heating from room

temperature to 1273 K at a heating rate of 0.16 K s^{-1} in argon flow of 1.67 cm^3 s^{-1}. The samples varied in weight from 15.0 to 30.0 mg.

Adsorption isotherms

Adsorption isotherms for $CuCl_2$ and $CoCl_2$ in ethanol solutions were determined with the use of the batch-wise method. A series of samples containing 100 mg of SF-AETS/MABA was shaken for 3 hours as previously established, in an orbital bath with variable concentrations of each metal halide at a constant temperature of 298 ± 1 K. The concentration of metal ions in solution in equilibrium with solid phase was determined by direct titration with EDTA (0.010 mol dm^{-3}) using murexide as an indicator. The amount of cations adsorbed, n_f, was determined by applying the equation: $n_f = (n_a - n_s)/m$, where m is the adsorbent mass and n_a and n_s are initial and equilibrium amounts of metal in the solution phase in moles, respectively, n_f is a measure of coverage degree in actual experimental conditions, defined according to:

$$n_f = \frac{n_a - n_s}{m} = \sum_m \frac{C_{(\text{SF-AETS/MABA})_m MCl_2}}{m} \quad (1)$$

In eq. (1), the summation extends over all species on the surface. The maximum number of moles of the adsorbed complex, n_f^{max}, is equal to the maximum value of n_f when the concentration of Co(II) and Cu(II) tends to infinity.

Adsorption of Co(II) and Cu(II) held in solution depends on the selectivity coefficients of complexes constituted with the ligand immobilized on the surface. The formation of equilibrium of the complex Co(II) and Cu(II) with SF-AETS/MABA was examined by a Filippov model [12,13].

The reaction of a metal (M) complex formation at the surface can be expressed by the following equation:

$$MX_z + nR \leftrightarrow MR_nX_z \quad (2)$$

where z is the charge of the metallic ion, X is an anion with unit charge and R is linking group, electrically neutral, and fixed on the support surface.

In the equilibrium, the following relation is applied:

$$\theta_n / (1 - \theta_n) = \gamma_n C \quad (3)$$

where the fraction of SF-AETS/MABA bonded to metal is $\theta_n = \tilde{n}\, n_f / n_0$ n_0 is the quantity of MABA immobilized on SF-AETS (mol g^{-1}), $\tilde{n}$ is the number of ligands bonded to the metal, and γ_n is the stability constant.

Substitution for θ_n in eq. (3) results in the ending expression [14]:

$$\frac{1}{n_f} = \frac{\tilde{n}}{NY_nC} + \frac{\tilde{n}}{N} \quad (4)$$

Considering that metallic ions Cu(II) and Co(II), when adsorbed on the surface (with a homogeneous covering ligands), form immobilized complexes with different ratios between them and are anchored at SF-AETS/MABA, the total concentration of immobilized ligand on the surface is equal to the sum of the concentrations of all species; *N* is the degree of functionalization, *C* is the concentration of the surface complex; $\tilde{n}$ is the average number of supported ligands bound to a metallic ion, defined as:

$$\tilde{n} = \frac{C_{MRX_z} + 2C_{MR_2X_z} + \ldots + mC_{MR_mX_z}}{n_f} \quad (5)$$

where m adsorbent mass and R is linking group.

Eq. (4) can be re-written as

$$\frac{1}{n_f} = \frac{\tilde{n}}{N\Gamma_n C} + \frac{\tilde{n}}{N} \quad (6)$$

where Γ_n is the selectivity coefficient, equal to $\sum_{m=1}^{n} y_m$.

Electrode preparation and electrochemical measurements

Modified CMCPE was prepared by mixing 30 mg of silica, 30 mg of graphite and a drop of mineral oil (2.0×10^{-2} cm^3). The paste was placed into a cavity on the area of a platinum disk, fused to the end of a glass tube with 1 mm of inner diameter. This proportion was used because of a great response reached with a preliminary test after a detailed study of the paste composition.

Electrochemical measurements were carried out using CMCPE as the working electrode, Ag/AgCl (sat. KCl) as the reference electrode and a platinum wire as the counter electrode. Electrochemical properties were explored by means of cyclic voltammetry with a PAR 273A (EG&G) potentiostat-galvanostat. All experiments were performed in 0.10 mol dm^{-3} PBS, under a pure argon atmosphere, and the pH value of electrolyte solutions was adjusted to 7.0 by adding HCl or NaOH solutions. Different supporting electrolytes were tested as well.

Results and discussion

Surface characterizations

Silica gel functionalized (SF) with [3-(2-aminoethyl)aminopropyl]trimethoxysilane group (AETS) was obtained according to the following reaction:

$$Si(OH)_3 + (CH_3O)_3Si(CH_2)_3NH(CH_2)_2NH_2 \rightarrow SiO_3Si(CH_2)_3NH(CH_2)_2NH_2 + 3CH_3OH \quad (7)$$

SF AETS SF-AETS

For SF-AETS silica, the amounts of supported groups were set by nitrogen analysis using the method described in the experimental part. The functionalization efficiency was determined for (silane) groups as 0.91±0.01 mmol g^{-1} in SF-AETS based on the nitrogen content.

Further modification of SF-AETS with m-aminobenzoic acid into SF-AETS/MABA was reached by the following reaction:

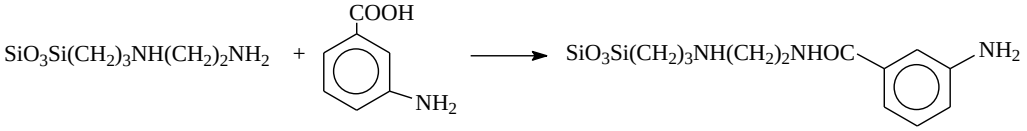

(8)

SF-AETS MABA SF-AETS/MABA

Subsequent coordination of metal ions at the surface of SF-AETS/MABA silica was obtained through reactions with metal chlorides, as shown below:

$$SF/AETS/MABA + M(II) \rightarrow SF/AETS/MABA/M(II) \quad (9)$$

Figure 1 presents infrared spectra of SF, SF-AETS and SF-AETS/MABA silicas. The assignment of vibrational frequencies to pure silica (SF) and functionalized silica (SF-AETS) are listed in Table 1.

The appearance of new bands attributed to the stretch CH_2, NH_2, CH_2N and $SiCH_2$ pointed to the effective functionalization of silica gel with AETS silylating agent on its surface. Infrared spectra of SF-AETS/MABA/Co(II) are shown in Figure 2.

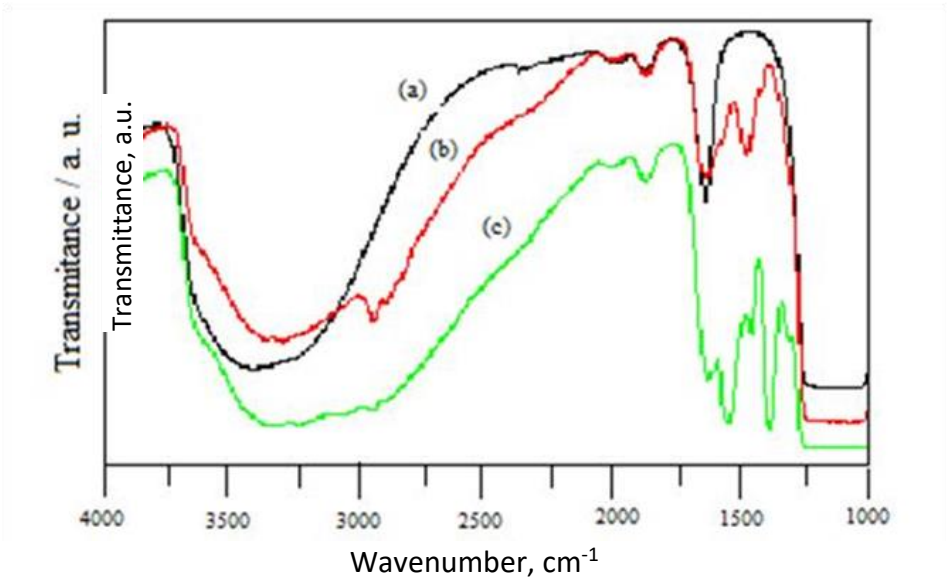

***Figure 1**. Infrared spectra of (a) SF, (b) SF-AETS and (c) SF-AETS/MABA*

***Table 1.** Vibrational frequencies assigned for SF and SF-AETS silica*

ν_{SF} / cm^{-1}	$\nu_{SF\text{-}AETS}$ / cm^{-1}	Assignment
3400 (vs)	3400 (vs)	ν_{OH}
--	2940 (w)	ν_{CH_2}
1992 (w)	1995 (w)	*
1871 (w)	1870 (w)	*
1637 (s)	1634 (s)	δ_{OH}
--	--	$\delta_{OH} + \delta_{NH_2}$
--	1575 (m)	δ_{NH_2}
--	--	$\nu_{C=C}$ ring
--	1480 (m)	δ_{CH_2N}
--	1418 (m)	δ_{SiCH_2}

* related to silica skeleton , vs = very strong band, m = mid band, s = short band, w = weak band

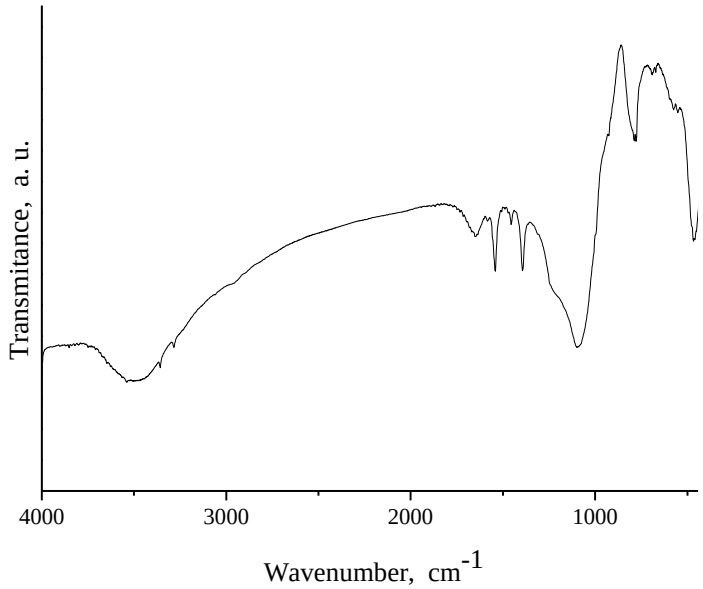

***Figure 2.** The infrared spectrum of SF-AETS/MABA/Co(II)*

The assignments for SF-AETS/MABA and SF-AETS/MABA/Co(II) silicas are shown in Table 2. The comparison of infrared spectra in Figures 1 and 2 shows that in all spectra, a strong and wide band

appears in the region of 3400 cm^{-1}, attributed to OH stretches of water and silane groups, a band in the region of 1634 cm^{-1}, which is characteristic of angular deformation of water [15], besides two bands close to 1900 cm^{-1} attributed to combinations of silica skeleton (Tables 1 and 2). Infrared spectra of SF-AETS/MABA silica with Co(II) ion anchored on its surface presented in Figure 2 showed a similar behavior (Table 2). The infrared spectra of the SF-AETS/MABA silica showed characteristic bands of amide bond (1626 + 1605 cm^{-1}) (δ_{HOH} + ($\nu_{C=O}$, Band I of amide) and (1549 cm^{-1}) (δ_{NH} + ν_{CN}, Band II of amide), of the band in (1386 cm^{-1}) (δ_{CN} of and so on primary aromatic amine), showing that the successive change in surface SF-AETS silica actually occurred (Table 2).

Table 2. *Vibrational frequencies assigned for SF-AETS/MABA and SF-AETS/MABA/Co(II).*

$\nu_{SF\text{-}AETS/MABA}$ /cm^{-1}	$\nu_{SF\text{-}AETS/MABA/Co}$ /cm^{-1}	Assignments
3400 (vs)	3400 (vs)	ν_{OH}
3343 (vw)	3253 (vw)	ν_{NH_2}
3226 (vw)		ν_{NH} amide
3067 (vw)		ν_{CH} aromatic
2940 + 2893 (vw)	2940 (vw)	ν_{CH_2}
2000 (vw)	2000 (vw)	(*)
1869 (w)	1871 (w)	(*)
1626 + 1605 (s)	1631 (s)	δ_{HOH} + $\nu_{C=O}$ Band I of the amide
1549 (vs)	1575(m)+1492 (vw)	δ_{NH} + ν_{CN} Band II of the amide
1452 (w)	1458 (m)	$\delta_{CH_2\text{-}N}$
-	1407 (s)	$\delta_{Si\text{-}CH_2}$
1386 (vs)	1387 (s)	ν_{CN} primary aromatic amine
1304 (vw)		δ_{NH} + ν_{CH} Band III of secondary amide

vs = very strong band, vw = very weak, m = mid band, s = short band, w = weak band

Thermogravimetric curves of pure silica (SF) and functionalized silica SF-AETS were obtained as described in the experimental part and shown in Figure 3. The SF and SF-AETS silica showed mass loss of 9.7 and 12.9 %, respectively. In examining these compounds, the following processes were detected: i) water molecules are lost from room temperature at near 500 K, and ii) the functional groups are lost from 453 up to 813 K.

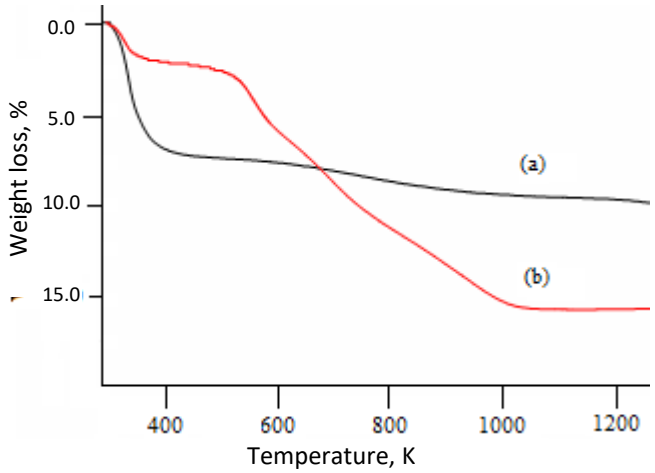

Figure 3. *Thermogravimetric curves of (a) SF and (b) SF-AETS silica*

The thermogravimetric curve of SF-AETS/MABA silica is shown in Figure 4 and presented a percentage of mass loss of 15.7 % and the greatest mass loss occurring between 453 and 813 K.

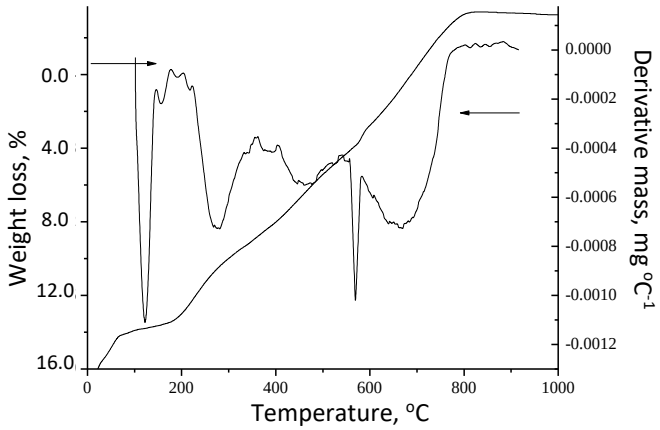

***Figure 4**. Thermogravimetric curves (integral and differential) of SF-AETS/MABA silica*

Adsorption of copper and cobalt

The corresponding isotherms of metal ion adsorption from ethanol solutions of selected cations Cu(II) and Co(II), at SF-AETS/MABA were also investigated. Early investigation showed that the original silica matrix does not adsorb these cations.

The solid adsorption capacity of metal halide on SF-AETS/MABA depends on the nature of the complex formed on the surface and the affinity of any particular ligand attached to the metal. Maximum adsorption capacity, n_f^{max}, for $CuCl_2$ and $CoCl_2$, was 0.17 and 0.64 mmol g^{-1}, respectively, indicating that cobalt binds more effectively than cooper to available basic centers. The average stability constant (Γ) and the average number of ligands bonded and coordinated to the metallic ion ($\tilde{n}$) were determined from the plot of $1/n_f$ and 1/C. The average stability values of $CuCl_2$ and $CoCl_2$ in SF-AETS/MABA were 391 and 191 $dm^3\,mol^{-1}$, respectively, and the average number of ligands ($\tilde{n}$) for SF-AETS/MABA was four to cooper and one to cobalt metallic ions. The values of calculated constants indicate the formation of stable complexes.

Electrochemical studies

Silica SF-AETS/MABA/Cu(II)

Voltammetry experiments using CMCPE modified with different silica materials were carried out. For the electrode modified with only SF-AETS/MABA, no current peaks were observed, while for CMCPE prepared with SF-AETS/MABA having complexed cooper (II) attached, some peaks were obtained. They can be observed in Figure 5, where stabilization of CMCPE/SF-AETS/ MABA/Cu(II) in 0.10 mol dm^{-3} PBS, pH 7.0 was followed by cyclic voltammograms recorded consecutively at 20 mV s^{-1} in the potential range of -1.0 to 1.0 V (*vs.* Ag/AgCl) at 298 K. In this potential range, a pair of peaks is observed in Figure 5, with almost reversible characteristics, $E_{1/2}$ = -0.11 V (where $E_{1/2}$ = (E_{pa} + E_{pc})/2 and E_{pa} and E_{pc} are anodic and cathodic peak potentials, respectively). These almost reversible peaks were assigned to the Cu(II)/Cu(I) redox pair, while the irreversible anodic peak at E_{pa}= 0.90 V was assigned to the Cu(III)/Cu(II) redox pair.

Cyclic voltammograms of stabilized CMCPE/SF-AETS/MABA/Cu(II) electrode, recorded at different potential scan rates, are shown in Figure 6. It is obvious that the value of the potential difference between anodic and cathodic peaks, ΔE_p ($\Delta E_p = E_{pa} - E_{pc}$), is increased at higher scan rates. This result reflects the kinetics of electron transfer on the electrode surface, which is not fast enough, as a consequence of having a matrix with considerable resistance. The graphs of anodic peak current as a function of the square root of scan rate and anodic peak current as a function of scanning rate (not shown here) presented linear behavior, which suggests a diffusion-controlled process [16,17].

Since it was shown earlier that electroactive species strongly adhere to the matrix, the mechanism may be explained by the transport of the ion of supporting electrolyte from the electrode surface for charge compensation [18,19].

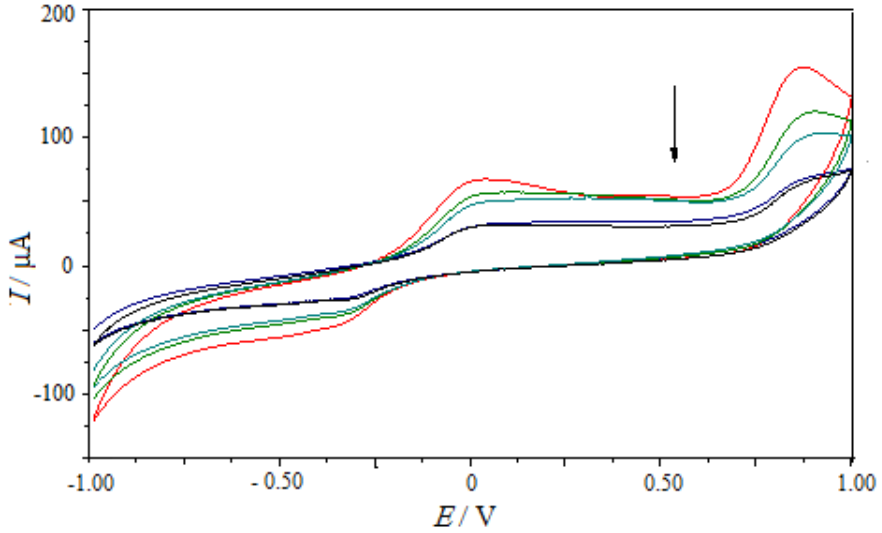

***Figure 5**. Cyclic voltammograms of CMCPE/SF-AETS/MABA/Cu(II) electrode stabilization in 0.10 mol dm^{-3} PBS, pH 7.0, at 20 mVs^{-1} and 298 K*

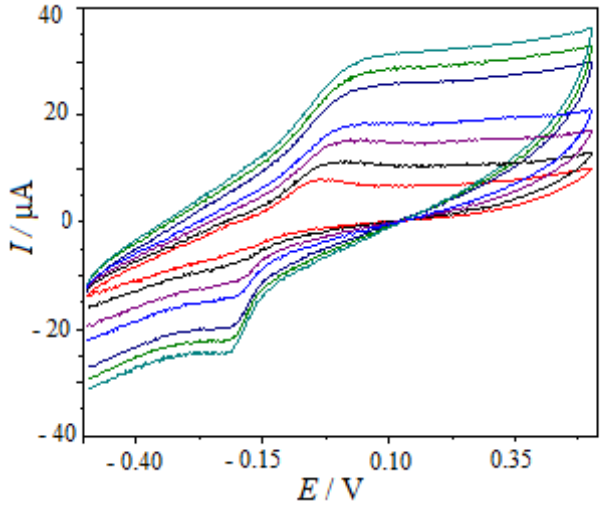

***Figure 6**. Cyclic voltammograms of CMCPE/SF-AETS/MABA/Cu(II) electrode in 0.10 mol dm^{-3} PBS pH 7.0, at 298 K, as a function of the scan rate (5, 10, 20, 30, 50 and 60 mVs^{-1})*

The nature of supporting electrolyte that was changed by varying the cation and anion (phosphate buffer, KCl, NH_4Cl, $NaNO_3$ and NH_4NO_3) did not produce any significant influence on $E_{1/2}$. Such results suggested that these supporting electrolytes are not interacting with the matrix surface and produce no significant change of the midpoint potential [20].

With CMCPE/SF-AETS/MABA/Cu(II) electrode, a preliminary study of oxidation of vitamin B_6 was made by voltammetric measurements. Figure 7 shows electrochemical responses of CMCPE/SF-AETS/MABA/Cu(II) without (curve a) and with 9.8×10^{-4} mol dm^{-3} of vitamin B_6 (curve b). It is obvious that the anodic oxidation potential of VB_6 is around E_{pa}= 0.95 V, as shown in Figure 7(b).

Figure 8 shows the electrochemical behavior of CMCPE/SF-AETS/MABA/ Cu(II) electrode in PBS containing 0.30 cm^3 of Revivan drug in the presence of vitamin B_6 (C_{VB6} = 9.8×10^{-4} mol dm^{-3}), and after successive additions of dopamine, in the concentration range of 9.6×10^{-5} to 2.5×10^{-4} mol dm^{-3}.

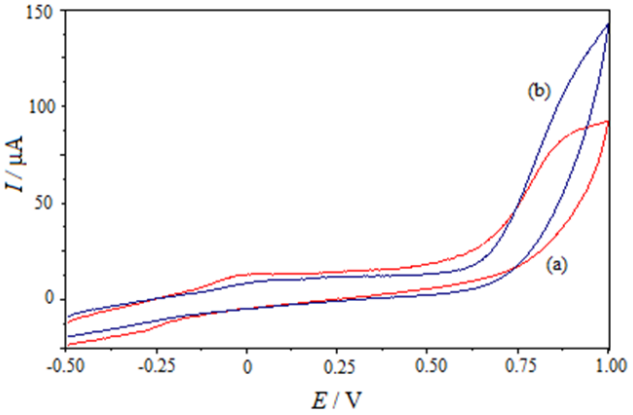

Figure 7. *Electrochemical behavior of CMCPE/SF-AETS/MABA/Cu(II) electrode in 0.10 mol dm^{-3} PBS, pH 7.0, at 20 mV s^{-1}and 298 K: (a) without, and (b) with 9.8×10^{-4} mol dm^{-3} vitamin B$_6$*

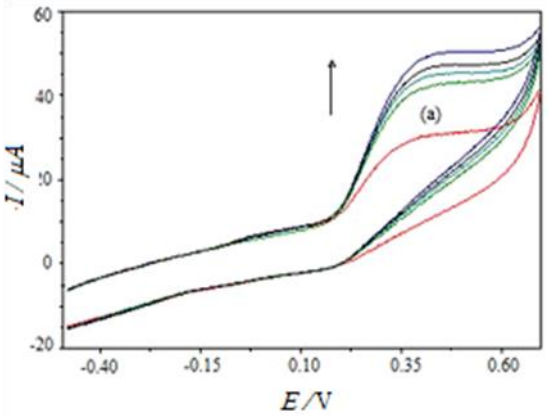

Figure 8*. Dopamine determination in Revivan by the standard multiple addition method on the CMCPE/SF-AETS/MABA/Cu(II) electrode in 0.10 mol dm^{-3} PBS, pH 7.0, at 20 mV s^{-1} and 298 K: (a) 0.30 cm^3 of Revivan in the presence of 9.8x10^{-4} mol dm^{-3} VB$_6$ and after successive additions of dopamine (9.6x10^{-5} to 2.5x10^{-4} mol dm^{-3})*

The oxidation potential of dopamine is at E_{pa}= 0.39 V, and anodic peak current graph *versus* dopamine concentration (C_{DA} = 9.6×10^{-5} to 2.5×10^{-4} mol dm^{-3}) allowed the quantification of dopamine present in the drug. A linear correlation was observed between I_p and DA concentration, with a detection limit of 9.4×10^{-5} mol dm^{-3}. The determined value in mol dm^{-3} was 5.1×10^{-2}, and after, this value was recalculated to g cm^{-3}. The value was found equal to (4.9 ± 0.3)×10^{-3} g cm^{-3} is in accordance with that supplied by the manufacturer.

The reproducibility of the electrode response to DA was also investigated by repetitive measurements. The results of 200 successive measurements showed a relative standard deviation of 1.03 %. Thus, the modified CMCPE/SF-AETS/MABA/Cu(II) electrode was found to be a very stable and highly reproducible electrode, appropriate for DA determination.

Silica SF-AETS/MABA/Co(II)

First, the stabilization of CMCPE/SF-AETS/MABA/Co(II) electrode was followed by recording consecutive CVs in 0.10 mol dm^{-3} PBS, pH 7.0 at 298 K. CVs were carried out at 20 mV s^{-1} going from 1.0 to -0.70 V (*vs*. Ag/AgCl) (cathodic scanning), and presented in Figure 9.

An almost reversible peak with $E_{1/2}$ = 0.84 V can be assigned to the Co(III)/Co(II) redox pair. After the stability of the CMCPE/SF-AETS/MABA/Co(II) electrode was attained, it was used the study of oxidation of dopamine in the presence of vitamin B$_6$. Up to now, the electrochemical oxidation of vitamin B$_6$ has been mostly studied on carbon paste electrodes.

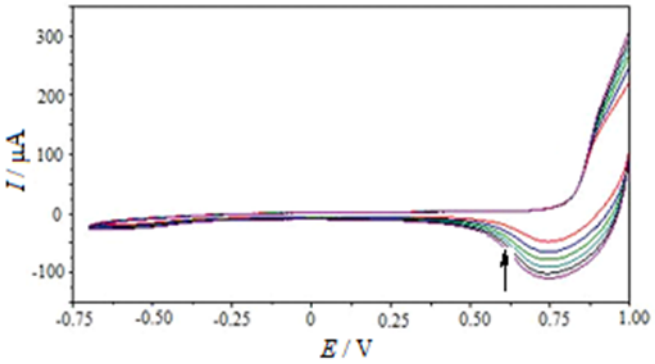

Figure 9. Cyclic voltammograms of CM*CPE/SF-AETS/MABA/Co(II) electrode* stabilization *in 0.10 mol dm^{-3} PBS , pH 7.0, at 20 mVs^{-1} and 298 K*

The reaction was supposed to involve the oxidation of pyridoxine (PYX) into pyridoxal derivative (PYO) [21]. The voltammetric response obtained with the CMCPE/SF-AETS/MABA/Co(II) after the successive additions of vitamin B_6 in the concentration range 9.9×10^{-5} to 3.9×10^{-4} mol dm^{-3}, however, did not present significant current variations (Figure 10). For this reason, CMCPE/SF-AETS/MABA/Co(II) cannot be used for the electrochemical determination of vitamin B_6 in the drug.

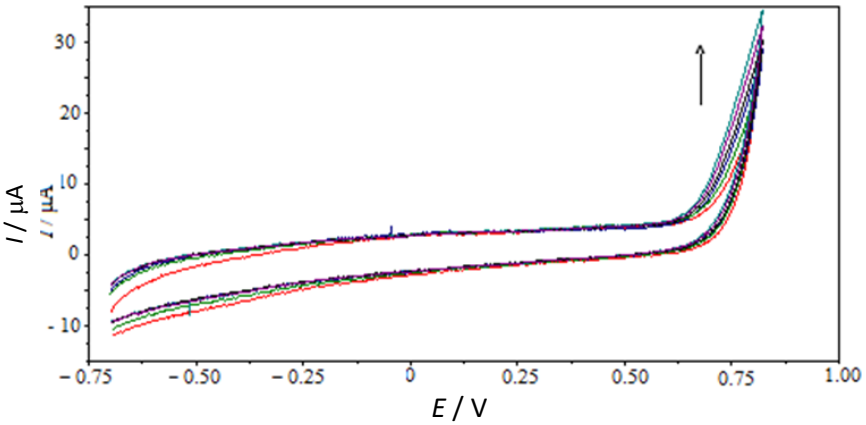

***Figure 10**. Electrochemical behavior of the CMCPE/SF-AETS/MABA/Co(II)electrode in 0.10 mol dm^{-3}PBS, pH 7.0, at 20 mV s^{-1} and 298 K without and with added vitamin B_6 in the concentration range of 9.9x10^{-5} to 3.9x10^{-4}mol dm^{-3}*

Figure 11 shows the electrochemical behavior of CMCPE/SF-AETS/MABA/Co(II) electrode in 0.10 mol dm^{-3} PBS, pH 7.0, after dopamine additions of 5.0×10^{-5} to 2.0×10^{-4} mol dm^{-3}.

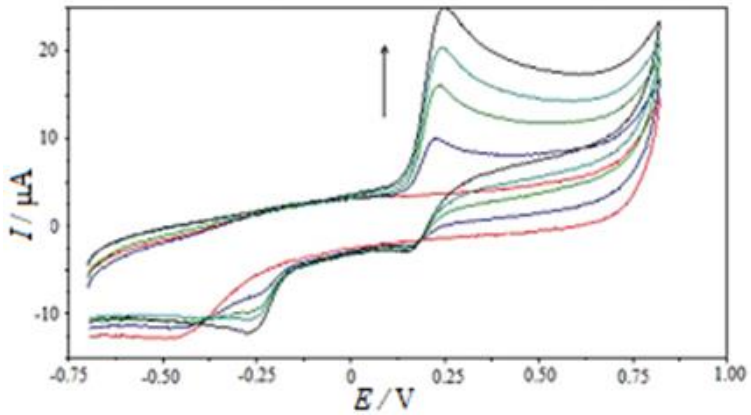

***Figure 11**. Electrochemical behavior of the CMCPE/SF-AETS/MABA/Co(II)electrode in 0.10 mol dm^{-3} PBS, pH 7.0, at 20 mV s^{-1} and 298 K without and with added DA in the concentration range of 5.0×10^{-5} to 2.0×10^{-4} mol dm^{-3}*

Electrochemical behavior of CMCPE/SF-AETS/MABA/Co(II**)** electrode as a function of scanning rate in the presence of 2.0×10^{-4} mol dm^{-3} dopamine is presented in Figure 12.

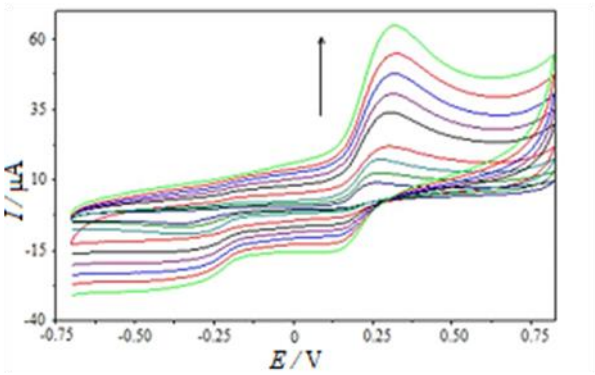

***Figure 12**. Electrochemical behavior of CMCPE/SF-AETS/MABA/Co(II) electrode* in *0.10 mol dm^{-3} PBS, pH 7.0, 298 K* and *2.0×10^{-4} mol dm^{-3} DA at different scan rates (2, 5, 10, 20, 30, 40, 50, 60, 70 mV s^{-1})*

The graph of anodic peak current for CMCPE/SF-AETS/MABA/Co(II) at the oxidation potential of dopamine (E_{pa}= 0.250 V) against $\nu^{1/2}$ presented linear behavior with two slopes, one at high and the other at low scan rates [22].

The electroanalytical determination of dopamine in Revivan ampoules was executed with this CMCPE/SF-AETS/MABA/Co(II) electrode by the method of multiple pattern addition. Dopamine concentration was varied from 4.9×10^{-5} to 1.93×10^{-4} mol dm^{-3} and the presence of B_6 vitamin 4.5×10^{-5} mol dm^{-3} did not show significant variation (Figure 13). A linear correlation is observed between peak current and dopamine concentration with a detection limit of 4.9×10^{-5} mol dm^{-3}. The graph of anodic peak current versus dopamine concentration allowed the quantification of dopamine present in the drug. The determined value in mol dm^{-3} was 8.9×10^{-2}, and after, this value was recalculated to g cm^{-3}. The value was found equal to $(4.8 \pm 0.3)\times10^{-3}$ g cm^{-3}, which coincides with that provided by the manufacturer (5 mg cm^{-3}).

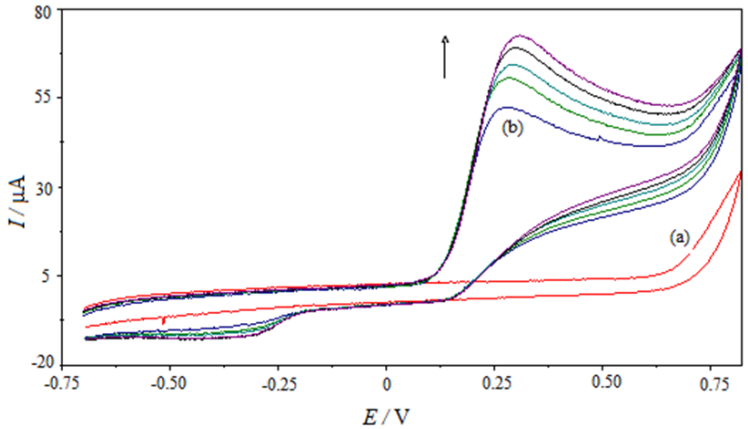

***Figure 13**. Determination of dopamine in Revivan by the multiple standard addition method at CMCPE/SF-AETS /MABA/Co(II) electrode in 0.1 mol dm^{-3} PBS, pH 7 at 20 mV s^{-1} and 298 K. (a) cyclic voltammogram in the presence of B_6 vitamin 4.5×10^{-5} mol dm^{-3} (b) after addition of 0.50 cm^3 of Revivan and successive additions of dopamine in the concentration range of 4.9×10^{-5} to 1.93×10^{-4} mol dm^{-3}*

The comparison of CMCPE/SF-AETS/MABA/Co(II) electrode response with that of glassy carbon electrode in the solution containing a mixture of vitamin B_6 and dopamine is presented in Figure 14. Compared to glassy carbon, for the CMCPE modified with silica, there is no appearance of the

oxidation peak of vitamin B_6 in the studied potential range. Also, the current catalysis for dopamine oxidation is clearly presented for CMCPE/SF-AETS/MABA/Co(II) electrode, showing much greater sensitivity than is observed for the glassy carbon electrode.

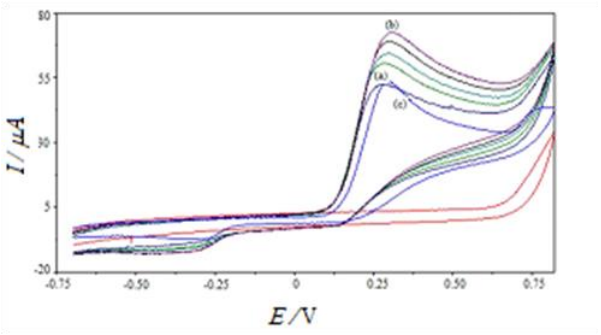

Figure 14. *Comparison of (a and b) CMCPE/SF-AETS/MABA/Co(II) electrode and (c) glassy carbon electrode responses in 0.10 mol dm^{-3} PBS, pH 7.0, and 4.5×10^{-5} mol dm^{-3} VB_6 at 20 mV s^{-1}, and 298 K after: (a) addition of 0.50 cm^3 of Revivan; (b and c) addition of 1.93x10^{-4} mol dm^{-3} of dopamine*

The performance of CMCPE/SF-AETS/MABA/Co(II) electrode over five months was followed by measurements of oxidation peak currents for dopamine in PBS on each consecutive day. This serves as an indicator of the stability of modified electrodes toward dopamine. The electrodes were used every day. The experimental results indicated that current responses showed a relative standard deviation of 2.0 %, suggesting that modified electrodes possess fine stability.

The reproducibility of electrodes was investigated. Repetitive measurements were performed in dopamine. The results of 200 successive measurements show a relative standard deviation of 1.03 %. Thus, the modified electrodes are found very stable, showing great reproducibility.

Conclusions

The enrichment of interfacial layer of silica gel by chemisorption, with interactions of covalent nature on its surface through the use of silylating agents with nucleophilic sites, favored the increased capacity of organofunctionalized silica to sequester metals, with complexes anchored on its surface. The analytical results obtained from the electrode containing Cu(II) and Co(II) complexes were very promising. The benefits to employ the suggested electrodes have been stated by our analytical processes, and its progress is easy. The electrodes did not present significant variation in response after five months of use, thus showing good chemical stability. These characteristics make this material very attractive for use as a sensor for dopamine determinations.

Acknowledgment: *The authors are indebted Josué A. Da Silva for manuscript revision.*

References

[1] X. Li, B. Wang, Y. Cao, S. Zhao, H. Wang, X. Feng, J. Zhou, X. Ma, *Chemical Engineering* **7(5)** (2019) 4548-4563. https://doi.org/10.1021/acssuschemeng.8b05751
[2] S. K. Parida, S. Dash, S. Patel, B. K. Mishra, *Advances in Colloid and Interface Science* **121(1-3)** (2006) 77-110. https://doi.org/10.1016/j.cis.2006.05.028
[3] K. Kalcher, *Electroanalysis* **2(6)** (1990) 419-433. https://doi.org/10.1002/elan.1140020603
[4] A. M. Faria, C. H. Collins, I. C. S. F. Jardim, *Journal of the Brazilian Chemical Society* **20(8)** (2009) 1385-1398. https://doi.org/10.1590/S0103-50532009000800002
[5] H. Maleki, A. T. Portugal, L. Durães, *Journal of Non-Crystalline Solids* **385** (2014) 55-74. http://dx.doi.org/10.1016/j.jnoncrysol.2013.10.017

[6] R. F. Silva, W. L. Vasconcelos, *Materials Research* **2(3)** (1999) 197-200. https://doi.org/10.1590/S1516-14391999000300014
[7] A. Mehdinia, S. Shegeftib F. Shemirani, *Journal of the Brazilian Chemical Society* **26(11)** (2015) 249-2257. https://doi.org/10.5935/0103-5053.20150211
[8] M. G. Vieira, G. Souza, G. H. B. Aristides, L. V. Lopes, A. M. Lazarin, *International Journal of Sensors and Sensor Networks* **5(2)** (2017) 27-33. https://doi.org/10.11648/j.ijssn.20170502.12
[9] [9] M. Parra, S. Stahl, H. Hellmann, *Cells* **7(7)** (2018) 84. https://doi.org/10.3390/cells707-0084
[10] A. Mobed, M. Hasanzadeh, A. Ahmadalipour, A. Fakhari, *Analytical Methods* **12(4)** (2020) 557-575. https://doi.org/10.1039/C9AY02390A
[11] C. A. Martínez-Huitle, M. Cerro-Lopez, M. A. Quiroz, *Materials Research* **12(4)** (2009) 375-384. https://doi.org/10.1590/S1516-14392009000400002
[12] A. P. Filippov, *Theoretical and Experimental Chemistry* **19** (1984) 427-433. https://doi.org/10.1007/bf00518093
[13] A. M. Lazarin, B. B. Cazula, *Materials Chemistry and Physics* **186(15)** (2017) 470-477. https://doi.org/10.1016/j.matchemphys.2016.11.021
[14] R. Golbedaghi, F. Khajavi, *Bulletin of the Chemical Society of Ethiopia* **28(1)** (2014) 1-8. https://doi.org/10.4314/bcse.v28i1.1
[15] A. Madejová, P. Komadel, *Clays and Clay Minerals* **49** (2001) 410-432. https://doi.org/-10.1346/CCMN.2001.0490508
[16] A. J. Bard, L. R. Faulkner, *Electrochemical Methods, Fundamentals and Applications*, Wiley & Sons, New York, 1980, 218.
[17] L. B. Panice, E. A. Oliveira, R. A. D. Molin Filho, D. P. Oliveira, A. M. Lazarin, E. I. S. Andreotti, R. L. Sernaglia, Y. Gushikem, *Materials Science and Engineering B* **188** (2014) 78-83. https://doi.org/10.1016/j.mseb.2014.06.010
[18] A. R. Harris, J. Zhang, R. W. Cattrall, A. M. Bond, *Analytical Methods* **5** (2013) 3840-3852. https://doi.org/10.1039/C3AY40769A
[19] M. Cuartero, R. G. Acres, R. De Marco, E. Bakker, G. A. Crespo, *Analytical Chemistry* **88(13)** (2016) 6939-6946. https://doi.org/10.1021/acs.analchem.6b01800
[20] A. A. Hoffmann, S. L. P. Dias, E.V. Benvenutti, E. C. Lima, F. A. Pavan, J. R. Rodrigues, R. Scotti, E. S. Ribeiro, Y. Gushikem, *Journal of the Brazilian Chemical Society* **18(8)** (2007) 1462-1472. https://doi.org/10.1590/S0103-50532007000800003
[21] J.-M. Zen, J.-C. Chen, A. S. Kumar, *Tamkang Journal of Science and Engineering* **5(4)** (2002) 219-222. http://dx.doi.org/10.6180/jase.2002.5.4.03
[22] H. Yin, Y. Zhou, Q. Zhang, Q. Ma, *Electrochimica Acta* **56(6)** (2011) 2748-2753. http://dx.doi.org/10.1016/j.electacta.2010.12.060

J. Electrochem. Sci. Eng. **12(2)** (2022) 331-341; http://dx.doi.org/10.5599/jese.1237

Open Access : : ISSN 1847-9286

www.jESE-online.org

Original scientific paper

Sensitive determination of uric acid at layered zinc hydroxide-sodium dodecyl sulphate-propoxur nanocomposite

Mohamad Hafiz Ahmad Tajudin[1,2], Mohamad Syahrizal Ahmad[2,3,✉], Illyas Md Isa[2,3], Norhayati Hashim[2,3], Anwar Ul-Hamid[4], Mohamad Idris Saidin[2,3], Rahadian Zainul[5] and Suyanta M. Si[6]

[1]*Faculty of Applied Sciences, Universiti Teknologi MARA, Perak Branch, Tapah Campus, Tapah Road, 35400 Perak, Malaysia*

[2]*Department of Chemistry, Faculty of Science and Mathematics, Universiti Pendidikan Sultan Idris, 35900 Tanjong Malim, Perak, Malaysia*

[3]*Nanotechnology Research Centre, Faculty of Science and Mathematics, Universiti Pendidikan Sultan Idris, 35900 Tanjong Malim, Perak, Malaysia*

[4]*Center for Engineering Research, Research Institute, King Fahd University of Petroleum & Minerals, Dhahran 31261, Saudi Arabia*

[5]*Department of Chemistry, Faculty of Mathematics and Natural Science, Universitas Negeri Padang, West Sumatera 25171, Indonesia*

[6]*Department of Chemistry Education, Faculty of Mathematics and Natural Science, Yogyakarta State University, Indonesia*

Corresponding author: ✉ *syahrizal@fsmt.upsi.edu.my; Tel.: +60-196266485; Fax: +60-54506000*

Received: January 15, 2022; Accepted: February 15, 2022; Published: February 26, 2022

Abstract

An electrochemical chemical sensor for the determination of uric acid (UA) with high sensitivity and a wide working range was fabricated using the layered zinc hydroxide-sodium dodecyl sulphate-propoxur (LZH-SDS-PRO) nanocomposite, modified with multiwall carbon nanotubes (MWCNT). The introduction of LZH-SDS-PRO as a conducting matrix has enhanced the conductivity of MWCNT. The morphology of LZH-SDS-PRO/MWCNT was characterized by transmission electron microscopy (TEM) and scanning electron microscopy (SEM), while electrochemical behavior of UA and $K_3[Fe(CN)_6]$ at LZH-SDS-PRO/MWCNT paste electrode was studied by square wave and cyclic voltammetry, respectively. Under the optimized experimental conditions, the electrode established linear plot for UA concentrations 7.0 mol L^{-1} to 0.7 mmol L^{-1} (R^2 = 0.9920) and LOD was calculated to be 4.28 µmol L^{-1} (S/N = 3). The fabricated LZH-SDS-PRO/MWCNT electrode was successsfully applied to urine samples, exhibiting excellent stability and reproducibility, which made it worthwhile for analytical applications.

Keywords

Electrochemical sensor; pharmaceutical sensor; modified MWCNT; layered metal hydroxide; functional nanocomposite; square wave voltammetry

Introduction

2,6,8-trihydroxypurine, also known as uric acid (UA), is a fundamental electroactive molecule resulting from the metabolism of endogenous purine, which occurs inside the human body [1,2]. Biological responses such as inflammation, vasoconstriction, oxidative stress and endothelial dysfunction can be stimulated by UA. Identifying diseases such as gout, hyperuricemia, kidney stone, type-2 diabetes, renal impairment, and Lesch-Nyan syndrome can be done by quantifying the concentration level of UA in blood and urine [3,4].

Various high precision, accurate and robust methods have been developed for analytical purposes, such as chromatography, fluorescence, electrophoresis, chemiluminescence and spectrophotometry, but all these methods are energy-consuming, high-cost, time-consuming and need complex operating processes [5-11]. Since UA is highly electrochemically active compound, alternative electrochemical methods were developed and characterized by cost-effectiveness, fastness, simplicity and portability for quantitative analysis.

Different functional materials have been introduced in developing UA sensors to improve the electron transfer of UA at electrodes, such as Co(II)-based zeolitic imidazolate framework [12], platinum nanoparticles (PtNPs) [13,14], nano resin [15] and ferrocene derivative and core-shell magnetic nanoparticles [16].

Since the first discovery of carbon nanotubes (CNT) in 1991, various materials have been incorporated into them and attracted widespread attention in the field of electroanalysis [17]. The unique electrochemical properties of CNT in terms of large surface area, excellent electron transfer, fine structure and light-weight make them be good electrodes for various applications [18-20]. In recent studies, multi-walled carbon nanotubes (MWCNT) were more preferable than single-walled CNT (SWCNT) due to rapid electron transfer for different reactions and better conductivity [21]. Besides, metal layered hydroxides have also gained much attention in carbon paste electrode (CPE) fabrication, owing to their remarkable capability of anion exchange and also excellent physicochemical properties in terms of low toxicity, chemical inertness and high surface area [22]. In our previous work, abilities of layered zinc hydroxide-ferulate (LZH-F), layered zinc hydroxide-*L*-phenylalanate (LZH-LP) and layered zinc hydroxide-sodium dodecyl sulphate-isoprocarb (LZH-SDS-ISO) applied as modifiers with MWCNT were demonstrated for the determination of hydroquinone (HQ) [23], acetaminophen (PCM) [24] and dopamine (DOP) [25], respectively.

Propoxur or 2-isopropoxyphenyl-*N*-methylcarbamate, was introduced to the market in 1959 and widely used in the pest control industry. Intercalation of propoxur with layered zinc hydroxide produces a nanocomposite material that has good electron transfer ability and a large surface-to-volume ratio. It has also been reported that this material shows low toxicity, high thermal stability, biocompatibility and the potential for controlled release [26,27]. Based on the listed advantages, in this work, we are presenting for the first time LZH-SDS-PRO material as a mediator used to increase the electrocatalytic activity of the redox reaction important for the determination of UA.

Experimental

Chemicals and reagents

The uric acid stock solution was prepared by dissolving the appropriate amount of UA in 0.1 mol L^{-1} NaOH solution. Potassium acetate, chloride salts (Sigma-Aldrich, USA), paraffin oil, copper(II) sulphate, potassium nitrate, potassium iodide, phosphate buffer solution (PBS) (K_2HSO_4 and KH_2SO_4) (Merck, Germany), barium chloride, glucose, fructose, sucrose and MWCNT (Timesnano, China) were of analytical grade and used as received. Ultra-pure water was used during the work.

Apparatus

FESEM model SU8020 UHR (Hitachi, Japan) and FETEM model JEM2100F (Jeol, Japan) were used for the characterization of surface morphologies of LZH-SDS-PRO/MWCNT and MWCNT. Potentiostat/galvanostat model Ref 3000 (USA) was used for electrochemical impedance spectroscopy (EIS) measurements, while cyclic voltammetry (CV) and square wave voltammetry (SWV) were conducted using Potentiostat series-G750 (USA). Three-electrode system was used in this study, where LZH-SDS-PRO/MWCNT, a platinum wire and Ag/AgCl electrode MF-2052 (Bioanalytical syst, USA) with fiber junction, acted as the working electrode, counter electrode and reference electrode, respectively.

Preparation of LZH-SDS-PRO nanocomposite

LZH-SDS was prepared by the addition of 40 mL of 0.5 M of $Zn(NO_3)_2{\cdot}6H_2O$ and 1.0 M NaOH into a solution of 40 mL of 0.25 M SDS. The pH value was adjusted to 6.5. Then, the slurry was centrifugated and dried in an oven at 70 °C.

Intercalation of propoxur into the interlayer of LZH-SDS was done by an ion-exchange method. 0.5 g of LZH-SDS was dissociated in 0.001 M propoxur solution and kept under a magnetic stirrer for 3 hours. The slurry was then aged 24 hours in an oil bath at 70 °C. After that, the slurry was centrifuged and the white solid was dried in an oven [26].

Electrode preparation

LZH-SDS-PRO (5 mg), MWCNT (100 mg) and paraffin oil (3 drops) were mixed using mortar and pestle. The homogenized mixture was firmly packed into Teflon tubing (*i.d.* 2.0 mm and 3 cm long). To establish the electrical contact, one of the ends of the paste was connected to the copper wire, and the other end was smoothened using soft paper. The non-modified MWCNT electrode was prepared with the same method but without LZH-SDS-PRO added.

Measurement procedure

UA solutions present at desired concentrations in 0.1 mol L^{-1} PBS (pH 6.4) as the supporting electrolyte were used throughout the work to perform voltammetry unless otherwise stated. The UA solutions were deoxygenated with N_2 before measurements for about 15 minutes. SWV experiments of UA determination were performed between 100 mV to 500 mV, with a frequency of 150 Hz, pulse height of 60.0 mV and step increment of 6.0 mV. CVs taken between -300 to 800 mV at the scan rate of 100 mV s^{-1} were applied for electrochemical characterization of the fabricated electrode with $K_3[Fe(CN)_6]$ as a redox probe. For EIS measurements, the frequency range of 10 kHz to 0.1 Hz and amplitude of the alternating voltage of 5.0 mV were used. All experiments were conducted at the ambient temperature of 25 ± 1 ^oC.

Results and discussion

Surface morphology

The SEM image of LZH-SDS-PRO shown in Figure 1, resembles nanoflower-like particles with a thickness of approximately 1.5 – 3.0 µm. To confirm the formation of LZH-SDS-PRO nanocomposite, EDS analysis was carried out. Different areas were focused during the EDS measurement and the conforming peaks were observed. The LZH-SDS-PRO can be seen in the synthesized composite nanostructure in the EDS spectrum. In the spectrum A, the quantity of C, Zn and O (measured in wt.%) were 40.1, 29.4 and 22.6, respectively, while in spectrum B, the values were 50.3, 29.5 and 17.0 % for C, Zn and O, respectively.

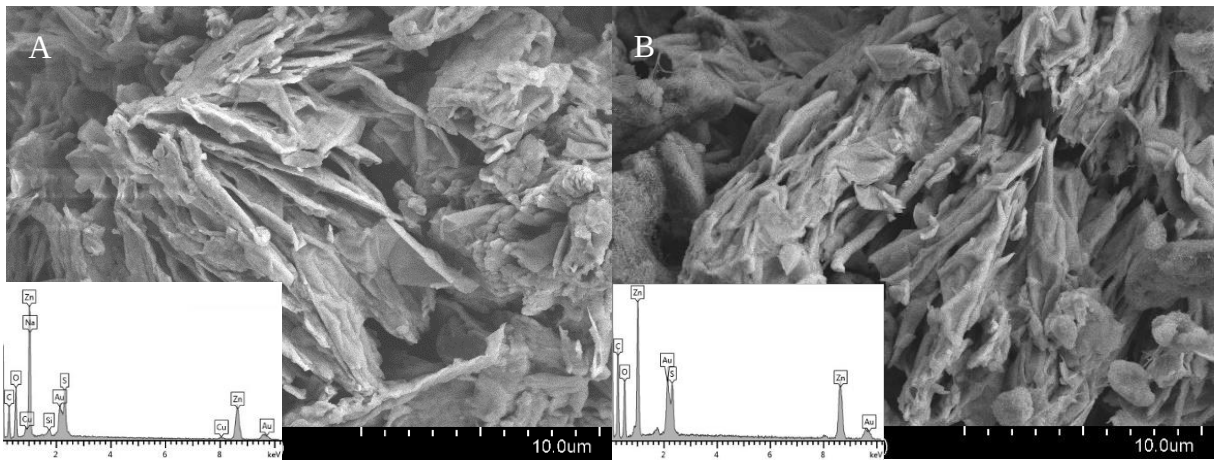

***Figure 1**. SEM image and EDS spectrum of (A) LZH-SDS-PRO and (B) LZH-SDS-PRO/MWCNT*

TEM analysis was performed to further investigate the morphology of the LZH-SDS-PRO composite. Figure 2 shows TEM images of the composite nanostructure at a low magnification where sharp edges and smooth surface of LZH-SDS-PRO (A) and carbon nanotubes strings (B) were observed, confirming the results from SEM images.

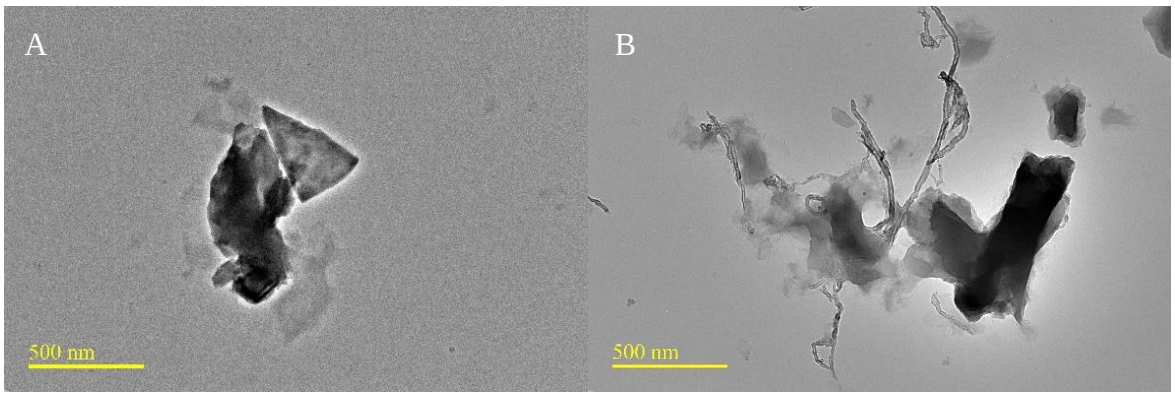

***Figure 2**. TEM image of (A) LZH-SDS-PRO and (B) LZH-SDS-PRO/MWCNT*

Electrochemical response of $K_3[Fe(CN)_6]$ at LZH-SDS-PRO/MWCNT paste electrode

Figure 3 shows CV voltammograms of 4.0 mmol L^{-1} $K_3[Fe(CN)_6]$ contained in 0.1 mol L^{-1} KCl at the LZH-SDS-PRO/MWCNT and unmodified MWCNT paste electrodes.

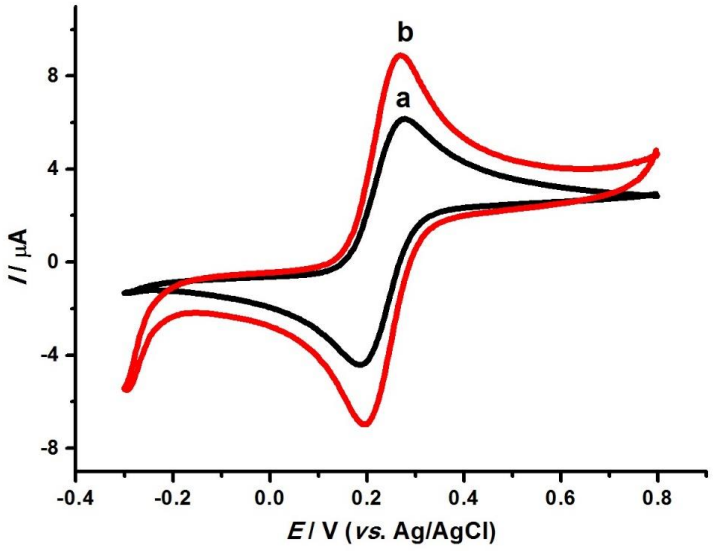

***Figure 3.** Cyclic voltammograms of (a) non-modified MWCNT and (b) LZH-SDS-PRO/MWCNT for 4.0 mmol L^{-1} $K_3[Fe(CN)_6]$ in 0.1 mol L^{-1} KCl, at scan rate 100 mV s^{-1}*

The LZH-SDS-PRO/MWCNT paste electrode showed redox peak current at I_{pa} = 8.743 µA, I_{pc} = 7.618 µA, and peak-to-peak separation (ΔE_p) = 71.6 mV. Meanwhile, redox peak current of the non-modified MWCNT paste electrode was I_{pa} = 5.854 µA, I_{pc} = 5.843 µA, and ΔE_p = 92.7 mV. It is evident from these findings that the introduction of LZH-SDS-PRO as an MWCNT modifier is responsible for improving electron transfer rate, electroactive surface area and the conductivity performance of the modified electrode.

The investigation of interfacial redox reaction kinetics of $[Fe(CN)_6]^{3-/4-}$ redox probe at LZH-SDS-PRO/ /MWCNT paste electrode was done by using the EIS method. The charge transfer resistance, R_{ct} values were estimated as diameters of semicircles appearing in high-frequency regions of Nyquist plots, where the diffusion process is represented by straight-line plots at lower frequencies [28]. In the inset of Figure 4, the Randles equivalent circuit used for fitting measured impedance spectra is presented. R_{ct} value for bare MWCNT paste electrode was 1.325 kΩ, while R_{ct} for LZH-SDS-PRO/ /MWCNT was 0.245 kΩ. It is clearly observed that LZH-SDS-PRO/MWCNT displayed lower charge transfer resistance within the interfacial layer, as suggested by more than five times smaller diameter of the semicircle.

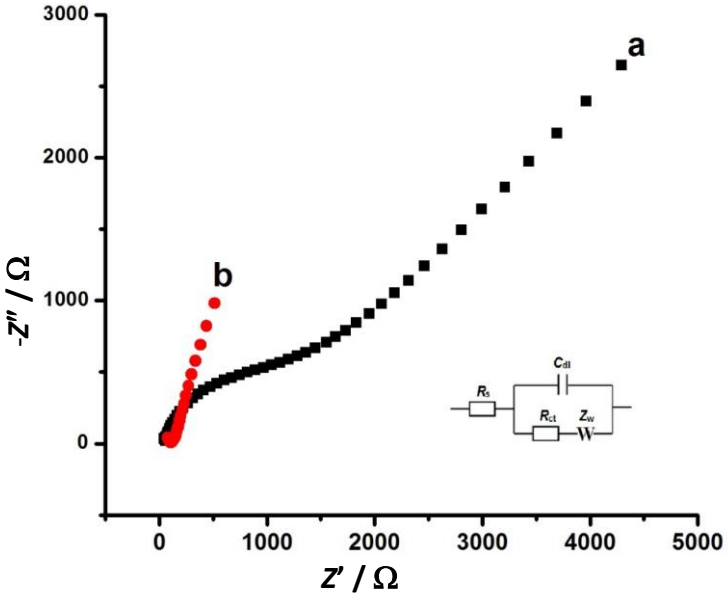

Figure 4. *Nyquist plots recorded in the solution of 4.0 mmol L^{-1} $K_3[Fe(CN)_6]$ in 0.1 mol L^{-1} KCl using (a) non-modified MWCNT, and (b) LZH-SDS-PRO/MWCNT paste electrode. Inset: Randles equivalent electrical circuit used for data fitting*

The apparent rate constant, k_{app} of the electron transfer on unmodified MWCNT and LZH-SDS--PRO/MWCNT paste electrode was 1.17×10^{-5} and 6.38×10^{-5} cm s^{-1}, respectively, which was calculated using the eq. (1):

$$k_{app} = RT/F^2 R_{ct} c \quad (1)$$

where T represents temperature, R is the gas constant, c is the concentration of $K_3[Fe(CN)_6]$ and F is Faraday's constant.

As a consequence of the high specific area and high conductivity, LZH-SDS-PRO/MWCNT electrode effectively promotes the electron transfer process.

The effect of scan rate (ν) change on the redox peak currents of 4.0 mmol L^{-1} $K_3[Fe(CN)_6]$ contained in 0.1 mol L^{-1} KCl at LZH-SDS-PRO/MWCNT paste electrode was also studied. As can be observed in Figure 5A, anodic and cathodic peak currents were progressively increased with increasing scan rate from 10 to 300 mV s^{-1}, while their E_p values shifted positively and negatively, respectively, suggesting kinetic limitation in the reaction [29]. In addition, there is also a straight-line relationship between peak current and scan rate (ν) with the linear regression equations, I_{pa} = 0.0635 ν + 3.9461 (R^2 = 0.9910) and I_{pc} = -0.0636 ν - 3.599 (R^2 = 0.9903) as shown in Figure 5B.

Besides that, the graph of peak currents versus square root of scan rate ($\nu^{1/2}$) was plotted in Figure 5C, showing a good linear relationship with the following linear equations: I_{pa} = 1.2679 $\nu^{1/2}$ - 1.1281 and I_{pc} = -1.2566 $\nu^{1/2}$ + 1.394. The correlation coefficients obtained were 0.9913 and 0.9927, respecttively. These results revealed that the redox reaction of $K_3[Fe(CN)_6]$ on LZH-SDS-PRO/MWCNT paste electrode is reversible, *i.e.* diffusion-controlled [30].

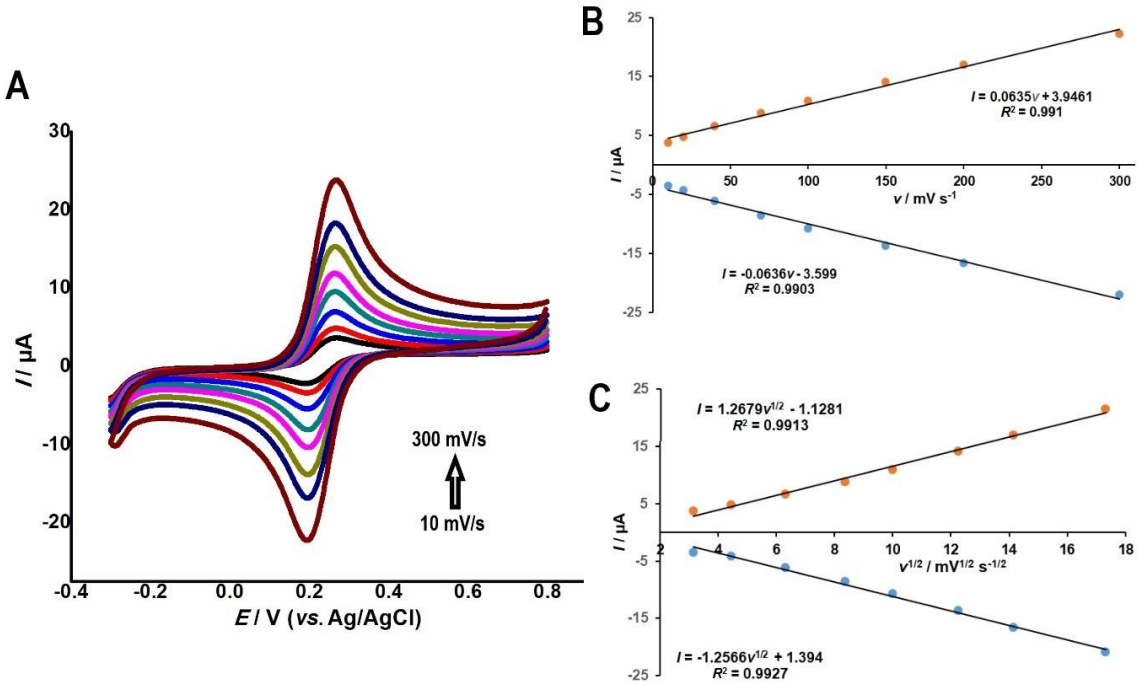

Figure 5. *(A) Cyclic voltammograms in the solution of 4.0 mmol L^{-1} $K_3[Fe(CN)_6]$ in 0.1 mol L^{-1} KCl at scan rates of 10, 20, 40, 70, 100, 150, 200 and 300 mV s^{-1}; (B) plot of peak currents versus scan rate; (C) plot of peak currents versus square root of scan rate*

Electrochemistry of UA on LZH-SDS-PRO/MWCNT paste electrode

The square wave voltammetry (SWV) measurements were carried out to compare electroanalytical performance of the non-modified MWCNT and LZH-SDS-PRO/MWCNT paste electrodes. As illustrated in Figure 6, the peak current of UA oxidation at the non-modified MWCNT is observed at 5.613 µA.

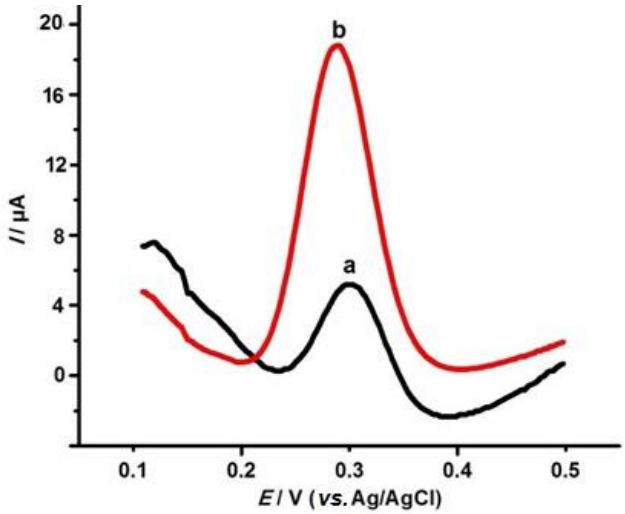

Figure 6. *SW Voltammograms in the solution of 0.1 mmol L^{-1} UA in 0.1 mol L^{-1} PBS at pH 6.4 using: (a) non-modified MWCNT and (b) LZH-SDS-PRO/MWCNT*

The oxidation peak current of LZH-SDS-PRO/MWCNT, however, is dramatically improved by the factor of 3 to 18.16 µA. Except for the effect of increased surface area, this might be due to the excellent electrical conductivity of LZH-SDS-PRO/MWCNT that can act as an effective electrons promoter during the electrochemical reaction. Hence, the addition of LZH-SDS-PRO into MWCNT has enhanced the electrode performance for the detection of UA.

Scheme 1 illustrates the proposed mechanism for the oxidation reaction of UA at the LZH-SDS--PRO/MWCNT paste electrode. By UA oxidation, imine alcohol is produced from UA by donating two protons and electrons, while two moles of propoxur at the electrode surface accept those protons and electrons to produce *o*-isopropoxyphenol [31,32].

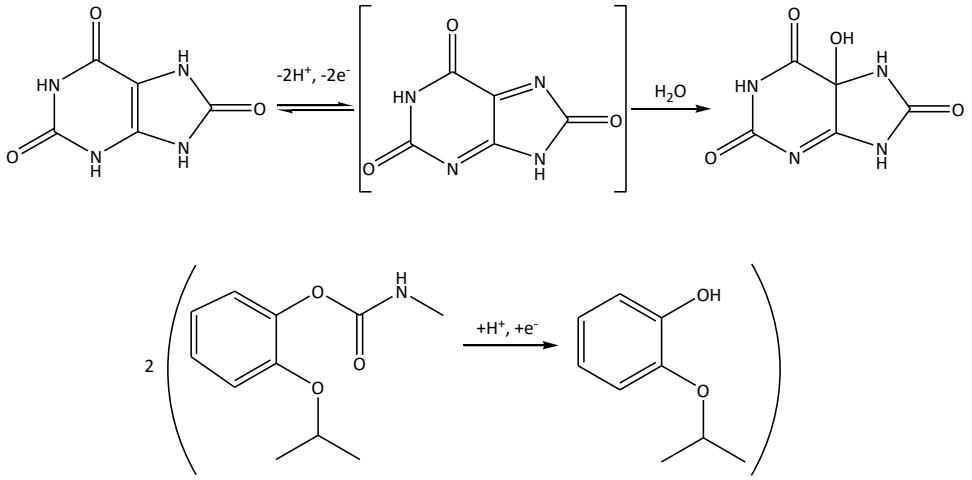

Scheme 1. *Probable mechanism of oxidation reaction of UA at LZH-SDS-PRO/MWCNT paste electrode*

The effect of pH

Figure 7 shows how pH values between 6.0 and 8.0 of 0.1 mol L^{-1} PBS affect the oxidation peak currents of 0.1 mmol L^{-1} UA at LZH-SDS-PRO/MWCNT paste electrode since PBS was optimized at the pH scale of 6.2 to 8.0 [33]. The oxidation peak current of UA increased with increasing the pH value from 6.0, reached a maximum point at pH 6.4, and then decreased with further pH increasing. Therefore, throughout the work for UA determination, the optimum pH was set at 6.4. It is clearly seen from Figure 7 that the peak potential shifted negatively with pH increase, proving thus the involvement of protons in the oxidation of UA.

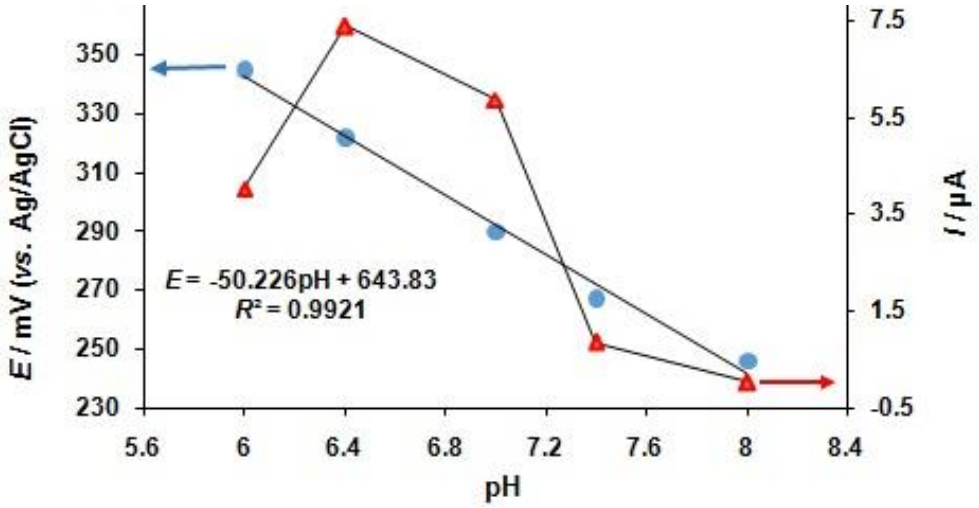

Figure 7. *Plot of oxidation peak current (I) and oxidation potential (E) vs. pH of 0.1 mol L^{-1} PBS containing 0.1 mmol L^{-1} UA at LZH-SDS-PRO/MWCNT paste electrode*

The relationship between pH and peak potential (E) of UA can be expressed as: E = -50.226 pH + + 643.83 (R^2 = 0.9921), suggesting the equal number of electrons and protons involved in the electrochemical oxidation of UA at LZH-SDS-PRO/MWCNT. This conclusion is based on the obtained slope of 50.226 mV pH^{-1}, close to the Nernst value of 59 mV pH^{-1} [34].

Calibration curve and limit of detection

In order to study the relationship between the concentration of UA and oxidation peak current (I) on the LZH-SDS-PRO/MWCNT paste electrode, a series of UA solutions was prepared, containing 7.0 µmol L^{-1} to 0.7 mmol L^{-1}. As shown in Figure 8A, I increased linearly as UA concentrations were increased. The plot of I *vs*. [UA] showed a linear relationship with the following linear regression equation: I = 0.058 c_{UA} – 1.417 (R^2 = 0.9920) and the limit of detection (LOD) was found to be 4.28 µmol L^{-1}. LOD was determined using eq. (2):

$$LOD = 3\sigma / m \quad (2)$$

where m = slope of the calibration curve and σ = relative standard deviation of its intercept.

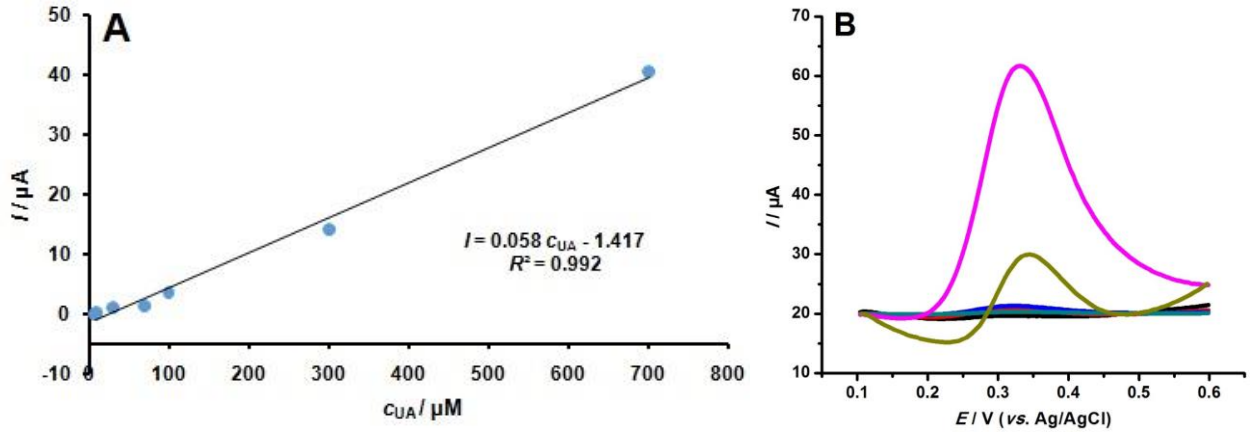

Figure 8. *(A) Linear plot of I vs. c_{UA} and (B) SWVs at different concentrations (7, 10, 30, 70, 100, 300 and 700 µM) of UA in 0.1 mol L^{-1} PBS (pH 6.4)*

The high sensitivity of the LZH-SDS-PRO/MWCNT paste electrode compared to those obtained for several other electrodes by different electroanalytical methods is presented in Table 1. The obtained results proved that the suggested sensor can be used for the determination of UA in environmental and even biological analytes.

Table 1. *Comparison of analytical properties of different fabricated electrodes for the determination of UA*

Electrode materials	Method	Linear range of concentration, µmol L^{-1}	LOD, µmol L^{-1}	Ref.
DMF / SPCE	DPV	100.0 – 500.0	0.19	[35]
Poly(Isoniazid) / CPE	CV	10.0 – 1000.0	1.173	[36]
PEDOT / GCE	CV	6.0 – 100.0	7.0	[37]
MWCNT-PEDOT / GCE	DPV	10.0 – 250.0	10.0	[38]
GF / $NiCo_2O_4$	SWV	10.0 – 26.0	0.2	[39]
MWCNT / GCE	SWV	10.0 – 200.0	1.0	[40]
LZH-SDS-PRO / MWCNT / CPE	SWV	7.0 – 700.0	4.28	This work

Selectivity, stability, reproducibility and repeatability of LZH-SDS-PRO/MWCNT paste electrode

The selectivity of the LZH-SDS-PRO/MWCNT paste electrode was tested by evaluating differrences in the oxidation peak current value of 0.1 mmol L^{-1} UA in 0.1 mol L^{-1} PBS (pH 6.4) in the presence of possible coexisting interfering species such as *D*-glucose, *L*-fructose, and Na^+, Mg^{2+}, Ca^{2+}, Cl^-, SO_4^{2-}

and NO_3^- ions. As illustrated in Figure 9, LZH-SDS-PRO/MWCNT paste electrode has the anti-interference ability in the presence of 10- and 50- fold higher concentrations of interfering species with the relative error of less than ± 10 %.

The stability of the fabricated paste electrode was recorded towards 0.1 mmol L^{-1} UA in 0.1 mol L^{-1} PBS (pH 6.4) within 14 days and the results were retained about 90 % from the initial response, indicating high stability of electrode over a long period.

The reproducibility of the fabricated paste electrode was conducted using five individual electrodes prepared by the same procedure. The relative standard deviation (RSD) of these electrodes was 3.19 %. Moreover, the RSD value of 4.73 % obtained after 10 successive measurements with similarly fabricated electrodes suggested that LZH-SDS-PRO/MWCNT paste electrode can be used repeatedly for the determination of UA.

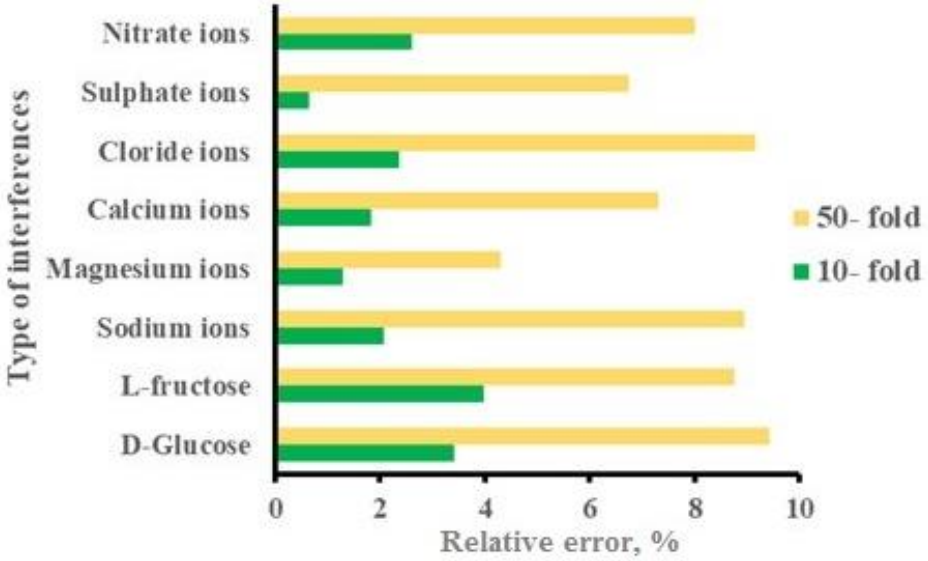

Figure 9. *Interference analysis of 0.1 mmol L^{-1} UA at LZH-SDS-PRO/MWCNT paste electrode*

Real samples analysis

The validity of the results obtained using the LZH-SDS-PRO/MWCNT paste electrode was studied by determining the concentration of UA in the urine sample *via the* standard addition method. The urine sample was directly diluted 30 times in 0.1 mol L^{-1} PBS (pH 6.4) without pre-treatment. Then, known concentrations of UA were spiked into the urine sample to study electrode recoveries. As a result, LZH-SDS-PRO/MWCNT paste electrode exhibited good recoveries, as summarized in Table 2.

Table 2. *Determination of UA in urine sample using LZH-SDS-PRO/MWCNT paste electrode (n = 3)*

Sample	c_{UA} / µmol L^{-1}			Recovery, %	RSD, %
	Determined	Spiked	Found		
Urine	140.3	100	243.8	101.5	3.81
		200	337.3	99.1	2.94
		300	445.7	101.2	3.72

Conclusions

In this experiment, a simple, highly sensitive, and cost-effective sensing material was proposed for the determination of UA with low LOD. These beneficial sensing electrode properties were realized through a combination of unique properties of LZH-SDS-PRO nanomaterial and MWCNT.

The prepared nanocomposite electrode exhibited significant electrocatalytic activity toward UA oxidation with satisfactory results of selectivity, stability and reproducibility, suggesting that LZH-SDS-PRO/MWCNT paste electrode is an attractive candidate for practical applications.

Acknowledment: *The authors would like to extend their gratitude to the Research Management and Innovation Centre (RMIC), Sultan Idris Education University (UPSI) for the University Research Grants (GPU-F: 2019-0218-103-01) that helped fund the research.*

References

[1] Y. V. M. Reddy, B. Sravani, S. Agarwal, V. K. Gupta, G. Madhavi, *Journal of Electroanalytical Chemistry* **820** (2018) 168-175. https://doi.org/10.1016/j.jelechem.2018.04.059
[2] L. Carvalho, J. Lopes, G. H. Kaihami, R. P. Silva, A. Brunicardoso, R. L. Baldini, F. C. Meotti, *Redox Biology* **16** (2018) 179-188. https://doi.org/10.1016/j.redox.2018.02.020
[3] L. Rana, R. Gupta, M. Tomar, V. Gupta, *Sensors and Actuators B* **261** (2018) 169-177. https://doi.org/10.1016/j.snb.2018.01.122
[4] J. Jiang, X. Du, *Nanoscale* **6** (2014) 11303-11309. https://doi.org/10.1039/C4NR01774A
[5] R. Ahmad, N. Tripathy, M. S. Ahn, Y. B. Hahn, *Scientific Reports* **7** (2017) 46475. https://doi.org/10.1038/srep46475
[6] L. Zhao, J. Blackburn, C. L. Brosseau, *Analytical Chemistry* **87** (2015) 441-447. https://doi.org/10.1021/ac503967s
[7] J. Wang, M. P. Chatrathi, B. Tian, R. Polsky, *Analytical Chemistry* **72** (2000) 2514-2518. https://doi.org/10.1021/ac991489l
[8] R. Sakuma, T. Nishina, M. Kitamura, *Clinical Chemistry* **33** (1987) 1427-1430. https://doi.org/10.1093/clinchem/33.8.1427
[9] M. Czauderna, J. Kowalczyk, *Journal of Chromatography B: Biomedical Sciences and Applications* **744** (2000) 129-138. https://doi.org/10.1016/S0378-4347(00)00239-5
[10] J. Yu, S. Wang, L. Ge, S. Ge, *Biosensensors and Bioelectronics* **26** (2011) 3284-3289. https://doi.org/10.1016/j.bios.2010.12.044
[11] J. C. Fanguy, C. S. Henry, *Electrophoresis* **23** (2002) 767-773. https://doi.org/10.1002/1522-2683(200203)23:5%3C767::AID-ELPS767%3E3.0.CO;2-8
[12] J. Tang, S. Jiang, Y. Liu, S. Zheng, L. Bai, J. Guo, J. Wang, *Microchimica Acta* **185** (2018) 486. https://doi.org/10.1007/s00604-018-3025-x
[13] B. Han, M. Pan, X. Liu, J. Liu, T. Cui, Q. Chen, *Materials (Basel)* **12** (2019) 214. https://doi.org/10.3390/ma12020214
[14] B. Demirkan, S. Bozkurt, A. Şavk, K. Cellat, F. Gulbagca, M. S. Nas, M. H. Alma, H. Sen, *Scientific Reports* **9** (2019) 12258. https://doi.org/10.1038/s41598-019-48802-0
[15] H. Rajabi, M. Noroozifar, N. Sabbaghi, *Journal of Materials & Applied Science* **1(1)** (2017) 1002. https://www.jscimedcentral.com/Materials/Articles/materials-1-1002.pdf
[16] S. Z. Mohammadi, H. Beitollahi, Z. Dehghan, R. Hosseinzadeh, *Applied Organometallic Chemistry* **32** (2018) e4551. https://doi.org/10.1002/aoc.4551
[17] S. Iijima, *Nature* **354** (1991) 56-58. https://doi.org/10.1038/354056a0
[18] A. Cernat, M. Tertis, R. Sandulescu, F. Bedioui, A. Cristea, C. Cristea, *Analytica Chimica Acta* **886** (2015) 16-28. https://doi.org/10.1016/j.aca.2015.05.044
[19] J. H. Zagal, S. Griveau, M. Santander Nelli, S. G. Granados, F. Bedioui, *Journal of Porphyrins and Phthalocyanines* **16** (2012) 713-740. https://doi.org/10.1142/S1088424612300054
[20] S. Wang, J. Yang, X. Zhou, J. Xie, L. Ma, B. J. Huang, *Journal of Electroanalytical Chemistry* **722** (2014) 141-147. https://doi.org/10.1016/j.jelechem.2014.04.001
[21] J. Simon, E. Flahaut, M. Golzio, *Materials (Basel)* **12** (2019) 624-644. https://doi.org/10.3390/molecules25245827

[22] N. A. Azis, I. M. Isa, N. Hashim, M. S. Ahmad, S. N. A. M. Yazid, M. I. Saidin, M. S. Suyanta, R. Zainul, A. Ulianas, S. Mukdasai, *International Journal of Electrochemical Sci*ence **14** (2019) 10607-10621. https://doi.org/10.20964/2019.11.46
[23] M. S. Ahmad, I. M. Isa, N. Hashim, M. S. Rosmi, S. Mustafar, *International Journal of Electrochemical Sci*ence **13** (2018) 373-383. https://doi.org/10.20964/2018.01.31
[24] M. S. Ahmad, I. M. Isa, N. Hashim, M. S. Suyanta, M. I. Saidin, *Journal of Solid State Electrochemistry* **22** (2018) 2691-2701. https://doi.org/10.1007/s10008-018-3979-y
[25] M. S. Ahmad, I. M. Isa, N. Hashim, M. I. Saidin, M. S. Suyanta, R. Zainul, A. Ulianas, S. Mukdasai, *International Journal of Electrochemical Sci*ence **14** (2019) 9080-9091. https://doi.org/10.20964/2019.09.54
[26] Z. Muda, N. Hashim, I. M. Isa, N. M. Ali, S. A. Bakar, M. Mamat, M. Z. Hussein, N. A. Bakar, W. R. W. Mahamod, *International Fundamentum Science Symposium*, *IOP Conferece Series: Materials Science and Engineering* **440** (2018) 012003. http://dx.doi.org/10.1088/1757-899X/440/1/012003
[27] Q. Yan, N. Zhi, L. Yang, G. Xu, Q. Feng, Q. Zhang, S. Sun*, Scientific Reports* **10** (2020) 10607. https://doi.org/10.1038/s41598-020-67394-8
[28] A. Xu, Y. Weng, R. Zhao, *Materials* **13** (2020) 1179-1198. https://doi.org/10.3390/ma13051179
[29] C. O. Chikere, N. H. Faisal, P. Kong Thoo Lin, C. Fernandez, *Nanomaterials* **10** (2020) 537-562. https://doi.org/10.3390/nano10030537
[30] W. Zhang, L. Liu, Y. Li, D. Wang, H. Ma, H. Ren, Y. Shi, Y. Han, B.C. Ye, *Biosensors and Bioelectronics* **121** (2018) 96-103. https://doi.org/10.1016/j.bios.2018.08.043
[31] M. F. Simoyi, E. Falkenstein, K. V. Dyke, K. P. Blemings, H. Klandorf, Comparative Biochemistry and Physiology Part B: Biochemistry and Molecular Biology **135** (2003) 325-335. https://doi.org/10.1016/s1096-4959(03)00086-1
[32] P. Kovacic, R. Somanathan, *Propoxur: A Novel Mechanism for Insecticidal Action and Toxicity. Reviews of Environmental Contamination and Toxicology*, Springer, Boston, United State, 2012, p. 141. https://doi.org/10.1007/978-1-4614-3137-4_4
[33] Z. Hua, Q. Qin, X. Bai, C. Wang, X. Huang, *Sensors and Actuators B* **220** (2015) 1169-1177. https://doi.org/10.1016/j.snb.2015.06.108
[34] J. Ning, Q. He, X. Luo, M. Wang, D. Liu, J. Wang, G. Li, J. Liu, *Catalysts* **8** (2018) 407. https://doi.org/10.3390/catal8100407
[35] M. Metto, S. Eramias, B. Gelagay, A. P. Washe, *International Journal of Electrochemistry* **2019** (2019) 1-8. https://doi.org/10.1155/2019/6318515
[36] M. P. Deepak, G. P. Mamatha, B. S. Sherigara, *International Journal of Pharmaceutical Chemistry* **4** (2014) 122-129. **ISSN:** 2249-734X
[37] M. Motshakeri, J. Travas Sejdic, A. R. J. Phillips, P. A. Kilmartin, *Electrochimica Acta* **265** (2018) 184-193. https://doi.org/10.1016/j.electacta.2018.01.147
[38] K. C. Lin, T. H. Tsai, S. M. Chen, *Biosensors and Bioelectronics* **26** (2010) 608-614. https://doi.org/10.1016/j.bios.2010.07.019
[39] Y. Peng, D. Zhang, C. Zhang, *Analytical Methods* **6** (2014) 8965-8972. https://doi.org/10.1039/C4AY01029A
[40] H. Q. Bi, Y. H. Li, S. F. Liu, P. Z. Guo, Z. B. Wei, C. X. Lv, J. Z. Zhang, X. S. Zhao, *Sensors and Actuators B* **171** (2012) 1132-1140. https://doi.org/10.1016/j.snb.2012.06.044

J. Electrochem. Sci. Eng. **12(2)** (2022) 343-358; http://dx.doi.org/10.5599/jese.1126

Open Access : : ISSN 1847-9286

www.jESE-online.org

Original scientific paper

Organic and inorganic compounds as corrosion inhibitors to reduce galvanic effect for the hybrid structure AA2024-CFPR

Roy Lopez-Sesenes[1,✉], Jose Gonzalo Gonzalez-Rodriguez[2], José Gerardo Vera-Dimas[1], Rene Guardian-Tapia[2] and Luis Cisneros-Villalobos[1]

[1]*Universidad Autónoma del Estado de Morelos, Facultad de Ciencias Químicas e Ingeniería, Av. Universidad 1001 Col. Chamilpa,CP. 62209, Cuernavaca Morelos, México*

[2]*Universidad Autónoma del Estado de Morelos, CIICAp, Av. Universidad 1001 Col. Chamilpa,CP. 62209, Cuernavaca Morelos, México*

Corresponding author: ✉rlopez@uaem.mx

Received: September 29, 2021; Accepted: October 30, 2021; Published: November 13, 2021

Abstract

The effect of the galvanic corrosion process taking place between aluminium alloy (AA2024--T3) and carbon fiber reinforced plastic (CFRP) immersed in 0.05 M NaCl was studied using organic and inorganic compounds as corrosion inhibitors. Electrochemical approaches such as electrochemical noise analysis (ENA) and electrochemical impedance spectroscopy (EIS) were carried out to evaluate efficiencies of 1,2,4-triazole ($C_2H_3N_3$) and cerium nitrate hexahydrate ($Ce(NO_3)_3{\cdot}6H_2O$) as corrosion inhibitors. The highest efficiency was reached for $Ce(NO_3)_3$ $6H_2O$, with some improvement observed by adding $C_2H_3N_3$ in a mixed inhibitor solution. The noise resistance (R_n) and polarization resistance (R_p) values calculated from ENA and EIS data showed almost identical behavior with different magnitudes but similar trends. Adsorption isotherm models estimated with fractional surface coverage (θ) parameter were fitted better to Langmuir model for $C_2H_3N_3$ and Temkin model for $Ce(NO_3)_3{\cdot}6H_2O$. The calculated values of Gibbs free energy suggested physisorption and chemisorption as spontaneous interactions between a metal surface and both inhibitors. Energy-dispersive X-ray spectroscopy (EDS) was carried out before and after immersing AA2024-T3 in the electrolyte, identifying rich zones in copper with cerium deposited over it and confirming the presence of rare-earth oxide deposition and oxide film products. The EDS analysis for CFRP revealed the deposition of Ce and Al particles over its surface after immersion in the electrolyte, especially in the areas rich in carbon.

Keywords

Electrochemical methods, rare earths, adsorption isotherm, Gibbs free energy, synergistic effect, power spectral density

Introduction

Hybrid structures have received great interest from the aerospace industry, especially in cases where a single material can not satisfy structural demands [1]. Materials with a high strength-to-density ratio, such as carbon fiber reinforced plastic (CFRP) and aluminum alloys, are promising candidates for modern aircraft structures since when both are combined, the mechanical properties of a material are improved [2].

Nevertheless, aluminum alloys such as AA2024-T3 in contact with other nobler materials (CFRP) tend to accelerate their electrochemically-driven degradation since they are more active in the galvanic series, showing an anodic behavior [3, 4]. For example, when CFRP is coupled to AA2024-T3 in NaCl solution, the structural integrity of this last material is compromised since CFRP has an open circuit potential (OCP) around +0.28 mV (nobler) [5] than AA2024-T3 having OCP around -500 mV (more active) [6]. Furthermore, AA2024-T3 contains impurities that stimulate the formation of galvanic microcells between the matrix and its intermetallic phases, thus increasing its susceptibility to the degradation processes [7].

A lot of efforts have been focused on analyzing mechanical properties of the hybrid structure AA2024-T3-CFRP, such as tensile and compressive properties, shear strength and damping behavior, and on establishing conditions under which this hybrid material could work without risk of damage during its operating life [8-10]. Based on the latter, Payan *et al*. did some experiments to find an adequate method for the analysis of the corrosion mechanism of aluminum matrix composite reinforced with graphite fibers, giving quantitative information on the morphology and kinetics of corrosion [11]. Sherif *et al*. investigated different aluminum-graphite composites, showing the graphite concentration effect in the matrix, and observing an increment in the corrosion rate with reduction of the polarization resistance [12].

It is certainly important to find a way to reduce the effect of the corrosion process that is taking place in these hybrid materials, with the aim to reduce the damage caused by the oxidetion/reduction process. An effective way to resolve it is the utilization of corrosion inhibitors. So far, only a few studies have focused on using inhibitors or their combination for corrosion protection of AA2024-CFRP hybrid structure. Wang *et al.* have studied the galvanic corrosion resistance of carbon fiber metal laminates (CARALL) with AA2024-T3 and CFRP and proposed a surface treatment technique combining anodizing in sulfuric acid to prevent galvanic corrosion [13]. These authors also showed that the corrosion rate decreased in the presence of the coating over the surface.

The goal of the present work was to reduce the effect of the galvanic corrosion process present in the hybrid structure AA2024-T3-CFRP with corrosion inhibitors. A systematic study of organic and inorganic inhibitors was conducted using a set of complementary electrochemical analyses.

Experimental

Materials and chemicals

The nominal composition of AA2024-T3 alloy is listed in Table 1. Several samples were cut to platelets with an exposed area of 2 cm^2 with 0.2 cm thickness. Platelets were ground with emery cloth of 300, 600 and 1000 grit size, degreased with ethanol, washed with distilled water, and dried with dry air. The carbon fiber composite was obtained from a fully cured carbon fiber composite sheet of 0.2 cm thickness. Samples with a nominal area of 2 cm^2 were cut. The carbon fiber composite specimen was prepared to expose one individual region, removing impurities with 320 grade emery paper to improve its conductivity.

***Table 1**. Composition of AA2024-T3 aluminum alloy*

Content, wt.%									
Cu	Cr	Fe	Mg	Mn	Si	Ti	Zn	Other	Al
3.8-4.9	0.1	0.5	1.2-1.8	0.3-0.9	0.5	0.15	0.25	0.15	Balance

Distilled water with a resistivity of 18 MΩ cm was used for rinsing and solution preparation. The test solution was naturally aerated at 25 °C. All electrochemical tests were done in 0.05 M NaCl with stirring at room temperature using a Gill AC computer-controlled potentiostat.

High-grade reagents $Ce(NO_3)_3{\cdot}6H_2O$ and $C_2H_3N_3$ received from Sigma-Aldrich with chemical structures shown in Figure 1 were used as corrosion inhibitors at three concentrations (0.5, 2 and 10 mM) with the aim to observe their protective efficiency against the corrosion process at the metal surface.

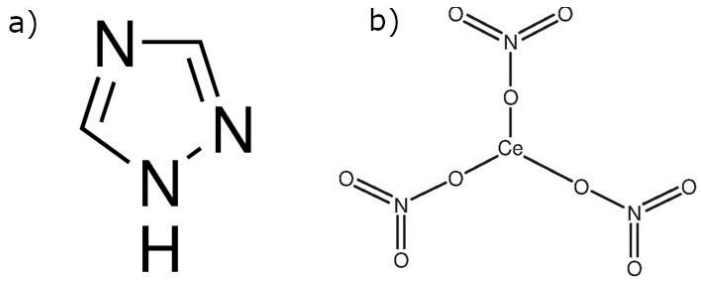

***Figure 1.** Chemical structures of compounds used as corrosion inhibitors: a) $C_2H_3N_3$ and b) $Ce(NO_3)_3{\cdot}6H_2O$*

Electrochemical techniques

Electrochemical noise analysis (ENA)

ENA technique was carried out recording 1024 points per second each hour for 24 h. Data were recorded simultaneously using a silver-silver chloride (Ag/AgCl) reference electrode (RE) and AA204-T3 and CFRP in the galvanic couple as working electrode one (WE_1) and working electrode two (WE_2), respectively. The exposed area of each WE was 0.5 cm^2. The galvanic couple was closed by a switch before each test, connected *via* a zero-resistance ammeter (ZRA).

Electrochemical impedance spectroscopy (EIS)

EIS measurements were conducted in a conventional cell of three electrodes, in the following arrangement: Ag/AgCl electrode was used as RE, a platinum wire as an auxiliary electrode (AE), and AA2024-T3 and CFRP in galvanic couple with an exposed area of 0.5 cm^2 as working electrodes (WE_1 or WE_2). EIS was performed at the open circuit potential value with a sinusoidal perturbation of 10 mV RMS (root mean square) amplitude at room temperature, in a frequency range from 30 kHz to 0.01 Hz. The electrochemical cell used for the experiment setup is shown in Figure 2.

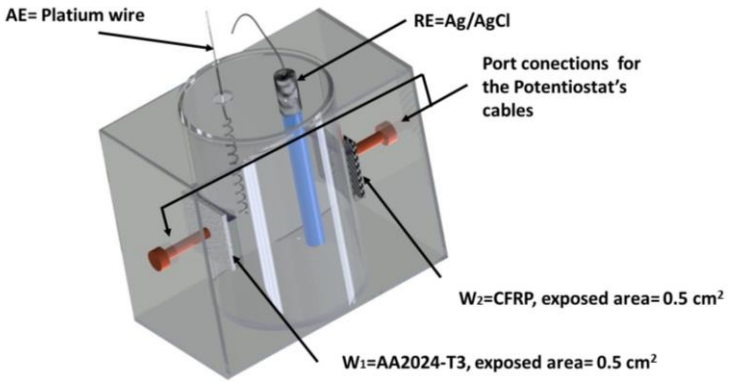

***Figure 2.** Electrochemical corrosion cell for ENA and EIS measurements*

Surface characterization of corroded surfaces

Micrographs of corroded AA2024-T3 and CFRP samples in solutions of 0.05 M NaCl with and without inhibitor, extracted after 24 h of immersion, were examined with a Tescan Vega3 SB scanning electronic microscope (SEM) with an EDX analyzer.

Results and discussion

Electrochemical noise analysis (ENA)

Inhibition effect of 1,2,4-TR.

Figure 3 and 4 shows the current and potential electrochemical noise time series recorded for AA2024-T3-CFRP galvanic couple in 0.05 M NaCl without and with different concentrations (0.5 to 10 mM) of $C_2H_3N_3$. The electrochemical current noise (ECN) and the electrochemical potential noise (EPN) plots measured after 1 h (Figure 3) showed a decrement in their fluctuations when the inhibitor was added into the solution. The single exception is seen for the concentration of 0.5 mM, which showed an increment in the current fluctuation from 10^{-5} to 5×10^{-5} mA cm^{-2}, increasing its frequency domain. The latter is attributed to the formation of a protective film on intermetallic sites, especially where there is copper contained in the sample, forming Cu-$C_2H_3N_3$. Moreover, copper reacts with Cl^- ions present in the solution to form $CuCl^-$ complexes with $C_2H_3N_3$ [14], minimizing the oxygen reduction processes at intermetallic particles. Figure 4 shows the current and potential time series recorded after 24 h, where it is evident that the test without inhibitor showed an increment in current fluctuations. For the test with 2 mM $C_2H_3N_3$ and 10 mM $C_2H_3N_3$, a diminishing in current fluctuations is appreciable. No change is evident for the test at 0.5 mM $C_2H_3N_3$.

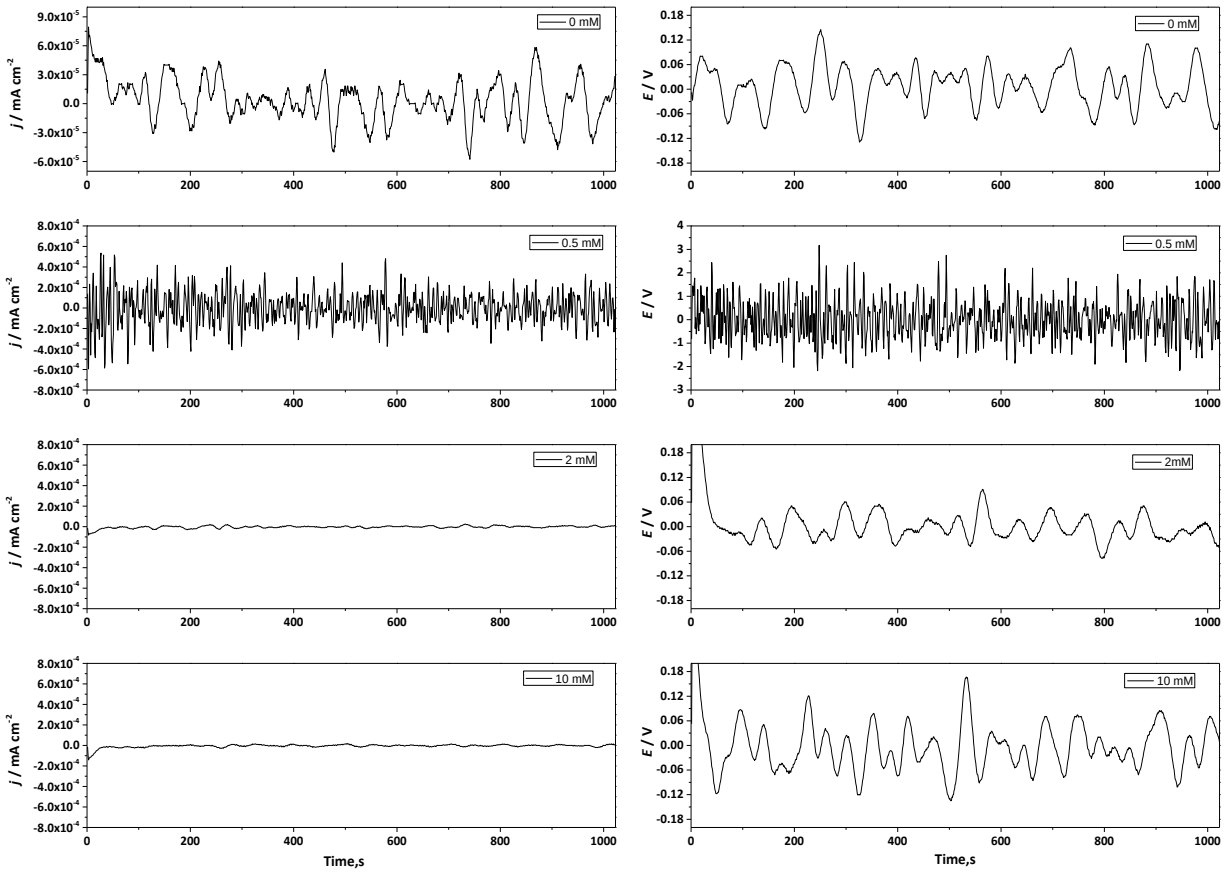

Figure 3. *Time series of ECN (left) and EPN (right) for AA2024-T3-CFRP in galvanic couple immersed in 0.05 M NaCl without and with 0.5-10 mM $C_2H_3N_3$ at the beginning of the test (1 h)*

AA2024-T3 is highly susceptible to pitting corrosion due to the existing intermetallic particles [15]. When CFRP is kept in contact with AA2024-T3, these species cause increased electrons flow between cathodic and anodic areas. Through the electrochemical noise analysis done, the noise resistance (R_n) was calculated by the ratio of standard deviations of the current and potential (σ_I/σ_P) measured after 24 h and shown in Figure 5. The highest value of R_n of 8.27 kΩ cm^2 was obtained at 10 mM of $C_2H_3N_3$ which remains almost constant until the end of the test. It is obvious that with addition and further increment of the inhibitor concentration in the solution, a decrement in the current fluctuation of the time series was recorded at the beginning of the test as shown in Figure 3, and kept almost constant until the end of the test (Figure 4). These suggest the almost constant corrosion resistance of AA2024-T3-CFPR in a galvanic couple (Figure 5).

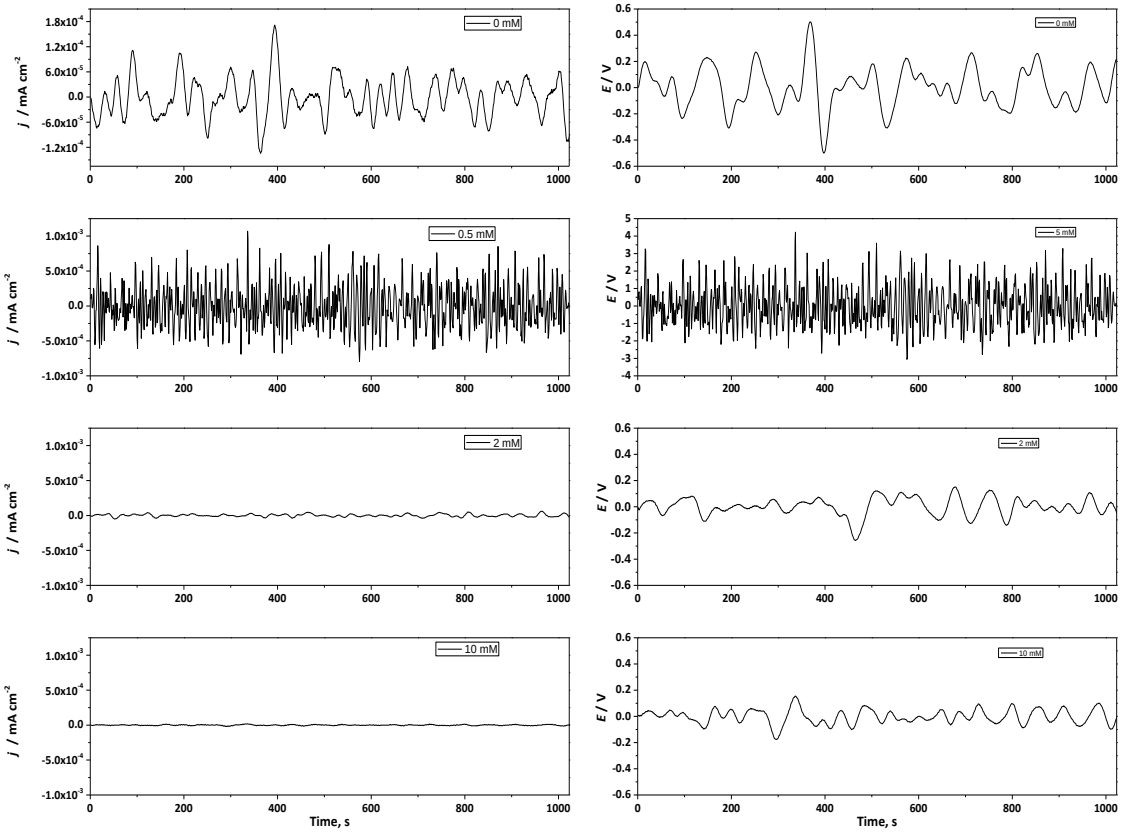

Figure 4. *Time series of ECN (left) and EPN (right) for AA2024-T3-CFRP in galvanic couple immersed in 0.05 M NaCl without and with 0.5-10 mM $C_2H_3N_3$ at the end of the test (24 h)*

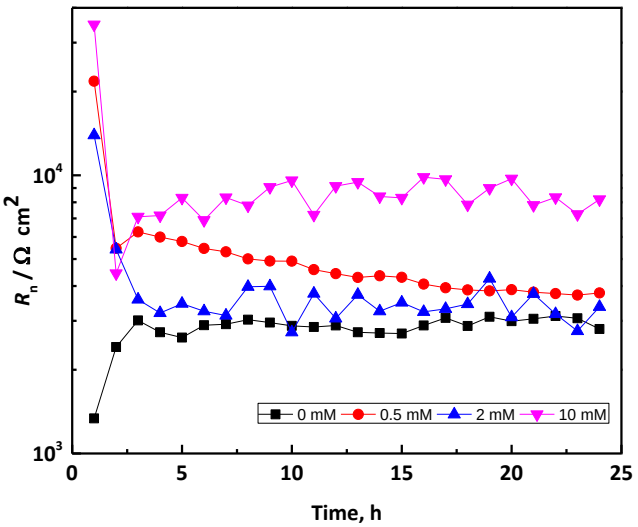

Figure 5. *Time behavior of R_n for AA2024-T3-CFRP in galvanic couple immersed in 0.05 M NaCl at different concentrations of $C_2H_3N_3$*

The single exception in Figure 5 is observed at 0.5 mM $C_2H_3N_3$, where R_n tends to decrease due to the accelerated degradation of the surface, which forms a passive film susceptible to metastable pitting.

The power spectral density (PSD) plots represent the potential and current fluctuations of ENA over time as functions of frequency, allowing to determine energy changes in the system and the stability of a passive film formed over the metal surface.

When an increment in current is observed, the mass transport increases too, and when the potential increases, corrosion over the metal surface increases also. PSD plots for AA2024-T3-CFPR with and without $C_2H_3N_3$ are shown in Figure 6. PSD plots for the current at the beginning and the end of the test (Figure 6a and 6c) did not show significant changes. At both testing times, the current density increased with the addition of 0.5 mM $C_2H_3N_3$ into the solution, which accelerates the mass transport phenomena from the bulk to the metallic surface and increases the exposed area due to the formation of porosities at the surface [16]. Moreover, PSD plots for the potential (Figure 6b and 6d) showed increments at 0.5 mM $C_2H_3N_3$, indicating rising corrosion over the metallic surface. For all the remainder concentrations, all is kept constant until the end of the test.

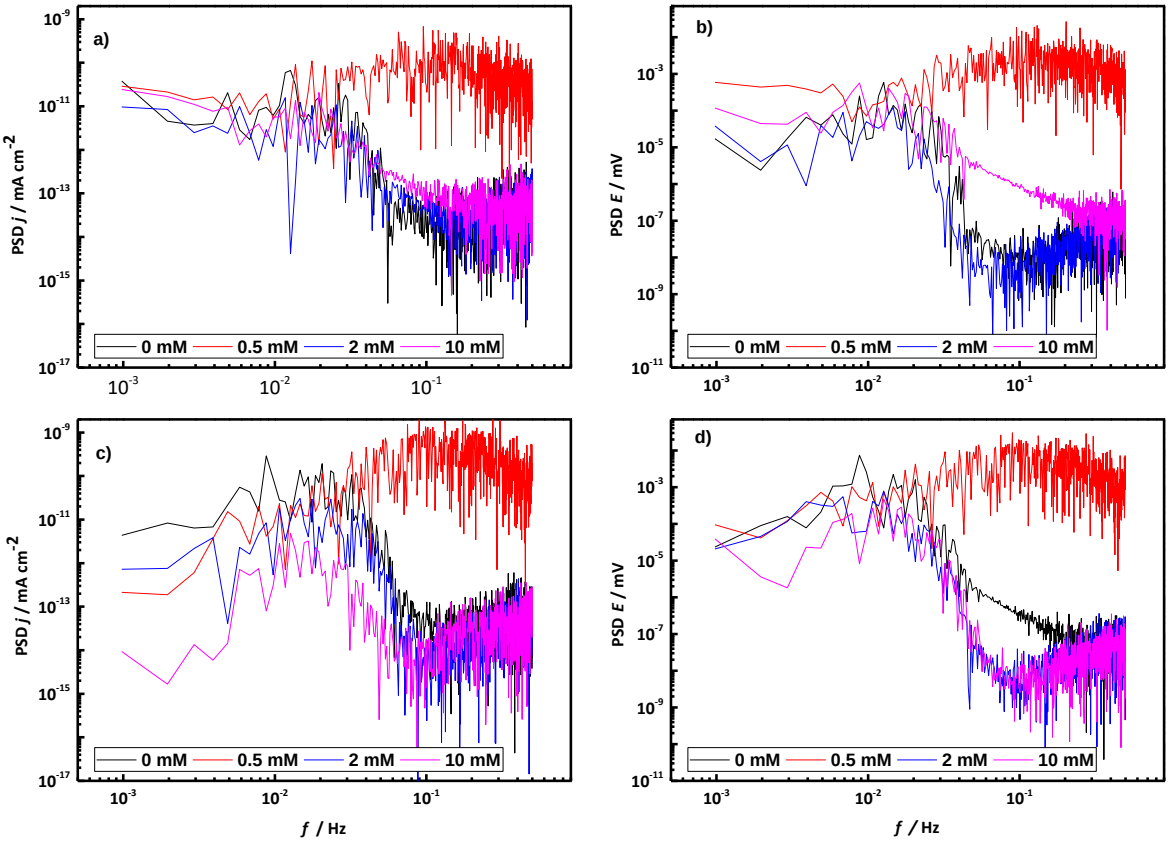

Figure 6. *PSD plots of current (left) and potential (right) for AA2024-T3-CFRP in galvanic couple immersed in 0.05 M NaCl without and with 0.5-10 mM $C_2H_3N_3$ at the beginning (a and b) and the end (c and d) of the test*

Inhibition effect of cerium nitrate

Time series of current and potential noise fluctuations for AA2024-T3-CFRP immersed in 0.05 M NaCl with and without $Ce(NO_3)_3{\cdot}6H_2O$ as corrosion inhibitor are shown in Figure 7. At the beginning of the test (1 h), the addition of $Ce(NO_3)_3{\cdot}6H_2O$ generated an increment in the current and potential fluctuations (Figure 7), accelerating the corrosion process at the metal surface, and forming a passive layer of corrosion products. At the end of the measurement (24 h), this layer promotes a magnitude decrement of current fluctuations from 10^{-4} to 10^{-6} mA/cm^2, which was lower than the test without inhibitor (Figure 8).

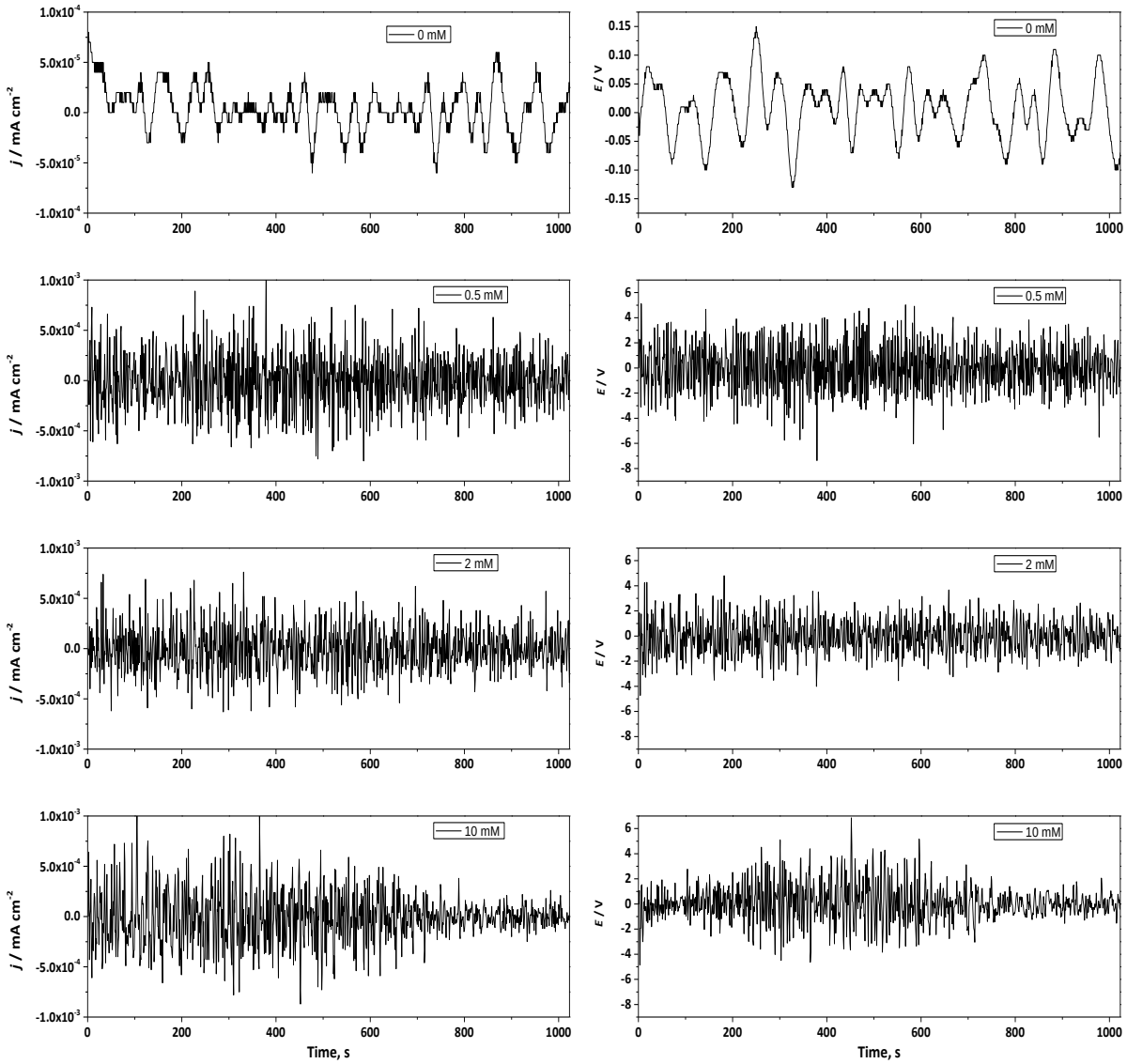

Figure 7. *Time series of ECN (left) and EPN (right) for AA2024-T3-CFRP in galvanic couple immersed in 0.05 M NaCl without and with 0.5-10 mM $Ce(NO_3)_3{\cdot}6H_2O$ at the beginning of the test (1 h)*

The potential time series showed a decrement in intensity fluctuations from the beginning to the end of the test and also sudden potential drops and recovery transients with high amplitude and high frequency, typical of localized corrosion [17]. In the presence of the inhibitor, R_n values presented in Figure 9 showed a clear trend of increase with time of exposure and significant increment with the addition of $Ce(NO_3)_3{\cdot}6H_2O$ into the solution. The highest value of R_n was obtained for 0.5 mM $Ce(NO_3)_3{\cdot}6H_2O$, reaching 29.9×10^4 Ω cm^2, which is at least one order of magnitude higher than without inhibitor (2.77 kΩ cm^2).

During the first hour, PSD for the current density showed an increment in the current density due to the mass transport phenomena (Figure 10. a), while PSD for the potential showed an increment correlated with the corrosion magnitude (Figure **10.** 10b). At the end of the test, PSD values for the current density and potential (Figure **10.** 10c and 10d) dropped slightly, suggesting improvement of the corrosion resistance of AA2024-T3-CFRP due to the formation of a passive film with high susceptibility to pitting corrosion.

Based on the fluctuations observed in Figures 3, 4, 7 and 8 for the time series for the current and potential, it was possible to determine that mixed corrosion (uniform type of corrosion combined with localized corrosion) is present over the metal surface of AA2024. The PSD for both inhibitors at the

beginning of the test had an increment in the current density and potential, the first one is due to a rise in the mass transport and the second one suggests an increment in the corrosion process.

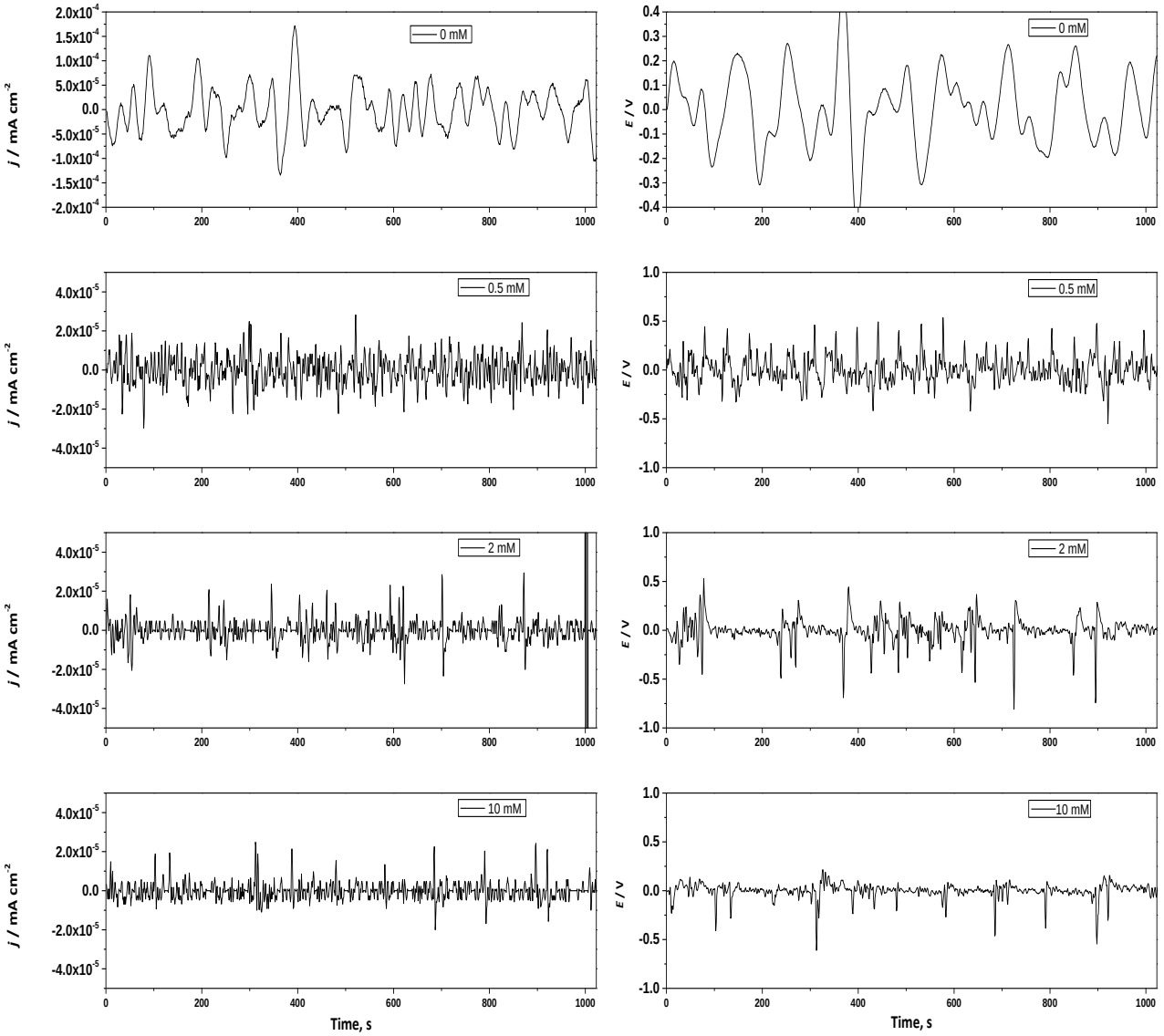

Figure 8. *Time series of ECN (left) and EPN (right) for AA2024-T3-CFRP in galvanic couple immersed in 0.05 M NaCl without and with 0.5-10 mM $Ce(NO_3)_3 \cdot 6H_2O$ at the end of the test (24 h)*

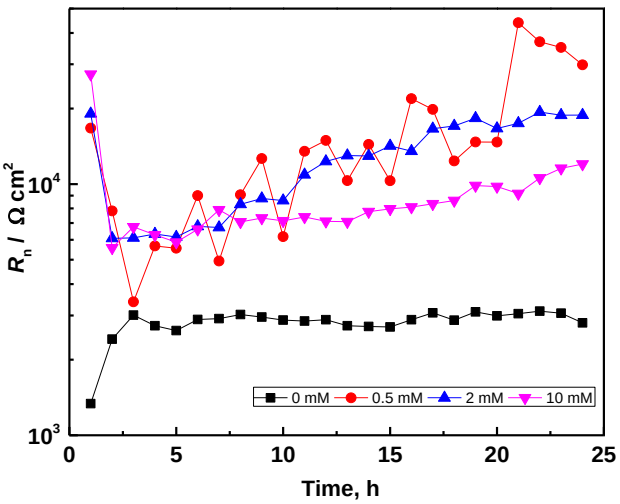

Figure 9. *Time behavior of R_n for AA2024-T3-CFRP in galvanic couple immersed in 0.05 M NaCl with different concentrations of $Ce(NO_3)_3 \cdot 6H_2O$*

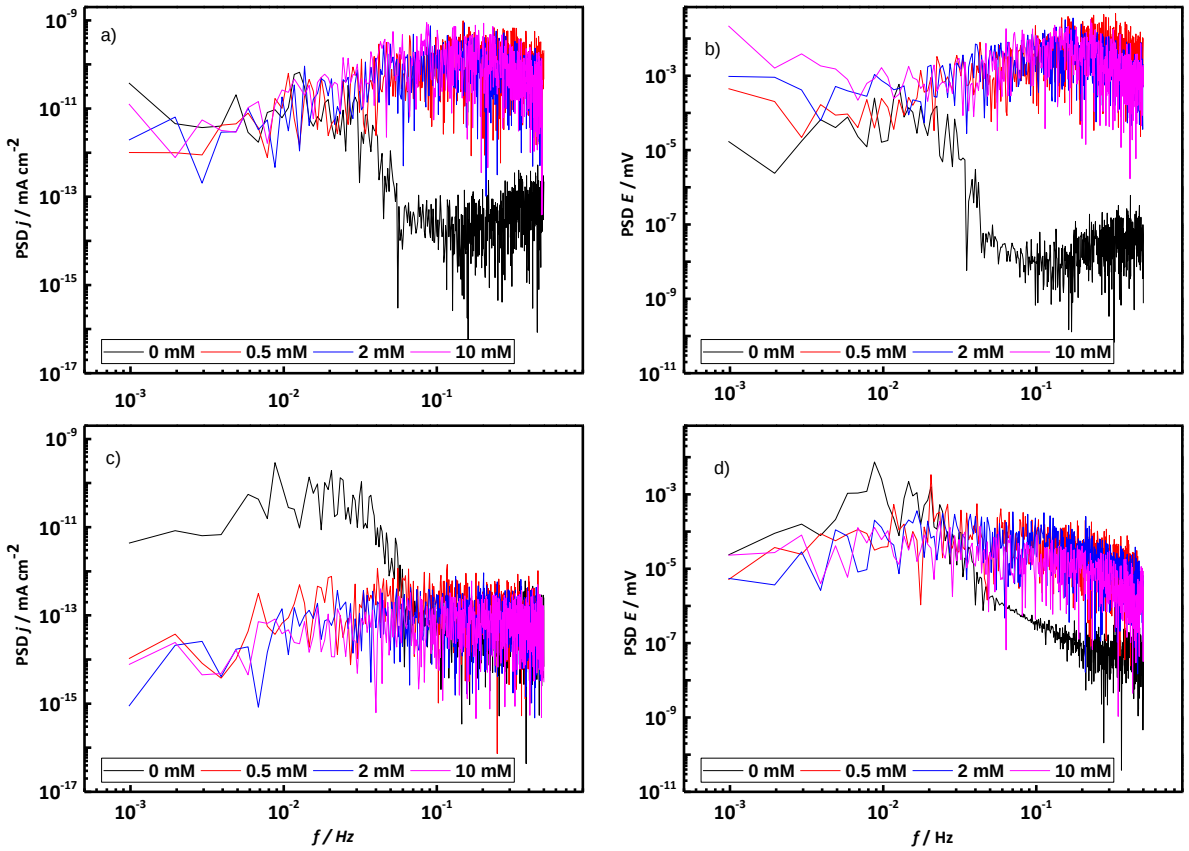

Figure 10. *PSD of current (left) and potential (right) for AA2024-CFRP in galvanic couple immersed in 0.05 M NaCl without and with 0.5-10 mM $Ce(NO_3)_3{\cdot}6H_2O$ at the beginning (a and b) and the end (c and d) of test*

EIS measurements

Figure 11. shows Nyquist and Bode's plots recorded for AA2024-T3-CFRP in galvanic couple immersed in 0.05 M NaCl with and without $C_2H_3N_3$. Nyquist plots in Figure 11a showed the formation of a depressed semicircle at high to middle frequencies for all tests, which is usually attributed to the charge transfer phenomena. In addition, from middle to low frequencies, a second semicircle was recorded for each test, except at 0.5 mM $C_2H_3N_3$, which can be associated with the corrosion process at the metal surface. For solution without inhibitor and 0.5 mM $C_2H_3N_3$, an inductive response is indicated at the lowest frequencies, usually related to intermediate adsorption/desorption and/or pitting corrosion.

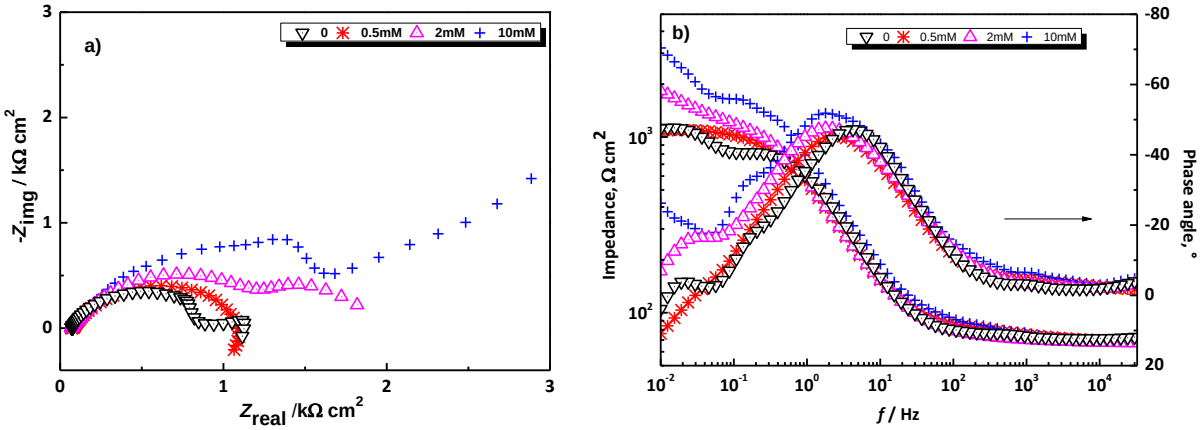

Figure 11. *Nyquist (a) and Bode (b) plots for AA2024-T3-CFRP galvanic couple immersed for 24 h in 0.05 M NaCl without and with different concentrations of $C_2H_3N_3$*

The impedance modulus values of Bode plots shown in Figure 11b increased gradually when $C_2H_3N_3$ was added into the solution, reaching the highest value at 10 mM $C_2H_3N_3$. Each phase angle plot of the galvanic couple presented in Figure 11b exhibits one well-defined time constant about 2 Hz, and one barely seen at about 1000 Hz. The high-frequency time constant can be associated with the presence of a native oxide layer over the metallic surface [18], while this at about 2 Hz to the intermediate layer of corrosion products, including a thin layer of inhibitor molecules adsorbed over the surface. At frequencies lower than 0.1 Hz, another time constant is present. Phenomena at the lowest frequencies are usually ascribed to the corrosion process at the substrate.

Figure 12. shows EIS spectra recorded for AA2024-T3-CFRP in galvanic couple exposed to 0.05 M NaCl without and with different concentrations of $Ce(NO_3)_3{\cdot}6H_2O$. It can be noticed that when $Ce(NO_3)_3.6H_2O$ was added into the solution, an increment in the impedance of the system occurs, particularly in the range of low frequencies, reaching its maximum value at 2mM $Ce(NO_3)_3{\cdot}6H_2O$. In the phase angle spectra, it is possible to observe the formation of two-time constants at middle and low frequencies (Figure 12b). As was previously explained, the first-time constant could be related to the formation of a passive layer of corrosion products over the metal surface, including a thin layer of inhibitor over it. The low frequency related constant phase angle and clear inductive response at 0.5 mM of $Ce(NO_3)_3{\cdot}6H_2O$ could be attributed to the corrosion process, which evidently changes with the concentration of inhibitor used for each test.

Several studies have already been done to establish the mechanism of corrosion in the presence of $Ce(NO_3)_3{\cdot}6H_2O$ as an inhibitor. In this way, it has been found that $Ce(NO_3)_3{\cdot}6H_2O$ acts as a cathodic inhibitor, blocking the occupied zones by intermetallic particles [19], preferentially in areas rich in copper, which has more cathodic potential with respect to the matrix [20].

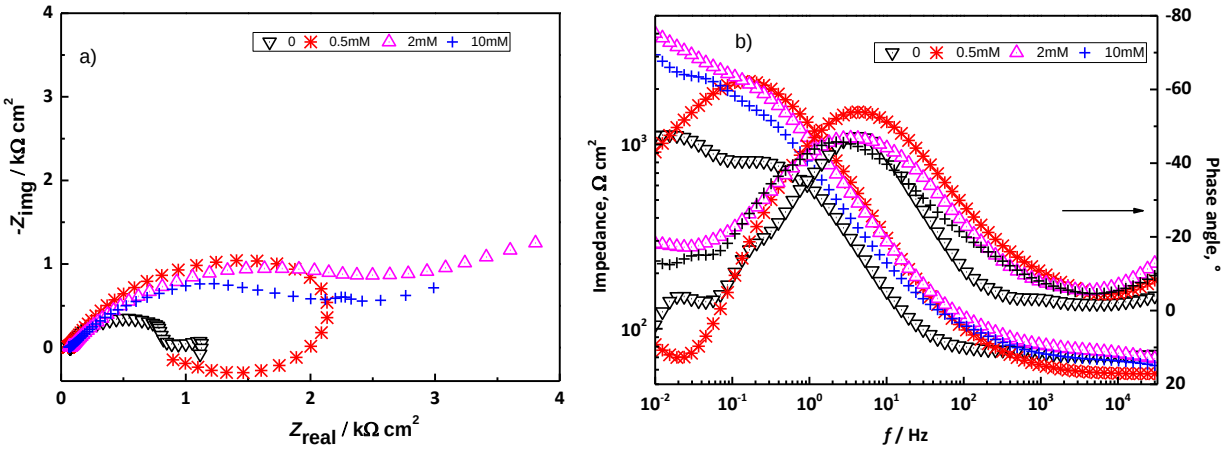

Figure 12. *Nyquist (a) and Bode (b) plots for AA2024-T3-CFRP galvanic couple immersed for 24 h in 0.05 M NaCl without and with different concentrations of $Ce(NO_3)_3{\cdot}6H_2O$*

A mix of the optimal concentrations of $C_2H_3N_3$ (10 mM) and $Ce(NO_3)_3.6H_2O$ (2 mM) was carried out to observe the effect of both inhibitors in a possible synergistic combination. The corresponding EIS spectra are presented in Figure 13. A significant increment of the semicircle diameter (Figure 13a) and impedance magnitude (Figure 13b) can be observed, which were both higher than for two inhibitors looking separately. This improvement of protection ability can be attributed to the fact that $Ce(NO_3)_3{\cdot}6H_2O$ is added preferentially to intermetallic sites (cathodic zones) through a hydroxide film formed over them, whereas $C_2H_3N_3$ is adsorbed over the aluminum matrix due to its polar groups, combined with double bonds in its structure, offering more stability to the film adsorbed over the metal surface. Based on the latter, it seems that each inhibitor enhanced the

other's inhibition efficiency, reducing microgalvanic effects that promote localized attacks around the matrix, delaying the cathodic and anodic reactions.

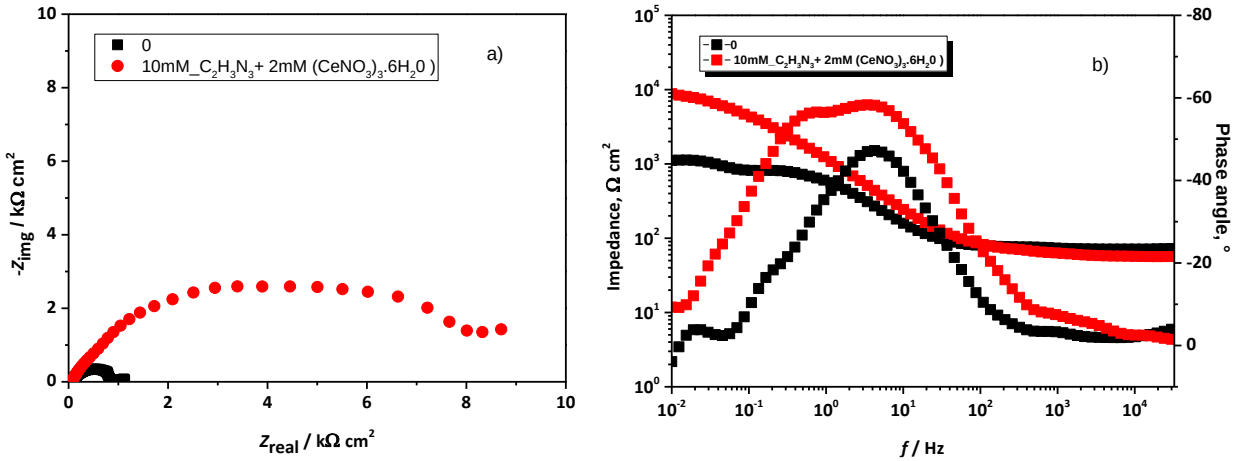

Figure 13. *Nyquist (a) and Bode (b) plots for AA2024-T3-CFRP galvanic couple immersed for 24 h in 0.05 M NaCl without and with 10 mM of $C_2H_3N_3$ + 2mM $Ce(NO_3)_3{\cdot}6H_2O$*

Electrical equivalent circuit

To simulate EIS data measured for AA2024-T3-CFRP in galvanic couple and evaluate polarization resistance (R_p) values, two electrical equivalent circuits were used for modeling (Figure 14). R_s is ascribed to the uncompensated solution resistance, while CPE_{dl} and R_{ct} are the constant phase element of double layer and charge transfer resistance, respectively. $CPE_{inh+oxy}$ is the constant phase element related to the film formed by corrosion products and adsorbed inhibitor, whereas $R_{inh+oxy}$ is ascribed to the corresponding surface film resistance.

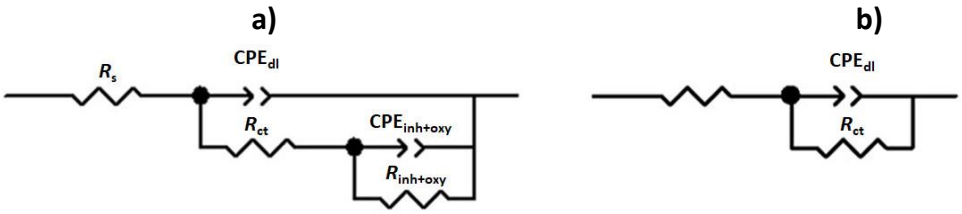

Figure 14. *Electrical equivalent circuits used to fit EIS data for AA2024-T3-CFRP in galvanic couple immersed in 0.05 M NaCl in a) presence and b) absence of inhibitor*

Table 2 summarizes R_p and IE values in solutions with and without $C_2H_3N_3$, $Ce(NO_3)_3{\cdot}6H_2O$ and their optimal concentrations mixture. All impedance parameter values, including R_{ct} and $R_{inh+oxy}$, were obtained by fitting an electrical equivalent circuit in Figure 14 to measured impedance spectra (Figures 11-13). R_p was calculated as the sum of R_{ct} + $R_{inh+oxy}$ [21].

Table 2. *EIS-based polarization resistance (R_p) and inhibition efficiency of $C_2H_3N_3$, $Ce(NO_3)_3{\cdot}6H_2O$ and their optimal concentrations mixture for AA2024-CFRP in galvanic couple immersed in 0.05 M NaCl.*

Inhibitor	$C_2H_3N_3$		$Ce(NO_3)_3{\cdot}6H_2O$		$C_2H_3N_3$+$Ce(NO_3)_3{\cdot}6H_2O$	
c_{inh} / mM	R_p / Ω cm^2	IE, %	R_p / Ω cm^2	IE, %	R_p / Ω cm^2	IE, %
0	9.90×10^2	--	9.90×10^2	--	9.90×10^2	--
0.5	1.12×10^3	11	2.54×10^3	61	--	--
2	1.97×10^3	49	5.28×10^3	81	8.36×10^3	88
10	5.05×10^3	80	3.39×10^3	70		

The inhibition efficiency of the inhibitor was calculated using Eq (2),

$$IE=\frac{R_{p/inh}-R_{p/o}}{R_{p/inh}}100 \quad (1)$$

where $R_{p/Inh}$ and $R_{p/0}$ are polarization resistance (R_p) with and without inhibitor in the electrolyte.

The repeatability and reproducibility of R_p values at optimal concentrations for both inhibitors were determined by the standard deviation obtained after repeating the tests three times for each inhibitor. At 10 mM $C_2H_3N_3$, R_p was calculated as 5.05 kΩ cm^2 with the standard deviation of ±47 Ω cm^2, while for 2 mM $Ce(NO_3)_3{\cdot}6H_2O$, R_p value of 5.28 kΩ cm^2 was estimated with the standard deviation of ±699 Ω cm^2.

Figures 15 and 16 compare R_n and R_p values obtained from ENA and EIS measurements, presenting them in dependence on concentrations of two inhibitors, showing seemingly close behavior between two resistances.

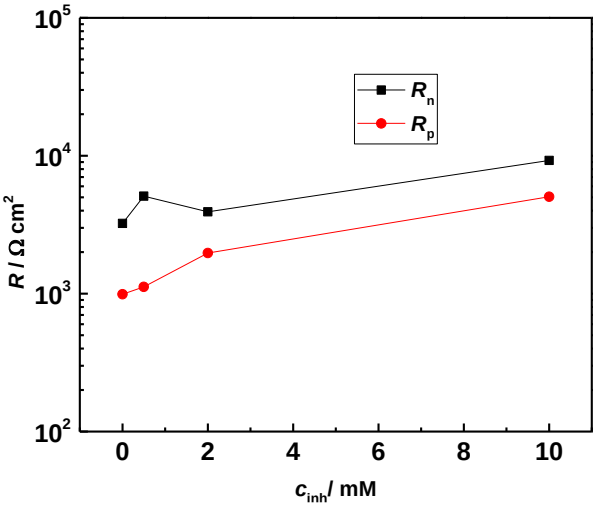

Figure 15. *R_n and R_P values in dependence on the concentration $C_2H_3N_3$ inhibitor*

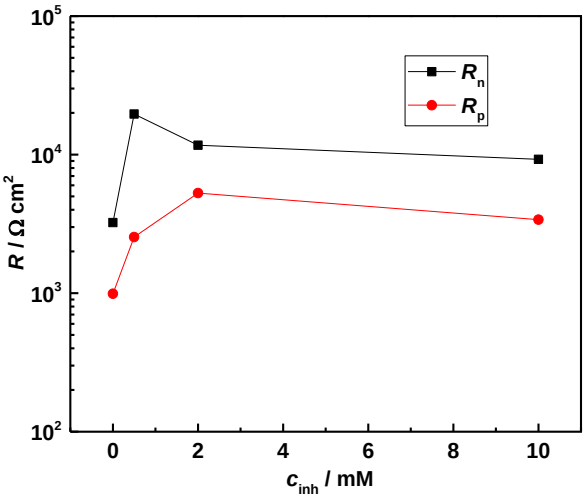

Figure 16. *R_n and R_P values in dependence on the concentration of $Ce(NO_3)_3{\cdot}6H_2O$ inhibitor*

Characterization of inhibitor adsorption

R_n and R_p values can be used to estimate the Gibbs free energy ($\Delta G°_{ads}$), which is an indicator of the type of molecular interaction between the inhibitor and metal surface through the establishment adsorption isotherm model. For this, it is necessary to estimate the fractional surface coverage (θ) values, which would give an idea about the surface covered by an inhibitor. The values of θ were estimated by equation (2), and the results are listed in Table 3.

$$\theta=\frac{R_{p,n/inh}-R_{p,n/0}}{R_{p,n/inh}} \quad (2)$$

Table 3. *Fractional surface coverage (θ) for different concentrations of two corrosion inhibitors at AA2024-T3-CFPR in a galvanic couple, calculated by R_n and R_p values obtained by EN and EIS analysis*

c_{inh} / mM	θ			
	$C_2H_3N_3$		$Ce(NO_3)_3.6H_2O$	
	Calculated by			
	R_n	R_p	R_n	R_p
0.5	0.37	0.12	0.84	0.61
2	0.17	0.50	0.72	0.81
10	0.65	0.80	0.65	0.71

Langmuir and Temkin isotherms are defined by the equations (3) and (4),

$$\frac{\theta}{1-\theta}=Kc_{inh} \quad (3)$$

$$\log\frac{\theta}{c_{inh}} = \log K + \theta g \quad (4)$$

where K is equilibrium adsorption constant, g is molecular interaction parameter, and c_{inh} is the concentration of the inhibitor. By determining K value, Gibbs free energy of adsorption can be calculated by equation (5):

$$\Delta G^{o}_{ads} = -RT \ln(55.5K) \quad (5)$$

where R is gas constant, T is the temperature in Kelvin grades, and 55.5 is the molar concentration of water in solution.

The interactions between the surface of AA2024-T3-CFRP in galvanic couple with either $C_2H_3N_3$ or $Ce(NO_3)_3{\cdot}6H_2O$ as corrosion inhibitors are best described by Langmuir isotherm in the first case and Temkin isotherm in the second case. The best-fitted results using models described by eqns. (3) and (4) are shown in Figures 17 and 18, respectively. The Langmuir model (Figure 17) assumes that there are sites with the capability to physically or chemically hold one molecule over the surface. All sites are equivalent and there are no interactions between molecules. The Temkin model (Figure 18) establishes a heterogeneous surface divided into zones, some of them without molecular interactions, establishing an attraction or repulsion of the inhibitor over the metal surface by zones.

The values of $\Delta G°_{ads}$ were calculated using R_n and R_p values reported in Table 3. Applying the eq. (5), values of $\Delta G°_{ads}$ of $C_2H_3N_3$ adsorption were calculated as -35 kJ/mol based on R_n, and -37 kJ/mol based on R_p. For $Ce(NO_3)_3{\cdot}6H_2O$, $\Delta G°_{ads}$ of -26.78 kJ/mol based on R_n, and -26.89 kJ/mol based on R_p were calculated. These $\Delta G°_{ads}$ values suggest physisorption and chemisorption of both inhibitors over the metal surface, since values below -20 kJ/mol are indicative of physisorption, while values higher than -40 kJ/mol suggest chemisorption. The values between -20 and -40 kJ/mol as obtained here, are indicative of a combination of both physisorption and chemisorption. In addition, negative values of $\Delta G°_{ads}$ are indicative of spontaneous adsorption. The estimated values of Gibbs free energy establish the exothermic adsorption process, in agreement with Langmuir and Temkin isotherms for $C_2H_3N_3$ and $Ce(NO_3)_3{\cdot}6H_2O$, respectively. Negative values of $\Delta G°_{ads}$ values suggest that chemisorption and physisorption proceed at the metallic surface as spontaneous processes.

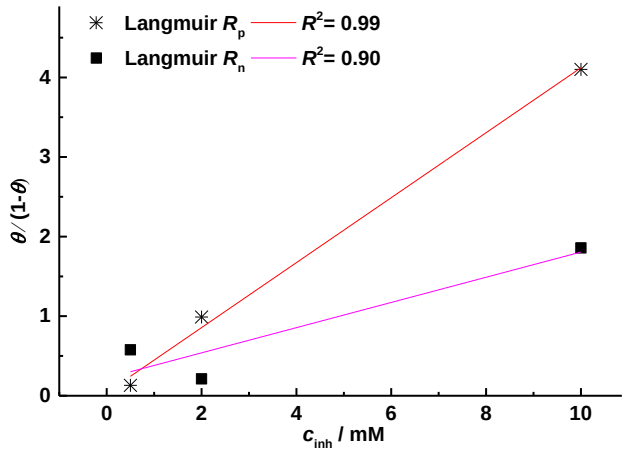

Figure 17. *Langmuir isotherm for adsorption of $C_2H_3N_3$ inhibitor*

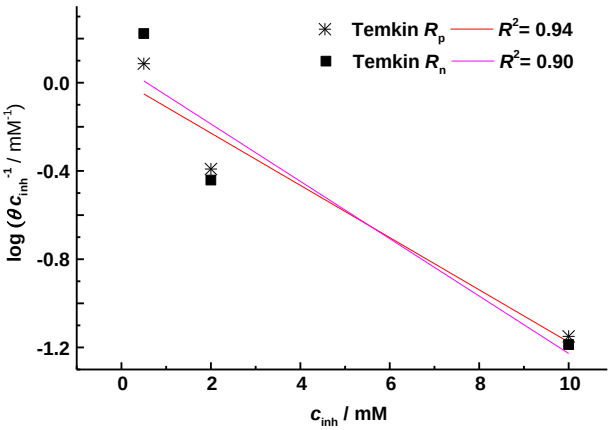

Figure 18. *Temkin isotherm for adsorption of $Ce(NO_3)_3{\cdot}6H_2O$ inhibitor*

Surface analysis

The scanning electron microscopy (SEM) allowed obtaining images of AA2024-T3 and CFRP surfaces. Figure 19 shows the surface of AA2024-T3 before and after its exposure for 24 h in the aggressive media containing $Ce(NO_3)_3{\cdot}6H_2O$. EDS analysis was also carried out before and after

immersion of AA2024-T3 into 0.05 M NaCl (Figure 19). Corrosion products can be identified in places with Cu particles, as demonstrated in previous research [23]. $Ce(NO_3)_3{\cdot}6H_2O$ was preferentially deposited over cathodic regions. EDS analysis confirms the presence of rare-earth oxide deposition, as well as the formation of oxide film products.

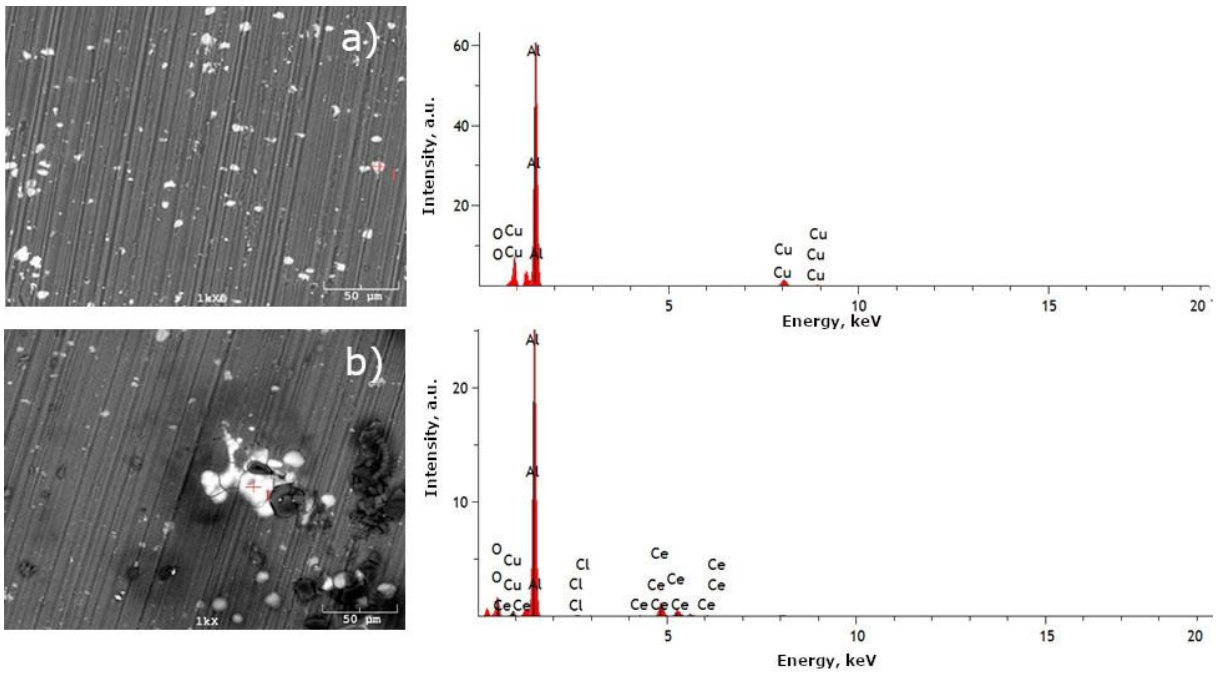

Figure 19. *SEM micrographs and EDS analysis for aluminum alloy AA2024-T3 before a) and after b) exposure for 24 h in 0.05 M NaCl with $Ce(NO_3)_3{\cdot}6H_2O$ as a corrosion inhibitor*

Figure 20 shows SEM micrographs taken for CFRP surface before and after it was immersed in the electrolyte with $Ce(NO_3)_3{\cdot}6H_2O$ as a corrosion inhibitor. The EDS analysis revealed the deposition of $Ce(NO_3)_3{\cdot}6H_2O$ and aluminum particles on its surface after it is immersed in the electrolyte, especially in the areas rich in carbon.

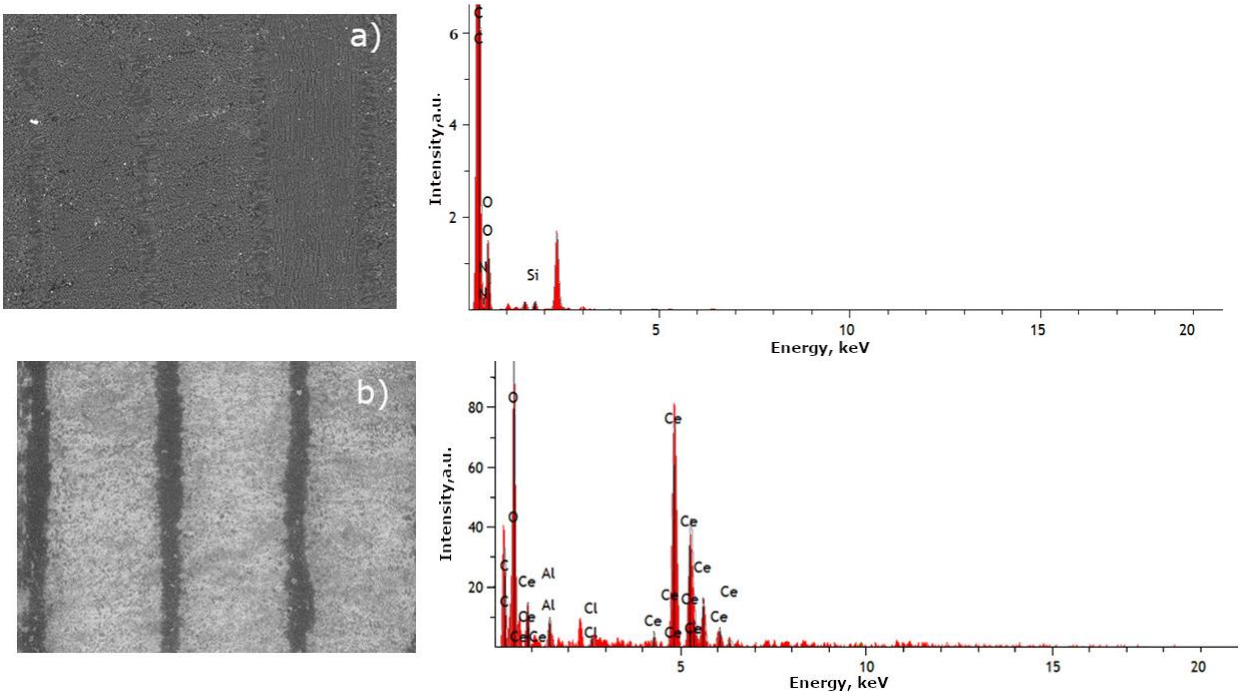

Figure 20. *SEM micrographs and EDS analysis for CFRP before a) and after b) exposition for 24 h to 0.05 M NaCl with $Ce(NO_3)_3{\cdot}6H_2O$ as a corrosion inhibitor*

Conclusion

The inhibition effect against the galvanic corrosion effect between the aluminum alloy 2024-T3 and CFRP immersed in 0.05 M NaCl was evaluated at different concentrations (0.5, 2, 10 mM) of inorganic ($Ce(NO_3)_3{\cdot}6H_2O$) and organic ($C_2H_3N_3$) compounds. The polarization resistance (R_p) measured using EIS for AA2024-CFRP galvanic couple increased slightly in the presence of $C_2H_3N_3$, reaching its maximum efficiency at 10 mM with 80 % of inhibition efficiency. $Ce(NO_3)_3{\cdot}6H_2O$ showed the highest polarization resistance at a lower concentration of 2 mM, with 81 % inhibition efficiency. For a mix of optimal concentrations of $C_2H_3N_3$ and $Ce(NO_3)_3{\cdot}6H_2O$, R_p of 8.36 kΩ cm^2 ± 243 Ω cm^2 was measured, suggesting a synergistic effect of these two inhibitors in enhancing corrosion protection. Similar behavior was observed for the noise resistance (R_n) obtained using ENA, where $Ce(NO_3)_3{\cdot}6H_2O$ showed higher resistance than $C_2H_3N_3$. Free energy of adsorption $\Delta G°_{ads}$ was calculated using R_n and R_p values obtained by ENA and EIS analysis, respectively. $\Delta G°_{ads}$ values of -35 kJ/mol for R_n and -37 kJ/mol for R_p were calculated for $C_2H_3N_3$, while for $Ce(NO_3)_3{\cdot}6H_2O$, -26.78 kJ/mol for R_n and -26.89 kJ/mol for R_p were obtained. These $\Delta G°_{ads}$ values suggest chemisorption and physisorption of both inhibitors over the metal surface.

Acknowledgement: *This work was supported by grant agreement 270252/232335 from CONACYT.*

References

[1] R. Alderliesten, R. Benedictus, *Journal of Aircraft* **45(4)** (2008) 1182-1189. https://doi.org/10.2514/1.33946

[2] T. Sinmazçelik, E. Avcu, M. Ö. Bora, O. Çoban, *Materials & Design* **32(7)** (2011) 3671-3685. http://dx.doi.org/10.1016/j.matdes.2011.03.011

[3] A. Pardo, M. C. Merino, A. E. Coy, R. Arrabal, F. Viejo, E. Matykina, *Corrosion Science* **50(3)** (2008) 823-834. http://dx.doi.org/10.1016/j.corsci.2007.11.005

[4] G. Song, B. Johannesson, S. Hapugoda, D. StJohn, *Corrosion Science* **46(4)** (2004) 955-977. http://dx.doi.org/10.1016/S0010-938X(03)00190-2

[5] Y. Pan, G. Wu, X. Cheng, Z. Zhang, M. Li, S. Ji, Z. Huang, *Corrosion Science* **98** (2015) 672-677. http://dx.doi.org/10.1016/j.corsci.2015.06.024

[6] M. Mokaddem, P. Volovitch, F. Rechou, R. Oltra, K. Ogle, *Electrochimica Acta* **55(11)** (2010) 3779-3786. http://dx.doi.org/10.1016/j.electacta.2010.01.079

[7] E. Matter, S. Kozhukharov, M. Machkova, V. Kozhukharov, *Scientific Papers of The University of Russia* **48(9)** (2009) 19-23. http://conf.uni-ruse.bg/bg/docs/cp09/9/9-3.pdf

[8] G. Wu, J. M. Yang, *JOM* **57(1)** (2005) 72-79. https://doi.org/10.1007/s11837-005-0067-4

[9] L. Dong-xia, L. Li, L. Ming, *IOP Conference Series: Materials Science and Engineering* **10** (2010) 012098. http://dx.doi.org/10.1088/1757-899X/10/1/012098

[10] D. Liu, Y. Tang, W. L. Cong, *Composite Structures* **94(4)** (2012) 1265-1279. http://dx.doi.org/10.1016/j.compstruct.2011.11.024

[11] S. Payan, Y. Le Petitcorps, J. M. Olive, H. Saadaoui, *Composites Part A: Applied Science and Manufacturing* **32(3-4)** (2001) 585-589. http://dx.doi.org/10.1016/S1359-835X(00)00126-3

[12] El-Sayed M. Sherif, F. H. Latif, H. Junaedi, *International Journal of Electrochemical Science* **6** (2011) 1085-1099. http://www.electrochemsci.org/papers/vol6/6041085.pdf

[13] W.-X. Wang, Y. Takao, T. Matsubara, *Proceedings of the 16th International Conference on Composite Materials, ICCM-16,* (2007) 1-10. https://www.iccm-central.org/Proceedings/ICCM16proceedings/contents/pdf/WedK/WeKM1-05ge_wangw224701p.pdf

[14] V. Palanivel, Y. Huang, W. J. van Ooij, *Progress in Organic Coatings* **53(2)** (2005) 153-168. http://dx.doi.org/10.1016/j.porgcoat.2003.07.008

[15] C.-M. Liao, R. P. Wei, *Electrochimica Acta* **45(6)** (1999) 881-888. http://dx.doi.org/10.1016/S0013-4686(99)00299-6

[16] C. Monticelli, F. Zucchi, G. Brunoro, G. Trabanelli, *Journal of Applied Electrochemistry* **27** (1997) 325-334. https://doi.org/10.1023/A:1018436931465

[17] A. Torres, J. Uruchurtu, J. G. González-Rodríguez, S. Serna, *Corrosion (Houston)* **63(9)** (2007) 866-871. http://dx.doi.org/10.5006/1.3278437
[18] M. L. Zheludkevich, K. A. Yasakau, S. K. Poznyak, M. G. S. Ferreira, *Corrosion Science* **47(12)** (2005) 3368-3383. http://dx.doi.org/10.1016/j.corsci.2005.05.040
[19] A. Aballe, M. Bethencourt, F. J. Botana, M. J. Cano, M. Marcos, *Materials and Corrosion* **52(5)** (2001) 344-350. https://doi.org/10.1002/1521-4176(200105)52:5%3C344::AID-MACO344%3E3.0.CO;2-S
[20] A. Decroly, J.-P. Petitjean, *Surface and Coatings Technology* **194(1)** (2005) 1-9. http://dx.doi.org/10.1016/j. surfcoat.2004.05.012.
[21] A. Salve, V. Kozhukharov, J. Pernas, E. Matter, M. Machkova, *Journal of University of Chemical Technology and Metallurgy* **47(3)** (2012) 319-328. https://www.researchgate.net/publication/268002945
[22] S. Kozhukharov, V. Kozhukharov, M. Wittmar, M. Schem, M. Aslan, H. Caparrotti, M. Veith, *Progress in Organic Coatings* **71(2)** (2011) 198-205. https://doi.org/10.1016/j.porgcoat.2011.02.013
[23] M. L. Zheludkevich, R. Serra, M. F. Montemor, K. A. Yasakau, I. M. M. Salvado, M. G. S. Ferreira, *Electrochimica Acta* **51(2)** (2005) 208-217. https://doi.org/10.1016/j.electacta.2005.04.021

J. Electrochem. Sci. Eng. **12(2)** (2022) 359-372; http://dx.doi.org/10.5599/jese.1147

Open Access : : ISSN 1847-9286

www.jESE-online.org

Original scientific paper

Modelling the effect of anode particle radius and anode reaction rate constant on capacity fading of Li-ion batteries

Vikalp Jha and Balaji Krishnamurthy✉

Department of Chemical Engineering, BITS Pilani, Hyderabad 500078, India

Corresponding author: ✉balaji@hyderabad.bits-pilani.ac.in

Received: October 21, 2021; Accepted: November 26, 2021; Published: December 6, 2021

Abstract

This paper investigates the effect of anode particle radius and anode reaction rate constant on the capacity fading of lithium-ion batteries. It is observed through simulation results that capacity fade will be lower when the anode particle size is smaller. Simulation results also show that when reaction rate constant is highest, the capacity loss is the lowest of lithium-ion battery. The potential drop across the SEI layer (solid electrolyte interphase) is studied as a function of the anode particle radius and anode reaction rate constant. Modelling results are compared with experimental data and found to compare well.

Keywords

SEI; potential drop; side reaction; discharge

Introduction

Side reactions can cause various adverse effects leading to capacity fading in lithium-ion batteries. The aging of Li-ion batteries usually occurs due to various parameters and electrochemical reactions, and capacity loss varies between all stages during a charge-discharge load cycle, depending on various parameters such as cell voltage, electrolyte concentration, temperature, and cell current. This work shows the model for aging and capacity loss in the anode of a Li-ion battery, where the formation of a thin film of solid-electrolyte-interface (SEI) shows an adverse capacity loss of cyclable lithium. Capacity fading in a lithium-ion battery has been studied under various load conditions.

Haran *et al.* [1] studied the effect of various temperatures during various cycles in the capacity fading of 18650 Li-ion cells. It is observed that with an increase in temperature of Li-ion batteries, capacity fading is increased. It is observed that at temperatures higher than 55 °C, the cell ceases to operate after 500 cycles due to ongoing SEI film formation over the anode surface. Han *et al.* [2] studied the cycle life of commercial Li-ion batteries with LTO anodes in electric vehicles. The author also found that at 55 °C, the capacity fading in the battery is more than lower operating temperature Lithium-ion battery. Liaw *et al.* [3] studied the correlation of Arrhenius behavior in power and capacity loss with cell impedance and heat generation at different temperatures and state of charge

in 18650 cylindrical Li-ion cells. It is observed that degradation in power and capacity fade seems to relate to impedance increase in the cell with the activation energy of cell at different temperatures. Ramadesigan *et al.* [4] studied the effect of the solid-phase diffusion coefficient and side reaction rate constant in the anode, cathode, and electrolyte as a function of cycling with various reformulated models. Colclasure *et al.* [5] studied various detailed chemistries and transport for SEI films on Li-ion batteries with various states of charge (SOC) at different cycles. The author states that SEI film grows with time according to net production rate from heterogeneous chemistry on SEI film surface because electric-potential and concentration profiles in the SEI layer are functions of the intercalation fraction [5].

Pinson and Bazant [6] also studied the formation of SEI layer in rechargeable batteries with capacity loss, aging, and lifetime prediction in Li-ion batteries. Various models are studied at different temperatures and C-rates to study SEI layer formation and capacity fading of Li-ion batteries. The authors postulate that capacity fading depends on time, not on the number of cycles. The temperature dependence of the diffusivity of the limiting reacting species through SEI can be modelled using an Arrhenius dependence. Ziv *et al.* [7] examined electrochemical performance and capacity loss of half and full Li-ion batteries with several cathode materials experimentally. The authors stated that the loss of lithium ions due to side reactions is the main reason for the capacity fading of Li-ion batteries. Liu *et al.* [8] studied a thermal-electrochemical model for SEI formation in Li-ion batteries during load cycles. The authors state that the growth of SEI film is very sensitive to the diffusion process and side reaction rate. It is also found that SEI film grows at a higher rate during charging than during the discharge cycle. *Guo et al.* [9] also studied the capacity fading of Li-ion batteries with different experiments. The authors stated that capacity fading occurred due to several reasons, including discharge rate, number of cycles, and battery type.

Ramesh *et al.* [10,11] developed a mathematical model to study capacity loss in Li-ion batteries due to temperature, formation, and dissolution rate constants of the SEI layer. The author also developed an empirical model to study capacity fading in Li-ion batteries under different temperatures. Xu *et al.* [12] also studied electrode side reactions, capacity loss and mechanical degradation of Li-ion batteries through experimental observations. The author states that during load cycles for higher reaction rates, columbic efficiency is lower, but capacity fading is also lower. Shirazi *et al.* [13] studied the effect of composite electrode's particle size effect on electrochemical and heat generation of Li-ion batteries. The author states that for smaller particle size, the thermal characteristics of the battery is improved in comparison to larger particle size [13]. Singhvi *et al.* [14] developed a mathematical model to observe the effect of acid attack on capacity fading in Li-ion batteries. The author considers SEI formation due to the transport and reaction of solvent species.

Cheng *et al.* [15] developed a mechanism for capacity loss of 18650 cylindrical Li-ion battery cells. The author postulates that the capacity loss of Li-ion batteries can be explained by continuous SEI layer formation over the surface of anode and side reactions. Side reaction products deposit on a separator and reduce its porosity, leading to capacity fading. Tomaszewska *et al.* [16] reviewed various research on fast charging of Li-ion batteries. It was observed that for fast charging, rate-limiting processes are beneficial to reduce battery degradation and increase in cycle life.

Meanwhile, Li plating, the structure of Li deposits, and temperature distribution during cycling lead to the degradation of Li-ion batteries. Gantenbein *et al.* [17] studied the capacity loss of Li-ion batteries over different SOC ranges. The author states that capacity fading originates from active electrodes and active lithium loss. Lee *et al.* [18] also studied the loss of cyclable Li on the performance degradation of Li-ion batteries. The author stated that the discharge behavior of the

cell had a strong dependence on discharge C-rate and loss of cyclable lithium. Khaleghi Rahiman *et al.* [19] developed a mathematical model to study cell life with various parameters. The author studied capacity loss and SEI formation in Li-ion batteries at different temperatures at different SOCs. The author postulates that cathode side reactions are accelerated at higher SOCs and temperatures. In our model, we compare the effect of anode particle radius and anode reaction rate constant on the capacity fading of a lithium-ion battery.

Model development

A 1D model of a Li-ion battery interface is created, as shown in Figure 1. The components of a Li-ion battery are the negative electrode, positive electrode, and separator. Graphite electrode (Li_xC_6) MCMB is used for negative electrode material, NCA electrode ($LiNi_{0.8}Co_{0.15}Al_{0.05}O_2$) is used for positive electrode material and $LiPF_6$ (3:7 in EC: EMC) is used as a liquid electrolyte.

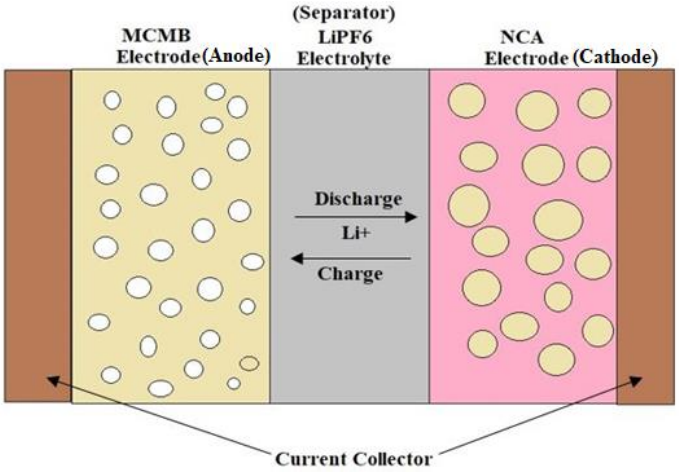

Figure 1. *Schematic of the 1D electrochemical model of Li-ion battery*

Model equations

The model equations analyze the current equilibrium in the electrolyte and electrodes, the mass balance for the lithium and electrolyte in Li-ion batteries. The Li-ion battery physics at interface analyses five dependent variables:

a) ϕ_s - the electric potential,
b) ϕ_e - the electrolyte potential,
c) $\Delta\phi_{SEI}$ - the potential losses due to solid-electrolyte interface (SEI),
d) c_{Li} - the concentration of lithium in the electrode particles
e) c_e - the electrolyte salt concentration.

The domain equations in the electrolyte are the conservation of current and the mass balance for the salt according to the following [20]:

$$i_{sum} + Q_e = \nabla\left(-\sigma_e \nabla\phi_e + \left(\frac{2\sigma_{e,eff}RT}{F}\right)\left(1+\frac{\partial \ln f}{\partial \ln c_e}\right)(1+t_+)\nabla \ln c_e\right) \quad (1)$$

$$\varepsilon_e \frac{\partial c_e}{\partial t} + \nabla\left(-\varepsilon_e D_e \nabla c_e\right) = R_e - \left(\frac{i_{sum}+Q_e}{F}\right)t_+ \quad (2)$$

where σ_e denotes the electrolyte conductivity, f is the activity coefficient for the salt, t_+ is the transport number for Li^+, i_{sum} is the sum of all electrochemical current sources, and Q_e denotes an arbitrary electrolyte current source. In the mass balance for the salt, ε_e denotes the electrolyte volume fraction, D_e is the electrolyte salt diffusivity, and R_e the total Li^+ source term in the electrolyte.

In the electrode, the current density, i_s is defined as

$$i_s = -\sigma_s \nabla \phi_s \quad (3)$$

where σ_s is electrical conductivity. The domain equation for the electrode is the conservation of current expressed as

$$\nabla i_s = -i_{sum} + Q_s \quad (4)$$

where Q_s is an arbitrary current source term. The electrochemical reactions in the physics interface are assumed to be insertion reactions occurring at the surface of small solid spherical particles of radius r_p in the electrodes.

The insertion reaction is described as:

During charging, at anode

$$xLi^+ + xe^- + \text{graphite} \rightarrow Li_xC_6 \quad (5)$$

at cathode

$$Li_xNi_{0.8}Co_{0.15}Al_{0.05}O_2 \rightarrow xLi^+ + xe^- + Ni_{0.8}Co_{0.15}Al_{0.05}O_2 \quad (6)$$

During discharging, at Anode

$$Li_xC_6 \rightarrow xLi^+ + xe^- + \text{graphite} \quad (7)$$

at cathode

$$xLi^+ + xe^- + Ni_{0.8}Co_{0.15}Al_{0.05}O_2 \rightarrow Li_xNi_{0.8}Co_{0.15}Al_{0.05}O_2 \quad (8)$$

An important parameter for lithium insertion electrodes is the state-of-charge variable for the solid particles, denoted SOC. This is defined as

$$SOC = \frac{c_{Li}}{c_{Li,max}} \quad (9)$$

The equilibrium potentials E_0 of lithium insertion electrode reactions are typically functions of SOC. The electrode reaction occurs on the particle surface and lithium diffuses to and from the surface in the particles. The mass balance of Li in the particles is described as

$$\frac{\partial c_{Li}}{\partial t} = \nabla(D_s \nabla c_{Li}) \quad (10)$$

where c_{Li} is the concentration of Li in the electrode. This equation is solved locally by this physics interface in a 1D pseudo dimension, with the solid phase concentrations at the nodal points for the element discretization of the particle as the independent variable. The gradient is calculated in Cartesian, cylindrical, or spherical coordinates, depending on if the particles are assumed to be best described as flakes, rods or spheres, respectively.

The boundary conditions are as follows:

$$\left.\frac{\partial c_{Li}}{\partial r}\right|_{r=0} = 0 \quad (11)$$

$$-D_s \left.\frac{\partial c_{Li}}{\partial r}\right|_{r=r_p} = -R_{Li}\big|_{r=r_p} \quad (12)$$

where R_{Li} denotes the molar flux of lithium at the particle surface caused by the electrochemical insertion reactions. In the porous electrodes, i_{sum} denotes the sum of all charge transfers current density contributions according to:

$$i_{sum} = \Sigma A_v i_{loc} \quad (13)$$

where, A_v denotes the specific surface area at any node of the lithium-ion battery interface. Active specific surface area (m^2/m^3) defines the area of an electrode-electrolyte interface that is catalytically active for porous electrode reactions. Equation 13 describing the total current source

in the domain is a function of active specific surface area and local current in the electrode. The source term in the mass balance is calculated from:

$$R_{\mathrm{l}} = -\sum A_{\mathrm{v}} \frac{\upsilon_{\mathrm{Li}} i_{\mathrm{loc}}}{nF} + R_{\mathrm{l,src}} \tag{14}$$

where $R_{\mathrm{l.src}}$ is an additional reaction source that contributes to the total species source.

At the surface of the solid particles, the following equation is applied:

$$R_{\mathrm{Li}} = -\sum \frac{A_{\mathrm{v}}}{\frac{S_{\mathrm{shape}} \varepsilon_{\mathrm{s}}}{r_{\mathrm{p}}}} \frac{\upsilon_{\mathrm{Li}} i_{\mathrm{loc}}}{nF} \tag{15}$$

where n is the number of electrons and S_{shape} (normally equal to 1) is a scaling factor accounting for differences between the surface area (A_{v}) used to calculate the volumetric current density and the surface area of the particles in the solid lithium diffusion model. S_{shape} is 1 for Cartesian, 2 for cylindrical, 3 for spherical coordinates and υ_{Li} is the stoichiometric coefficient.

A resistive film (also called solid-electrolyte interface, SEI) might form on the solid particles resulting in additional potential losses in the electrodes. To model a film resistance, an extra solution variable for the potential variation over the film is introduced in the physics interface. The governing equation is then according to

$$\nabla \phi_{\mathrm{SEI}} = R_{\mathrm{SEI}} i_{\mathrm{sum}} \tag{16}$$

where R_{SEI} denotes generalized film resistance, which can be expressed by:

$$R_{\mathrm{SEI}} = \frac{\delta_0 + \Delta\delta}{\sigma_{\mathrm{SEI}}} \tag{17}$$

where, δ_0 is initial film thickness, $\Delta\delta$ is film thickness change and σ_{SEI} is film conductivity. The activation overpotentials, η, for all electrode reactions in the electrode then receives an extra potential contribution, which yields

$$\eta = \phi_{\mathrm{s}} - \phi_{\mathrm{e}} - \phi_{\mathrm{SEI}} - E_{\mathrm{eq}} \tag{18}$$

where, E_{eq} is the equilibrium potential of a cell. The battery cell capacity, $Q_{\mathrm{cell,0}}$ is equal to the sum of the charge of cyclable species in the positive and negative electrodes and additional porous electrode material if present in the model [20].

$$Q_{\mathrm{cell,0}} = Q_{\mathrm{cycle,pos}} + Q_{\mathrm{cycle,neg}} + Q_{\mathrm{cycl,addm}} \tag{19}$$

Butler-Volmer equation is used to calculate the local current density in the electrode.

$$i_{\mathrm{loc}} = i_0 \left(\exp\left(\frac{\alpha_{\mathrm{a}} F \eta}{RT} \right) - \exp\left(\frac{-\alpha_{\mathrm{c}} F \eta}{RT} \right) \right) \tag{20}$$

$$i_0 = F k_{\mathrm{c}}^{\alpha_{\mathrm{a}}} k_{\mathrm{a}}^{\alpha_{\mathrm{c}}} (c_{\mathrm{Li,max}} - c_{\mathrm{Li}})^{\alpha_{\mathrm{a}}} c_{\mathrm{Li}}^{\alpha_{\mathrm{c}}} \left(\frac{c_{\mathrm{e}}}{c_{\mathrm{e,eff}}} \right) \tag{21}$$

where α_{a} and α_{c} are the anode and cathode transfer coefficient and k_{a} and k_{c} are reaction rate constant for anode and cathode.

Numerical methods

1D model of Li-ion battery consists of 3 geometric regions for analysis: negative electrode, separator and a positive electrode. For numerical analysis of the computational domain, 1D meshing is done for 49,59 and 95 mesh elements. The 1D mathematical model is developed for transient analysis of our computational domain in Comsol 5.3a on viable concerns of Li-ion battery, electrochemical parameters, species transport and current distribution, consisting of the principal

model assumptions and equations with different initial conditions, boundary conditions and numerical solver strategies for solution.

Results and discussion

Capacity fading of Li ion battery is studied with the effect of various parameters. A summary of the list of parameters used for simulation is shown in Table 1.

Table 1. *List of parameters*

Description	**Value**
Particle radius, µm	0.5, 1, 2, 2.5
Reaction rate coefficient, pmol m^{-3} s^{-1}	200 , 20 , 2
Initial capacity, C m^{-2}	55761
1C discharge current, A	15.767
Thickness of negative electrode, µm	55
Thickness of separator, µm	30
Thickness of positive electrode, µm	55
Cell temperature, ℃	45
Maximum cell voltage, V	4.1
Minimum cell voltage, V	2.5
Initial electrolyte salt concentration, mol m^{-3}	1200
Constant current (charge and discharge), A	15.767, -15.767
SEI Layer conductivity, S m^{-1}	5×10^{-6}
Initial SEI layer thickness, nm	1
Number of cycles	2000

The battery cycling consists of 3 various stages of charging and discharging, as shown in Figure 2:

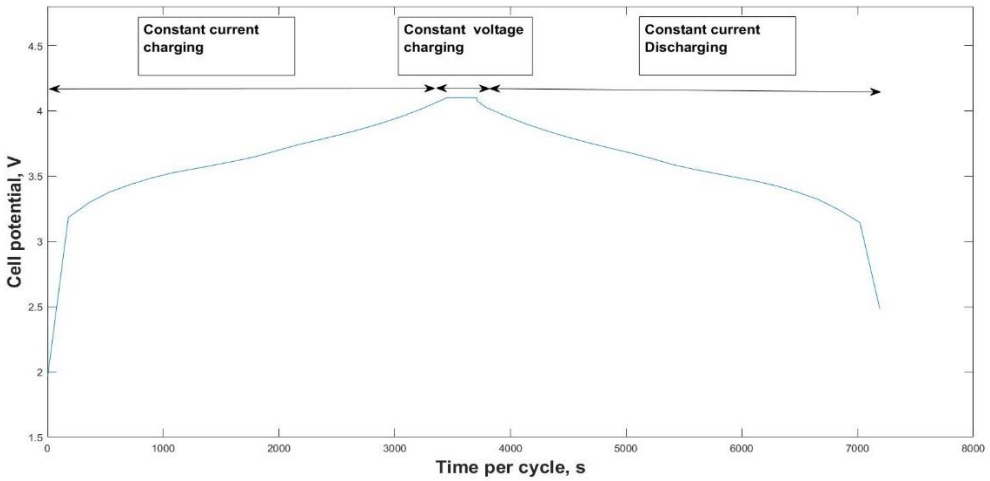

Figure 2. *Charge-discharge load cycle*

- charging at a constant current rate of 1 C until the cell potential reaches 4.1 V.
- Charging at a constant voltage of 4.1 V.
- Discharging at constant current discharge rate at 1 C until the cell potential reaches the minimum voltage of 2.5 V.

Effect of particle radius on capacity fading in lithium-ion batteries

Research on anode particle radius on capacity fading in lithium-ion batteries has been done previously. Rai [21] postulated that batteries with smaller anode particle sizes generate better capacity. The authors postulated that smaller particles(graphite) allow quicker lithium-ion intercalation and deintercalation due to the short distances for lithium-ion transport within the particles. There is no agreed-upon consensus for optimal particle size in lithium-ion batteries though particles less than 150 nm are mainly used. Wu [22] investigated the effect of silicon particle size in the micrometer range when used as a lithium-ion battery anode. The authors have found out in their study that particle size of 3µm shows better outcomes with respect to the 20 µm particle size with an initial capacity of 800 mAh/g and retention of 600 mAh/g after 50 cycles. Buqa [23] investigated three different graphite particle sizes (6, 15 and 44 µm) and showed that smaller particles could achieve better capacity retention. Several authors like Drezen [24] and Fey [25] have postulated that smaller particles improve capacity retention. Mei has [26] postulated that energy and power density increase with smaller particle sizes due to lower overpotential. Mei [26] has also postulated that smaller particle size increases the surface area for reaction. Our focus was to study the effect of the anode particle radius on the capacity fading in lithium-ion batteries taking into consideration lithium losses during cycling.

Figure 3 shows the capacity fading of a lithium-ion battery with cycling for various anode particle radii. The model assumes zero lithium loss during the process of cycling. Four different anode particle radii (0.5, 1, 2 and 2.5 µm) were considered for analysis. It is seen that the least capacity fading (high relative capacity) is seen for an anode particle radius of 0.5 µm. Relative capacity is defined as the capacity of the battery at any point of time divided by the initial capacity of the battery. It can be seen that as the anode particle radius increases from 0.5 to 2.5 µm, the relative capacity decreases over 2000 cycles.

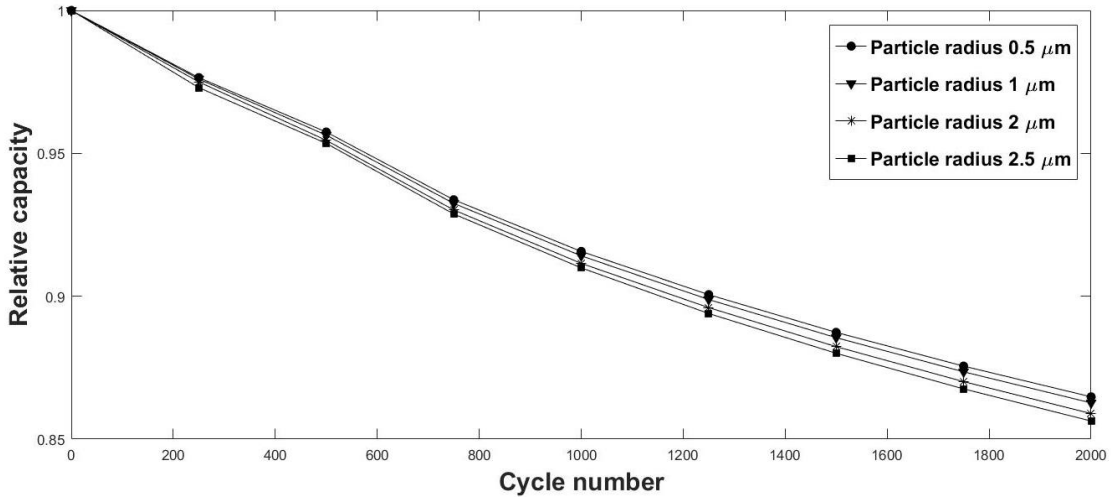

Figure 3. *Capacity fading with cycling for various anode particle radius with zero lithium loss*

Figure 4 shows the capacity fading in a lithium-ion battery cycling for four different particle radii (0.5, 1, 2 and 2.5 µm) with 10 percent lithium loss during cycling. During charge-discharge cycling, there is more lithium loss during initial cycles. A comparison of Figures 3 and 4 shows that the capacity loss is seen to be less without cyclable lithium loss compared to 10 % initial lithium loss as the number of cycles increases. This is clearly shown in Figure 5. It is seen from Figure 5 that there is less capacity loss of around 3 % when we go from zero percent lithium loss to 10 percent lithium loss during cycling.

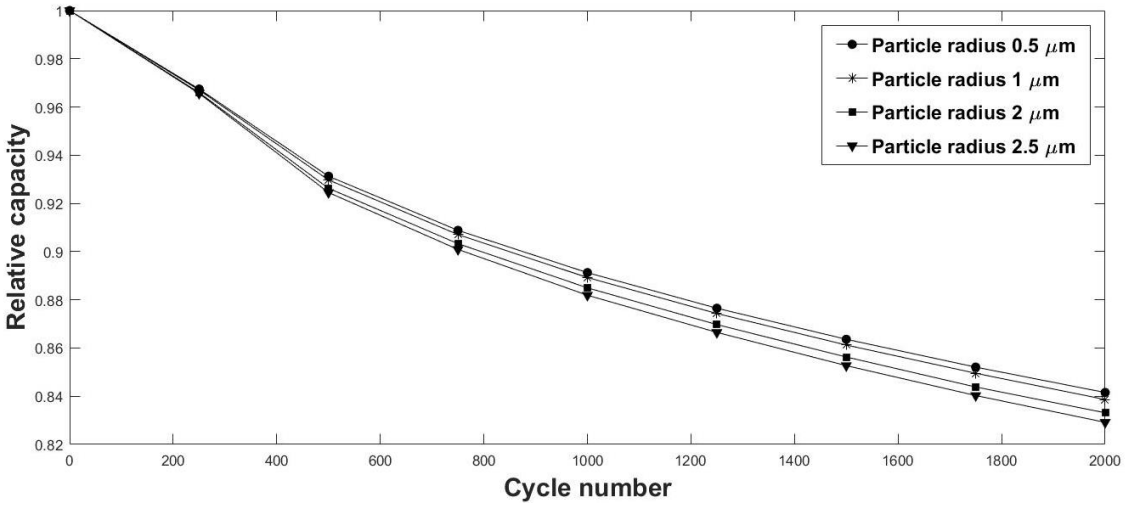

Figure 4. *Capacity fading with cycling for various anode particle radius with lithium loss*

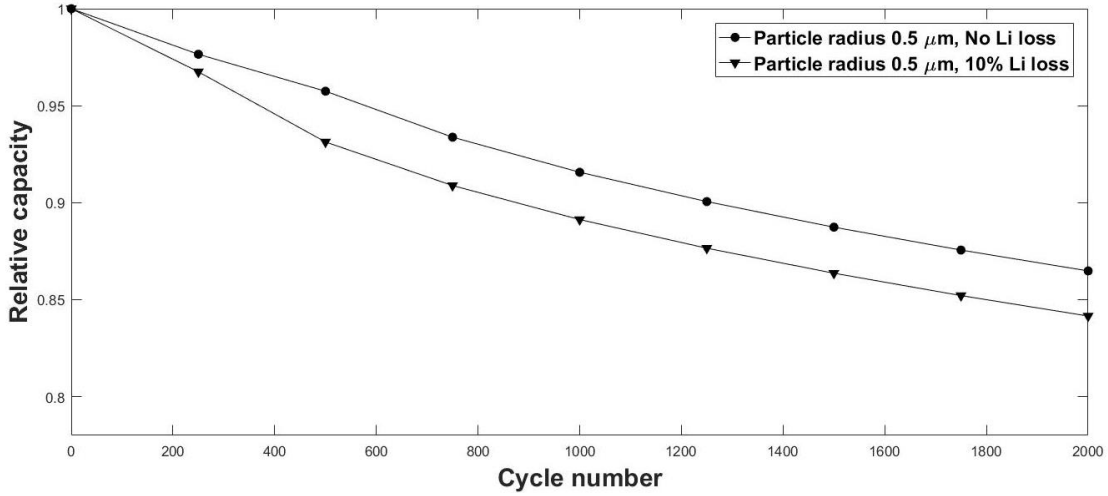

Figure 5. *Comparison of relative capacity with and without lithium loss*

Figures 6 and 7 show the capacity loss in the battery as a function of the anode reaction rate constant.

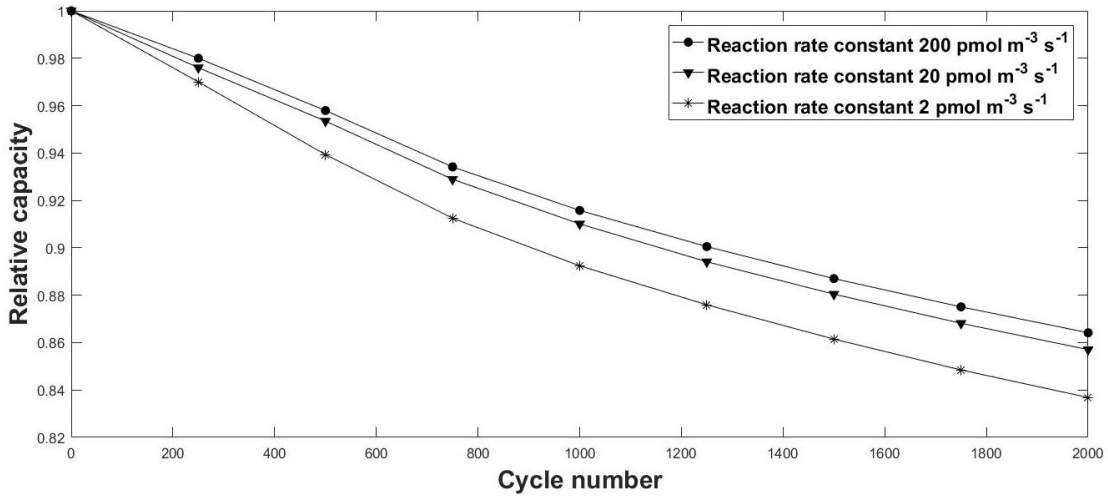

Figure 6. *Capacity loss with cycling for various anode reaction rate constant without lithium loss*

The anode reaction rate constant indicates the intercalation/deintercalation reaction rate constant. Figure 6 shows that when the intercalation/deintercalation reaction rate constant is the

highest, the capacity loss is the lowest. With increasing intercalation/deintercalation reaction rate, the rate of lithium transport increases, effectively increasing the capacity of the battery. While Figure 6 shows the capacity loss when there is no initial cyclable lithium loss during cycling, Figure 7 shows the capacity loss when there is 10 % initial lithium loss during cycling.

Figure 8 shows the comparison of the capacity losses when there are 0 and 10 % lithium losses during cycling. The figure shows that when the initial lithium loss during cycling increases from zero percent to 10 percent, there is a 4 % differential in the capacity loss due to side reactions.

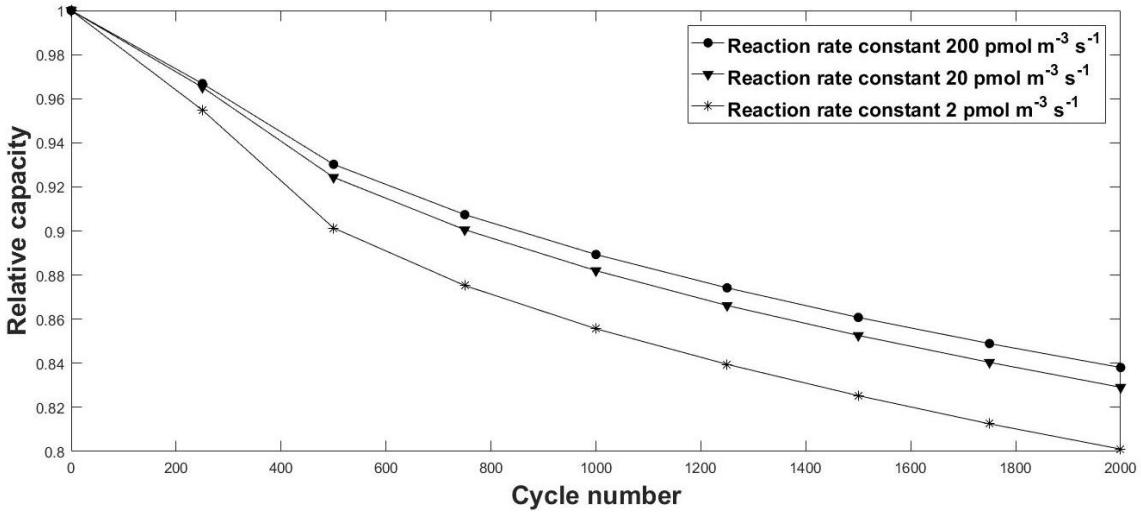

Figure 7. *Capacity loss with cycling for various anode reaction rate constants with 10 % Li loss during cycling*

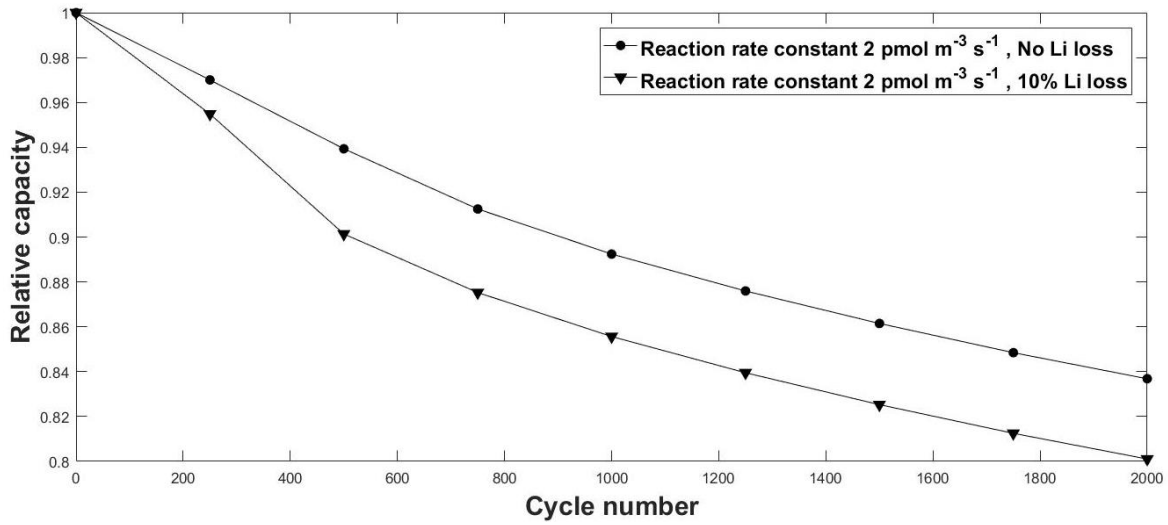

Figure 8. *Comparison of capacity loss for 0 % Li loss and 10 % Li loss*

Effect of anode radius on lithium-ion concentration at the anode/SEI interphase

Figure 9 shows the concentration of lithium ions at the anode/SEI interphase as a function of anode particle radius (4 different particle radii are shown in the figure). It is seen that the highest concentration of lithium ions at the anode/SEI interphase occurs at the smallest particle radius. Smaller anode particles allow lithium ions to intercalate and deintercalated quickly due to the short diffusion path for lithium ion transport within the particles. This leads to a higher concentration of lithium ions at the anode/SEI interphase.

Figure 10 shows the concentration of lithium ions at the anode/SEI interphase as a function of the reaction rate constant for lithium intercalation. With the increasing rate constant of deintercalation, the concentration of lithium ions at the anode/SEI interphase is seen to increase.

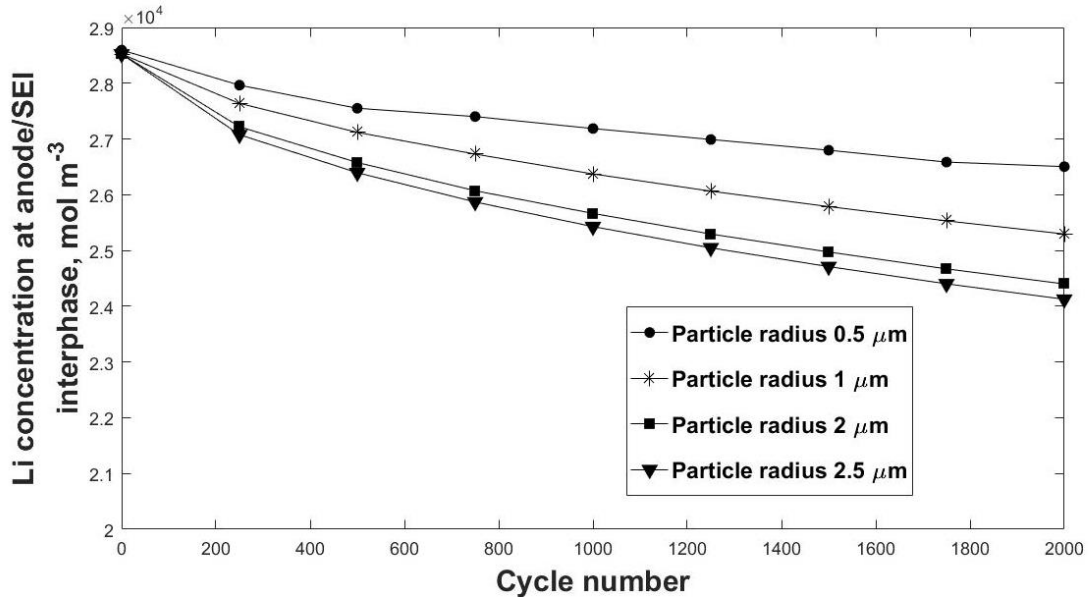

Figure 9. *The concentration of lithium ions at the anode/SEI interphase as a function of anode particle radius*

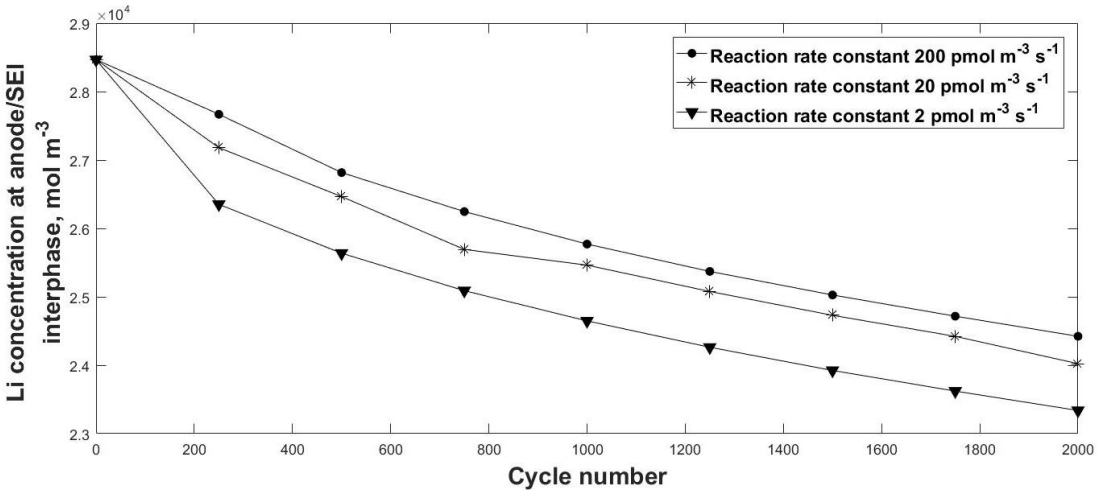

Figure 10. *The concentration of lithium ions at the anode/SEI interphase as a function of the anode reaction rate constant*

Figure 11 shows the concentration of lithium ions at the anode/SEI interphase varying with anode radius in the first and the 2000th cycle.

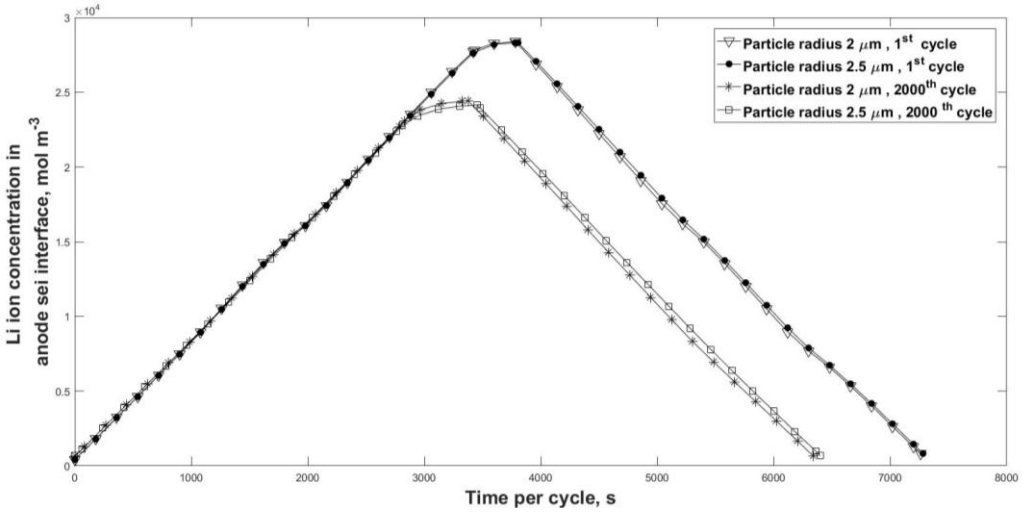

Figure 11. The concentration of lithium ions at the anode/SEI interphase in the first and 2000th cycle

During the charging cycle, lithium from the cathode moves to the anode and hence the concentration of lithium ions at the anode/SEI interphase increases. The lithium ions move from the anode to the cathode during the discharging cycle. Hence, the concentration of lithium ions at the anode/SEI interphase is seen to go from maximum to zero. As the battery cycles, lithium ions are lost in the intercalation deintercalation process. Hence, the concentration of lithium ions at the anode/SEI interphase is lower in the 2000th cycle than in the 1st cycle.

The potential drop across the SEI layer as a function of anode particle radius

Figure 12 shows the effect of anode particle radius on the potential drop across the SEI layer. The figure analyses the effect of four different particles sizes on the potential drop across the SEI layer. The least potential drop across the SEI layer occurs when the anode particle size is the smallest. As explained earlier, smaller anode particle sizes lead to higher intercalation deintercalation rates leading to higher current densities. Given a constant power output, this indicates a lower potential drop across the cell and hence a lower potential drop across the SEI layer.

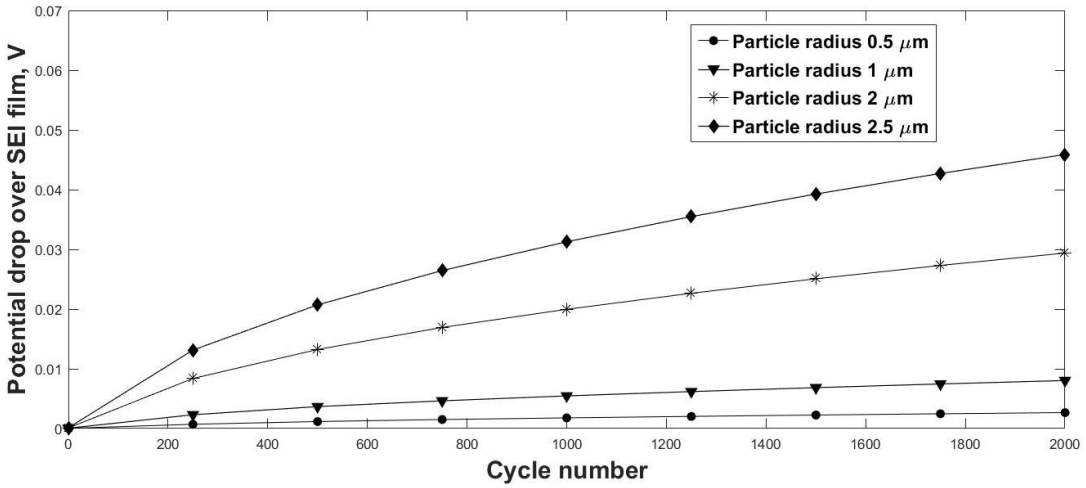

Figure 12. *Potential drop over the SEI film with cycle number for various anode particle radius*

Figure 13 shows the effect of the anode reaction rate constant on the potential drop across the SEI layer.

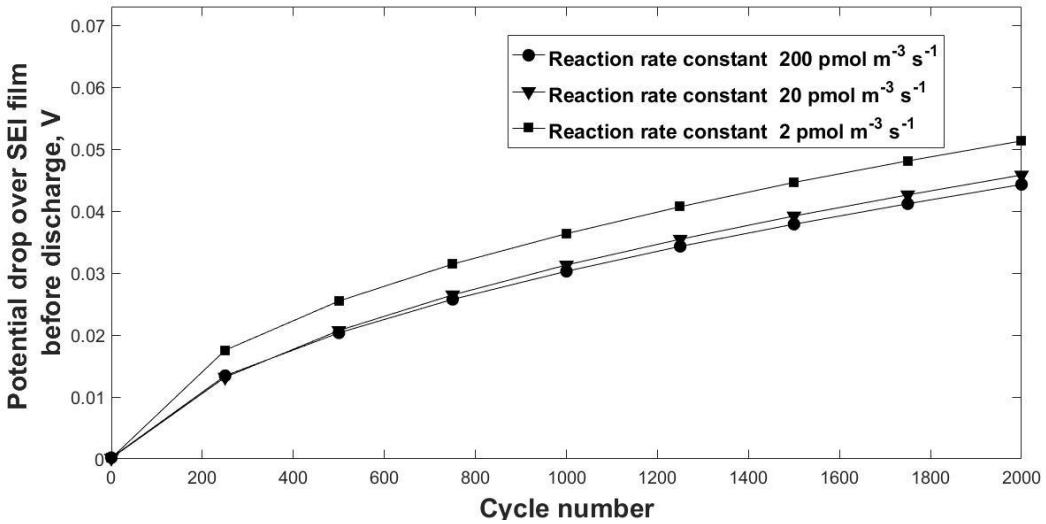

Figure 13. *Potential drop over the SEI layer as a function of anode reaction rate constant*

The graph shows that the potential drop across the SEI layer increases with decreasing rate constant. The anode reaction rate constant indicates the rate of intercalation deintercalation of lithium ions in the anode particles. When the anode reaction rate constant is lower, the intercalation/deintercalation of lithium ions in the anode is reduced, giving rise to a lower current density. Given a constant power output, this indicates an increased potential drop across the cell and, hence, a potential drop across the SEI layer. This is shown in Figure 13.

Figure 14 shows the comparison of modelling predictions with experimental data [3,11]. Modeling predictions are found to compare well with experimental data. The model comparisons are made for 1 C discharge at 45 ^{o}C operating conditions for the lithium-ion battery cell. The parameters used for data fitting are shown in Table 1.

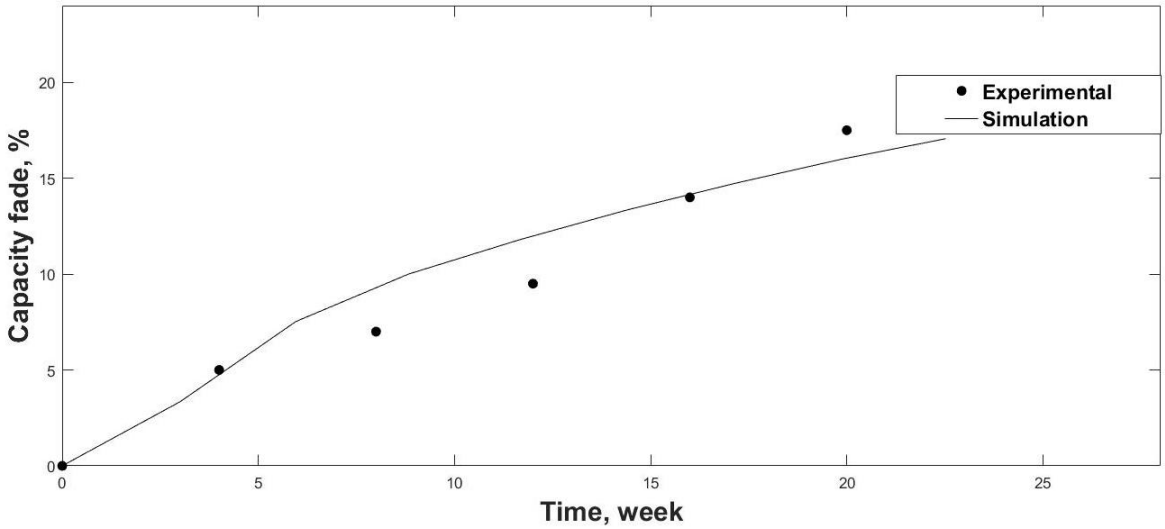

Figure 14. *Comparison of modelling predictions with experimental data of capacity fading percentage at 1C discharge rate and 45 °C [3,11]*

Conclusion

A 1-dimensional mathematical model is developed to study the effect of anode particle radius and anode reaction rate constant on capacity fading of a Li-ion battery. Simulation results predict that for the smallest anode particle radius of 0.5 μm, capacity fading is less in comparison to 2.5 μm. Smaller anode particle radii lead to faster lithium intercalation/deintercalation rates leading to higher current densities and lesser capacity fade. Smaller anode particle radii also lead to increasing anode surface area for reaction. The anode reaction rate constants are also found to play a major role in the capacity fading of lithium-ion batteries. It is found that the higher the anode reaction rate constant, the lesser is the capacity fade in the battery. Model results are compared with experimental data and found to compare well.

Nomenclature

ϕ_s	The electric potential at electrode
ϕ_e	Electrolyte potential
$\Delta\phi_{SEi}$	The potential losses due to SEI layer
C_{Li}	Concentration of lithium in the electrode particles
C_e	Electrolyte salt concentration
σ_e	Electrolyte conductivity
F	Activity coefficient for the salt

t_+	Transport number for Li^+
i_{sum}	Sum of all electrochemical current sources
Q_e, Q_s	Arbitrary electrolyte and electrode current source
ε_e	Electrolyte volume fraction
D_e	Electrolyte salt diffusivity,
R_e	Total Li+ source term in the electrolyte
i_s	Current density in electrode
σ_s	Electrical conductivity of electrode
r_p	Particle radius
$C_{Li,max}$	Total concentration of reaction sites,
D_s	Salt diffusivity at electrode
R_{Li}	Molar flux of lithium at the particle surface
A_v	Specific surface
$R_{l,src}$	Additional reaction sources that contributes to total species source
R_{SEI}	Film resistance
δ_0	Film thickness
$\Delta\delta$	Film thickness change
σ_{SEI}	Film conductivity
H	Activation over potential
E_{eq}	Equilibrium potential of cell
$Q_{cell,0}$	Battery cell capacity
α_a , α_c	Anode and cathode transfer coefficient
k_a , k_c	Reaction rate constant for anode and cathode

Acknowledgement: *The authors would like to acknowledge BITS Pilani, Hyderabad and Council for Scientific and Industrial Research, CSIR Grant No: (No:22/0784/19/EMR II), which helped us in publishing this article.*

Data availability statement*: Data used for this paper can be provided on request*

References

[1] B. S. Haran, P. Ramadass, R. E. White, B. N. Popov, *Seventeenth Annual Battery Conference on Applications and Advances, Proceedings of Conference (Cat. No. 02TH8576),* Long Beach, CA, USA, 2002, 13-18. https://doi.org/10.1109/BCAA.2002.986361.

[2] X. Han, M. Ouyang, L. Lu, J. Li, *Energies* **7(8)** (2014) 4895-4909. https://doi.org/10.3390/en7084895

[3] B. Y. Liaw, E. P. Roth, R. G. Jungst, G. Nagasubramanian, H. L. Case, D. H. Doughty, J*ournal of Power Sources* **119–121** (2003) 874-886. https://doi.org/10.1016/S0378-7753(03)00196-4.

[4] V. Ramadesigan, K. Chen, N. A. Burns, V. Boovaragavan, R. D. Braatz, V. R., *Journal of the Electrochemical Society* **158** (2011) A1048. https://doi.org/10.1149/1.3609926.

[5] A. M. Colclasure, K. A. Smith, R. J. Kee, *Electrochimica Acta* **58** (2011) 33-43. https://doi.org/10.1016/j.electacta.2011.08.067.

[6] M. B. Pinson, M. Z. Bazant, *Journal of the Electrochemical Society* **160** (2013) A243-A250. https://doi.org/10.1149/2.044302jes.

[7] B. Ziv, V. Borgel, D. Aurbach, J.-H. Kim, X. Xiao, B.R. Powell, *Journal of the Electrochemical Society* **161** (2014) A1672-A1680. https://doi.org/10.1149/2.0731410jes.

[8] L. Liu, J. Park, X. Lin, A.M. Sastry, W. Lu, *Journal of Power Sources* **268** (2014) 482-490. https://doi.org/10.1016/j.jpowsour.2014.06.050.

[9] J. Guo, Z. Li, T. Keyser, Y. Deng, *Proceedings of the 2014 Industrial and Systems Engineering Research Conference,* Montréal, Canada (2014) 913-919.

[10] S. Ramesh, B. Krishnamurthy, *Journal of the Electrochemical Society* **162** (2015) A545-A552. https://doi.org/10.1149/2.0221504jes.
[11] S. Ramesh, K.V. Ratnam, B. Krishnamurthy, *International Journal of Electrochemistry* **2015** (2015) 1-9. https://doi.org/10.1155/2015/439015
[12] J. Xu, R. D. Deshpande, J. Pan, Y.-T. Cheng, V. S. Battaglia, *Journal of the Electrochemical Society* **162** (2015) A2026-A2035. https://doi.org/10.1149/2.0291510jes
[13] A. H. N. Shirazi, M. R. Azadi Kakavand, T. Rabczuk, *Journal of Nanotechnology in Engineering and Medicine* **6(4)** (2015) 041003. https://doi.org/10.1115/1.4032012
[14] R. Singhvi, R. Nagpal, B. Krishnamurthy, *Journal of the Electrochemical Society* **163** (2016) A1214-A1218. https://doi.org/10.1149/2.0601607jes.
[15] J. Liang Cheng, X. Hai LI, Z. Xing Wang, H. Jun Guo, *Transactions of Nonferrous Metals Society of China* **27** (2017) 1602-1607. https://doi.org/10.1016/S1003-6326(17)60182-1.
[16] A. Tomaszewska, Z. Chu, X. Feng, S. O'Kane, X. Liu, J. Chen, C. Ji, E. Endler, R. Li, L. Liu, Y. Li, S. Zheng, S. Vetterlein, M. Gao, J. Du, M. Parkes, M. Ouyang, M. Marinescu, G. Offer, B. Wu, *eTransportation* **1** (2019) 100011. https://doi.org/10.1016/j.etran.2019.100011
[17] S. Gantenbein, M. Schönleber, M. Weiss, E. Ivers-Tiffée, *Sustainability* **11(23)** (2019) 6697. https://doi.org/10.3390/su11236697
[18] D. Lee, B. Koo, C. B. Shin, S. Y. Lee, J. Song, I. C. Jang, J. J. Woo, *Energies* **12(22)** (2019) 4386. https://doi.org/10.3390/en12224386
[19] S. Khaleghi Rahimian, M. M. Forouzan, S. Han, Y. Tang, *Electrochimica Acta* **348** (2020) 136343. https://doi.org/10.1016/j.electacta.2020.136343
[20] C. Inc., *Batteries & Fuel Cells Module User's Guide*, COMSOL Multiphysics Help (2012).
[21] A. K. Rai, B. J. Paul, J. Kim, *Electrochimica Acta* **90** (2013) 112-118. https://doi.org/10.1016/j.electacta.2012.11.104
[22] H. Wu, G. Chan, J.W. Choi, I. Ryu, Y. Yao, M.T. Mcdowell, S.W. Lee, A. Jackson, Y. Yang, L. Hu, Y. Cui, *Nature Nanotechnology* **7(5)** (2012) 310-315. https://doi.org/10.1038/nnano.2012.35
[23] H. Buqa, D. Goers, M. Holzapfel, M. E. Spahr, P. Novak, *Journal of the Electrochemical Society* **152(2)** (2005) A474-A481. https://doi.org/10.1149/1.1851055
[24] T. Drezen, H. E. Kwon, P. Bowen, I. Teerlinck, M. Isono, I. Exnar, *Journal of Power Sources* **174** (2007) 949-953 https://doi.org/10.1016/j.jpowsour.2007.06.203
[25] G. T. K. Fey, Y. G. Chen, H. M. Kao, *Journal of Power Sources* **189** (2009) 169-178. https://doi.org/10.1016/j.jpowsour.2008.10.016
[26] W. Mei, H. Chen, J. Sun, Q.Wang, *Sustainable Energy and Fuels* **3** (2019) 148-165 https://doi.org/10.1039/C8SE00503F

J. Electrochem. Sci. Eng. **12(2)** (2022) 373-382; http://dx.doi.org/10.5599/jese.1017

Open Access : : ISSN 1847-9286

www.jESE-online.org

Original scientific paper

Decolorization of industrial wastewater using electrochemical peroxidation process

Elin Marlina[1,✉], Purwanto Purwanto[2] and Sudarno Sudarno[3]

[1]*Doctoral Program of Environmental Science, School of Postgraduate Studies, Universitas Diponegoro, Semarang, Indonesia*

[2]*Department of Chemical Engineering, Faculty of Engineering, Universitas Diponegoro, Semarang, Indonesia*

[3]*Department of Environmental Engineering, Faculty of Engineering, Universitas Diponegoro, Semarang, Indonesia*

Corresponding author: ✉elin.marlina95@gmail.com

Received: June 8, 2021; Accepted: December 3, 2021; Published: December xx, 2021

Abstract

In this study, decolorization of wastewater samples taken from the paper industry is investigated using an electrochemical peroxidation process. The electrochemical peroxidation process is a part of electrochemical advanced oxidation processes, which is based on the Fenton's chemical reaction, provided by the addition of external H_2O_2 into the reaction cell. In this study, iron is used as anode and graphite as cathode placed at the fixed distance of 30 mm in a glass reaction cell. The cell was filled with the solution containing wastewater and sodium chloride as the supporting electrolyte. Factors of the process such as pH, current intensity, hydrogen peroxide concentration, and time of treatment were studied. The results illustrate that all these parameters affect efficiencies of dye removal and chemical oxygen demand (COD) reduction. The maximal removal of wastewater contaminants was achieved under acid (pH 3) condition, with the applied current of 1 A and hydrogen peroxide concentration of 0.033 M. At these conditions, decolorization process efficiency reached 100 and 83 % of COD removal after 40 minutes of wastewater sample treatment. In addition, the electrical energy consumption for wastewater treatment by electrochemical peroxidation was calculated, showing an increase as the current intensity of the treatment process was increased. The obtained results suggest that the electrochemical peroxidation process can remove dye compounds and chemical oxygen demand (COD) from industrial wastewaters with high removal efficiency.

Keywords

Paper industry wastewater; electrochemical peroxidation; Fenton's reaction; decolorization efficiency; chemical oxygen demand

Introduction

Dyes are widely used in various industries such as paper, textile, leather tanning, and printing industries, causing environmental pollution, especially water pollution. Five million quintals of azo dyes are produced each year worldwide, which constitute half of the total dyes produced [1,2].

The paper industry is a type of industry that uses a lot of water and many active ingredients, including dyes [2]. Therefore, besides some active compounds, the wastewater may contain different dyes. Since dye wastewater becomes a problem for the environment, the industry is forced to carry out treatment procedure(s) that can overcome this problem [3–5]. In this context, the removal of active compounds measured as chemical oxygen demand (COD), and decolorization of wastewater, are considered crucial because many dyes and decomposition products are poisonous. Elimination of colours in wastewaters, especially industrial wastewaters, is essential because colour could severely affect the water-living system.

The electro-Fenton's processing is a part of electrochemical advanced oxidation processes (EAOPs) technology. The EAOP process itself pertains to the advanced oxidation processes (AOPs) developed mostly over the last decade by using clean, efficient, and economical processing in removing pollutants in water [6–8]. On the other hand, EAOPs form a group of emerging technologies, where pollutant removal is based on the Fenton's chemical reaction. There are two types of processing, the first one is carried out with the addition of external H_2O_2, and the second involves internal regeneration of H_2O_2 [3]. The electrochemical peroxidation process is part of the first type, where a sacrificial iron or steel anode is used for electro-generation of Fe^{2+} ions by anodic dissolution. H_2O_2 is externally added to the treated solution to degrade organic pollutants with hydroxyl radicals (•OH) generated by Fenton's reaction [9–11].

The electrochemical peroxidation process has a similar mechanism to electrocoagulation, but better COD removal results were obtained with the addition of H_2O_2 [12–14]. Several studies have reported that COD of coke wastewater can be removed up to 90 % by electrochemical peroxidation, whereas by electrocoagulation, up to 30 % was removed only [13].

During past decades, the electrochemical peroxidation process showed a promising perspective in treating several kinds of dyes that contaminated water, causing pollution. In this experimental study, the application of the electrochemical peroxidation process for the decolorization of paper industrial wastewater was explored. Based on previous studies that showed successful decolorization by the Fenton's oxidative processes, in the present study, the opportunity of decolorization of paper industry wastewater has been investigated using the Fenton's oxidation processing. This study will explore the effects of various operating parameters, including the initial pH of the solution, applied current strength, the dosage of H_2O_2, and treatment time on decolorization and COD removal. Energy consumption was also studied to determine the most efficient process conditions for paper industry wastewater treatment. Positive results of this research should increase the knowledge of those responsible for wastewater treatment in the paper industry.

Experimental

Materials and chemicals

Paper wastewater samples were taken from the equalization tank effluent in the paper mill plant in Kudus, District Central Java Province, Indonesia. The physicochemical characterization of these effluents showed COD of 240 mg/L, pH 6.8 and dark yellow colour. H_2O_2 (30 %, w/w), H_2SO_4, and

NaCl were obtained from Merck, Germany. All chemicals were of analytical grade and directly used without purification process.

The experiments were performed at room temperature, using the open single-cell glass reactor with dimensions of 12 × 10 ×12 cm (1.4 L) (Figure 1). The reactor is equipped with two vertical plate electrodes, graphite as cathode and iron plate as anode with 376.2 cm^2 of the total surface area (10×9×0.3 cm). Two electrodes were put at a distance of 3 cm and connected to a DC power supply (MDS PS-305DM). A magnetic stirrer was used to homogenize the electrolyte solution. Distilled water was used throughout this experiment.

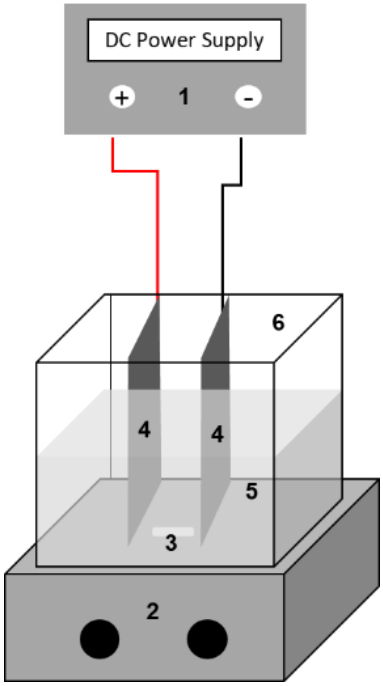

Figure 1. *Glass reactor setup: DC power supply (1); magnetic stirrer (2); magnetic bar-stirrer (3); electrodes (4); solution (5)*

Experimental procedures

The electrodes were cleaned before the experiment by soaking in 0.5 M H_2SO_4 solution for 15 minutes. One litre of wastewater solution was put into the reactor, together with 0.585 g of NaCl (0.01 M) as the electrolytic support, and H_2O_2 was added externally. The batch experiments were carried out in a homogeneous solution. To decrease the pH value, 0.5 M H_2SO_4 was added stepwise to reach the desired pH value. 15 ml of the treated solution were taken at regular intervals and filtered before further analysis.

A water quality meter (Trans Instruments HP9000) was used to test solution pH values. COD samples were tested using a closed reflux titrimetric method based on SNI-06-6989.2-2009 and colour tested using SNI 6989.80:2011. A double-beam UV–vis spectrophotometer (Shimadzu UV-1700, Japan) equipped with a 10 mm quartz cell was used to measure colour and COD concentration by determining absorbance at λ = 450–465 nm for colour and 600 nm for COD.

The removal efficiency was determined by the following equation:

$$Ef = \frac{C_o - C_s}{C_o} 100 \quad (1)$$

where C_o and C_s refer to initial dye concentration and dye concentration at time t, respectively. The electrical energy consumption for a liter of the solution was calculated by:

$$E = Vit \quad (2)$$

Here *E* is the energy consumption in J, *V* is the cell voltage in V, *I* is the current in A, and *t* is the reaction time in s [15].

Results and discussion

The electrochemical peroxidation is one kind of electro-Fenton's process, where the anode is used for electro-generation of Fe^{2+} ions according to:

$$Fe \rightarrow Fe^{2+} + 2e^{-} \quad (3)$$

H_2O_2 is added from outside to degrade organic pollutants with hydroxyl radicals (•OH) created from the Fenton's reaction:

$$Fe^{2+} + H_2O_2 \rightarrow Fe^{3+} + OH^{-} + \cdot OH \quad (4)$$

Fe^{3+} ions formed by Fenton's reaction (4) are continuously reduced at the cathode according to:

$$Fe^{3+} + e^{-} \rightarrow Fe^{2+} \quad (5)$$

In this process, a part of Fe^{3+} ions formed by the Fenton's reaction (4) precipitates as $Fe(OH)_3$ by the reaction, which depends on pH and the applied current value. These deposits can catalytically decompose H_2O_2 to O_2 but also be an alternative for the removal of organic pollutants by coagulation [9].

Effect of initial solution pH

As pointed out in previous studies, the pH of the solution is one of the significant factors affecting the electrochemical work process [16–18]. pH value determines the speciation of iron in solution, and pH 3 was found as the optimum value for dye degradation by electro-Fenton's process. In acidic conditions, iron anode dissolves as Fe^{2+} ions in water according to reaction (3), which will be the catalyst to produce •OH radicals with the added H_2O_2 according to reaction (4). At pH 3, iron ions (Fe^{2+}) and hydrogen peroxide will remain stable. Therefore, the Fenton's reaction can occur perfectly under this condition [20,21].

As presented in Figure 2, 100 % decolorization in acidic conditions (pH 3) was obtained after 60 min of treatment at 0.5 A, when the blue colour changed into clear watercolor. On the other hand, when pH was 6.8 (normal pH), 99 % decolorization was obtained only at the maximum electrolysis time of 120 min.

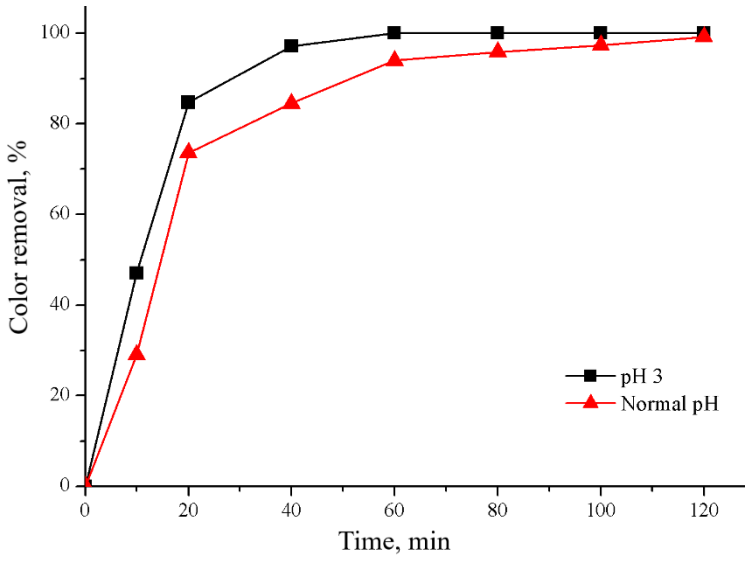

Figure 2. *Decolorization efficiency vs. treatment time at 0.5 A of wastewater samples containing 0.033 M H_2O_2 and 0.01 M NaCl, at pH 3 and 6.8*

COD levels were also tested at two pH values, and Figure 3 presents the results of these experiments. By acidifying the solution, COD was removed up to ~65 % in 120 min. COD removal started immediately with a decrease in COD value, reaching 100 mg/L after 20 min of treating (140 mg/L removed). After 20 min, COD removal did not increase significantly, which can be due to the pH increase of the solution to 5. Previous research on optimal electrochemical peroxidation processes in acidic conditions showed that increased solution pH significantly inhibited COD removal [18,20]. The electrochemical peroxidation process removal decreases rapidly at higher pH values, especially at pH higher than 5 [19]. An increase of pH during the electrochemical peroxidation process leads to the domination of the electrocoagulation process due to the conversion of Fe^{2+} and Fe^{3+} to $Fe(OH)_n$ [21].

In acidic solutions, pH increased significantly during COD removal. As seen in Figure 3, COD removal slowed down after 20 min (pH 4.3 and removal efficiency 59 %). After 120 min, however, pH 9.21 and 62 % removal efficiency were reached. This reinforces the common statement of previous researchers that the best removal in the electrochemical peroxidation process is carried out in acidic conditions [21–23].

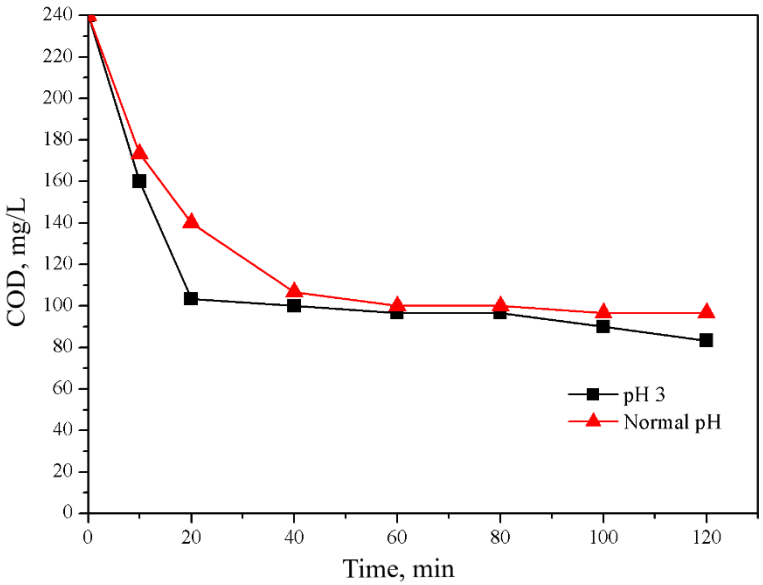

Figure 3 *COD concentration vs. treatment time at 0.5 A of wastewater samples containing 0.033 M H_2O_2 and 0.01 M NaCl, at different pH*

Effect of H_2O_2

As the main source of hydroxyl radicals, the initial concentration of H_2O_2 plays an important role in the electrochemical peroxidation process of oxidizing the pollutants. It has already been found that the removal efficiency increases with the increasing concentration of H_2O_2 in the solution [13,22,24–26]. As presented in Figure 4, increasing the initial concentration of H_2O_2 in wastewater solution containing 0.585 g NaCl, pH 3, improves colour removal. In the absence of H_2O_2, where only the electrocoagulation process is operative, the rate of colour removal after 10 min was 19 %, while after the addition of 0.0165 M H_2O_2, colour removal after 10 min increased to even 30 %. This is due to the presence of more OH• provided by Fenton's reaction (4) in the reactor, which oxidized more organic compounds. The further increase of H_2O_2 concentration to 0.033 M and 0.0495 M improved decolorization after 10 min to 43% and 79%, respectively. Note that for the highest concentration of 0.0495 M H_2O_2, full depolarization is

reached within 20 min. This refinement is related to the generation of more hydroxyl radical species in the presence of increasing amounts of hydrogen peroxide [27].

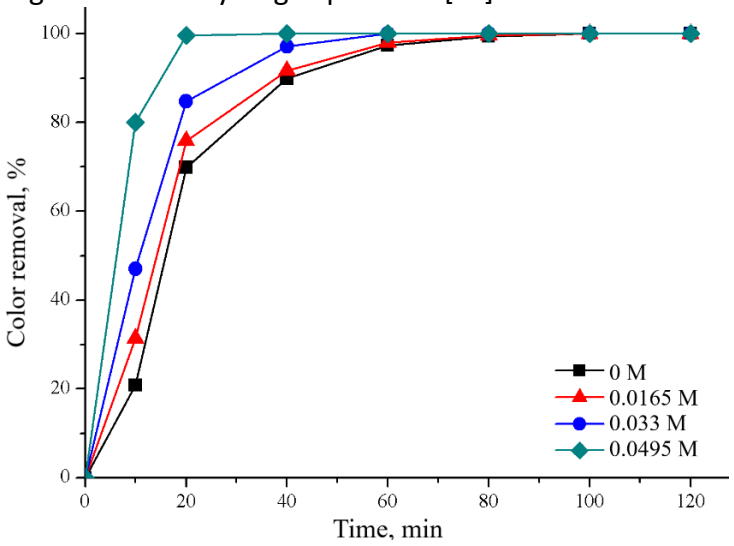

Figure 4. *Decolorization efficiency vs. treatment time at 0.5 A of wastewater samples containing 0.01 M NaCl, pH=3 and different concentrations of H_2O_2*

The effect of H_2O_2 concentration on COD removal was evaluated at the constant current of 0.5 A and started with the solution of pH 3. The results are presented in Figure 5, where it is seen that in the absence of H_2O_2, the rate of COD removal is 13 % since only electrocoagulation is effective in this case. It has already been revealed by previous researchers that the electrocoagulation process has not a significant effect on COD removal [28]. The mechanism of COD removal in the electrocoagulation process is going exclusively through the adsorption process by $Fe(OH)_3$. At H_2O_2 concentration of 0.0165 M, however, COD was reduced by 30 % in 20 min, and this is due to hydroxyl radicals produced in the electro peroxidation process caused by added H_2O_2 [9,29–31]. Figure 5 indicates that increased concentration of H_2O_2 improves COD removal since efficiencies after 20 and 120 min were increased from 29.2 to 63.9 % for 0.0165 M H_2O_2, 33.3 to 65.3 % for 0.033 M and 40.2 to 69.4 % 0.0495 M H_2O_2.

It is also seen in Figure 5 that after 20 min, COD removal increased only slightly for all samples, which is due to the increasing pH value to 5 in 20 min, and 11.2 in 120 min.

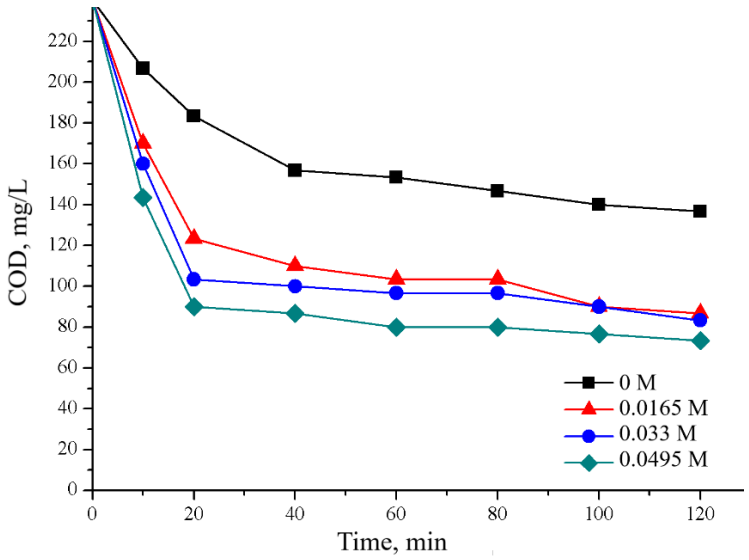

Figure 5. *COD removal vs. treatment time at 0.5 A of wastewater samples containing 0.01M NaCl, pH 3, and different concentrations of H_2O_2*

This suggests that uncontrolled pH conditions affect the process significantly. The performance of the electrochemical peroxidation process is optimal in acidic solutions, where generation of iron ions would occur and react by the classic Fenton's reaction, developing OH• as efficient oxidizers of organic compounds [9].

Effect of applied current

The effect of applied current intensity on the electrochemical peroxidation process was also tested. The influence of different applied current intensities on colour and COD degradations was evaluated in 1 L of wastewater solution with 0.05 M NaCl, pH 3 and 0.033 M H_2O_2. The obtained results are shown in Figures 6 and 7.

Figure 6 shows that different processing results are obtained at different applied current intensities. Generally, colour removal increased with increasing current strength. At 0.3 A, the results showed 10 % decolorization after 10 minutes, while 99 % degradation was observed after 120 minutes. At higher currents of 0.75 and 1 A, respectively, the colour removals reached 79 and 90 % after 10 minutes and 100 % after 120 minutes of treatment. Better colour degradations observed at higher currents may be due to the fact that an increased amount of oxidized iron is generated from the anode at higher currents [32]. On the other side, the high current density is a trigger factor for the oxygen reduction process, which serves to regenerate hydrogen peroxide at the cathode [29,33–35]. The high currents cause an increase in the amount of OH• so that the degradation process is more reactive and responsive [25]. In addition to the increasing amount of OH• in solution, the use of high currents also causes the regeneration of iron ions, and the Fenton process's efficiency also increases [36].

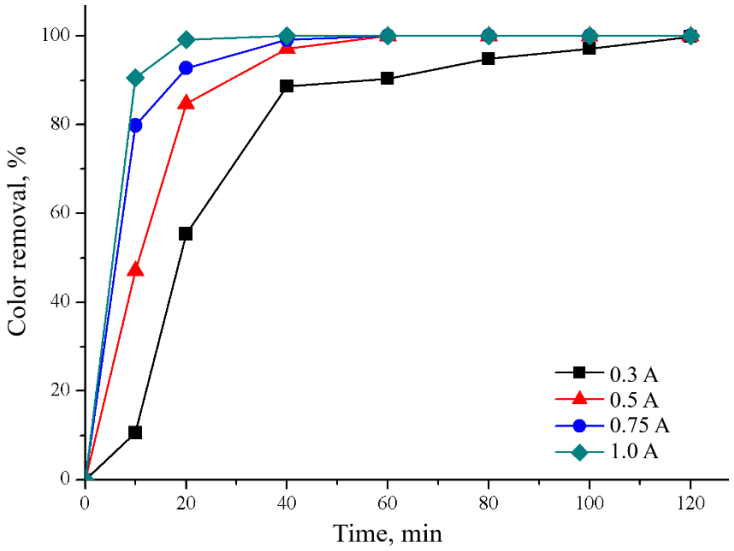

Figure 6. *Decolorization efficiency vs. treatment time of wastewater samples containing 0.033 M H_2O_2 and 0.05M NaCl, pH 3 at different current intensities*

Figure 7 shows that a decrease in COD concentration with treatment time was observed at all current intensities. For the highest current of 1.0 A, there is a significant reduction of COD in 40 min, leaving the lowest COD concentration of 40 mg/L with a removal ratio of 83 %. At 0.3 A, the lowest removal efficiency was obtained, where the removal ratio reached only 54 and 61% in 120 min, with the remaining COD content 110 mg/L in 40 min. When applying the current intensity of 1 A, there is a decrease in the COD removal efficiency in the treatment period of 60 to 120 min. This is probably due to the increase in the amount of Fe^{2+} ions released at the anode through the electrolysis time,

thereby reducing the efficiency electro-Fenton's process [18]. This study has similarities with previous studies [38–40], which showed that an excessive current or voltage would cause a decrease in COD removal.

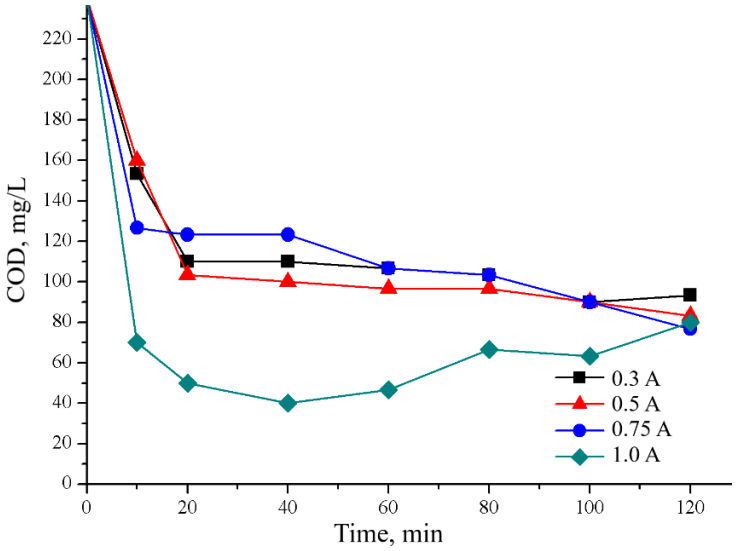

Figure 7 *COD concentration vs. treatment time of wastewater samples containing 0.033 M H_2O_2, 0.05M NaCl, pH 3 at different current intensities*

On the other hand, high currents will increase energy consumption in the electrochemical process [37]. The energy consumption in the process was calculated by eq. (2), where electric voltages recorded after 120 min for current values between 0.3 and 1.0 A (Figure 7), were 7.2, 10.5, 14 and 15 V, respectively. It is obvious from these values that rising currents caused rising voltage. According to eq. (2), energy consumption was calculated to be 15.6, 37.8, 75.6 and 108 kJ. The linear correlation between current, voltage, and energy consumption has already been investigated, giving similar results [15].

Conclusions

In this study, a detailed exploration of the electrochemical peroxidation treatment of paper industrial wastewater is described. It was found that process factors such as pH, applied current, and concentration of added H_2O_2 significantly affect decolorization efficiency and COD removal from the paper wastewater solution. The following conclusions can be derived from the present study:

- The electrochemical peroxidation process is facilitated in an acid condition.
- Colour and COD removal continuously increased as H_2O_2 was added to the process up to the concentration of 0.0495 M.
- The current intensity influences colour and COD degradation in the electrochemical peroxidation process, where clear water was obtained for the current of 1 A in 20 min of treatment.
- The electrochemical peroxidation process can be used as an efficient operational process to remove colour and COD from paper industrial wastewater.

Acknowledgement: *Authors thank Deputy for Strengthening Research and Development, Ministry of Research and Technology / National Research and Innovation Agency of the Republic of Indonesia for funding this research through PMDSU Research Grant 2020 contract: 647-02/UN7.6.1/PP/2020.*

References

[1] A. D. Bokare, R. C. Chikate, C. V. Rode, K. M. Paknikar, *Applied Catalysis B* **79(3)** (2008) 270-278. https://doi.org/10.1016/j.apcatb.2007.10.033

[2] G. Thompson, J. Swain, M. Kay, C. F. Forster, *Bioresource Technology* **77(3)** (2001) 275-286. https://doi.org/10.1016/S0960-8524(00)00060-2

[3] E. Brillas, I. Sirés, M. A. Oturan, *Chemical Reviews* **109(12)** (2009) 6570–6631. https://doi.org/10.1021/cr900136g

[4] C. A. Martınez-Huitle, E. Brillas, *Applied Catalysis B* **87(3-4)** (2009) 105-145. https://doi.org/10.1016/j.apcatb.2008.09.017

[5] N. Klidi, F. Proietto, F. Vicari, A. Galia, S. Ammar, A. Gadri, O. Scialdone, *Journal of Electroanalytical Chemistry* **841** (2019) 166-171. https://doi.org/10.1016/j.jelechem.2019.-04.022

[6] N. Oturan, M. A. Oturan, in: *Electrochemical Water and Wastewater Treatment,* Chap. **8** (2018) 193-221. https://doi.org/10.1016/B978-0-12-813160-2.00008-0

[7] S. Loaiza-Ambuludi, M. Panizza, N. Oturan, A. Özcan, M. A. Oturan, *Journal of Electroanalytical Chemistry* **702** (2013) 31-36. https://doi.org/10.1016/j.jelechem.2013.05.006

[8] T. M. Do, J. Y. Byun, S. H. Kim, *Catalysis Today* **295** (2017) 48-55. https://doi.org/10.1016/j.cattod.2017.05.016

[9] H. Lin, *Removal of Organic Pollutants from Water by Electro-Fenton and Electro-Fenton like Processes,* Ph.D. Thesis, Université Paris-Est, 2015.

[10] P. A. Diaw, N. Oturan, M. D. G. Seye, A. Coly, A. Tine, J.-J. Aaron, M. A. Oturan, *Separation and Purification Technology* **186** (2017) 197-206. https://doi.org/10.1016/j.seppur.2017.06.005

[11] O. Iglesias, M. A. Fernández de Dios, T. Tavares , M. A. Sanromán, M. Pazos, *Journal of Industrial and Engineering Chemistry* **27** (2015) 276-282. https://doi.org/10.1016/-j.jiec.2014.12.044

[12] M. J. Bashir, J. H. Lim, S. S. A. Amr, L. P. Wong, Y. L. Sim, *Journal of Cleaner Production* **208** (2020) 716-727. https://doi.org/10.1016/j.jclepro.2018.10.073

[13] F. Ozyonar, B. Karagozoglu, *Separation and Purification Technology* **150** (2015) 268-277. https://doi.org/10.1016/j.seppur.2015.07.011

[14] G. Selvabharathi, S. Adishkumar, J. R. Banu, *Desalination and Water Treatment* **156** (2019) 340-348. http://dx.doi.org/10.5004/dwt.2019.23935

[15] P. Rafiee, M. Hosseini, S. Ebrahimi, *Reaction Kinetics, Mechanisms and Catalysis* **131** (2020) 319-334. https://doi.org/10.1007/s11144-020-01846-0

[16] A. Baiju, R. Gandhimathi, S. T. Ramesh, P. V. Nidheesh, *Journal of Environmental Management*, **210** (2018) 328-337. https://doi.org/10.1016/j.jenvman.2018.01.019

[17] H. Zhang, X. Ran, X. Wu, *Journal of Hazardous Materials* **241–242** (2012) 259-266. https://doi.org/10.1016/j.jhazmat.2012.09.040

[18] C. T. Wang, W. L. Chou, M. H. Chung, Y. M. Kuo, *Desalination* **253(1-3)** (2010) 129-134. https://doi.org/10.1016/j.desal.2009.11.020

[19] P. V. Nidheesh, R. Gandhimathi, *Desalination* **299** (2012) 1-15. https://doi.org/10.1016/j.desal.2012.05.011

[20] H. Olvera-Vargas, X. Zheng, O. Garcia-Rodriguez, O. Lefebvre, *Water Research* **154** (2019) 277-286. https://doi.org/10.1016/j.watres.2019.01.063

[21] M. Y. A. Mollah, R. Schennach, J. R. Parga, D. L. Cocke, *Journal of Hazardous Materials* **84(1)** (2001) 29-41. https://doi.org/10.1016/S0304-3894(01)00176-5

[22] M.J. Bashir, J.H. Lim, S. S. A. Amr, L. P. Wong, Y. L. Sim, *Journal of Cleaner Production* **208** (2020) 716-727. https://doi.org/10.1016/j.jclepro.2018.10.073

[23] C. Comninellis, G. Chen (Eds.), *Electrochemistry for the Environment,* Springer, London, 2008.
[24] A. Akyol, O. T. Can, E. Demirbas, M. Kobya, *Separation and Purification Technology* **112** (2013) 11-19. https://doi.org/10.1016/j.seppur.2013.03.036
[25] F. C. Moreira, R. A. R. Boaventura, E. Brillas, V. J. P. Vilar, *Applied Catalysis B: Environmental* **202** (2017) 217-261. https://doi.org/10.1016/j.apcatb.2016.08.037
[26] G. Moussavi, M. Aghanejad, *Separation and Purification Technology* **132** (2014) 182-186. https://doi.org/10.1016/j.seppur.2014.05.007
[27] I. A. Alaton, S. Teksoy, *Dyes and Pigments* **73(1)** (2007) 31-39. https://doi.org/10.1016/j.dyepig.2005.09.027
[28] S. Sharma, H. Simsek, *Chemosphere* **221** (2019) 630-639. https://doi.org/10.1016/j.chemosphere.2019.01.066
[29] I. Khatri, S. Singh, A. Garg, *Journal of Environmental Chemical Engineering* **6(6)** (2018) 7368-7376. https://doi.org/10.1016/j.jece.2018.08.022
[30] S. Suhartana, P. Purwanto, A. Darmawan, *Journal of Physics: Conference Series* **1524** (2020) 012086. http://dx.doi.org/10.1088/1742-6596/1524/1/012086
[31] P. Purwanto, R. Riska, *Journal of Physics: Conference Series* **1295** (2019) 012045. http://dx.doi.org/10.1088/1742-6596/1295/1/012045
[32] A. Babuponnusami, K. Muthukumar, *Chemical Engineering Journal* **183** (2012) 1-9. https://doi.org/10.1016/j.cej.2011.12.010
[33] Z. I. Abbas, A. S. Abbas, *Journal of Environmental Chemical Engineering* **7(3)** (2019) 103108. https://doi.org/10.1016/j.jece.2019.103108
[34] E. Marlina, P. Purwanto, *E3S Web of Conferences* **125** (2019) 03003. https://doi.org/10.1051/e3sconf/201912503003
[35] F. G. Camacho, P. A. Latoh de Souza, M. L. Martins, C. Benincá, E. F. Zanoelo, *Journal of Electroanalytical Chemistry* **865** (2020) 114163. https://doi.org/10.1016/j.jelechem.2020.114163
[36] E. Atmaca, *Journal of Hazardous Materials* **163(1)** (2009) 109-114. https://doi.org/10.1016/j.jhazmat.2008.06.067
[37] M. Panizza, M. Delucchi, A. Giuliano, G. Cerisola, A. Barbucci, M. P. Carpanese, M. Cataldo-Hernández, *Separation and Purification Technology* **118** (2013) 394-398. https://doi.org/10.1016/j.seppur.2013.07.023

J. Electrochem. Sci. Eng. **12(2)** (2022) 383-398; http://dx.doi.org/10.5599/jese.1196

Open Access : : ISSN 1847-9286

www.jESE-online.org

Original scientific paper

Pouteria sapota as green CO_2-corrosion inhibition of carbon steel

Guillermo Salinas-Solano[1], Jesus Porcayo-Calderon[2], Ana Karen Larios-Galvez[1] and Jose Gonzalo Gonzalez-Rodriguez[1,✉]

[1]*Universidad Autonoma del Estado de Morelos, Centro de Investigación en Ingeniería y Ciencias Aplicadas, Av. Universidad 1001, 62209-Cuernavaca, Morelos, Mexico*

[2]*Universidad del Estado de Sonora, Departamento de Ingenieria QUimica y Metalurgica, Hermosillo, Sonora 83000, Mexico*

Corresponding author: ✉ggonzalez@uaem.mx; Tel: 52777 3297084

Received: October 21, 2021; Accepted: January 21, 2022; Published: January 31, 2022

Abstract

Imidazoline obtained from the essential oil contained in Pouteria sapota seed was tested as an environmentally-friendly corrosion inhibitor of 1018 carbon steel in a CO_2 saturated 3.5 % NaCl solution using electrochemical techniques. This imidazoline contains fatty acids with long hydrophobic chains, with 52.73 % of unsaturated (oleic and linolenic acids) and 40 % of saturated (palmitic and myristic acids) compounds. Polarization curves revealed that this inhibitor is a highly efficient mixed-type of inhibitor with the inhibitor efficiency of 99.9 % reached at 25 ppm. Also, the lowest pitting potential value was observed at 25 ppm of inhibitor, making the carbon steel highly susceptible to the pitting type of corrosion. Corrosion current density value decreased by nearly four orders of magnitude, and a passive film formation was induced for inhibitor concentrations higher than 5 ppm. Accordingly, polarization resistance values were increased from 100 $\Omega\,cm^2$ up to about $10^6\,\Omega\,cm^2$ at 25 ppm of inhibitor. The inhibitor forms a protective film of corrosion products adsorbed on the metal surface in a very strong chemical way, following a Langmuir type of adsorption isotherm. This was supported by electrochemical impedance spectra that showed two relaxation processes ascribed to electrode interface and film regions. In agreement with polarization resistance data, the total electrode resistance determined by interfacial charge transfer and film resistance increased up to $8.2 \times 10^5\,\Omega\,cm^2$ in the presence of 25 ppm of inhibitor. SEM images additionally showed that type of corrosion was fully changed from uniform to a localized type when 25 ppm of inhibitor was added into the solution.

Keywords

Acid corrosion; naturally occurring inhibitor; electrochemical impedance

Introduction

The presence of water in the oil and gas field, together with high content of CO_2, acetic acid, and H_2S, has increased the corrosion rate of involved metals [1,2]. One of such involved metals is carbon steel, which is extensively used in the oil industry as the most common material for tubing. One of the most frequently used methods to mitigate CO_2-corrosion is by applying organic inhibitors, where the presence of heteroatoms including phosphorus, nitrogen, sulfur and carbon protects steel surface by forming a barrier of corrosion products. In such a way, metals are protected from the action of the environment [3-10]. However, due to serious environmental concerns, a lot of research concerning less toxic, cheaper, and more environmentally friendly compounds has been undertaken in the last years [11-13]. Thus, *Allium cepa* [11], expired drugs [14-18], *Thymbra capitate* [15], amino surfactants and imidazolines obtained from palm, avocado and rice bran oil [13,19,20] were already evaluated as corrosion inhibitors for iron and steel in different media. Abdallah *et al*. [12] evaluated natural nutmeg oil as a green inhibitor for carbon steel in 1.0 M HCl solution, finding that inhibitor efficiency increased with its concentration, reaching a maximum value of 94 % at 500 ppm. According to Langmuir adsorption isotherm, this inhibitor acted as a mixed type of inhibitor and was adsorbed on the steel. Similarly, Carmona-Hernandez *et al.* [13] studied imidazole obtained from palm oil as a corrosion inhibitor for UNS S41425 type supermartensitic stainless steel in an H_2S-containing environment. The authors found that at inhibitor concentrations between 0 and 100 ppm, the maximum inhibitor efficiency was obtained at 25 ppm, decreasing with a further increase of inhibitor concentration. Imidazole was physically adsorbed onto the steel according to Langmuir adsorption isotherm, behaving as a mixed-type of inhibitor. In another work, Abdallah *et al.* [16] evaluated curcumin, parsley and cassia bark extracts as green inhibitors for carbon steel corrosion in 0.5 M sulfuric acid. They found that inhibition efficiency increased with inhibitor concentration, while inhibition efficiency of each particular inhibitor decreased in the following order: cassia bark extract > parsley extract > curcumin extract. Imidazolines obtained from avocado and rice bran oil were obtained and evaluated as CO_2-corrosion inhibitors for X-52 steel [19,20]. Both inhibitors contained fatty acids and were evaluated in concentrations of 0, 5, 10, 25, 50 and 100 ppm. It was found that in both cases, the maximum inhibition efficiency was reached at 25 ppm and decreased with a further increase of inhibitor concentration.

Mamey sapote [*Pouteria sapota*] is a very popular fruit growing in Mexico and Central America [21]. It is a fruit tree that has the potential to be cultivated in 15 of 32 states, *i.e.,* over almost 50 % of the Mexican territory. Its production is concentrated in the south, southeast, west and some central states with an area of 1,618 hectares, with a total production of 20,120 tons of fruit, and a national average yield of 12.4 tons ha^{-1} [22]. It is a cheap fruit, less than U.S. $1000 per ton, although currently, oil extraction is somehow expensive. Antioxidant activity of *Pouteria sapota* pulp has already been assessed, finding different phenolic acids, flavonoids, and carotenoids, and the inclusion of such fruit has been recommended in daily diets [23].

Nevertheless, such studies have considered only the flesh and little information exists regarding the seed or bone, although some information suggests the existence of fatty acids [24]. Recently, different researchers evaluated fatty acids contained in palm, avocado and rice bran oil, similar to antioxidants reported for *Pouteria sapota,* as green corrosion inhibitors for steel in CO_2 and H_2S-containing environments [13,19,20]. Thus, the goal of this research is to evaluate use of the oil contained in the *Pouteria sapota* seed to obtain an imidazoline as corrosion inhibitor for 1018 carbon steel in a CO_2-saturated NaCl solution.

Experimental procedure

Materials and sample preparation

The material used in this research work includes bars of 1018 carbon steel having a chemical composition given in Table 1. Specimens were grounded with 1200 grade emerging paper, rinsed with distilled water, acetone and blown with hot air.

Table 1. *Chemical composition of 1018 carbon steel*

Element	Content, wt.%
Fe	Balance
C	0.14
Mn	0.60
S	<0.05
P	<0.05

Inhibitor synthesis

Imidazoline from *Pouteria sapota* seed oil was obtained by the Soxhlet method to extract the crude oil using hexane as a solvent. Afterward, a bleaching process was carried out on the crude oil using Tonsil and activated carbon in concentrations of 2 and 0.5 %, respectively. This process was performed at 95 °C under constant stirring during 20 min. The oil obtained was filtered under a suction method and mixed with water at 95 °C. Finally, the obtained emulsion was centrifuged to obtain the semi-refined oil. This semi-refined oil was the precursor solution in the synthesis of the imidazoline-based inhibitor. The inhibitor synthesis process was carried out in two stages, as illustrated in Figure 1.

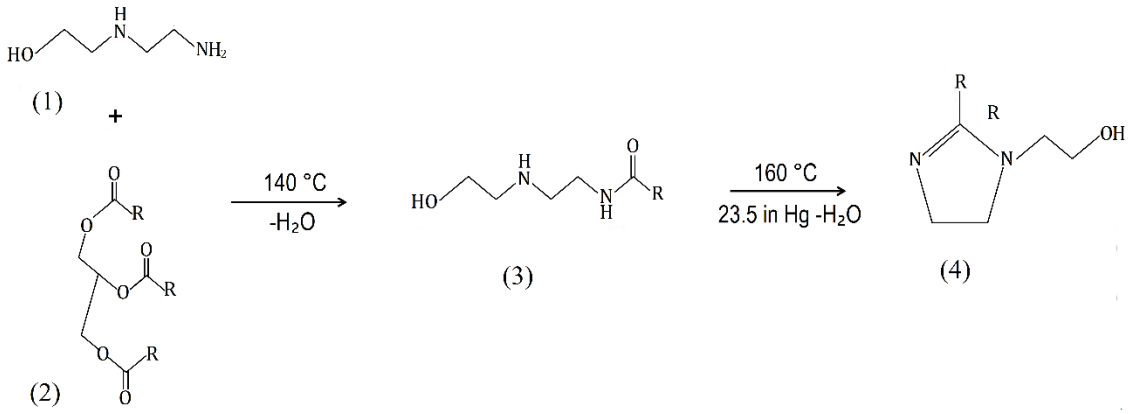

Figure 1. *Synthesis of the imidazoline-based inhibitor from semi-refined Pouteria sapota oil: (1) N-(2-hydroxyethyl) amino ethylamine; (2) Pouteria sapota oil; (3) N-[2−[(2-hydroxyethyl) amino]ethyl]−amide, fatty amide, and (4) fatty-imidazoline derivative from the raw Pouteria sapota oil, where R=alkyl chain of Pouteria sapota oil fatty acid*

At first, amidation was carried out by hydroxyethyl ethylene diamine during 2.5 hours at 140 °C. This reaction was monitored by the thin layer chromatography technique (TLC) using heptane-ethyl acetate (Sigma Aldrich) (9:1) as eluent. The reaction products were removed by washing and filtering and analysed by the Fourier transform infrared spectroscopy (FTIR) technique. The second synthesis step consisted of performing the imidazoline cyclization reaction. This was carried out once purified fatty-amide was placed at vacuum (79.58 kPa) and heated at 160 °C for 16 hours using (8.5:1.5:5) dichloromethane (Sigma Aldrich), methanol (Baker), ammonium hydroxide (Baker) as eluent while the reaction products were analysed using FTIR. The obtained inhibitor was stored inside a glass beaker

at room temperature. Gas chromatography was used in order to know the type of fatty acids found in the *Pouteria sapota* seed oil as described elsewhere [25]. The oil extracted from *Pouteria sapota* seed was analyzed with an FTIR *Spectrophotometer from* Bruker. As a corrosive environment, a CO_2-saturated 3.5 % NaCl heated at 50 °C was used according to the NACE standard method NACE TM 177-2005, widely used in the literature [13,19,20,25]. Before starting with corrosion tests, the solution was bubbled with CO_2 gas during 2 hours and the gas bubbling continued during testing. Inhibitor concentrations were chosen to be 0-100 ppm, as were also used in previous works [13,19,20]. These concentrations have also been recommended by manufacturers for commercial imidazolines. Tests were carried out under stagnant conditions as a first inhibitor screening in order to know the optimum inhibitor concentration.

Electrochemical tests

Electrochemical measurements were conducted in a conventional glass cell using a potentiostat from ACM Instruments. Rods of 1018 carbon steel were encapsulated in polymeric resin with an exposed working area of 0.5 cm^2. As auxiliary and reference electrodes, graphite cylindrical bars and a saturated calomel electrode (SCE) were used. Tests were performed at the temperature of 50 °C. Before starting the experiments, 30 minutes was given for the open circuit potential value (OCP) to reach a steady-state value. Potentiodynamic polarization curves were obtained by applying a cathodic potential 800 mV more negative than the free corrosion potential (E_{corr}) and then the sweeping started in an anodic direction at the scan rate of 1 mV s^{-1}, ending at a potential of 800 mV more anodic than E_{corr}. Tafel extrapolation was used to calculate the corrosion current density values, j_{corr}. Electrochemical impedance spectroscopy (EIS) measurements were performed at the E_{corr} by applying an alternating potential of ± 10 mV in the frequency range between 10 kHz and 0.04 Hz. In order to know the change in the corrosion behavior with time, linear polarization resistance (LPR) measurements were carried out. For this, specimens were polarized ±15 mV every hour during 24 hours. All experiments were performed three times. The surface of specimens used for LPR experiments was analyzed by the scanning electronic microscope (SEM) LEO VP 1450, whereas chemical analysis of corroded specimens was performed with an X-ray energy dispersive spectrometer (EDS) attached to it.

Results and discussion

Inhibitor characterization

Palmitic acid is the major fatty acid contained in the *Pouteria sapota* oil with 25.5 wt.%, followed by 19.1 % of oleic acid, 16.1 % of myristic acid and 14.1 % of linoleic acid. In Table 2, the full profile of fatty acids contained in the *Pouteria sapota* oil is shown. Chemical structures of palmitic and oleic acids are given in Figure 2.

Table 2. *Fatty acid composition of Pouteria sapota oil*

Fatty acid	Structure	Type of fatty acid	Content of fatty acid, wt. %
Palmitic acid	C16:0	Saturated	24.5
Myristic acid	C14:0	Saturated	16.1
Oleic acid	C18:1 *n*-9 cis	Unsaturated	19.1
Linoleic acid	C18:2 *n*-6 cis	Unsaturated	14.1
Linolenic acid	C18:3 *n*-3 cis	Unsaturated	2.4
Arachidic acid	C20:0	Unsaturated	0.6

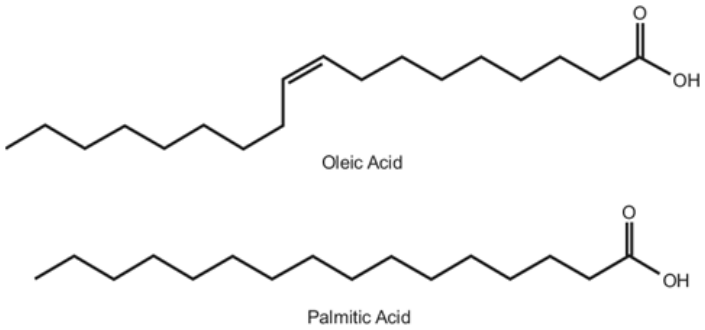

Figure 2. *Chemical structures of oleic and palmitic acids*

IR spectra of *Pouteria sapota* oil and synthesized inhibitor are shown in Figure 3. The observed C=O stretching signal at 1743 cm^{-1} corresponds to the ester vibration, whereas at 1642 cm^{-1} was assigned to the fatty amide. The inhibitor response presents a signal observed at 1720 cm^{-1} which was assigned to the ester group. Observed peaks at 1560 and 1470 cm^{-1} were assigned to C=C and C=N stretches in the ring of imidazole, whereas another signal observed at 1080 cm^{-1} to C-H stretch. The group N-H of imidazole at 3150 cm^{-1} is due to the aromaticity of the ring. On the other hand, the peak observed at 1630 cm^{-1} corresponds to the C=O stretch of the amide. In addition, observed peaks at 1280 and 1200 cm^{-1} correspond to the stretching of C-N and C-O groups, respectively. Finally, observed signals at 2920 and 2852 cm^{-1} were assigned to the methyl and methylene groups, respectively.

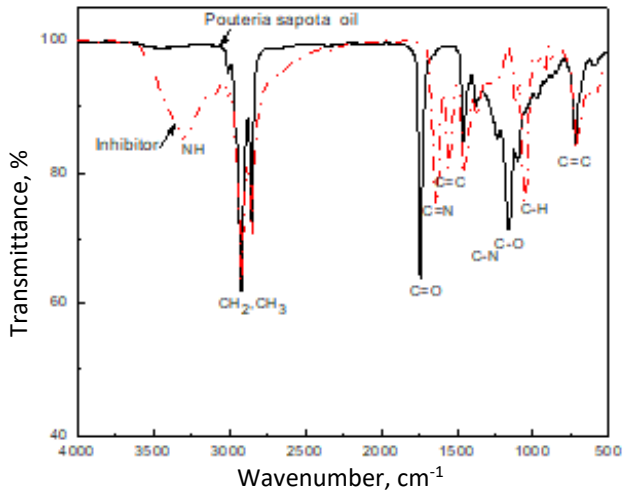

Figure 3. *FTIR spectra of Pouteria sapota oil and synthesized inhibitor*

Open circuit potential

The time changes of OCP values for 1018 carbon steel exposed to the CO_2-saturated 3.5 % NaCl solution, without and with different inhibitor concentrations, are shown in Figure 4.

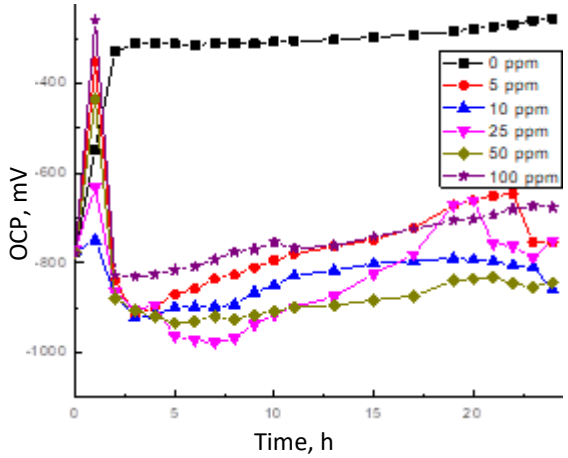

Figure 4. *Variation of OCP value with time for 1018 carbon steel in CO_2-saturated 3.5 % NaCl solution containing different concentrations of inhibitor at 50°C*

Figure 4 shows that the OCP value is rapidly shifted towards the noble direction for the blank, uninhibited solution, reaching a steady-state value after 2 or 3 hours of exposure to the environment. This shift can be due to the protection of steel by the formation of iron carbonate film on its surface [26-29]. When the lowest inhibitor concentration (5 ppm) was introduced into the solution, the OCP value became more negative, reaching a steady-state value within 2-3 hours of testing. At higher inhibitor doses, *i.e.,* at 10 and 25 ppm, the OCP value became more negative. With higher doses of inhibitor, however, the OCP value shifted to a noble direction, reaching the noblest value with the addition of 100 ppm. A shift of the OCP value towards more negative values means that the metal is getting corroded, dissolving any protective film formed on the metal surface. On the contrary, if the OCP value moves toward the noble direction, it indicates that the metal has been protected by the formation of a film made from corrosion products [30].

Polarization curves

The effect of inhibitor concentrations on the polarization curve of 1018 carbon steel in the CO_2-saturated 3.5% NaCl solution is shown in Figure 5.

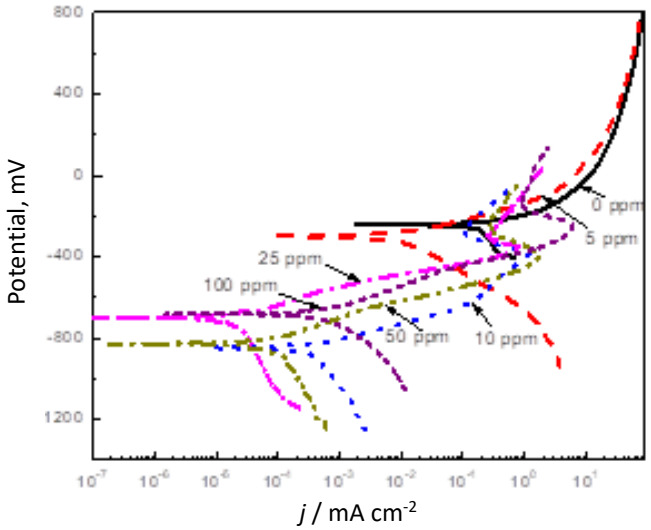

Figure 5. *Effect of inhibitor concentrations on polarization curve of 1018 carbon steel in CO_2-saturated 3.5 % NaCl solution at 50°C*

Figure 5 shows that in the uninhibited solution, there is no evidence of the existence of any passive layer on the steel surface. Similar behavior is observed when 5 ppm of inhibitor were added into the system, although j_{corr} value decreased from a value of 2.0×10^{-1} mA/cm^2 down to 10^{-2} mA/cm^2 as shown in Table 3. In the absence of inhibitor and in the CO2 environment, iron carbonate film, which is not protective, is developed on the steel surface, which is why the passive layer was not formed. With the addition of low doses of inhibitor, inhibitor reacts with the released iron ions, forming a layer of corrosion products that acts as a barrier between the metal and the environment. This barrier makes their contact more difficult, which results in a decrease of j_{corr} value. As the inhibitor doses increased up to 25 ppm, a significant reduction in the j_{corr} value can be observed, reaching its lowest value of 3.0×10^{-5} mA/cm^2. After a further increase of the inhibitor concentration, however, j_{corr} increased again. Generally, a decrease of j_{corr} value with the addition of inhibitor is due to its adsorption on the steel surface and the formation of a passive layer. As the inhibitor concentration increases, the number of its molecules covering the steel surface increases too, and due to the existence of the same electric charge, there is an electrostatic repulsion among

inhibitor molecules. This results in the inhibitor desorption from the steel surface, leaving the unprotected metal at the places of desorption. Salinas-Solano *et al.* [19] reported the lowest j_{corr} value of 2.34 × 10^{-4} mA/cm^2 whereas Cruz-Zabalegui *et al*. [20] reported the value of 6.0 × 10^{-3} mA/cm^2 for carbon steel in CO_2-saturated 3.5 % NaCl solution, by using amino surfactants and imidazolines obtained from avocado and rice bran oil, respectively. Both reported j_{corr} values are, however, much higher than the minimal value of j_{corr} = 3.0×10^{-5} mA/cm^2 reported in this study (Table 3). Polarization curves for inhibitor concentrations higher than 5 ppm in Figure 5 displayed the presence of a passive layer.

The values of j_{corr} were used to calculate the inhibitor efficiency values (*IE*) as follows:

$$IE = \frac{j_{corr} - j_{corr/inh}}{j_{corr}} 100 \quad (1)$$

where the corrosion current density values obtained in the absence and presence of the inhibitor are represented by j_{corr} and $j_{corr/inh}$, respectively. Calculated *IE* values are listed in Table 3.

Table 3. *Electrochemical parameters obtained from polarization curves*

C_{inh} / ppm	E_{corr} / mV	j_{corr} / mA cm^{-2}	E_{pit} / mV	β_a / mV dec^{-1}	β_c / mV dec^{-1}	*IE* / %	θ
0	-240	2.0 × 10^{-1}	-	50	245		
5	-300	3.0 × 10^{-2}	-	60	200	95.0	0.95
10	-850	3.0 × 10^{-4}	-255	65	380	99.8	0.99
25	-700	3.0 × 10^{-5}	-290	70	400	99.9	0.99
50	-830	2.0 × 10^{-5}	-230	75	450	99.9	0.99
100	-680	6.0 × 10^{-4}	-110	80	300	99.7	0.99

Data in Table 3 show an increase in the inhibitor efficiency value with an increase in its concentration up to 25 ppm, and a decrease for higher concentrations. The fractional surface coverage by the inhibitor (θ), which was calculated by dividing the inhibitor efficiency value by 100, behaves in the same fashion as the inhibitor efficiency. The highest efficiency value of 99 % was obtained with the addition of 25 ppm, which is similar to the reported by Salinas-Solano *et al*. [19] but higher than 93 % reported by Cruz-Zabalegui *et al*. [20]. Zheng *et al*. [31] used a mercaptopropionic acid-modified oleic imidazoline as a highly efficient corrosion inhibitor for carbon steel in CO_2-saturated formation water and obtained *IE* value of 95 % with the addition of 20 ppm. At the same time, j_{corr} value was decreased for 2 orders of magnitude. Sotelo-Mazon *et al*. [32] obtained *IE* of 99 % with-imidazoline synthesized from wasted avocado oil for carbon steel in CO_2-saturated 3.5 % NaCl solution, and j_{corr} value was reduced for 2 orders of magnitude, from 0.1 to 0.001 mA cm^{-2}. Okafor *et al*. [33] obtained an inhibitor efficiency of 97 % with the addition of 200 ppm of a rosin amide imidazoline for N80 carbon steel in CO_2-saturated simulated formation water, with the reduction of j_{corr} value from 0.1 down to 0.005 mA cm^{-2}. Therefore, the present results, which show that for a relatively low inhibitor concentration of 25 ppm, high inhibitor efficiency of 99 % is attained and j_{corr} value is reduced for even four orders of magnitude, are very encouraging. All these justify the use of *Pouteria sapota,* not only because it is a green inhibitor but also because it is obtained from a waste agro-industrial product that is a very abundant product in our country that can be utilized in this way.

A possible effect of pitting corrosion, which is a localized type of corrosion characteristic for breaking of passive film on stainless steel in solutions containing chloride ions, is further explored. The effect of the inhibitor concentration on the pitting potential (E_{pit}) value can be seen in Table 2. Since no passive film formation at 0 and 5 ppm was observed, there is no value for E_{pit} at these inhibitor concentrations. However, it can be seen that at the inhibitor concentration of 10 ppm, E_{pit}

value of -255 mV is observed, and it became more active at 25 ppm, showing E_{pit} of -290 V. As the inhibitor concentration increased further, E_{pit} attained more positive values of -230 and -110 mV at inhibitor concentrations of 50 and 100 ppm, respectively.

Data in Table 2 clearly shows that anodic Tafel slopes remained virtually unaffected by the addition of the inhibitor, unlike the cathodic one, which was greatly affected, indicating that this inhibitor behaves as a mixed-type of inhibitor with a predominant cathodic effect. This way, it can be said that anodic reactions such as iron dissolution remained practically unaffected by the addition of the inhibitor, whereas cathodic reactions such as oxygen reduction and hydrogen evolution (HE) were severely affected. This indicates that this inhibitor blocked the sites where protons can be adsorbed on the metal surface for the HE reaction [34,35].

It has already been established that the adsorption of an organic compound such as an inhibitor on a metal surface depends, among other things, upon its chemical structure and chemical compositions of substrate and electrolyte [36]. At the steel/electrolyte interface, an organic compound can be absorbed by: i) electrostatic interaction between metal and inhibitor, ii) interaction between the inhibitor uncharged electron pairs and metal surface, and iii) interaction of π electrons of inhibitor with the metal [25]. In order to get more information about the way of interaction between an inhibitor and metal, it is necessary to know the adsorption isotherm. In Figure 6, different adsorption isotherm models, *i.e*., Langmuir, Temkin and Frumkin, are tested with data obtained for different concentrations of Pouteria sapota oil as an inhibitor for 1018 carbon steel in CO_2 saturated 3.5 % NaCl.

It is obvious from Figure 6 that the best fit to predicted linear dependences, measured by the correlation factor (R^2), were obtained for the Langmuir type of adsorption isotherm. For this isotherm, this factor was 0.99, whereas, for Temkin and Frumkin isotherms, it had values of 0.70 and 0.79, respectively. This factor is a measure of the correlation between experimental and predicted data, and closer to the unit, the better is the correlation.

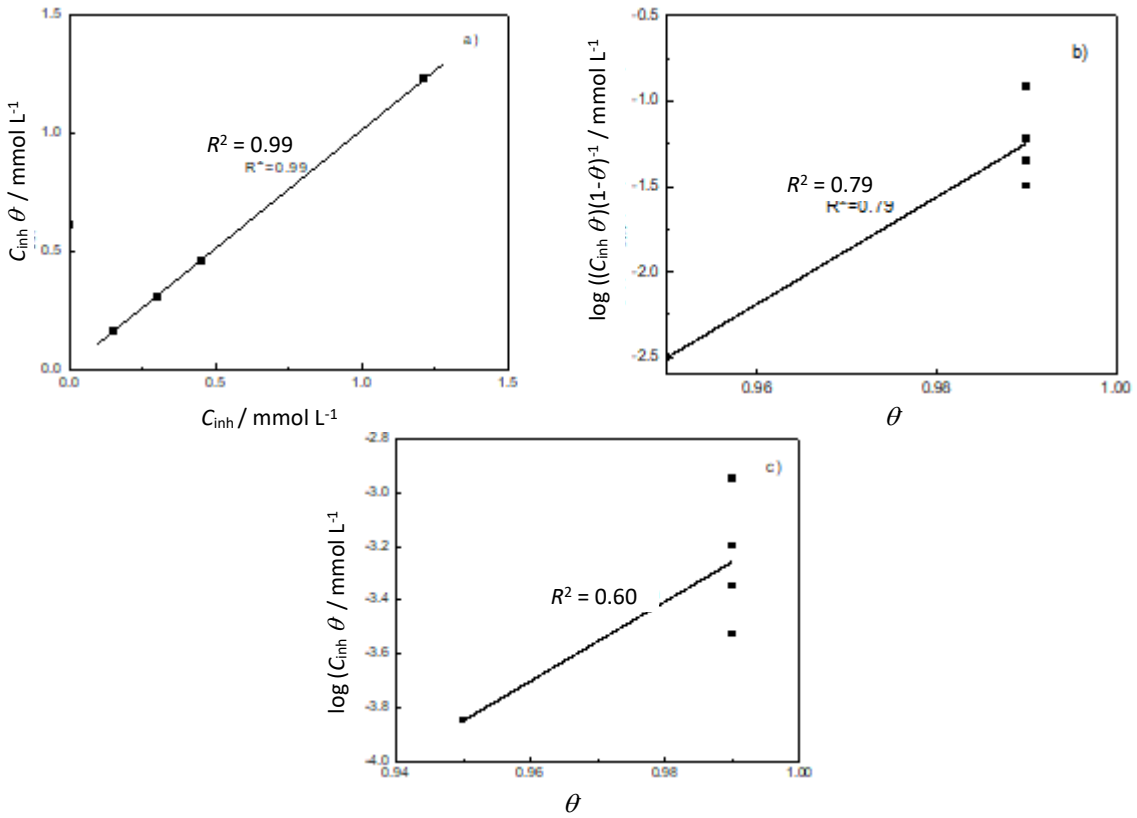

Figure 6. *a) Langmuir, b) Frumkin and c) Temkin isotherm plots for 1018 carbon steel in CO_2-saturated 3.5% NaCl solution containing different concentrations of inhibitor at 50 °C*

Langmuir isotherm assumes that the interaction between molecules and a surface can be described by a simple equilibrium, with the equilibrium constant K_{ads}. It does not take the interaction between adsorbed molecules into account, nor modification of the surface by the adsorption. Langmuir adsorption isotherm is a function between the fractional surface coverage by the inhibitor (θ) and its concentration (C_{inh}) according to equation (2):

$$\frac{C_{inh}}{\theta} = \frac{1}{K_{ads}} + C_{inh} \quad (2)$$

The adsorption equilibrium constant K_{ads} has a relationship with the standard free energy of adsorption (ΔG^0_{ads}) through the following equation (3):

$$G^0_{ads} = -RT \ln(10^6 K_{ads}) \quad (3)$$

where R is the universal gas constant, and T is the absolute temperature. Using data from Figure 6a, the calculated value for ΔG^0_{ads} was −43.34 kJ mol^{-1}, indicating strong adsorption on the metal surface due to the sharing of charges between the molecules and/or the formation of coordinated type bonds (chemisorption).

One of the explanations for the high inhibitory effect of imidazoline is the presence of nitrogen atoms located in the structural ring, as well as the high number of carbon atoms in the molecule, which will act as a barrier against electrolyte. Also, double bonds in the compound chemical structure have been reported as part of this high inhibitory efficiency [36]. Compounds found by the gas chromatography analysis detected the presence of palmitic (C16:0), myristic (C14:0), oleic (C18:1 n-9 cis), linoleic (C18:2 n-6 cis) and linolenic (C18:3 *n*-3 cis) acids in proportions of 24.5, 16.1, 19.1, 14.1 and 2.4 wt.% [36]. These compounds meet two characteristics that make an organic compound a very efficient inhibitor, i.e., long chains of hydrocarbons and the presence of double bonds.

Linear polarization resistance (LPR) measurements

Data given in Figure 7 represent the variation on the polarization resistance (R_p) value with the inhibitor concentration in the CO_2 environment.

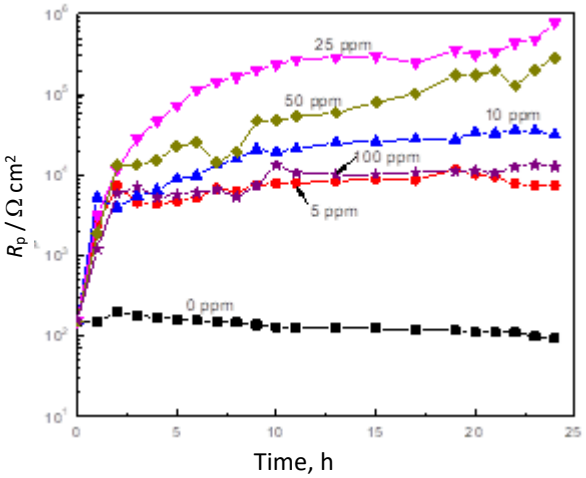

Figure 7. *Effect of inhibitor concentration on R_p value for 1018 carbon steel in CO_2-saturated 3.5 % NaCl solution containing different concentrations of inhibitor at 50 °C*

For uninhibited solution, R_p value remained practically constant throughout the testing time, exhibiting a relatively low value, close to 100 Ω cm^2. A remarkable increase of R_p value was observed as soon as the inhibitor was added into the solution, which is believed to be due to the adsorption of the inhibitor onto the steel surface. As long as the metal surface area covered by the inhibitor increases, the value for R_p increases too. In the same way, as the inhibitor concentration increases, an increase of R_p value was also observed, but only up to the inhibitor concentration of 25 ppm. The

obtained R_p values were up to four orders of magnitude higher than that obtained in the uninhibited solution. With a further increase of the inhibitor concentration, R_p values decreased, which can be due to the electrostatic repulsion between inhibitor molecules, when they are too many and very close to each other that a desorption process occurs.

It was already shown [36] that the tested inhibitor is not a pure compound because it contains fatty acids (Table 2), where the main are oleic and palmitic acids with chemical structures given in Fig. 3, although the presence of myristic and linoleic acids is important also. It is not very clear which one of these compounds is responsible for corrosion inhibition, but it is very likely that it is due to a synergistic effect of different compounds. The presence of N atoms in the imidazole group makes these fatty acids highly susceptible to protonation [37]. However, as established above, organic compound structure affects its performance, and according to Jovancicevic *et al*. [38], it was found that the longer the alkyl group's hydrocarbons chain is, the compound is a more efficient inhibitor. Alternatively, the presence of double bonds into the inhibitor structure improved the inhibitor adsorption onto the steel surface [38]. Thus, the presence of compounds with long hydrophobic chains and double bonds, in addition to the presence of N atoms susceptible to protonation, makes this inhibitor highly efficient.

EIS measurements

In order to elucidate the corrosion mechanism for 1018 carbon steel in CO_2-saturated 3.5 % NaCl solution in the absence and presence of inhibitor, some EIS measurements at the open circuit potential were performed. Figure 8 shows the results presented in both Nyquist and Bode formats.

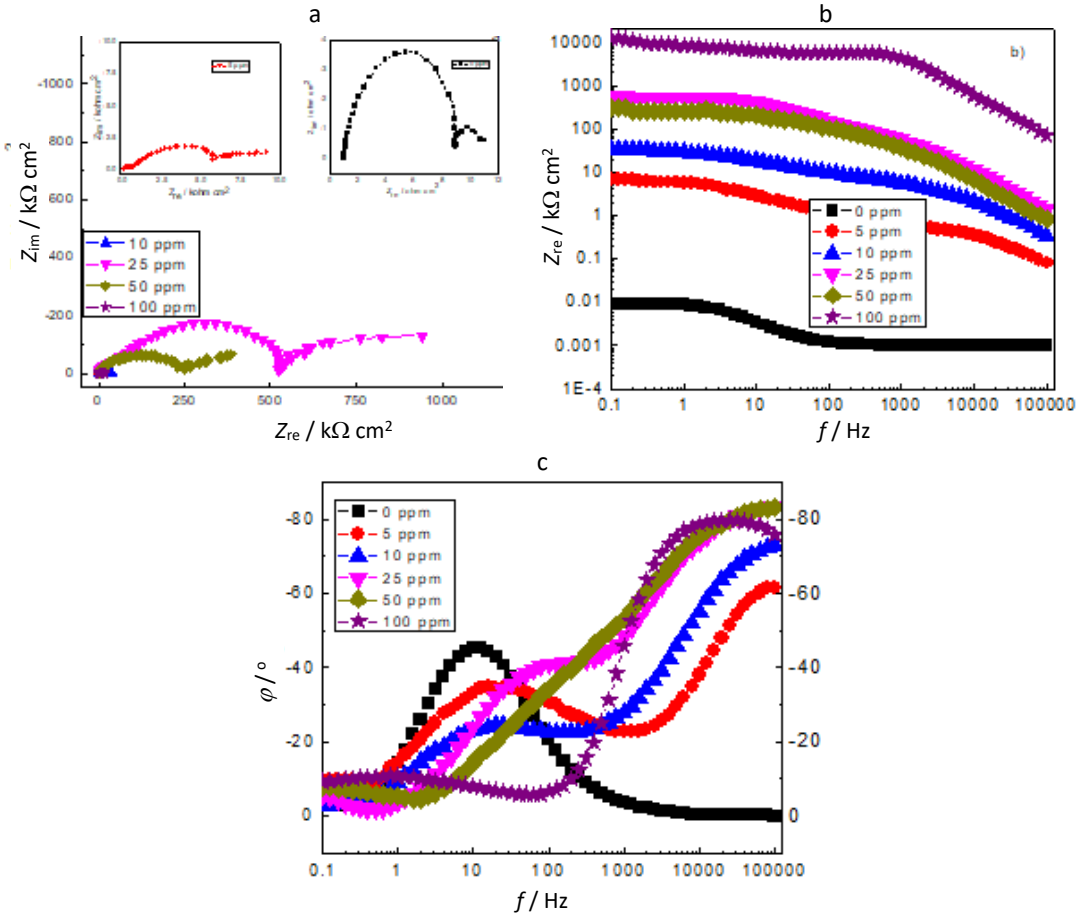

Figure 8. *Effect of inhibitor concentration on: a) Nyquist and b) and c) Bode plots of 1018 carbon steel in CO_2-saturated 3.5 % NaCl solution containing different concentrations of inhibitor at 50 °C*

Nyquist data display two capacitive semicircles, one at high to medium frequencies and the other at the lowest frequencies (Figure 8a). The resulting semicircles seem to be imperfect due to the heterogeneity and roughness of the sample surface. The first, high-frequency semicircle, is related to the formation of corrosion products, whereas the second, lower frequency semicircle, is related to the electrochemical double-layer and charge transfer reaction due to corrosion. The shapes of Nyquist and Bode plots did not change with the addition of inhibitor, indicating that the corrosion mechanism is not affected by inhibitor addition. The semicircle diameters, however, increased with an increase of inhibitor concentration, reaching the highest values at 25 ppm of inhibitor. A further increase of the inhibitor concentration above 25 ppm caused a decrease of semicircle diameters.

On the other hand, Bode plots in the modulus format (Figure 8b) showed that at the lowest frequencies, impedance modulus is the lowest for the solution in the absence of an inhibitor. Impedance modulus increased with the inhibitor concentration, attaining more than four orders higher magnitude with the addition of 25 ppm of inhibitor. A further increase in the inhibitor concentration caused a decrease in the low-frequency impedance modulus value. The modulus impedance value at the lowest frequency takes into account all resistance contributions such as electrolyte or solution resistance (R_s), charge transfer resistance through double electrochemical layer (R_{ct}) and the resistance of the film formed by the corrosion products (R_f). Since the sum of the last two, *i.e.,* $R_{ct} + R_f$ is defined as the polarization resistance value (R_p), we can see that the variation of the lowest frequency impedance modulus value observed in Figure 8b behaves in the same way as R_p in Figure 7.

At higher frequencies, impedance modulus data in Figure 8b show sloping lines characteristic of capacitive impedance responses, where higher impedance values imply lower capacitance values. It is seen in Figure 8b that capacitive impedances increased (capacitance decreased) with the addition of inhibitor up to 25 ppm, and decreased (capacitance increased) for higher inhibitor concentrations. It has already been known that two different electric interface values, such as electrical resistance and capacitance, are inversely proportional [37-43], and thus, an increase in the resistance value decreases the capacitance value. This proves the ability of the studied extract to reduce the aggressive action of the acid medium. According to the Helmholtz model, the reduction in the capacitance value indicates an increase of the double layer thickness, which can be referred to as the development of a compact protective film on the metal surface by the inhibitor adsorption [44-46].

The phase angle Bode plots (Figure 8c) show the presence of two peaks, one at higher and the other at lower frequencies, defining two separate relaxations (RC) time constants characteristic for interfacial and film regions. These suggest two phenomena are happening and that the corrosion process is not only under interfacial charge transfer control.

Surface analysis

SEM micrographs of corroded steel surfaces in CO_2-saturated 3.5 % NaCl solution in the absence and presence of inhibitor are shown in Figure 9. For corroded steel surface in the absence of inhibitor, Figure 9a presents a high area that corroded uniformly, just as predicted by polarization and R_p results.

Similar is observed in Figure 9b, presenting the image of steel surface when 5 ppm of inhibitor were added to the solution, although the corroded surface area is somewhat smaller in the presence of the inhibitor. As the amount of inhibitor was increased further, the corrosion type shifted from uniform to a localized type of corrosion such as pitting corrosion, which is clearly seen in Figure 9c. The surface with the lowest damaged area by corrosion was found for steel corroded in the presence of 25 ppm of inhibitor, shown in Figure 9d. Here, the number of pits is the lowest, as predicted by polarization curves and R_p measurements shown in Figures 3 and 6, respectively.

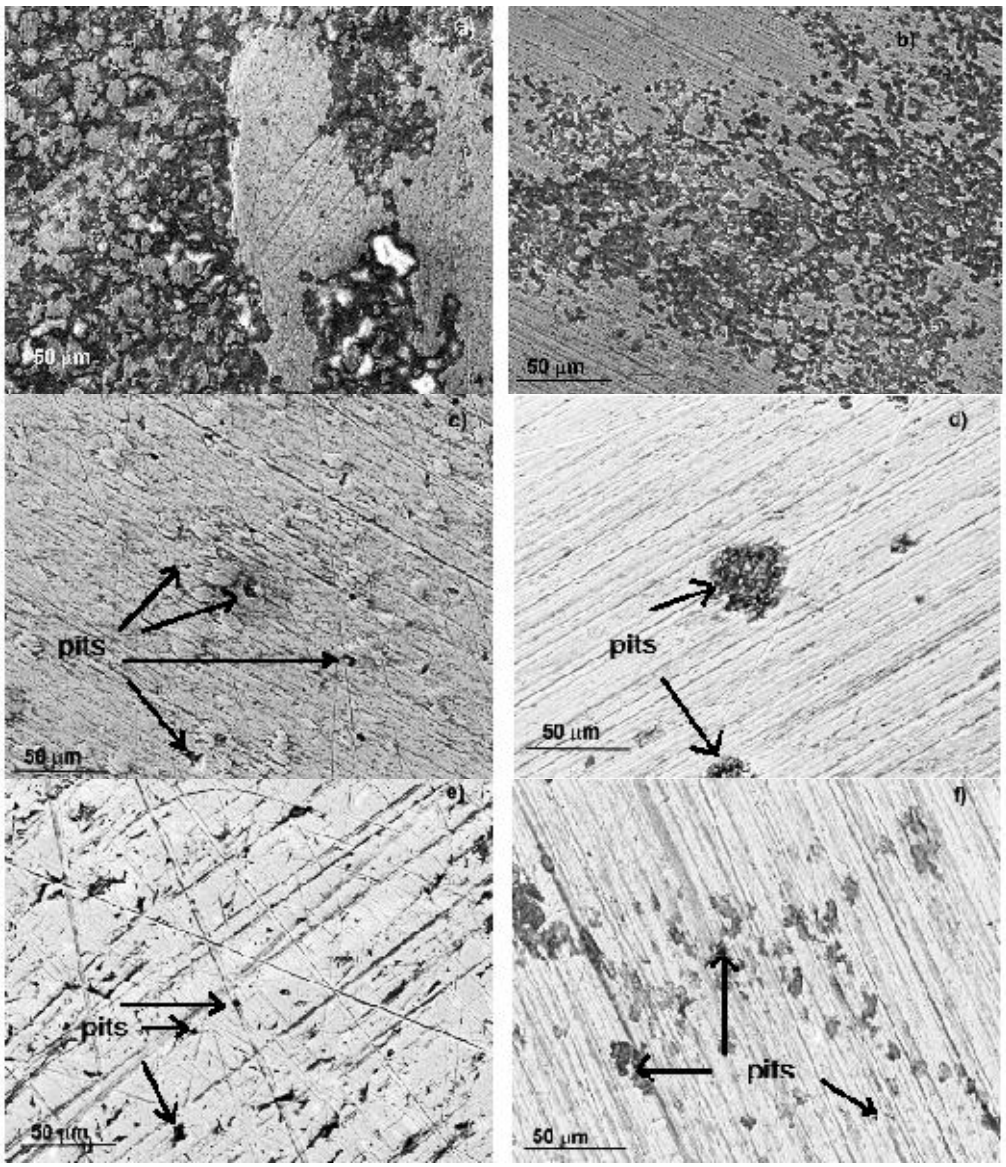

Figure 9. *SEM micrographs of 1018 carbon steel corroded in CO_2-saturated 3.5% NaCl solution at 50 °C containing following concentrations of inhibitor: a) 0; b) 5; c) 10; d) 25; e) 50; f) 100 ppm*

EDS microchemical analysis performed on the corrosion products layer is presented in Figure 10. For specimens corroded in the absence of inhibitor, Figure 10a shows only chemical elements present in the steel and the corrosive environment such as Fe, C and O. For specimens corroded in the presence of the inhibitor (Figure 10b-d), Fe, C and O were also present, but the amounts of C and O were higher than found in specimens corroded in the absence of inhibitor since imidazoline contains both chemical elements. Elements present in the abrasives, such as Al from Al_2O_3 particles and SiC in the abrading paper, were also present.

Thus, the addition of the inhibitor decreased not only the corrosion rate but also the type of corrosion, changing it from the uniform type in the absence of inhibitor to a localized type of corrosion when the inhibitor is added. This is expected since for inhibitor concentrations higher than 5 ppm a passive layer is formed on the top of the steel according to polarization curves shown in Figure 5, and this passive layer can be disrupted, giving place to localized type of corrosion such as pitting.

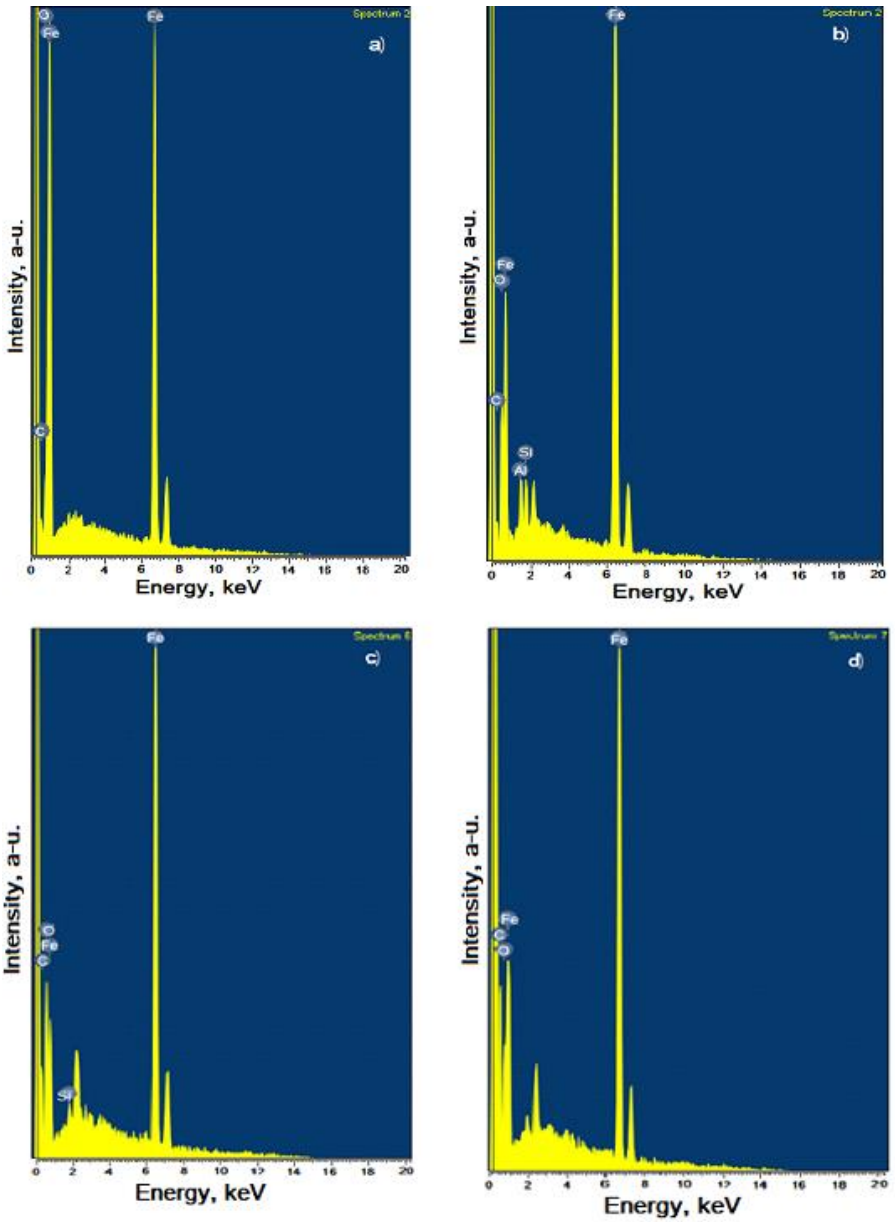

Figure 10. *EDS microchemical analysis of corrosion products layer formed on 1018 carbon steel corroded in CO_2-saturated 3.5% NaCl solution at 50 °C, containing following concentrations of inhibitor: a) 0; b) 5; c) 10; d) 25 ppm*

Corrosion inhibition mechanism

As mentioned above, the obtained imidazoline is chemically adsorbed on the steel surface due to the sharing of charges between molecules and/or the formation of coordinated type bonds. Imidazoline contains a hydrophilic, imidazole group, and a hydrophobic alkyl group given by fatty acids, which present saturated and unsaturated structures. The high inhibitory effect of imidazoline compounds has been related to the structure of the inhibitor due to the nitrogen atoms located in the structural ring, to the long chain of hydrocarbons acting as a barrier against water and chlorides, and finally, to unsaturated double bonds present in the inhibitor which is chemically adsorbed on the surface of Fe (which form a very stable protective film). To give a better explanation about the corrosion inhibition process in the presence of the antioxidant constituents of the extract on the steel surface, a schematic diagram of the adsorption is shown in Figure 11.

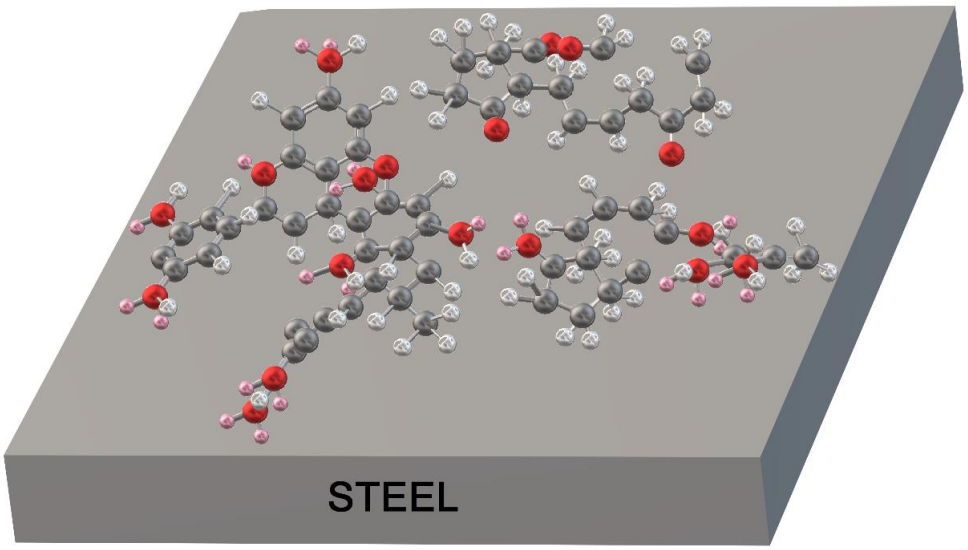

Figure 11. *Chemisorption process between antioxidant constituents in Pouteria sapota extract. Unshared pairs of electrons are in pink color, heteroatoms in red, and π bond orbitals are the dotted line*

Compounds contained in the *Pouteria sapota* extract have a strong electron-donating and chelating capacity with steel, giving the extract the ability to inhibit metal corrosion. This chemisorption is preferable by an electronic interaction between unshared pairs of electrons from heteroatoms and π bond orbitals from the molecules and the benzene rings with the d orbitals on the metallic surface until the formation of a very adherent barrier of molecules.

Conclusions

An imidazoline obtained from fatty acids contained in *Pouteria sapota* seed oil has been evaluated as an inhibitor for CO_2 corrosion of 1018 carbon steel in 3.5 % NaCl at 50 °C. It was found that the main fatty acids are palmitic, oleic, myristic and linoleic acid. The obtained imidazoline was proved to be an excellent mixed-type of inhibitor, which affected both cathodic and anodic reactions but with a stronger effect on the cathodic one. The inhibitor is chemically adsorbed onto the steel surface according to the Langmuir type of adsorption isotherm. Inhibitor efficiency increased with its concentration up to 25 ppm, but after this critical concentration, its efficiency decreased. Polarization curves indicated that I_{corr} value decreased more than four orders of magnitude when 25 ppm of inhibitor were added due to the formation of a passive layer onto the steel surface. This is supported by EIS data that showed two separate relaxation processes due to interfacial and film regions. The type of corrosion was affected by the addition of inhibitor, changing from the uniform to a localized type of corrosion.

References

[1] T. Pojtanabuntoeng, M. Salasi, *Electrochimica Acta* **258** (2017) 442-452. https://doi.org/10.1016/j.electacta.2017.11.081

[2] T. Doi, T. Adachi, T. Kudo, N. Usuki, *Corrosion Science* **117** (2020) 108931. https://doi.org/10.1016/j.corsci.2020.108931

[3] F. E. Abeng, V. Anadebe, P. Y. Nkom, K. J. Uwakwe, E. G. Kamalu, *Journal of Electrochemical Science and Engineering* **11(1)** (2021) 11-26. https://doi.org/10.5599/jese.887

[4] W. Boukhedena, S. Deghboudj, *Journal of Electrochemical Science and Engineering* **11(4)** (2021) 227-239. https://doi.org/10.5599/jese.1050

[5] S. Bashir, V. Sharma, H. Lgaz, I. M. Chung, A. Singh, A. Kumar, *Journal of Molecular Liquids* **263** (2018) 454-462. https://doi.org/10.1016/j.molliq.2018.04.143

[6] R. T. Loto, C. A. Loto, *Journal of Materials Research and Technology* **7(3)** (2018) 231-239. https://doi.org/10.1016/j.jmrt.2017.07.004
[7] A. Kahyarian, A. Schumaker, B. Brown, S. Nesic, *Electrochimica Acta* **258** (2017) 639-652. https://doi.org/10.1016/j.electacta.2017.11.109
[8] M. Chellouli, D. Chebabe, A. Dermaj, H. Erramli, N. Bettach, N. Hajjaji, M. P. Casaletto, C. Cirrincione, A. Privitera, A. Srhiri, *Electrochimica Acta* **204** (2016) 50-59. https://doi.org/10.1016/j.electacta.2016.04.015
[9] L. Pezzato, M. Lago, K. Brunelli, M. Breda, I. Calliari, *Journal of Materials Engineering and Performance* **27(8)** (2018) 3859-3668. https://doi.org/10.1007/s11665-018-3408-5
[10] X. Liu, J. Jing, Q. Fu, Q. Li, S. Li, Y. Qu, A. Singh, *International Journal of Electrochemical Science* **14(6)** (2019) 8819-8835. https://doi.org/10.20964/2019.09.26
[11] G. T. Galo, A. de A. Morandim-Gianneti, F. Cotting, I. V. Aoki, I. Pacifico Aquino, *Metals* and *Materials International* **27(10)** (2021) 3238-3249. https://doi.org/10.1007/s12540-020-00679-9
[12] M. Abdallah, H. M. Altass, A. S. Al-Gorair, J. H. Al-Fahemi, B. A .A. L. Jahdaly, K. A. Soliman, *Journal of Molecular Liquids* **323** (2021) 115036. https://doi.org/10.1016/j.molliq.2020.115036
[13] A. Carmona-Hernandez, E. Vazquez-Velez, J. Uruchurtu-Chavarin, J. G. Gonzalez-Rodriguez, L. Martinez-Gomez, *Green Chemistry Letters and Reviews* **12(1)** (2019) 89-99. https://doi.org/10.1080/17518253.2019.1578997
[14] M. Abdallah, A. Al Bahir, H. M. Altass, A. Fawzy, N. El Guesmi, A. S. Al-Gorai, F. Benhiba, I. Warad, A. Zarrouk, *Journal of Molecular Liquids* **330** (2021) 115702**.** https://doi.org/10.1016/j.molliq.2021.115702
[15] A. Chraka, I. Raissouni, N. B. Seddik, *Journal of Bio- and Tribo-Corrosion* **6(1)** (2020) 80. https://doi.org/10.1007/s40735-020-00377-4
[16] M. Abdallah, H. M. Altass, B. A. AL Jahdaly, M .M. Salem, *Green Chemistry Letters and Reviews* **11(3)** (2018) 189-196. https://doi.org/10.1080/17518253.2018.1458161
[17] M. Abdallah, K. A. Soliman, A. S. Al-Gorair, A. Al Bahir, J. H. Al-Fahemi, M. S. Motawea, S. S. Al-Juaid, *RSC Advances* **11(28)** (2021) 17092-17107. https://doi.org/10.1039/D1RA01010G
[18] A. H. Al-Bagawi, *Green Chemistry Letters and Reviews* **14(1)** (2021) 73-84. https://doi.org/10.1080/17518253.2020.1862923
[19] G. Salinas-Solano, J. Porcayo-Caldero, L. M. Martinez de la Escalera, J. Canto, M. Casales-Diaz, O. Sotelo-Mazon, J. Henao, L. Martinez-Gomez, *Industrial Crops and Products* **119** (2018) 111-124. https://doi.org/10.1016/j.indcrop.2018.04.009
[20] A. Cruz-Zabalegui, E. Vazquez-Velez, G. Galicia-Aguilar, M. Casales-Diaz, R. Lopez-Sesenes, J. G. Gonzalez-Rodriguez, L. Martinez-Gomez, *Industrial Crops and Products* **133** (2019) 203-211. https://doi.org/10.1016/j.indcrop.2019.03.011
[21] R. M. Martínez-Casares, H. Pérez, N. Manjarrez, M. Solís-Oba, L. Ortega, A. Solís, *Industrial Crops and Products* **153** (2020) 112606. https://doi.org/10.1016/j.indcrop.2020.112606
[22] J. Martínez-Castillo, N. H. Blancarte-Jasso, G. Chepe-Cruz, N. G. Nah-Chan, M. M. Ortiz-García, *Tree Genetics & Genomes* **15** (2019) 61-68. https://doi.org/10.1007/s11295-019-1368-z
[23] E. Murillo, A. Agócs, V. Nagy, S. B. Király, T. Kurtán, E. M. Toribio, J. Lakey-Beitia, J. Deli, *Chirality* **32(5)** (2020) 579-587. https://doi.org/10.1002/chir.23206
[24] E. Reyes-Dorantes, J. Zuñiga-Díaz, A. Quinto-Hernandez, J. Porcayo-Calderon, J. G. Gonzalez-Rodriguez, L. Martinez-Gomez, *Journal of Chemistry* **2017** (2017) 2871034. https://doi.org/10.1155/2017/2871034
[25] L. Zeng, G. A. Zhang, X. P. Guo, C.W. Chai, *Corrosion Science* **90** (2015) 202-215. https://doi.org/10.1016/j.corsci.2014.10.011

[26] H. Liu, T. Gu, G. Zhang, H. Liu, Y. F. Cheng, *Corrosion Science* **136** (2018) 47-59. https://doi.org/10.1016/j.corsci.2018.02.038
[27] Z, Liu, X. Gao, L. Du, J. Li, P. Li, C. Yu, R. D. K .Misra, Y. Wang, *Electrochimica Acta* **232** (2017) 528-541. https://doi.org/10.1016/j.electacta.2017.02.114
[28] D. Burkle, R. De Motte, W. Taleb, A. Kleppe, T. Comyn, S.M. Vargas, A. Neville, R. Barker, *Electrochimica Acta* **255** (2017) 127-144. https://doi.org/10.1016/j.electacta.2017.09.138
[29] K. Rahmouni, M. Keddam, A. Srhiri, H. Takenouti, *Corrosion Science* **47(12)** (2005) 3249-3266. https://doi.org/10.1016/j.corsci.2005.06.017
[30] M. Vemula, A. S. Shaikh, S. Chilakala, M. Tallapally, V. Upadhyayula, *Food Additives and Contaminants A* **37(10)** (2020) 1601-1609. https://doi.org/10.1080/19440049.2020.1794055
[31] Z. Zheng, J. Hu, N. Eliaz, L. Zhou, X. Yuan, X. Zhong, *Corrosion Science* **194** (2021) 109930. https://doi.org/10.1016/j.corsci.2021.109930
[32] O. Sotelo-Mazon, S. Valdez, J. Porcayo-Calderon, M. Casales-Diaz, J. Henao, G. Salinas-Solano, J. L. Valenzuela-Lagarda, L. Martinez-Gomez, *Green Chemistry Letters and Reviews* **12(3)** (2019) 255-270. https://doi.org/10.1080/17518253.2019.1629698
[33] P. C. Okafor, C. B. Liu,Y. J. Zhu, Y. G. Zheng, *Industrial Engineering and Chemical Research* **50(12)** (2011) 7273-7281. https://doi.org/10.1021/ie1024112
[34] S. A. Pauline, S. Sahila, C. Gopalakrishnan, S. Nanjundan, N. Rajendran, *Progress in Organic Coatings* **72(3)** (2011) 443-452. https://doi.org/10.1016/j.porgcoat.2011.06.001
[35] Z. Liu, X. Gao, L. Du, J. Li, P. Li, C. Yu, R. D. K. Misra, Y. Wang, *Electrochimica Acta* **232** (2017) 528-541. https://doi.org/10.1016/j.electacta.2017.02.114
[36] D. Burkle, R. De Motte, W. Taleb, A. Kleppe, T. Comyn, S. M. Vargas, A. Neville, R. Barker, *Electrochimica Acta* **255** (2017) 127-144. https://doi.org/10.1016/j.electacta.2017.09.138
[37] K. Rahmouni, M. Keddam, A. Srhiri, H. Takenouti, *Corrosion Science* **47(12)** (2005) 3249-3266. https://doi.org/10.1016/j.corsci.2005.06.017
[38] V. Jovancicevic, S. Ramachandran, P. Prince, *Corrosion* **55(5)** (1999) 449-456. https://doi.org/10.5006/1.3284006
[39] M. Vemula, A. S. Shaikh, S. Chilakala, M. Tallapally, V. Upadhyayula, *Food Additives and Contaminants: Part A* **37(10)** (2020) 1601-1609. https://doi.org/10.1080/19440049.2020.1794055
[40] Z. Zheng, J. Hu, N. Eliaz, L. Zhou, X. Yuan, X. Zhong, *Corrosion Science* **194** (2022) 109930. https://doi.org/10.1016/j.corsci.2021.109930
[41] O. Sotelo-Mazon, S. Valdez, J. Porcayo-Calderon, M. Casales-Diaz, J. Henao, G. Salinas-Solano, J. L. Valenzuela-Lagarda, L. Martinez-Gomez, *Green Chemistry Letters and Reviews* **12(3)** (2019) 255-270. https://doi.org/10.1080/17518253.2019.1629698
[42] P. C. Okafor, C. B. Liu, Y. J. Zhu, Y. G. Zheng, *Industrial & Engineering Chemistry Research* **50(12)** (2011) 7273-7281. https://doi.org/10.1021/ie1024112
[43] S. A. Pauline, S. Sahila, C. Gopalakrishnan, S. Nanjundan, N. Rajendran, *Progress in Organic Coatings* **72(3)** (2011) 443-452. https://doi.org/10.1016/j.porgcoat.2011.06.001
[44] C. Verma, L. O. Olasunkanmi, E. E. Ebenso, M. A. Quraishi, *Results in Physics* **8** (2018) 657-670. https://doi.org/10.1016/j.rinp.2018.01.008
[45] B. Chugh, A. K. Singh, S. Thakur, B. Pani, A. K. Pandey, H. Lgaz, I.-M. Chung, E. E. Ebenso, *Journal of Physical Chemistry C* **123(37)** (2019) 22897-22917. https://doi.org/10.1021/acs.jpcc.9b03994
[46] P. Khodaei, M. I. Shabani-Nooshabadi, M. Behpour, *Progress in Organic Coatings* **136** (2019) 105254. https://doi.org/10.1016/j.porgcoat.2019.105254